Modèles réduits pour l'etude des mécanismes et de la modulation de l'oscillation australe El Niño

Sulian Thual

Université de Toulouse

THÈSE

En vue de l'obtention du

DOCTORAT DE L'UNIVERSITÉ DE TOULOUSE

Délivré par : *l'Université Toulouse III – Paul Sabatier*
Discipline ou spécialité : *Interactions Océan-Atmosphère et Climat*

Présentée et soutenue par SULIAN THUAL
Le 18 octobre 2012

Titre :

Modèles Réduits pour l'Etude des Mécanismes et de la Modulation de l'Oscillation Australe El Niño

---

Jury :

Nicholas Hall, Université Toulouse III -LEGOS, Président
Gilles Reverdin, CNRS - LOCEAN, Rapporteur
Fei-Fei Jin, University of Hawaii at Manoa, Rapporteur
Xavier Rodó, Institut Català de Ciències del Clima, Examinateur
Francis Codron, CNRS - LMD, Examinateur
Boris Dewitte, IRD - LEGOS, Directeur de thèse
Nadia Ayoub, CNRS - LEGOS, Co-directrice de thèse

Ecole doctorale : *Sciences de l'Univers, de l'Environnement et de l'Espace (SDU2E)*
Unité de recherche : *Laboratoire d'Etudes en Géophysique et Océanographie Spatiales (LEGOS)*
Directeurs de Thèse : *Boris Dewitte (directeur de recherche IRD)*
et Nadia Ayoub (chargée de recherche CNRS)

J’aimais ce joli temps où je t’aimais

Ouapdapdapdoua tu m’avais plu

L’amour est à 100 kilomètres par temps calme

Je trempe ma main dans ta main

Et il fait beau

Manu Galure, Quelque chose en Mi.

Remerciements

Voici venu le moment de remercier ceux qui, de près ou de loin, m'ont permis de mener à bien cette thèse.

Je tiens à remercier Boris Dewitte de m'avoir fait confiance, et ce déjà bien avant la thèse, lorsque j'ai commencé à travailler au Pérou. Sa passion pour l'océanographie a été contagieuse. Son engouement, sa disponibilité et ses conseils m'ont beaucoup formé. Je garde un bon souvenir de ces nombreuses années sous sa direction, scientifiquement et humainement. Je remercie vivement Nadia Ayoub d'avoir accepté la co-direction de cette thèse. Tout était à construire sur le sujet d'assimilation de données et elle a su, à travers des discussions patientes et approfondies, me guider dans ce travail conséquent et m'y passionner. Je la remercie aussi pour ses encouragements et sa subtilité dans les moments difficiles. Je remercie évidemment Fei-Fei Jin et Gilles Reverdin qui ont accepté d'être rapporteurs de ma thèse, ainsi que les autres membres du jury : Nick Hall, Xavier Rodó, et Francis Codron. Enfin, je remercie le CNRS et la région Midi-Pyrénées d'avoir financé ma thèse ainsi que Yves du Penhoat puis Yves Morel de m'avoir accueilli au LEGOS.

Je voudrais remercier l'ensemble des chercheurs du LEGOS qui m'ont reçu pour des discussions et des interactions scientifiques, mêmes courtes ou informelles. Merci à l'équipe ECOLA en général, le GOAT, Serena Illig, Katerina Goubanova, Pierre de Mey, Nick Hall, Patrick Marchesiello, Thierry Delcroix, Isabelle Dadou, Laurent Roublou et Benoit Meyssignac. Je remercie très vivement les chercheurs péruviens de l'IGP, Ken Takahashi et Kobi Mosquera, ainsi que l'IMARPE et l'IRD Pérou, qui m'ont accueilli dans un cadre de travail chaleureux lors de plusieurs années d'expatriation. Merci aussi aux professeurs Soon-Il An et Sang-Wook Yeh ainsi que leurs élèves pour leur accueil lors de passages à Séoul. Je remercie également Martine Mena, Nadine Lacroux, Brigitte Cournou et Marie-Claude Cathala au LEGOS, ainsi que Miriam Soto à l'IRD Pérou, pour leur aide attentionnée dans mes démarches administratives, et pour leur bonne humeur.

Un très grand merci aux compagnons de routes du LEGOS pour tous les bons moments partagés : Florent, Rajesh et Maria dans les lointains algécos, Vanessa, Hindumathi et Minh, et l'ensemble des thèsards.

Enfin, je voudrais remercier ma famille pour leur soutien indéfectible. Je tiens à remercier tout particulièrement mon père Olivier, qui a su me donner l'envie de faire de la recherche, et qui m'a toujours transmis et écouté lors de ces longues années d'étude. Je garde en mémoire des discussions enflammées de maths et de mécanique des fluides, après les repas en famille. Un grand merci à ma mère Véronique, qui a déniché les dernières fautes de français du manuscrit. Enfin, je remercie du fond du cœur ma femme Andrea, pour sa présence à mes côtés, son soutien, et pour tout ce que nous partageons.

Résumé

L'Oscillation Australe El Niño (ENSO pour El Niño Southern Oscillation) est la fluctuation climatique la plus intense sur Terre après le cycle saisonnier. L'observation, la compréhension et la prévision de cette fluctuation aux retombées mondiales sont des enjeux scientifiques majeurs. Cette thèse documente divers aspects d'ENSO tels que ses mécanismes, sa modulation et sa prévision. Ces divers aspects sont abordés en développant une hiérarchie de modèles du Pacifique équatorial, de complexité croissante, qui s'étend de modèles conceptuels à une méthode d'assimilation de données dans un modèle de complexité intermédiaire.

Nous étudions dans un premier temps les mécanismes de formation d'ENSO. Nous développons une dérivation alternative du modèle conceptuel de recharge/décharge où ENSO résulte d'un ajustement de la thermocline équatoriale à échelle de bassin. Nous implémentons par ailleurs un diagnostic original dans un modèle d'instabilités couplées équatoriales, ce qui met en avant un nouveau mécanisme de formation d'ENSO où les réflexions aux frontières océaniques jouent un rôle secondaire. La stratification moyenne de l'océan contribue à la modulation décenalle des caractéristiques d'ENSO. Cette relation est abordée dans un nouveau modèle réduit qui prend en compte les premiers modes baroclines d'un océan continûment stratifié. L'espace des solutions du modèle est exploré, indiquant un contrôle de la stabilité d'ENSO par les caractéristiques de la thermocline équatoriale. La sensibilité à la stratification au cours des dernières décennies est mise en perspective avec la sensibilité aux rétroactions thermodynamiques et atmosphériques. Nous soulignons en particulier certaines limitations des méthodes usuelles d'estimation de la rétroaction de thermocline dans le Pacifique central. Finalement, nous implémentons une méthode de Filtre de Kalman d'Ensemble dans un modèle intermédiaire du Pacifique équatorial déjà existant, afin d'assimiler des observations de niveau de la mer et d'initialiser des prévisions rétrospectives d'ENSO. Nous montrons que la contrainte majeure du modèle porte sur les modes de bassin qui sont associés au processus de recharge/décharge du Pacifique équatorial.

Notre travail fournit un formalisme pour diagnostiquer la modulation des caractéristiques d'ENSO dans les observations, les prévisions et projections climatiques. Les résultats soutiennent la nécessité d'étendre la compréhension des mécanismes d'ENSO, afin de rendre compte de la diversité des régimes observés et d'améliorer les prévisions.

Mots clefs : Oscillation Australe El Niño, Modes Baroclines, Modèles Conceptuels, Modèles de Complexité Intermédiaire, Assimilation de Données, Filtre de Kalman d'Ensemble, Variabilité Décennale, Processus de Recharge/Décharge, Instabilité Absolue/Convective.

Abstract

The El Niño Southern Oscillation (ENSO) is the most intense climatic fluctuation on Earth after the seasonal cycle. The observation, understanding and forecast of this fluctuation with worldwide impacts are major scientific issues. This thesis (entitled “Simple Models for Understanding the Mechanisms and Modulation of ENSO”) documents various aspects of ENSO such as its mechanisms, its modulation and its forecast. Those various aspects are tackled by developing a hierarchy of models of the equatorial Pacific, of increasing complexity, ranging from conceptual models to a data assimilation method in an intermediate complexity model.

We study at first mechanisms of ENSO formation. We develop an alternative derivation of the recharge/discharge conceptual model where ENSO arises from a basin-wide adjustment of the equatorial thermocline. We also implement an original diagnostic in a model of equatorial coupled instabilities, which evidences a new mechanism of ENSO formation where reflections at the ocean boundaries are secondary. The background ocean stratification contributes to the decadal modulation of ENSO characteristics. This relation is adressed in a new reduced model that takes into account the gravest baroclinic modes of a continusouly stratified ocean. The space of model solutions is explored, indicating a control on ENSO stability by characteristics of the equatorial thermocline. The sensitivity to stratification over the recent decades is put in perspective with the sensitivity to thermodynamic and atmospheric feedbacks. We stress in particular certain limitations of usual methods of estimation of the thermocline feedback in the central Pacific. Finally, we implement an Ensemble Kalman Filter method in an already existing intermediate model of the equatorial Pacific, in order to assimilate sea level observations and to initialize retrospective forecasts. We show that the major model constraint is on the basin modes that are associated to the recharge/discharge process of the equatorial Pacific.

Our work provides a formalism to diagnose the modulation of ENSO characteristics in observations, climate projections and forecasts. Results support the need to extent the understanding of ENSO mechanisms, in order to account for the diversity of observed regimes and to improve forecasts.

Keywords: El Niño Southern Oscillation, Baroclinic modes, Conceptual models, Intermediate Complexity Models, Data assimilation, Ensemble Kalman Filter, Decadal variability, Recharge/Discharge process, Absolute/convective instability.

Table of Contents

Préambule

Les sciences du climat ont connu un véritable essor au cours des dernières décennies, grâce à des avancées technologiques telles que les réseaux d'observations ou la simulation numérique, tout en étant l'objet d'intérêts scientifiques, économiques et sociaux grandissants. Historiquement, l'étude de la météorologie et de l'océanographie consistait à cartographier les vents régionaux et les courants de navigation ainsi qu'éventuellement leurs variations selon la saison. Cette vision traditionnelle, locale et annuelle, est bien illustrée par la définition du mot climat donnée dans le dictionnaire, qui désigne les conditions météorologiques prévalentes d*'une région au cours de l'année*. Aujourd'hui, les sciences du climat se sont largement étendues au-delà de cette définition. Nous savons maintenant qu'il existe des fluctuations importantes du climat autour du cycle saisonnier. Ces fluctuations peuvent connecter des régions très éloignées et varier dans une large gamme de fréquences. Pour cette raison, on distingue en général le cycle annuel d'une région, appelé climatologie, des fluctuations climatiques. Des fluctuations climatiques connues sont par exemple l'Oscillation Australe El Niño, la mousson asiatique, ou encore l'Oscillation Nord Atlantique qui varient sur des mois voire des années et affectent simultanément des continents entiers. Le réchauffement climatique est sans précédent dans l'histoire du climat, et, contrairement aux fluctuations naturelles mentionnées précédemment, ce dernier est d'origine anthropique. Les causes (les émissions de gaz à effet de serre) ainsi que les retombées (le réchauffement climatique) de ce phénomène sont mondiales. Nous avons aujourd'hui une vision mondiale du climat, au sens où nous savons que les différents climats de la planète sont connectés.

La fluctuation climatique la plus énergétique connue sur terre est l'Oscillation Australe El Niño (ENSO pour El Niño Southern Oscillation). Elle consiste en une modification de la circulation de l'océan et de l'atmosphère qui affecte l'ensemble du Pacifique équatorial (de l'Australie au Pérou environ) et qui se répète tous les 2 à 7 ans. La découverte de cette fluctuation est représentative de l'évolution des sciences du climat. En accord avec la définition traditionnelle du climat, le nom El Niño se référait autrefois à un courant chaud qui était observé autour de Noël le long des côtes péruviennes. Il signifie garçon en espagnol en référence à la naissance de Jésus à la même époque. Le nom a été donné par les pécheurs péruviens, peut être avec une pointe d'ironie car ce courant chaud raréfiait considérablement leurs prises. A cette époque personne ne s'imaginait que ce courant chaud avait une contrepartie à l'autre bout du Pacifique. C'est pourtant en essayant de prévoir l'intensité de la mousson indienne que Sir Walker découvrit pour la première fois, vers le début du 20eme siècle, l'existence d'une connexion entre l'est et l'ouest du Pacifique. Il observa que les pressions atmosphériques de surface relevées à Tahiti et Darwin étaient remarquablement opposées et oscillaient interannuellement, ce qu'il qualifia de phénomène d'Oscillation Australe. Il restait encore à relier les variations de l'atmosphère à celles de l'océan. La première vision d'ensemble fut donnée par J. Bjerknes dans les années 1960, qui relia le courant chaud péruvien et l'Oscillation Australe en un même phénomène : le cycle ENSO. Le cycle ENSO est une oscillation incessante du Pacifique équatorial entre un état chaud et

un état froid avec un cycle irrégulier qui dure entre 2 et 7 ans. Le nom El Niño désigne aujourd'hui l'état chaud de ce cycle, pendant lequel on peut observer non seulement le courant péruvien mais aussi un ensemble de conditions associées dans le Pacifique équatorial. Dans les années 80, les scientifiques ont nommé l'état froid du cycle La Niña (fille en espagnol), par opposition à l'état chaud El Niño.

Chapitre

1. Introduction

Dans ce chapitre, nous faisons un rappel de l'état des connaissances sur l'Oscillation Australe El Niño (ENSO pour El Niño Southern Oscillation). Cette présentation est non-exhaustive et porte une attention particulière sur les mécanismes de formation, la modulation et la prévision d'ENSO, éléments qui seront repris dans les chapitres suivants. A la fin de l'introduction, nous présentons les motivations de cette thèse ainsi qu'un plan du manuscrit.

Le Pacifique équatorial est le siège d'une circulation atmosphérique et océanique intense (la circulation de Walker) qui est reliée à la circulation climatique générale. Cette circulation équatoriale est déstabilisée lors des évènements El Niño, et intensifiée lors des évènements La Niña. L'oscillation interanuelle entre états El Niño et La Niña constitue le cycle ENSO, reconnu comme la fluctuation climatique la plus énérgétique au monde après le cycle saisonnier. Les modèles réduits de type oscillateur décrivent raisonnablement cette dynamique, qui a pour origine une interaction couplée entre l'océan et l'atmosphère. Les théories actuelles expliquent également l'irrégularité du cycle ENSO ainsi que la modulation de ses caractéristiques à échelle décennale.

Le phénomène ENSO a des retombées mondiales et ainsi sa prévision est un enjeu sociétal majeur. Cette prévision est permise par un large réseau d'observations ainsi qu'une vaste hiérarchie de modèles de complexité croissante. Les modèles actuels prévoient le phénomène de manière réaliste à échéance de 6 à 12 mois, bien que les avancées en modélisation laissent envisager que cette limite puisse être repoussée. La modélisation d'ENSO dans les projections climatiques est également un enjeu majeur pour comprendre les retombées futures du changement climatique.

1.1. L'Oscillation Australe El Niño

1.1.1. La Circulation de Walker

La principale source d'énergie que reçoit la surface terrestre vient du rayonnement solaire. Cet apport n'est pas uniformément réparti. Il est en particulier maximal à l'équateur et minimal aux pôles en raison de l'inclinaison de la Terre. Pour redistribuer l'excédent d'énergie de l'équateur vers les pôles, une immense machine thermique est en place avec une circulation de grande échelle dans l'océan et l'atmosphère. La circulation atmosphérique générale est représentée en figure 1.1. Elle redistribue environ la moitié de l'excédent d'énergie. Cette circulation est à la fois méridionale et zonale, avec une symétrie entre l'hémisphère nord et l'hémisphère sud. La circulation méridionale s'organise en plusieurs cellules qui communiquent de proche en proche (la cellule de Hadley, puis la cellule de Ferrel et enfin la cellule polaire). La circulation zonale est constituée de vents d'est (i.e. dirigés vers l'ouest) en surface à l'équateur et aux pôles et de vents d'ouest en altitude aux latitudes moyennes (le jet-stream). Cette géométrie est due à la force de Coriolis, qui en raison de la rotation de la Terre induit une déviation des courants de grande échelle (vers la droite dans l'hémisphère nord, et vers la gauche dans l'hémisphère sud). Cette circulation atmosphérique s'accompagne d'une importante circulation océanique de surface, dont les courants s'organisent à grande échelle en gyres qui suivent le sens de rotation de l'atmosphère. Une circulation océanique de profondeur, la circulation thermohaline, redistribue également l'excédent d'énergie, de manière beaucoup plus lente mais plus efficace en raison de la capacité calorifique de l'eau (mille fois plus importante que celle de l'air). La circulation du Pacifique équatorial (lieu du phénomène ENSO) est fortement liée à la circulation générale. Elle est marquée par une circulation atmosphérique de surface orientée vers l'ouest (les alizés), une circulation océanique de surface également orientée vers l'ouest, ainsi qu'une intense convection atmosphérique (dans la zone de convergence intertropicale).

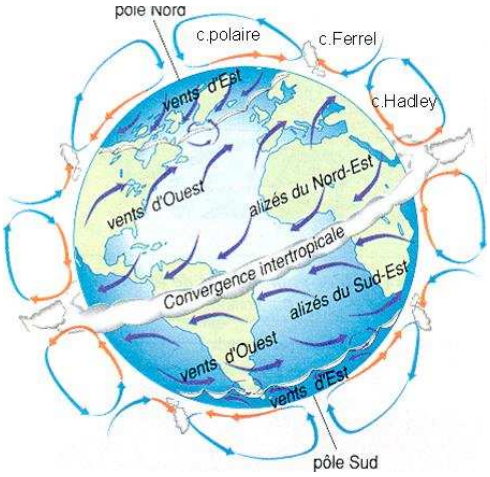

Figure 1.1 : Schéma de la circulation atmosphérique générale (http://www.educnet.education.fr)

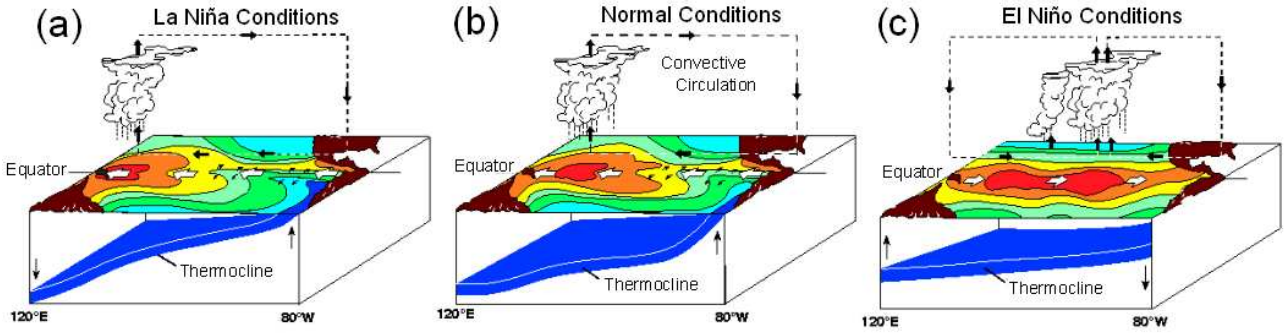

Figure 1.2 : Représentation de l'état (a) La Niña, (b) de référence, (c) El Niño du Pacifique équatorial. Sont indiqués les températures de surface de la mer (couleurs), la profondeur de la thermocline, le sens de circulation des masses d'air (flèches noires) et des masses d'eaux (flèches blanches), ainsi que les zones de convection atmosphérique (nuages) (Source : NOAA).

L'état moyen du Pacifique équatorial (obtenu en moyennant les conditions dans le temps) est représenté sur la figure 1.2.b. De manière générale, les eaux chaudes de l'océan (moins denses) sont situées en dessous de la surface et au dessus des eaux froides de profondeur (plus denses). Ce volume d'eaux chaudes, ou contenu thermique, est délimité par la surface appelée thermocline qui le sépare des eaux froides de profondeur : plus la thermocline est profonde et plus la réserve d'eaux chaudes est importante. Le Pacifique équatorial contient les réserves d'eaux chaudes les plus importantes de la planète, en raison de son ensoleillement maximal. Toutefois, la circulation océanique transporte ces eaux vers l'ouest. Ce sont notamment les vents de surface (les alizés) qui entretiennent ce transport océanique par friction. En conséquence le volume d'eaux chaudes est situé à l'ouest du Pacifique équatorial, ce qui se traduit par une thermocline plus profonde et des températures de surface plus élevées. On nomme cette zone la piscine d'eaux chaudes, ou Warm Pool. A l'est, les eaux sont renouvelées par des eaux plus froides (par transport d'Ekman vertical ou méridien) et on nomme cette zone la langue d'eaux froides. Aussi, le niveau moyen de la mer est de 60 cm plus haut à l'ouest qu'à l'est, tandis qu'en subsurface la thermocline est de 100 m plus profonde. Le gradient zonal de température de l'océan entretient une circulation atmosphérique zonale en altitude dans laquelle les masses d'air s'élèvent par convection au-dessus des eaux chaudes de l'ouest puis subsident au-dessus des eaux froides de l'est. Cette circulation d'altitude se boucle avec les vents alizés en surface pour former une cellule de convection zonale, la cellule de Walker. On retrouve une cellule similaire à l'équateur dans l'océan Atlantique, et une cellule inversée dans l'océan Indien. Par ailleurs la variabilité océanique et atmosphérique de ces trois océans est en partie connectée (Illig et Dewitte, 2006; Jansen et al., 2009; Chen, 2011), mais ce sujet ne sera pas abordé ici.

Cet état de référence du Pacifique équatorial peut toutefois être déstabilisé pour basculer en état El Niño (figure 1.2.c), ou de manière opposée, La Niña (figure 1.2.a). On attribue de manière générale cette déstabilisation à la rétroaction de Bjerknes, dans laquelle la cellule atmosphérique de Walker et le gradient zonal de température de l'océan s'intensifient ou s'atténuent mutuellement (Bjerknes, 1969). En supposant

une légère intensification de la cellule de Walker par rapport à l'état de référence, les alizés forcent un transport océanique additionnel vers l'ouest, ce qui intensifie le gradient zonal de température de l'océan. En retour, le gradient zonal de température intensifie la convection à l'ouest et la subsidence à l'est, et donc la cellule de Walker. En conséquence la perturbation initiale est amplifiée, ce qui peut conduire le système à l'état La Niña, marqué par un gradient zonal de température et une cellule de Walker plus intense. On peut suivre le même raisonnement pour une légère réduction de la cellule de Walker, ce qui peut conduire le système en état El Niño. En état El Niño, les alizés s'affaiblissent et les eaux chaudes de l'ouest envahissent le reste du bassin. Comme la zone de convection atmosphérique suit le déplacement des eaux les plus chaudes, pour des épisodes de grande ampleur où ces eaux atteignent le centre du Pacifique, il est possible d'observer une double cellule de convection atmosphérique avec des subsidences à la fois dans l'est et l'ouest. Ainsi l'état El Niño n'est pas exactement l'état opposé à La Niña.

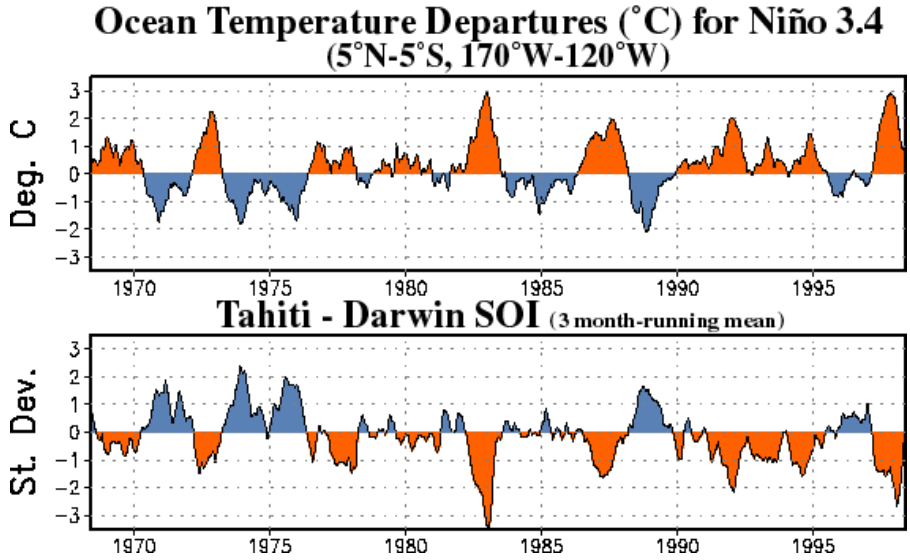

Figure 1.3 : Evolution temporelle des indices Nino3.4 SSTA et SOI (Source : NOAA).

Pour caractériser l'état du Pacifique à un instant donné, on utilise des indices d'anomalies représentatifs de la grande échelle, tels que par exemple l'indice Niño 3.4-SST ou l'indice SOI qui sont montrés en figure 1.3. Pour calculer ces indices, on retire la climatologie (i.e. les moyennes saisonnières) du signal total. Un indice de temperature positif par exemple signifie un état anormalement chaud par rapport aux moyennes saisonnières. L'indice Niño 3.4-SSTA mesure la température des eaux de surface moyennée le long de l'équateur (170°W-120°W, 5°N-5°S). Il est positif pendant El Niño et négatif pendant La Niña. L'indice SOI mesure la différence de pression atmosphérique de surface entre l'est (Tahiti) et l'ouest (Darwin) du Pacifique. Cette pression augmente à l'ouest avec l'intensité de la convection et diminue à l'est avec l'intensité de la subsidence. Ainsi, l'indice SOI mesure l'intensité de la cellule atmosphérique de Walker. Les signaux sont très correlés et montrent une oscillation interannuelle entre états El Niño et La Niña, ce qui constitue le cycle ENSO. D'autres indices sont utilisés comme la position zonale de l'isotherme ~28°C en SST ou de l'isohaline ~34.8 PSU qui quantifient l'étendue des eaux chaudes de la Warm Pool vers l'est (Delcroix et al., 2000; Singh et al., 2011). L'intensité du gradient zonal de la profondeur de thermocline

est également très représentatif, mais ce n'est pas un indice usuel. Ces signaux sont très corrélés, ce qui met en évidence un lien fort entre la circulation atmosphérique et océanique de grande échelle du Pacifique équatorial.

1.1.2. Oscillateurs

La forte corrélation entre les différentes composantes du système du Pacifique équatorial (cf. figure 1.3) suggère que l'on peut décrire l'évolution du cycle ENSO dans un espace réduit de variables. Cet exercice est courant pour appréhender la complexité des systèmes climatiques (notamment le très grand nombre de variables et de processus mis en jeu). En suivant cette approche, les modèles réduits ont pu décrire les mécanismes essentiels du cycle ENSO. Les modèles réduits les plus simples sont des oscillateurs parfaits, linéaires, dans lequel El Niño est l'exact opposé de La Niña. Ce sont des modèles d'anomalies, dans lequel l'état moyen du Pacifique équatorial est prescrit. Ces modèles expliquent en particulier deux composantes essentielles du cycle ENSO : le développement des épisodes El Niño et la Niña ainsi que la transition entre ces épisodes. Dans ces modèles, c'est la présence d'une rétroaction positive rapide et d'une rétroaction négative lente qui permet au système d'osciller. A partir d'une perturbation initiale du système, la rétroaction positive rapide entraîne la croissance d'un événement El Niño (ou La Niña). La rétroaction négative lente vient ensuite renverser la croissance initiale en sa phase opposée, et le même mécanisme de croissance/renversement se répète ensuite ce qui résulte en une oscillation régulière. La rétroaction positive communément envisagée est la rétroaction de Bjerknes décrite précédemment, dans laquelle la cellule atmosphérique de Walker et le gradient zonal de température de l'océan s'intensifient ou s'atténuent mutuellement. La rétroaction négative lente du système est communément attribuée à l'ajustement de l'océan. Plusieurs modèles réduits existent pour expliquer cette rétroaction négative, dont les fondements sont similaires mais qui divergent par les processus mis en jeu ou encore leur représentation.

L'oscillateur retardé (Suarez et Schopf, 1988 ; Battisti et Hirst, 1989) est un modèle dans lequel l'ajustement de l'océan est décrit par des composantes transitoires, les ondes équatoriales de Kelvin et Rossby. Il est représenté en figure 1.4. Les ondes équatoriales de Kelvin et Rossby ont une échelle planétaire (>1000 km, plus que la taille de la France). Elles se propagent le long de l'équateur, sont supposées non dispersives, et sont confinées en latitude (5°N-5°S) en raison de la force de Coriolis. Les ondes de Kelvin se propagent vers l'est (~3 cm/s) et les ondes de Rossby vers l'ouest (~1cm/s), ce qui correspond respectivement à 2 et 8 mois pour traverser le Pacifique équatorial. Elles se réfléchissent partiellement aux frontières que forment, à l'ouest, le réseau d'îles à faible bathymétrie de l'archipel indonésien/malaisien et du continent océanique (130°E), et, à l'est, les côtes sud-américaines (80°W). Ces ondes transportent plusieurs propriétés. On distingue les ondes dites de downwelling (i.e. approfondissement) qui réchauffent l'océan de surface en approfondissant la thermocline, des ondes dites d'upwelling (i.e. soulèvement) avec l'effet

opposé. Lorsque un évènement El Niño se développe, la réduction des alizés (qui se traduit dans le modèle par des anomalies positives de vent de surface) force une onde de Kelvin de downwelling et une onde de Rossby d'upwelling. L'onde de Kelvin de downwelling réchauffe l'est du Pacifique et intensifie El Niño (en participant à la rétroaction positive de Bjernkes). Plus tard, l'onde de Rossby d'upwelling (qui se propage plus lentement) se réfléchit au bord ouest du Pacifique en une onde de Kelvin d'upwelling. C'est ensuite le retour de cette onde d'upwelling qui refroidit l'est du bassin et peut renverser les conditions en La Niña. En résumé c'est la propagation des ondes qui explique le retard entre la rétroaction positive rapide (par onde de Kelvin de downwelling directement forcée) et la rétroaction négative lente (par onde de Kelvin d'upwelling réfléchie). En réalité le vent ne force pas une seule onde mais une succession d'ondes d'upwelling et de downelling (cf. figure 1.4**)**, et c'est le résidu entre ces ondes qui fait lentement osciller le système entre El Niño et La Niña. Des variantes de l'oscillateur retardé existent, qui ont la même formulation explicite du retard dû à la propagation d'ondes mais diffèrent par les processus considérés. Dans l'oscillateur advectif-réflectif (Picaut et al., 1997; Clarke et al., 2000), les ondes réchauffent l'océan de surface à travers les processus d'advection zonale plutôt que de thermocline. Dans l'oscillateur WPO (Weisberg and Wang, 1997), les réflexions d'ondes au bord ouest s'affranchissent de la frontière océanique et s'opèrent plutôt par un couplage local entre l'océan et l'atmosphère.

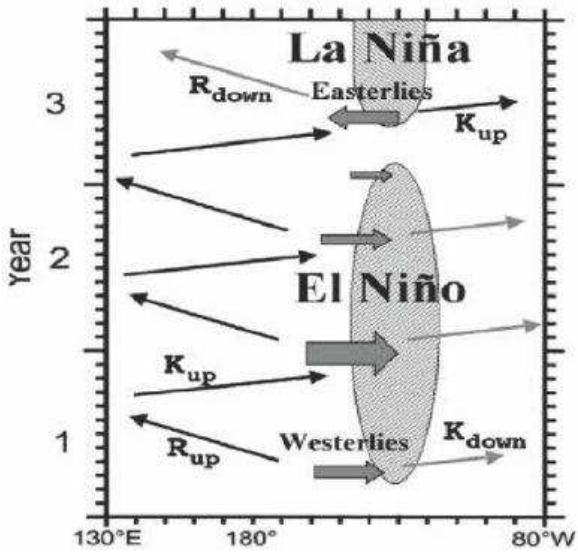

Figure 1.4 : Schéma d'évolution du modèle d'oscillateur retardé, à l'équateur en fonction de la longitude et du temps. Sont indiqués les anomalies de SST (zones grisées), les anomalies de vents de surface (flèches en trait gras), et les faisceaux de propagation des ondes équatoriales de Kelvin et Rossby (flèches en trait fin, up pour upwelling et down pour downelling) (Source: Wang et Picaut, 2004).

Le modèle de recharge/décharge se distingue des modèles précédents car il considère un ajustement à échelle de l'ensemble du bassin (Jin, 1997a). A l'équateur, les vents alizés induisent un transport zonal de surface mais aussi un transport méridien en raison de la force de Coriolis, le transport de Sverdrup. Ce transport méridien recharge ou décharge lentement le contenu thermique (i.e. la profondeur de la thermocline) de toute la bande équatoriale du Pacifique, ce qui constitue la rétroaction négative lente

permettant au système d'osciller. Les quatre phases d'évolution du modèle de recharge/décharge sont représentées sur la figure 1.5. En phase El Niño (I) l'est du Pacifique se réchauffe, par conséquent l'affaiblissement des alizés force une diminution de l'inclinaison zonale de la thermocline ainsi qu'un transport de Sverdrup vers les hautes latitudes. Ce transport décharge ensuite lentement le contenu thermique sur l'ensemble de l'équateur, ce qui se traduit par un soulèvement homogène de la thermocline (II). Ce soulèvement homogène refroidit les eaux de surface de l'Est ce qui permet au système de basculer en phase La Niña (III). Les mêmes rétroactions permettent ensuite la recharge du contenu thermique (IV) et le re-basculement en phase El Niño (I).

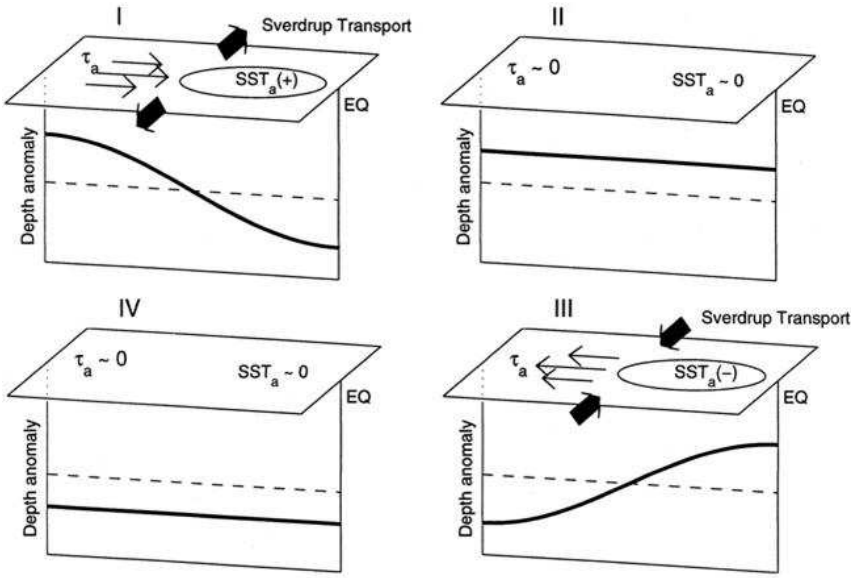

Figure 1.5 : Schéma des quatre phases d'évolution (de I à IV) du modèle de recharge/décharge, à l'équateur dans le plan de surface (longitude et latitude) et le plan vertical (longitude et profondeur). Sont indiqués les anomalies de température de surface de la mer (SST_a), de tension de vent zonal (τ_a, flèches en trait fin), de transport de Svedrup méridien (flèches en trait gras), ainsi que les anomalies de profondeur de la thermocline équatoriale (trait gras) par rapport à une profondeur de référence (trait pointillés) (Source : Meinen et McPhaden, 2000).

Le mécanisme fondamental d'oscillation est donc le retard entre l'ajustement des anomalies de SST et celui du contenu thermique sur l'ensemble du bassin (appelé WWV pour Warm Water Volume). Notons que l'on peut caractériser l'ajustement de l'océan dans ce modèle à travers l'évolution temporelle de deux modes zonaux de la profondeur de thermocline, le mode de Tilt (ou inclinaison zonale, I et III) et le mode de WWV (ou approfondissement/soulèvement homogène, II et IV). Clarke (2010) montre en particulier que ces modes intègrent à échelle interannuelle la propagation rapide des ondes équatoriales Kelvin et Rossby. Ainsi, on peut aussi expliquer le mécanisme de recharge/décharge à travers l'évolution lente du résidu (le WWV) issu de la propagation des ondes équatoriales, tout comme dans les théories de type oscillateur retardé. Dans les observations toutefois, d'autres processus que celui de recharge/décharge contrôlent aussi l'évolution du WWV (Lengaigne et al., 2011). Une revue complète des modèles ENSO de type oscillateurs parfaits est

proposée par Wang et Picaut (2004). Ils proposent également un oscillateur unifié qui par modification de ses paramètres passe d'une dynamique de type oscillateur retardé à une dynamique de type recharge/décharge.

1.1.3. Instabilités Couplées

Les oscillateurs parfaits décrits précédemment proposent un ensemble de rétroactions positives et négatives qui permettent au système couplé du Pacifique équatorial d'osciller entre phases El Niño et La Niña, et qui sont décrites de manière heuristique. D'autres études ont systématisé l'identification des rétroactions positives et négatives du Pacifique équatorial et ont proposé leur classification, décrite en termes d'instabilités. La description des instabilités est appréhendée en général à travers l'analyse de stabilité linéaire, pour des anomalies à un état moyen prescrit. On identifie les instabilités dominantes qui sont potentiellement les plus à mêmes de se développer (e.g. pour une légère perturbation du système). Cette approche a permis d'étendre la compréhension des mécanismes ENSO à travers deux composantes essentielles : l'identification des échelles spatiales et temporelles ainsi que des processus dominants du couplage entre l'océan et l'atmosphère (Neelin et al., 1998).

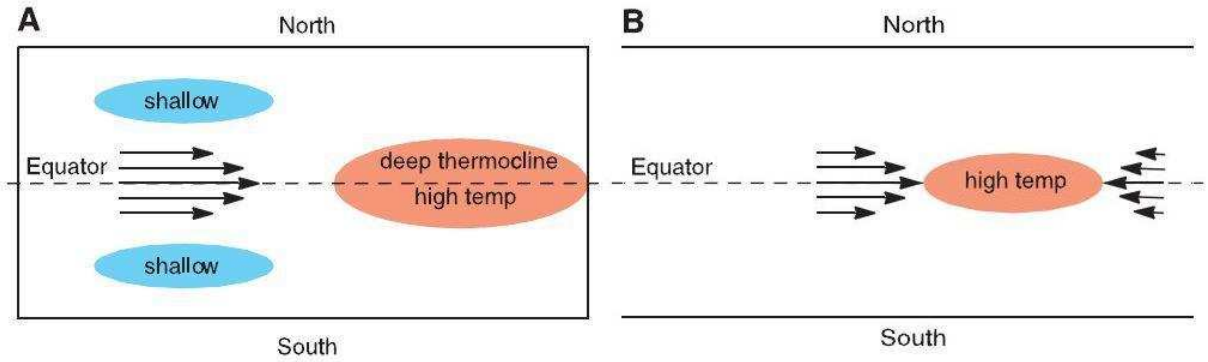

Figure 1.6 : Schéma de la structure spatiale des instabilités couplées du modèle de Fedorov et Philander (2001), en fonction de la longitude et de la latitude, pour (A) les processus de thermocline (B) les processus d'advection zonale. Sont indiqués les zones d'anomalies de SST et de profondeur de thermocline (couleurs), ainsi que les anomalies de tension de vent zonal (flèches).

Les instabilités dominantes dans le Pacifique équatorial à échelle interannuelle sont couplées, c'est-à-dire résultent d'une interaction entre l'océan et l'atmosphère. On considère généralement leur propagation le long de l'équateur (en 1D), parfois en milieu infini (i.e. sans frontières). Les instabilités sont classées notamment selon le type de processus physiques qui les maintient. On distingue deux types de processus importants dans l'océan. Ce sont les processus de thermocline où l'approfondissement de la thermocline réchauffe les eaux de surface, et les processus d'advection zonale où les courants océaniques zonaux transportent de la chaleur en raison du gradient zonal moyen de Température (Hirst, 1986 ; An et Jin, 2001). Fedorov et Philander (2001) identifient deux types d'instabilités couplées associées à ces processus dans un modèle du Pacifique équatorial. Elles sont représentées sur la figure 1.6. Les processus de thermocline

induisent une rétroaction à distance entre l'est et l'ouest du bassin, similaire à celle décrite dans le modèle de recharge/décharge. En revanche, les processus d'advection zonale induisent une instabilité couplée locale, se propageant lentement vers l'ouest. Ces instabilités sont différenciables de par leur structure spatiale, leur propagation ainsi que les processus mis en jeu. D'autres processus notables ont été identifiés, tels que par exemple les interactions entre l'atmosphère et la couche de mélange océanique (Dommenget, 2010; Wang et Xie, 1998). Les instabilités sont également classées selon les temps d'ajustement des différentes composantes du système couplé. Neelin (1991) a identifié les instabilités de type slow SST mode, que l'on rencontre à la limite asymptotique où le temps d'ajustement de la SST est grand devant le temps d'ajustement de la dynamique océanique. Ainsi, les échelles temporelles d'ENSO dépendent de l'ajustement dynamique de l'océan, mais aussi de l'ajustement thermodynamique de la couche de mélange océanique.

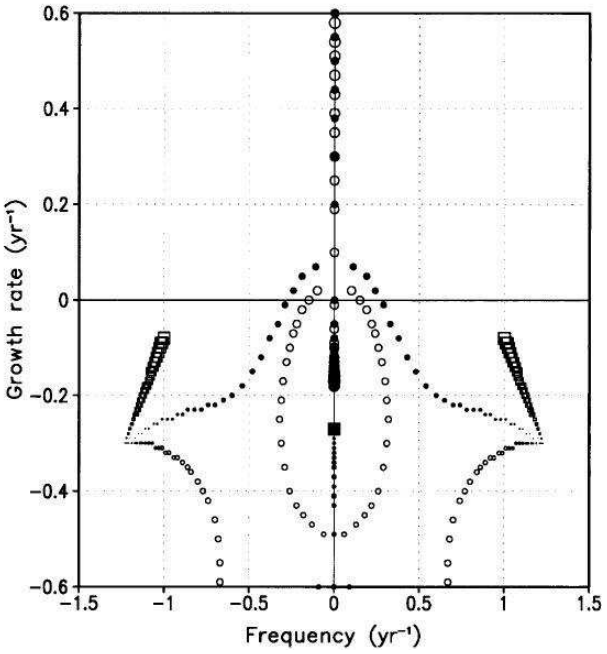

Figure 1.7**:** Fréquence (yr^{-1}) et taux de croissance (yr^{-1}) des solutions du modèle conceptuel de An et Jin (2001). Les solutions sont représentées en fonction de l'intensité du couplage océan-atmosphère (taille des symboles, de 0 à 200% de la valeur nominative), pour les processus de thermocline seuls (cercles blancs), les processus d'advection zonale seuls (carrés), et les processus combinés (cercles noirs). Les solutions oscillantes admettent un complexe conjugué, symétrique par rapport à l'axe vertical. Pour les processus combinés, on observe une solution oscillante (fréquence~0.25 yr^{-1}) et légèrement instable (taux de croissance~0.05 yr^{-1}) représentative du cycle ENSO.

Le cycle ENSO nait en partie d'une déstabilisation de la circulation moyenne, et l'approche des instabilités couplées permet d'envisager cette relation. Dans les modèles d'ENSO linéarisés, l'état moyen prescrit agit comme une source d'énergie pour la croissance des anomalies. Il contrôle les échelles spatiales et temporelles du cycle ENSO qui est simulé (taux de croissance, période d'oscillation, structure spatiale, propagation…). Ainsi plusieurs études ont cartographié un ensemble de régimes ENSO en fonction de l'intensité des divers processus reliés à l'état moyen. La figure 1.7 montre la stabilité du modèle conceptuel

de An et Jin (2001). L'analyse de stabilité met en évidence un mode dominant (le mode ENSO) qui est représentatif du cycle ENSO. Ce mode est représenté pour différentes valeurs du couplage entre l'océan et l'atmosphère (qui caractérise l'intensité de la réponse en vent aux anomalies de SST), ainsi que pour différentes configurations des processus thermodynamiques. Lorsque les processus sont considerés isolément, les processus de thermocline (d'advection zonale) favorisent un mode ENSO dissipé et à basse (haute) fréquence. Pour la combinaison de ces processus en revanche, le modèle simule un mode ENSO plus représentatif, légèrement instable et à basse fréquence. Bejarano et Jin (2008) suggèrent plutôt que ces deux processus conduisent à la coexistence de modes couplés indépendants : les processus de thermocline favorisent le mode de recharge/décharge d'ENSO, proche du quadri-annuel, tandis que les processus d'advection zonale favorisent un mode biannuel que l'on retrouve aussi dans les observations.

La sensibilité d'ENSO à l'état moyen du Pacifique équatorial ne se limite pas aux processus de thermocline et d'advection zonale, mais aussi à un grand nombre de processus qui sont à l'œuvre dans l'océan (dont la couche de mélange océanique en particulier) et dans l'atmosphère. On peut citer entre autres la stratification océanique (e.g. structure barocline, Dewitte, 2000; Dewitte et al., 2007; 2009), l'affleurement océanique équatorial (relié à l'intensité des alizés, Fedorov et Philander, 2001), les courants de friction dans la couche d'Ekman (Neelin et al., 1994), la réponse atmosphérique aux anomalies de SST (An et Wang, 2000), ou encore les couches barrières de sel (Maes et al., 2002).

1.1.4. Irrégularité

Les modèles réduits expliquent la nature oscillatoire d'ENSO, toutefois des considérations théoriques supplémentaires sont nécessaires pour expliquer l'irrégularité du cycle ENSO. L'évolution temporelle des indices d'anomalies de SST et de contenu thermique (WWV) est montrée sur la figure 1.8. Les indices sont oscillants et déphasés (les anomalies de contenu thermique précèdent celles de SST), ce qui est en accord avec la théorie de recharge/décharge. Toutefois l'oscillation n'est pas régulière. Elle est marquée premièrement par l'asymétrie entre phases El Niño et La Niña, les phases El Niño étant de plus grande intensité et de plus courte durée. Par ailleurs, après une phase de décharge du contenu thermique, le cycle peut marquer une pause : la recharge est en fait de plus longue durée que la décharge. Ces caractéristiques sont illustrées plus clairement sur la figure 1.9, qui montre l'évolution du cycle dans l'espace de phase des anomalies de SST et de contenu thermique. Cette répresentation montre l'intensité ainsi que la durée de chacune des phases du cycle ENSO (qui suit principallement le sens horaire). La phase de recharge/La Niña (en haut à gauche) est plus longue et moins intense que les autres phases. Cette observation amène Kessler (2002) à considérer ENSO plutôt comme un cycle incomplet qui commencerait par un événement El Niño (en haut à droite) et se terminerait après décharge du contenu thermique en phase de recharge/La Niña.

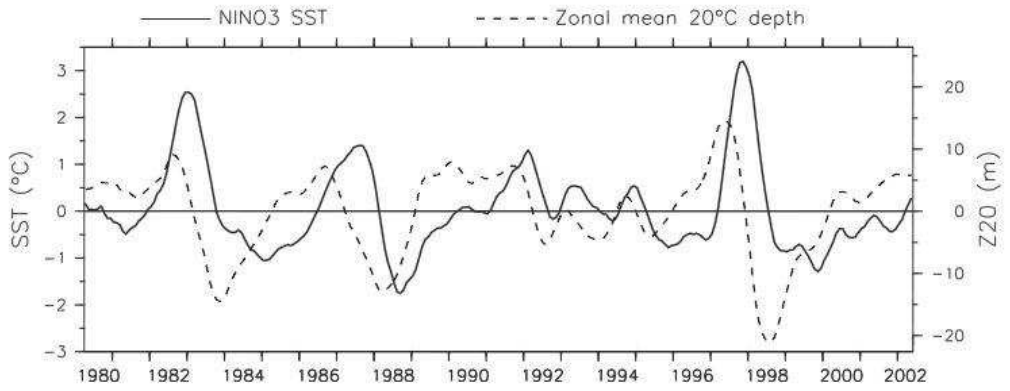

Figure 1.8: Evolution temporelle des indices Niño3-SST et WWV. Nino3 SST est la moyenne des anomalies de températures de surface de la mer dans la région 150°W-90°W et 5°N-5°S (Est du Pacifique). WWV est la moyenne des anomalies de profondeur de thermocline (isotherme 20°C) dans la région 130°E-80°W et 5°N-5°S (i.e. moyenne zonale) (Source : Kessler, 2002).

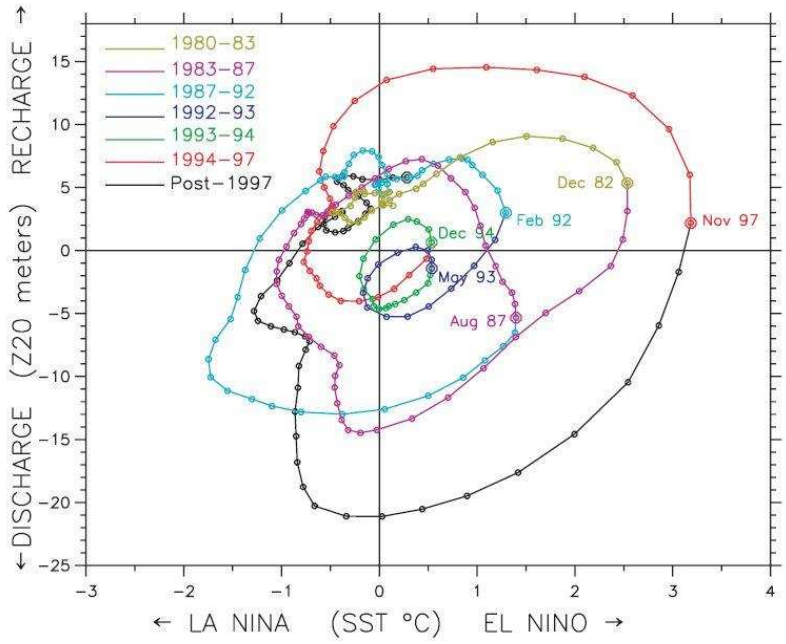

Figure 1.9: Evolution temporelle du cycle ENSO dans le plan de phase des indices Niño3-SST et WWV de la figure 1.8. Sont indiqués les phases Niño, Niña, de recharge et de décharge. L'évolution suit principalement le sens horaire (Source : Kessler, 2002).

Une des composantes du Pacifique équatorial qui tend à rendre le cycle ENSO en partie évènementiel est la variabilité haute fréquence de l'atmosphère. Le Pacifique central en particulier est le siège d'une convection atmosphérique intense au dessus de la Warm Pool. Cette variabilité haute fréquence est en grande partie stochastique (i.e. aléatoire), bien que l'on observe un cycle marqué à 60 jours nommé Madden Julian Oscillation auquel sont associés des coups de vents d'ouest (Majda et Stechmann, 2009 ; Zhang, 2005; Cassou, 2008). Cette variabilité haute fréquence peut déclencher des évènements El Niño/La Niña par déstabilisation des instabilités couplées plus lentes du Pacifique équatorial (Kleeman, 2008; Timmermann et Jin, 2008). Un tel comportement est envisageable du point de vue d'un système couplé

oscillant, dans lequel ce dernier est légèrement dissipé et la variabilité atmosphérique agit comme une source de forcage extérieure (Philander et Fedorov, 2003). Jin et al. (2007) étend le problème au cas où le bruit atmosphérique dépend des anomalies de SST (on parle alors de bruit multiplicatif plutôt qu'additif), ce qui rend le cycle légèrement plus instable (voir aussi Eisenman et al., 2005).

Le système couplé du Pacifique équatorial est également marqué par plusieurs non-linéarités fondamentales qui peuvent expliquer certaines des asymétries du cycle ENSO. Le signal de SST montre une asymétrie positive à l'est et négative à l'ouest du bassin, ce qui peut s'expliquer au premier ordre par l'advection zonale des masses d'eau dans un gradient zonal de température constant (Schopf et Burgman, 2006). Dans l'est du bassin, les processus de thermocline sont asymétriques, avec une rétroaction plus importante lors des événements El Niño que lors des évènements La Niña (Dewitte et Perigaud, 1996). Par ailleurs, le bilan thermodynamique de la couche de mélange est en partie non-linéaire dans cette région, ce qui entraîne un réchauffement à la fois lors des évènements El Niño et La Niña (An et Jin, 2004). Clarke (2008) met également en avant le rôle du seuil de déclenchement de la convection atmosphérique profonde pour une SST aux alentours de 28°C (au-delà de ce seuil la réponse atmosphérique est très différente). Cette caractéristique différencie fortement la dynamique couplée du Pacifique central, où les eaux de la Warm Pool sont proches de 28°C, de celle du Pacifique est. Timmermann et al. (2003) a proposé une version modifiée du modèle réduit de recharge/décharge sans linéarisation (en particulier sur les processus thermodynamiques, la source la plus importante de non-linéarité étant associé à l'advection verticale). Ce modèle montre, dans un intervalle restreint de paramètres toutefois, un cycle irrégulier et très asymétrique qui est marqué par intermittence par des évènements El Niño extrêmes.

Une autre source d'irrégularité (mais aussi de régularité) du cycle ENSO provient de l'interaction entre variabilité interannuelle et cycle saisonnier (Kleeman, 2008). La figure 1.10 montre une représentation en composites d'évènements El Niño. Les évènements El Niño (ainsi que les évènements La Niña) ont tendance à développer une amplitude d'anomalies maximale aux alentours de décembre. Cet accrochage du cycle ENSO sur le calendrier peut s'expliquer par un accrochage en amplitude ou en fréquence (Stein et al., 2011). Le cycle saisonnier modifie la stabilité du système couplé du Pacifique équatorial (supposé linéaire) au cours de l'année, et ainsi certaines périodes de l'année sont plus propices aux développements d'anomalies associées à ENSO. C'est l'accrochage en amplitude. L'intensité de la circulation de Walker notamment fait varier la stabilité. La convection profonde dans le Pacifique ouest par exemple est maximale pendant le printemps boréal (avril), tandis que le gradient zonal de température de l'océan est maximal en septembre. Par ailleurs, comme le système couplé du Pacifique équatorial est en partie non-linéaire, l'interaction entre un (ou plusieurs) mode(s) interannuel(s) et le mode annuel peut générer un accrochage en fréquence. Jin et al., (1994) et Tziperman et al. (1994) montrent dans un modèle réduit ainsi qu'un modèle intermédiaire que cet accrochage suit une loi de type devil staircase. Il favorise des périodes d'oscillation qui sont des multiples de la période annuelle, et peut éventuellement générer un comportement chaotique contribuant à l'irrégularité du cycle ENSO. Le mécanisme dominant qui est observé est toutefois celui

d'accrochage en amplitude, tandis qu'il est plus difficile de déduire des observations si l'accrochage en fréquence est effectif (Stein et al., 2011).

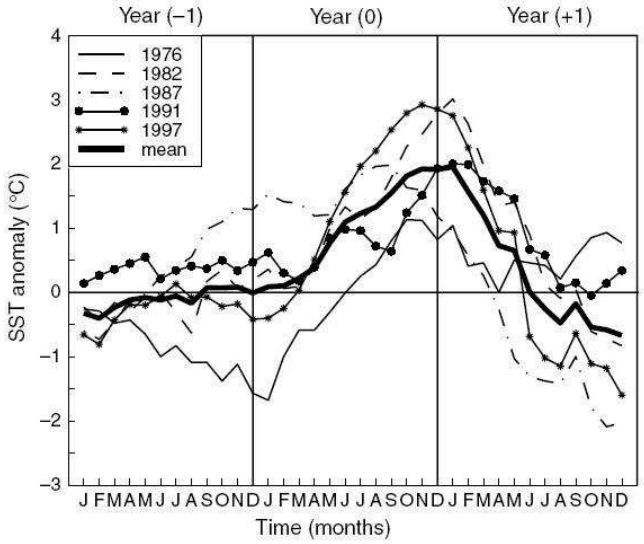

Figure 1.10: Composites de l'indice Niño3.4 SSTA pour plusieurs évènements de la période 1976-1998, en fonction du temps (de l'année -1 à +1 par rapport au pic d'anomalies) (Source : Clarke, 2008).

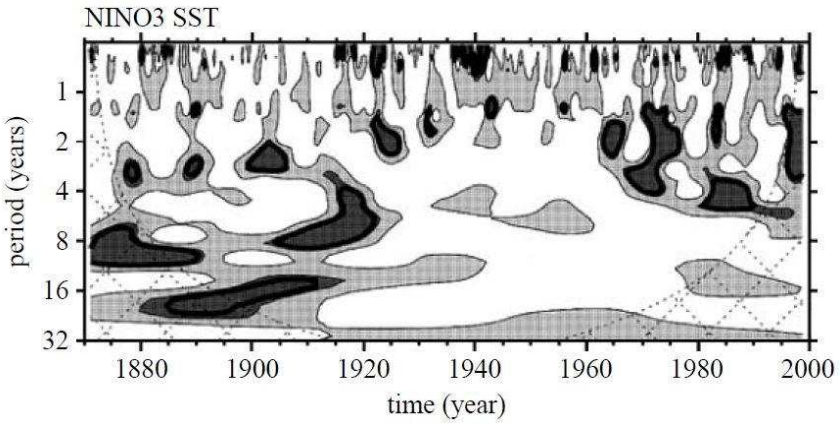

Figure 1.11: Analyse en ondelettes du spectre en fréquence de l'indice Niño3 SSTA. Cette représentation montre localement l'évolution temporelle (X-axis) du spectre en fréquence (Y-axis). L'analyse est significative hors des zones hachurées sensibles aux effets de bords (Source : Kleeman, 2008, adapté de Torrence et Webster, 1999).

1.1.5. Modulation Décennale

La variabilité du Pacifique équatorial montre un spectre en fréquence étendu, qui s'étend de l'intrasaisonnier jusqu'au décennal (voir au delà). Ceci est illustré sur la figure 1.11 par une analyse en ondelettes du spectre en fréquence des anomalies de SST. Le lien entre variabilité décennale et variabilité interannuelle est intéressant du point de vue de la modulation de l'activité ENSO. La répartition d'énergie dans la bande interannuelle (2-7 ans) varie d'une décennie à l'autre, ce qui suppose une modulation à basse fréquence de l'activité ENSO (à différencier de la variabilité basse fréquence elle-même). Cette modulation décennale est en partie expliquée par les sources d'irrégularités du cycle ENSO décrites précédemment qui rendent chaque évènement El Niño/La Niña différent. On remarque aussi que les processus sous-jacents peuvent varier d'un évènement à l'autre. Les dernières décennies par exemple ont été marquées par l'occurrence accrue d'un type d'El Niño différent du El Niño canonique (Yeh et al., 2009; Lee et McPhaden, 2010; Takahashi et al., 2011). La structure en SST des deux types d'évènements est montrée sur la figure 1.12 (voir aussi Yu et al., 2011 pour la structure de subsurface). L'évènement El Niño du Pacifique Central (CP pour Central Pacific) est marqué par des anomalies de SST maximales dans le centre du bassin, tandis que pour l'évènement El Niño canonique (EP pour Eastern Pacific) les anomalies sont maximales dans l'est du bassin. El Niño CP est également désigné dans les premières études comme El Niño Modoki, qui signifie en japonais semblable mais différent en référence à l'évènement canonique (Ashok et al., 2007). Les mécanismes sous-jacents de El Niño CP n'ont pas encore été clairement identifiés, mais seraient assez différents de El Niño EP. Kug et al. (2009) suggèrent notamment un rôle accru des processus d'advection zonale et de dissipation atmosphérique. Par ailleurs, le processus de recharge/décharge permettant le

renversement en phase La Niña serait quasiment absent, ce qui suggèrerait que ce type d'épisode soit évènementiel plutôt que cyclique. Ceci montre que la modulation décennale de l'activité ENSO s'illustre aussi par une modification des processus dominants.

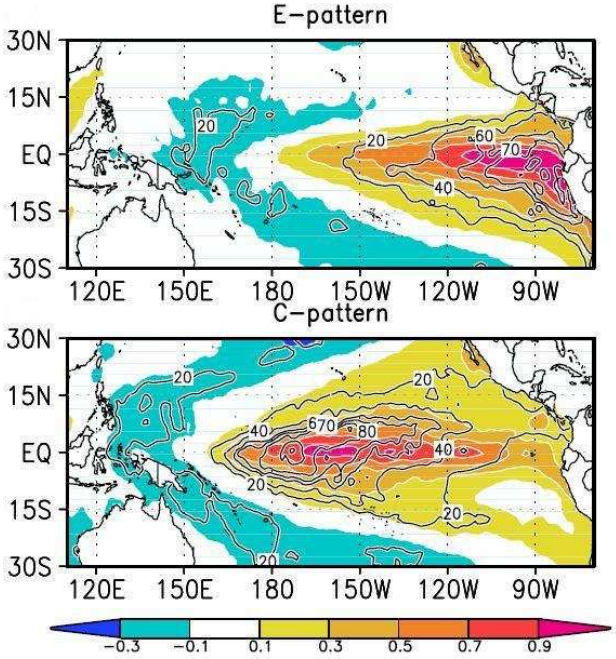

Figure 1.12: Regression des anomalies de SST sur les indices statistiques EP (E-pattern, haut) et CP (C-pattern, bas). Les indices statistiques EP et CP sont obtenus à partir d'une rotation des EOFS (Empirical Orthogonal functions) d'anomalies de SST (Source : Takahashi et al., 2011).

On peut relier en partie la modulation décennale de l'activité ENSO aux changements de l'état moyen. Ceci peut se concevoir notamment à travers l'approche linéaire (e.g. les instabilités couplées) dans laquelle l'état moyen prescrit permet la croissance des anomalies associées à ENSO. Un cas d'école pour cette approche est le shift climatique de 1976 (Wang et Wang, 1996; Guilderson et Schrag, 1998). Plusieurs études ont montré que l'on pouvait reproduire dans les modèles les changements de certaines caractéristiques d'ENSO (période, amplitude, structure spatiale) observés durant ce shift à partir des changements de l'état moyen (An et Wang, 2000; An et Jin, 2000; Moon et al., 2004). Si l'état moyen module l'activité ENSO, il devient intéressant d'en éluder les mécanismes de variations décennales (Kirtman et Schopf, 1998; Seager et al., 2004). Les théories considèrent le rôle du forçage extratropical, ou encore des processus de rectification internes au système du Pacifique équatorial où variabilité interannuelle et décennale sont liées dynamiquement. Mantua et Hare (2002) suggèrent l'interaction avec la PDO (Pacific decadal modulation) qui est un mode de variabilité décennale à échelle de tout le Pacifique. L'activité ENSO peut également modifier en retour l'état moyen à travers les non-linéarités du système couplé du Pacifique équatorial (notamment l'asymétrie entre El Niño et La Niña), le forcage de modes lents de l'océan, ou par le résultat de fluctuations interannuelles aléatoires (Sun et Zhang, 2006; Dewitte et al., 2007; An, 2009; Choi et al., 2009). Par ailleurs, on ne peut exclure l'effet du forçage anthropique sur l'évolution de la variabilité au cours des dernières décennies (Fedorov et Philander, 2000).

1.2. Prévision de l'Oscillation Australe

1.2.1. Enjeux

La prévision des épisodes El Niño et La Niña est un enjeu économique, politique et social majeur à échelle mondiale (McPhaden et al., 2006; Hsiang et al., 2011). Bien que la variabilité ENSO soit décrite en termes de processus du Pacifique équatorial, elle influence le climat de nombreuses régions à travers le monde par le biais des téléconnexions. Ceci est illustré sur la figure 1.13. Le phénomène influence, entre autres, la variabilité saisonnière des Etats-Unis (avec un hiver doux lors des années El Niño), l'intensité de la mousson asiatique, la circulation océanique le long des côtes sud-américaine, et la convection amazonienne. La prévision du phénomène permet de mettre en place de nombreuses planifications pour la gestion des ressources agricoles, électriques, forestières, ainsi que pour la pêche, le transport, le tourisme voire même les marchés financiers. Elle permet aussi la gestion de crises associées d'ordre écologique, telles que des inondations au Pérou et en Equateur, des sécheresses et feux de forêts en Indonésie et Papouasie-Nouvelle-Guinée, une intensification (lors de La Niña) de l'activité cyclonique dans les Caraïbes. Ces crises affectent les populations les plus démunies face aux évènements climatiques extrêmes : épuisement des ressources en eau potable, épidémies, problèmes de santé publique, conflits civils. Les retombées mondiales d'ENSO expliquent les efforts considérables déployés au cours des dernières décennies autour de l'observation, la compréhension et la prévision du phénomène.

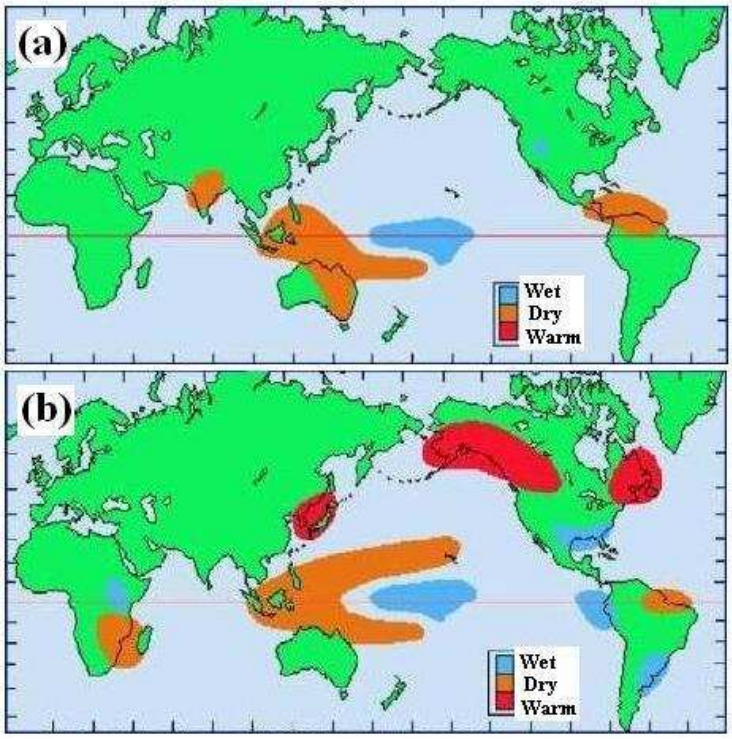

Figure 1.13: Schéma des téléconnexions ENSO durant (a) l'été boréal et (b) l'hiver boréal (Source : NOAA).

1.2.2. Réseau d'Observations

Le réseau d'observations qui surveille en continu l'activité ENSO est représenté sur la figure 1.14. Ce réseau s'est remarquablement densifié au cours des dernières décennies (McPhaden et al., 1998). Le lancement des observations satellites (TOPEX/Poséidon, JASON, QUICKSCAT…) depuis les années 1990 a permis une couverture globale des conditions de surface (SST, niveau de la mer…). De manière complémentaire, un ensemble de stations récolte des données in-situ, dont les bouées fixes le long de l'équateur (le réseau TOGA) qui permettent d'observer le contenu thermique et la variabilité de subsurface. Ce système est complété par des bouées dérivantes et des systèmes autonomes qui appareillent certains des navires marchands. Les reconstructions historiques nous donnent également une vision de la variabilité passée d'ENSO (Cane, 2005). Ces mesures sont par exemple les archives historiques, les données isotopiques de coraux tropicaux, les carottes de glaciers andins, les cernes d'arbres et dépôts sédimentaires. Les reconstructions avèrent l'existence de l'activité ENSO dans le Pacifique depuis plusieurs centaines voir plusieurs milliers d'années. Par exemple, l'activité ENSO aurait été très faible au début et milieu de l'Holocène (<5000 ans). Elle aurait aussi diminué pendant la période médiévale chaude (du Xe au XIIe siècle) en comparaison à la période du petit âge glaciaire (du XVIIe au XVIIIe siècle) (Cobb et al., 2003). Par ailleurs, grâce aux techniques d'assimilation, les produits de réanalyse permettent de combiner objectivement les observations historiques et actuelles avec la dynamique des modèles simulant la variabilité ENSO. Ces produits proposent une couverture globale (notamment en subsurface) qui s'affranchit dans une certaine mesure de la répartition inhomogène des mesures existantes (Behringer et al., 1998; Carton et Giese, 2008; Giese et Ray, 2011).

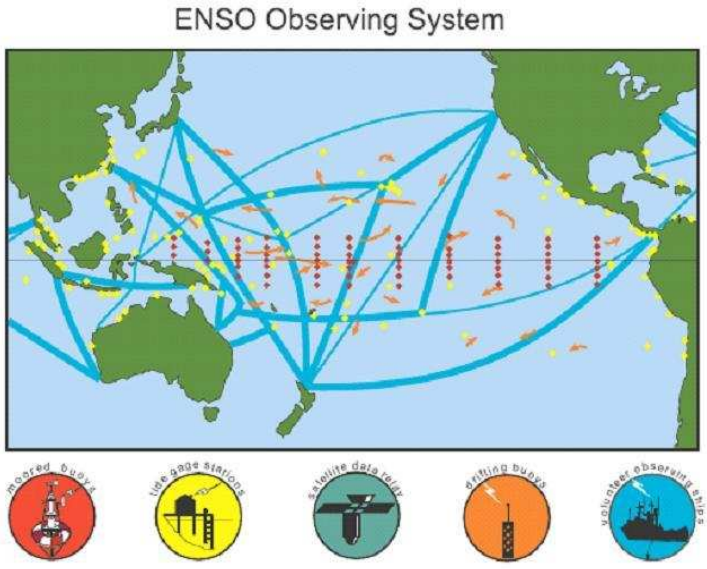

Figure 1.14: Répartition des mesures in-situ du système d'observation ENSO (Source : Wang et Picaut, 2004, adapté de McPhaden et al., 1998).

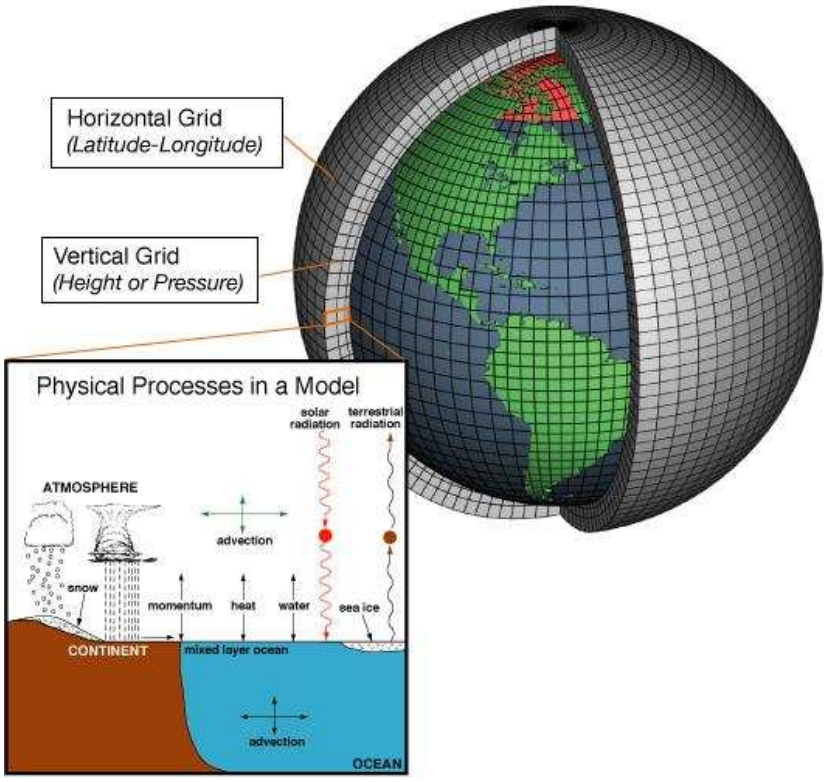

Figure 1.15: Schéma de la structure d'un modèle GCM. Les processus physiques des différentes composantes du climat (encadré) sont résolus en chaque point d'une grille couvrant l'ensemble du globe terrestre, de coordonnées longitude, latitude, et altitude (Source : NOAA).

1.2.3. Hiérarchie de Modèles

Une hiérarchie de modèles de complexité croissante permet de simuler la dynamique du Pacifique équatorial. Les modèles les plus simples sont les modèles réduits qui expliquent les mécanismes fondamentaux du cycle ENSO (Neelin et al., 1998; Wang et Picaut, 2004). Les modèles de complexité intermédiaire ICM (Intermediate Coupled Models) ont permis les premières prévisions réussies d'El Niño (Zebiak et Cane, 1987). Dans ces modèles l'état moyen climatologique (variant saisonnièrement) est prescrit, et on résout un système d'équations simplifiées, de type shallow-water pour la dynamique océanique et atmosphérique, ainsi qu'un bilan thermodynamique dans la couche de mélange océanique. Les modèles hybrides HCM sont une variante dans laquelle on considère une atmosphère statistique. Les modèles de complexité supérieure sont les modèles GCM (Global Coupled Model). La figure 1.15 montre un exemple d'architecture de modèle GCM. Ces modèles sont conçus à l'origine pour simuler le climat à échelle mondiale, avec éventuellement la capacité de coupler différentes grandes composantes du climat : hydrosphère, aérosphère, cryosphère, voir biosphère. Ils résolvent les équations de la mécanique des fluides

avec un réalisme maximal (e.g. une résolution spatiale et temporelle à la limite des ressources de calcul). Les OGCM simulent la dynamique océanique en mode forcé par l'atmosphère. Les AGCM simulent la dynamique atmosphérique en mode forcé par l'océan. Les CGCM couplent la dynamique de l'océan et de l'atmosphère, et sont donc naturellement les meilleurs candidats pour reproduire la variabilité ENSO (Terray et al., 1995; Guilyardi et al., 2009; Belmadani et al., 2010).

1.2.4. Prévisibilité

ENSO est la fluctuation climatique la plus prévisible au monde après le cycle saisonnier. Ceci est dû essentiellement à la dynamique déterministe d'ENSO, que nous avons décrite dans un cadre réduit, et dans laquelle l'inertie du système couplé (notamment de l'océan) est très grande. Le contenu thermique équatorial (ou WWV) par exemple est l'un des précurseurs majeurs du phénomène, ainsi que le dipôle de l'océan indien (Meinen et McPhaden, 2000; Clarke et Van Gorder, 2003; Izumo et al., 2010) La grande inertie du système couplé résulte aussi des échanges énergétiques associés au cycle ENSO, qui sont considérables à échelle de bassin (de l'ordre du Tera Watt) (Brown et Fedorov, 2010).

Il existe une limite à la prévisibilité d'ENSO, intrinsèque au système du Pacifique équatorial, qui dépend du poids relatif de la dynamique déterministe et des sources d'irrégularités du phénomène évoquées précédemment. Cette limite montre notamment des variations saisonnières. Le printemps boréal par exemple (vers avril) est la période de l'année la moins prévisible (aussi appelée spring barrier). La limite de la prévisibilité d'ENSO dépend entre autres de la stabilité du système du Pacifique équatorial (Philander et Fedorov, 2003). Si le système est fortement dissipé, c'est une source extérieure telle que le bruit atmosphérique (moins prévisible) qui contrôle la variabilité interannuelle. Si le système est fortement instable, il est sensible aux conditions initiales en raisons de ses non-linéarités, ce qui limite également sa prévisibilité. Les observations suggèrent toutefois que le système est proche de la marginalité (légèrement dissipé, ou encore légèrement instable) (Fedorov et Philander, 2001; Kessler, 2002; Sun et Zhang, 2006). Le phénomène El Niño est ainsi prévisible au-delà des échelles hautes fréquences du bruit atmosphérique et le système peut par ailleurs être considéré comme faiblement non linéaire. Dans ce cas les échelles spatiales et temporelles de la variabilité sont déterminées par les instabilités dominantes du système linéarisé, et sont donc plus facilement modélisables (Neelin et al., 1998).

1.2.5. Prévisions et Projections Climatiques

La prévision opérationelle d'ENSO est aujourd'hui permise par la hiérarchie de modèles présentée précédemment (iri.columbia.edu/climate/ENSO/currentinfo/QuickLook.html). En dépit de leur complexité croissante, les modèles montrent des scores de prévision relativement similaires, qui sont réalistes pour des échéances de l'ordre de 6 à 12 mois. Cette similitude s'explique par la dynamique réduite et déterministe d'ENSO, qui est raisonnablement reproduite dans la plupart des modèles (Chen et Cane, 2008; Latif et al., 1998). Toutefois, certaines études suggèrent que la limite de prévisibilité intrinsèque du système n'est pas encore atteinte dans les modèles, espérant même des prévisions réalistes à échéance de 24 mois (Chen et al., 2004). Les méthodes d'assimilation de données en particulier ont contribué et contribuent encore à améliorer la simulation et la prévision d'ENSO dans les modèles de manière significative (Bennett et al., 1998; Sun et al., 2002; Weaver et al., 2003; Zheng et al., 2006). Les scores de prévision varient aussi fortement en fonction des processus dominants qui contrôlent la variabilité ENSO, reproduits avec plus ou moins de succès. Ceci s'illustre notamment par des scores différents d'une décennie à l'autre en raison de la modulation de l'activité ENSO et du changement des processus dominants (Kirtman et Schopf, 1998).

Les projections climatiques sur l'évolution de l'activité ENSO sont également un enjeu de société, notamment pour appréhender le réchauffement climatique à venir (Cane, 2010; Stevenson et al., 2012). A échéance de plusieurs décennies, on ne peut prévoir les conditions exactes, mais en revanche on peut évaluer la forme générale (e.g. statistique) que prendront les fluctuations climatiques. Par rapport aux prévisions, les projections climatiques ont donc pour objectif principal d'évaluer l'évolution à long terme des processus dominants. Les projections climatiques qui prennent en compte l'augmentation des gaz à effet de serre prévoient un état moyen plus chaud et plus stratifié dans le Pacifique équatorial. Ceci est illustré sur la figure 1.16 qui montre un exemple de tendances d'évolution des températures à l'équateur. An et al. (2008) suggèrent notamment que l'augmentation du gradient vertical de température (i.e. de la stratification) serait plus influente sur ENSO que le changement de température en surface. Les projections climatiques prévoient également une diminution de l'intensité de la cellule de Walker (Timmermann et al., 1999; Vecchi et Soden, 2007; DiNezio et al., 2009). La diminution de l'intensité de la cellule de Walker, si elle est avérée, devrait diminuer la rétroaction de Bjerknes. Le changement des processus dominants pourrait ainsi privilégier une variabilité ENSO différente de celle que nous connaissons (e.g. Yeh et al., 2009). Il est difficile toutefois de se prononcer sur une amplification ou une réduction de l'activité ENSO, en raison de compensations attendues entre plusieurs processus de l'état moyen (Collins et al., 2010). Le GIEC (ou IPCC, Groupes d'experts Intergouvernemental sur l'Evolution du Climat) regroupe et compare l'ensemble des projections climatiques des principaux CGCM pour le réchauffement climatique à venir (divisé en plusieurs scénarios selon les émissions futures de gaz à effet de serre). Cet exercice est répété tous les 5 ans et alimente un rapport destiné au grand public et aux décideurs qui fait l'état des connaissances sur le réchauffement climatique (IPCC, 2007).

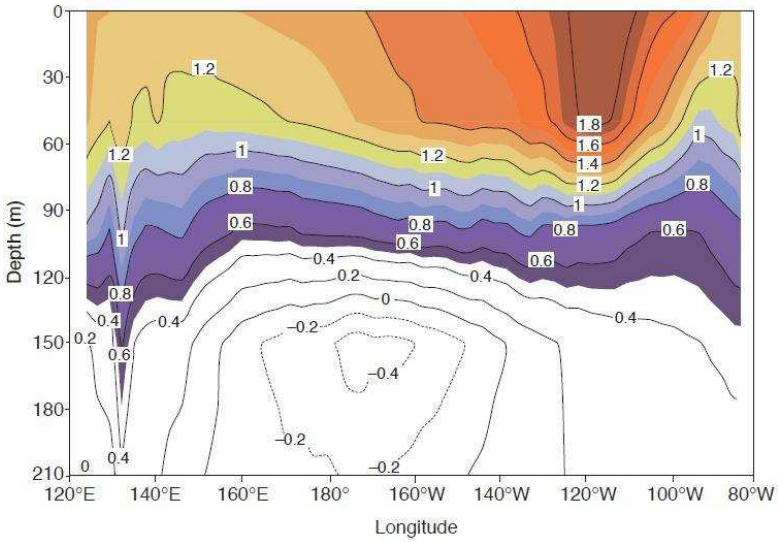

Figure 1.16**:** Tendances de température à l'équateur (°C par centaine d'années), en fonction de la longitude et de la profondeur, pour une projection de changement climatique d'un CGCM. Le réchauffement de surface et le refroidissement de subsurface traduisent un renforcement de la thermocline (i.e. de la stratification verticale) (Source : Timmermann et al., 1999).

Pour une introduction générale à ENSO et ses mécanismes, nous invitons également le lecteur à se référer (par ordre de complexité croissante) à McPhaden et al. (2006), Dijkstra (2006), Wang et Picaut (2004), ainsi que Neelin et al. (1994; 1998). Pour une introduction complète se référer par ailleurs au livre de Clarke (2008).

1.3. Motivations

Version Francaise

Cette thèse aborde diverses thématiques liées aux mécanismes, à la modulation et à la prévision d'ENSO. Chaque chapitre (du chapitre 2 au chapitre 6) aborde une thématique spécifique et peut être considéré indépendamment, bien que les thématiques soient liées et que le manuscrit suive une progression logique et technique (voir aussi le plan en section 1.4). Par ordre d'apparition, les thématiques suivantes seront abordées :

- Ch.2 : Le processus de recharge-décharge dans l'océan Pacifique équatorial.
- Ch.3 : Le rôle du couplage océan-atmosphère dans la formation d'ENSO.
- Ch.4 : La sensibilité d'ENSO à la stratification océanique.
- Ch.5 : Le rôle de l'état moyen sur la modulation décennale d'ENSO.
- Ch.6 : L'assimilation de données altimétriques dans les modèles d'ENSO.

Chapitre 2 : Dans les théories majeures d'ENSO, l'ajustement de l'océan équatorial à échelle de bassin permet l'oscillation entre phases El Niño et La Niña (Jin, 1997a). Cet ajustement consiste notamment en une évolution du contenu thermique équatorial (Warm Water Volume), qui intègre à échelle interannuelle la propagation et la réflexion des ondes océaniques équatoriales. Il a été décrit dans plusieurs études avec des degrés de complexité différents (e.g. Jin, 1997a; Clarke, 2010; Fedorov, 2010). Nous dériverons un modèle d'évolution du WWV en nous appuyant sur ces études, avec des hypothèses supplémentaires permettant d'obtenir des solutions simplifiées. Nous fournirons également un formalisme qui permet d'estimer, additionellement à l'ajustement de l'océan à échelle de bassin, le bilan d'énergie associé (Brown et Fedorov, 2010). Ce formalisme diffère des études précédentes car il considère les premiers modes baroclines d'un océan continûment stratifié.

Chapitre 3 : L'interaction océan/atmosphere dans le Pacifique équatorial est un élément essentiel de la dynamique ENSO. Le formalisme des instabilités couplées a reçu une grande attention pour comprendre une telle interaction, car il permet d'identifier les échelles et processus dominants qui y sont associés (Neelin et al., 1998). Alors que les diagnostics existants sont basés sur l'analyse de stabilité temporelle, nous implémenterons un diagnostique original (Huerre et Monkewitz, 1990) qui détermine par ailleurs la nature absolue ou convective des instabilités couplées. Ce diagnostic permettra de discuter le rôle de la variabilité stochastique de l'atmosphère ainsi que le rôle des réflexions aux frontières dans la formation d'ENSO, qui sont toujours en partie méconnus (e.g. Weisberg and Wang, 1997).

Chapitre 4 : La dynamique du cycle ENSO est sensible aux caractéristiques de la stratification océanique dans le Pacifique équatorial (Moon et al., 2004; Dewitte et al., 2007; 2009). Cette sensibilité est intéressante à comprendre pour appréhender les changements de dynamique d'ENSO dans un contexte de

réchauffement climatique global, pour lequel les projections des modèles montrent une augmentation significative de la stratification océanique dans le Pacifique équatorial (Timmermann et al., 1999; An et al., 2008). La stratification océanique moyenne modifie en particulier la projection du forcage en vent sur les premiers mode baroclines de l'océan, et ainsi leurs contributions à la dynamique océanique (Dewitte et al., 1999; Dewitte, 2000; Yeh et al., 2001). Nous proposons de traiter ce sujet dans un cadre conceptuel, où nous construirons un modèle réduit couplé qui retient la dynamique essentielle d'ENSO et prend en compte les premiers modes baroclines d'un océan continûment stratifié. La stabilité du modèle permettra de documenter la sensibilité d'ENSO à la stratification moyenne de l'océan, et en particulier aux caractéristiques de la thermocline équatoriale. Nous mettrons également en évidence certaines limitations provenant de l'estimation statistique de la rétroaction de la thermocline (Zelle et al. 2004).

Chapitre 5 : Le cycle ENSO montre une modulation décennale de ses caractéristiques qui est reliée en partie aux changements des rétroactions de l'état moyen du Pacifique équatorial (An et Jin, 2001; Fedorov et Philander, 2001). Plusieurs diagnostics permettent, dans un cadre linéaire, d'étudier cette relation (Jin et al., 2006). Ces diagnostics peuvent s'appliquer par exemple dans les observations, les réanalyses ou les projections climatiques. Ils permettent de comprendre comment l'état moyen module en partie la variabilité ENSO sur des échelles de temps décennales (An et Wang, 2000; An et Jin, 2000). Par ailleurs, il reste encore à déterminer les rétroactions qui seront les plus influentes pour le changement climatique à venir, afin de pouvoir se prononcer sur une amplification ou une réduction de l'activité ENSO (Collins et al., 2010). Nous utiliserons un modèle réduit couplé pour diagnostiquer les rétroactions de l'état moyen et la stabilité ENSO associée au cours des dernières décennies. Cette approche permettra notamment de comparer la sensibilité d'ENSO à la stratification océanique, aux rétroactions atmosphériques et thermodynamiques. Nous discuterons aussi jusqu'à quel point notre diagnostic peut rendre compte de l'augmentation récente de l'occurrence des évènements El Niño du Pacifique Central, dont les mécanismes restent partiellement méconnus (Ashok et al., 2007; Yeh et al., 2009; Takahashi et al., 2011).

Chapitre 6 : La simulation et la prévision d'ENSO sont des sujets de grand intérêt, pour lequels les méthodes d'assimilation de données qui prennent en compte les incertitudes des modèles et des observations peuvent fournir des améliorations significatives (Chen et Cane, 2008). Nous construirons et implémenterons un Filtre de Kalman d'Ensemble (Evensen, 2003) dans un modèle de complexité intérmédiaire du Pacifique équatorial déjà existant (Dewitte, 2000), afin d'assimiler des observations de niveaux de la mer et d'initialiser des prévisions rétrospectives. Dans la continuité des autres chapitres, nous déterminerons les apports de la méthode d'assimilation sur la dynamique réduite d'ENSO qui est simulée par le modèle. Un élement clé que nous aborderons est la contrainte de l'ajustement de l'océan à échelle de bassin, qui suit le paradigme de recharge/décharge (Jin, 1997a; Meinen et McPhaden, 2000).

English Version

This thesis treats a various topics related to ENSO mechanisms, modulation and forecast. Each chapter (from chapter 2 to chapter 6) treats a specific topic and can be considered independently, though the thematics are related and the manuscript follows a logical and technical progession (see also the plan in section 1.4). In order of appareance, the following topics will be treated:

- Ch.2: The recharge-discharge process in the Pacific equatorial ocean.
- Ch.3: The role of the ocean-atmosphere coupling on ENSO formation.
- Ch.4: The sensitivity of ENSO to ocean stratification.
- Ch.5: The role of the mean state on the decadal modulation of ENSO.
- Ch.6: The assimilation of altimetric data in ENSO models.

Chapter 2: In major ENSO theories, the adjustment of the equatorial ocean at basin scale permits the oscillation between phases of El Niño and La Niña (Jin, 1997a). This adjustment consists notably in an evolution of the equatorial heat content (Warm Water Volume), which integrates at interannual timescale the propagation and reflection of ocean equatorial waves. It has been described in various studies with different degrees of complexity (e.g. Jin ,1997a; Clarke, 2010; Fedorov, 2010). We will derive a model for the evolution of the WWV based on those studies, with supplementary hypotheses that permit to obtain simplified solutions. We will also provide a formalism that allows estimating, additionnaly to the ocean adjustment at basin scale, the associated energy budget (Brown and Fedorov, 2010). This formalism differs from previous studies because it considers the first baroclinic modes of a continuously stratified ocean.

Chapter 3: The ocean/atmosphere interaction in the equatorial Pacific is an essential feature of ENSO dynamics. The formalism of coupled instabilities has been given great focus to understand such interaction, because it permits to identify the leading scales and processes associated to it (Neelin et al., 1998). While existing diagnostics relate on temporal stability analysis, we will implement an original diagnostic (Huerre and Monkewitz, 1990) that further assesses the absolute or convective nature of coupled instabilities. This diagnostic will permit to discuss the role of atmospheric stochastic variability and the role of boundary reflections in the formation of ENSO, which are still partly unknown (e.g. Weisberg and Wang, 1997).

Chapter 4: The dynamics of the ENSO cycle is sensitive to the characteristics of the ocean stratification over the equatorial Pacific (Moon et al., 2004; Dewitte et al., 2007; 2009). This sensitivity is interesting to understand in order to apprehend changes in ENSO dynamics in a context of global warming, for which model projections evidence a significant increase in ocean stratification over the equatorial Pacific (Timmermann et al., 1999; An et al., 2008). The background stratification modifies in particular the projection of wind stress forcing onto the gravest ocean baroclinic modes, and as so their contributions to the ocean dynamics (Dewitte et al., 1999; Dewitte, 2000; Yeh et al., 2001). We propose to treat this topic in a conceptual framework, where we will design a reduced coupled model that retains the essential ENSO

dynamics and takes into account the gravest baroclinic modes of a continuously stratified ocean. The model stability will permit to document the sensitivity of ENSO to the background ocean stratification, and in particular to characteristics of the equatorial thermocline. We will also stress certain limitations arising from the statistical estimation of the thermocline feedback (Zelle et al. 2004).

Chapter 5: The ENSO cycle shows a decadal modulation of its characteristics that is related to some extent to changes in the retroactions of the equatorial Pacific mean state (An and Jin, 2001; Fedorov and Philander, 2001). Various diagnostics permit, in a linear framework, to study this relation (Jin et al., 2006). Those diagnostics can be used for example in observations, reanalyses or climate projections. They permit to understand how the mean state modulates in part the ENSO variability on decadal timescales (An and Wang, 2000; An and Jin, 2000). Also, there is still at this time the need to determine which feedbacks will be most influent for the future climate change, in order to give an opinion on an amplification or a reduction of the ENSO activity (Collins et al., 2010). We will use a reduced coupled model to diagnose mean state feedbacks and associated ENSO stability over the recent decades. This approach will permit notably to compare the sensitivity of ENSO to the ocean stratification, the atmospheric and thermodynamic feedbacks. We will also discuss to which extent our diagnostic can account for the recent increase in the occurrence of Central Pacific El Niño events, which mechanisms remain partially unknown (Ashok et al., 2007; Yeh et al., 2009; Takahashi et al., 2011).

Chapter 6: The simulation and forecast of ENSO is a topic of great interest, for which data assimilation methods that account for uncertainties in models and observations can provide significant improvements (Chen and Cane, 2008). We will design and implement an Ensemble Kalman Filter method (Evensen, 2003) in an already existing intermediate complexity model of the equatorial Pacific (Dewitte, 2000), in order to assimilate sea level observations and to initialize retrospective forecasts. In the continuity of the other chapters, we will assess the improvements from the assimilation method on the low-order ENSO dynamics that is simulated by the model. A key feature that we will overlook is the constraint of the ocean adjustement at basin scale, which follows the recharge/discharge paradigm (Jin, 1997a; Meinen and McPhaden, 2000).

1.4. Plan

This section details the organization of the manuscript. In addition to the introduction, conclusion and appendixes, the core of the manuscript accounts for five chapters in total.

The core of the manuscript (chapters 2 to 6) treats various topics related to ENSO mechanisms, modulation and forecast. Each chapter treats a specific topic and can be considered independently, though the topics are related and the manuscript follows a logical and technical progession. The chapters are ordered such that the lecture of each chapter is useful for the following ones. We treat successively elements of ocean dynamics (chapter 2), coupling with the atmosphere (chapter 3), reduced models invoking ENSO oscillations (chapter 4), ENSO decadal modulation (chapter 5), and ENSO prevision with data assimilation methods (chapter 6). Background elements, whenever necessary, are recalled at the beginning of each chapter, and also sirve for the next chapters. We recall background elements on ocean dynamics in chapter 2, on atmosphere dynamics and mixed-layer thermodynamics in chapter 3, and on data assimilation in chapter 6.

Noteworhty, we present in those chapters a hierarchy of models with a general continuity. The chapters are also ordered with respect to the increasing complexity of this hierarchy of models. The main characteristics of this hierarchy are summarized in the table next page. All models are of the equatorial Pacific, and simulate the evolution of anomalies around a prescribed mean state. The evolution of model variables may depend on time (0-D), longitude and time (1-D), or longitude, latitude and time (2-D). Although each model is designed for the specific needs of its associated topic, there is a general continuity in the hierarchy. This is best described by successive approximations from the most complex LODCA model to the TW model. The LODCA model considers shallow-water dynamics of the gravest equatorial baroclinic modes, coupled with the evolution of sea surface temperatures and the atmosphere. The TD model can be seen as a reduced version of LODCA, with a projection of shallow-water dynamics on equatorial waves and only main processes controlling sea surface temperatures. The AC model is a more specific coupled model that does not include reflections at the eastern and western boundaries of the equatorial Pacific. Finally, the TW model considers only the evolution of the ocean, with a further asymptotic expansion at low frequencies.

The time spent on each chapter represents approximately 10% (ch.2), 10% (ch.3), 20% (ch.4), 20% (ch.5), and 30% (ch.6) of the total investment, with the remaining 10% dedicated to the redaction of the manuscript. This is, however, difficult to estimate exactly, because the different works have largely complemented one another.

Hierarchy of Models

TW Model Chapter 2	**AC Model** Chapter 3	**TD Model** Chapter 4-5	**LODCA Model** Chapter 6
Developed during the thesis			Extended with an assimilation method
Model = of the Equatorial Pacific, with Prescribed Mean State			
0-D	1-D		2-D
Ocean = Shallow-Water with Projection on Equatorial Waves $(\partial_t+\varepsilon)K+c\partial_x K=F(\tau_x)$ $(\partial_t+\varepsilon)R-(c/3)\partial_x R=G(\tau_x)$ $h=(K+R)\psi_0+R\psi_2$ $u=(K-R)\psi_0+R\psi_2$			**Ocean** = Shallow-Water $\partial_t \underline{u}+\beta y\wedge\underline{u}=-\frac{\nabla p}{\rho_0}+\frac{\underline{\tau}}{\rho_0 h_{mix}}$ $\partial_t\partial_z\left(\frac{\partial_z p}{N^2}\right)-\rho_0 \mathrm{div}_H(\underline{u})=0$
3 Baroclinic Modes Eastern/Western Boundaries	1 Baroclinic Mode No Boundaries	**3 Baroclinic Mode** Eastern/Western Boundaries	
Asymptotic Expansion at low frequencies	**Sea Surface Temperature** = Main Processes $(\partial_t+e)T=\gamma h+\lambda u$		**Sea Surface Temperature** $(\partial_t+e)T+\underline{u}.\underline{\nabla}T+w\partial_z T=0$
	Atmosphere. = Eq. Waves $\varepsilon_a k+c_a\partial_x k=f(T)$ $\varepsilon_a r-(c_a/3)\partial_x r=g(T)$	**Atmosphere** = Statistic $\tau_x=a(T)$	**Atmosphere** = Statistic or Shallow-Water $\tau_x=a(T)$ $\tau_y=b(T)$

Chapter

2. Ocean Dynamics

This chapter is dedicated to the study of ocean dynamics in the equatorial Pacific. We recall at first general elements of ocean dynamics that are relevant to ENSO. In this thesis, we focus on a representation of the baroclinic structure of the ocean in the continuously stratified case (which is different from the two-layer approximation). Leading assumptions and limitations of this representation are discussed, in particular the fact that in the linear framework zonal changes in stratification are not taken into account. Elements of shallow water dynamics and equatorial wave dynamics are also recalled. Those elements serve as a reminder of previous studies. We also propose the adaptation of an integrated ocean energy budget to the particular case of shallow water dynamics with a baroclinic structure.

In the equatorial Pacific, the adjustment of the ocean to wind stress forcing at basin scale and at interannual timescale is a central feature of the ENSO cycle. Several studies stress in particular the link between the fast component of equatorial wave dynamics and the slow adjustment of the equatorial heat content (or Warm Water Volume) at larger timescales. We propose a reduced ocean model (the TW model for Tilt and WWV model) that is derived in the low-frequency approximation, which permits to filter the fast component of equatorial waves. As compared to previous studies, we propose additional working hypothesis in order to derive simpler yet representative solutions. With this view, the thermocline adjustment at basin scale and interannual timescale is described by the temporal evolution of two zonal modes, the so-called Tilt and WWV modes. Those zonal modes are associated to the popular recharge/discharge paradigm. A submitted article is included that presents main results. Supplementary materials are also provided, where we discuss sensitivity of the WWV mode adjustment to the ocean baroclinic structure.

2.1. Background

2.1.1. The Boussinesq Approximation

We derive linearized ocean dynamics in the equatorial Pacific, in the case of a continuously stratified ocean. We consider departure of anomalies from a reference mean state constant in time, at rest and in hydrostatic balance. The mean state depends only on depth z. For convenience the total density is separated as $\rho_o + \bar{\rho}(z) + \rho$, where ρ_o is the mean water density (~1024 kg.m^{-3}), $\bar{\rho}(z)$ accounts for continuous variations of mean density with depth ($\bar{\rho}(z) << \rho_o$) and ρ is density anomalies relatively to the mean state. For small departures from mean state, linearized momentum equations read

$$\rho_0 (\partial_t u - \beta y v) = -\partial_x p + X_z \tag{2.1}$$

$$\rho_0 (\partial_t v + \beta y u) = -\partial_y p + Y_z \tag{2.2}$$

$$\partial_z p = -\rho g \tag{2.3}$$

where β is the beta-plane parameter and g the gravity constant, u and v are zonal and meridional current anomalies, p is pressure anomalies. X_z and Y_z are respectively zonal and meridional component of wind stress forcing vertical derivative. They are equal to $X_z = \tau_x / h_{mix}$ and $Y_z = \tau_y / h_{mix}$ in the ocean mixed layer of depth h_{mix}, and are null below. τ_x and τ_y are respectively zonal and meridional wind stress forcing. The incompressibility equation and continuity equation read respectively

$$\partial_x u + \partial_y v + \partial_z w = 0 \tag{2.4}$$

$$\partial_t \rho + w \, d_z \bar{\rho}(z) = 0 \tag{2.5}$$

where w is vertical current anomalies. The Boussinesq approximation is considered, therefore density anomalies are accounted for only in the vertical momentum equation 2.3 and continuity equation 2.5. Vertical current anomalies w are directly related to density anomalies ρ. This relation depends on the mean vertical gradient of density that is described conveniently by the Brunt-Väisälä frequency N (in s^{-1}), also called mean buoyancy or mean stratification, where $N^2(z) = -g d_z \bar{\rho}(z) / \rho_o$. In general N^2 is positive. Noteworthy, N^2 sets the ratio between the vertical displacement of layers (isopycnes) and horizontal convergence/divergence. Supposing that N^2 constant locally, the vertical stretching of layers $M^2 = -g \partial_z \rho / \rho_o$ is related to horizontal convergence/divergence as $\partial_t M^2 = N^2 (\partial_x u + \partial_y v)$, therefore the greater the mean buoyancy N^2 the greater the stretching at equivalent horizontal convergence/divergence.

2.1.2. Baroclinic Modes Projection

We project equations 2.1-2.5 on a basis of ocean baroclinic modes, where we recall that density changes are continous with depth. For the physical processes that are relevant to our problem, horizontal scales are very large as compared to vertical scales. Therefore we separate horizontal and vertical dependency using a baroclinic mode projection, which reads

$$\left(u, v, \frac{p}{\rho_0}, \frac{X_z}{\rho_0}, \frac{Y_z}{\rho_0}\right) = \sum_{n=0}^{\infty} (u_n, v_n, p_n, X_n, Y_n) F_n(z) \tag{2.6}$$

where vertical functions F_n depend on depth z, and baroclinic variables in the right hand side of equation 2.6 do not depend on depth. For each baroclinic mode, baroclinic variables verify the system of equations 2.1-2.5 as well as a free surface condition and a no-slip condition at the ocean bottom taken at depth H. This forms a Sturm-Liouville problem for each baroclinic mode that reads

$$d_z\left(\frac{d_z F_n}{N^2}\right) + \frac{F_n}{c_n{}^2} = 0 \tag{2.7}$$

$$\frac{F_n}{N^2} + \frac{F_n}{g} = 0 \text{ at } z=0 \tag{2.8}$$

$$d_z F_n = 0 \text{ at } z=H \tag{2.9}$$

We use a shooting-method (from a discretised verticale profile) to solve the Sturm-Liouville problem (see Press et al., 2007, its section 18.1). This gives an infinite set of baroclinic modes with associated phase speed c_n (that are roots of the Sturm-Liouville problem) and associated vertical functions F_n. The baroclinic modes are usually classified and truncated with decaying eigenvalues c_n. The vertical functions F_n are orthogonal according to the norm

$$\int_H^0 F_n F_m dz = \delta_{nm} \tag{2.10}$$

where δ_{nm} is the Kronecker delta. They are further normalised such that $F_n(0)=1$. The projection of variables from the ocean dynamics is straightforward using this scalar product, except for wind stress vertical derivatives that vanish below the mixed-layer, and for which a projection coefficient P_n is introduced. For each baroclinic mode wind stress vertical derivatives are equal to $X_n = P_n \tau_x/\rho_o$ and $Y_n = P_n \tau_y/\rho_o$, where projection coefficients P_n are computed as

$$P_n = \frac{\int_{hmix}^0 F_n dz}{h_{mix} \int_H^0 F_n{}^2 dz} \text{ or alternatively } P_n = \left(\int_H^0 F_n{}^2 dz\right)^{-1} \tag{2.11}$$

$$\text{and verify } \sum_{n=0}^{\infty} P_n = \frac{1}{h_{mix}} \tag{2.12}$$

The alternate expression of P_n is valid for the gravest baroclinic modes that are approximately constant in the ocean mixed layer. To solve the ocean dynamics, one solves independently the dynamics for each baroclinic mode then sums each component to reconstruct dynamical variables. At a given depth, height anomalies can be reconstructed from pressure anomalies as $h_n=(d_zF_n/N^2)p_n$. This permits to reconstruct thermocline depth anomalies (by summing contributions of h_n at the mean thermocline depth). In the ocean mixed-layer it is assumed a null stratification, therefore height anomalies (e.g. sea level anomalies) are rather reconstructed as $h_n=p_n/g$. We further introduce a dissipation coefficient ε_n that accounts for viscous dissipation in the form of Rayleigh friction in the horizontal momentum equations. An identical dissipation coefficient is included in the vertical momentum equation equation, which facilitates the analytical treatment, even though the two dissipation coefficients are not required to be equal. Following Gent et al. (1983) the dissipation coefficients may be parametrised as following a power law in $\varepsilon_n \sim c_n^{-q}$, where q is chosen depending on the type of friction considered (q=0.5 for a Rayleigh friction, 1.5 for Laplacian damping, 2.5 in McCreary, 1981). The dynamics for each baroclinic mode is similar to the one of shallow water dynamics, which reads

$$(\partial_t + \varepsilon_n)u_n - \beta y v_n = -\partial_x p_n + P_n \tau_x/\rho_0 \tag{2.13}$$

$$(\partial_t + \varepsilon_n)v_n + \beta y u_n = -\partial_y p_n + P_n \tau_y/\rho_0 \tag{2.14}$$

$$(\partial_t + \varepsilon_n) p_n + c_n^2(\partial_x u_n + \partial_y v_n) = 0 \tag{2.15}$$

A more detailed derivation of the baroclinic mode projection can be found in Clarke (2008, its chapter 3). See also for example McCreary (1981), Dewitte (2000), Keenlyside and Kleeman (2002), and Shu and Clarke (2002).

2.1.3. Baroclinic Structure

We describe the structure of the gravest ocean baroclinic modes in the equatorial Pacific. Figure 2.1 shows the mean density and Brunt-Väisälä frequency of the equatorial Pacific, as a function of longitude and depth. The mean density depends on temperature and salinity. It increases with depth, and also shows a zonal contrast with minimal values in the western Pacific Warm Pool, marked by warmer (though saltier) waters. The Brunt-Väisälä frequency is proportional to the vertical gradient of mean density, and shows maximal values around the equatorial mean thermocline. The mean thermocline is located at around 150 meters in the central Pacific and shoals in the eastern Pacific. Although the equatorial Pacific shows important zonal variations in density, the linear formalism of baroclinic modes is able to consider only a single vertical structure of mean density. Strategies to overcome this issue are proposed in Keenlyside and Kleeman (2002) and Dewitte et al. (1999), but will not be considered here. Following Dewitte (2000), a mean density profile is chosen that is representative of the central Pacific stratification. This is because wind stress anomalies that force ocean dynamics are maximal in this area.

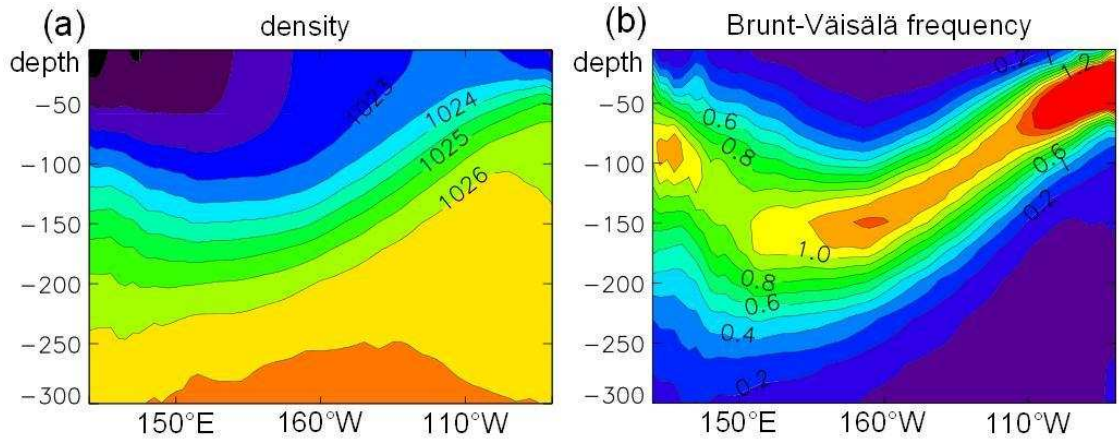

Figure 2.1**:** (a) Mean density (kg.m^{-3}) and (b) Brunt-Väisälä frequency (mn^{-2}), of the equatorial Pacific as a function of longitude and depth (m). Fields are deduced from the SODA reanalysis (Carton and Giese, 2008) over 1958-2008.

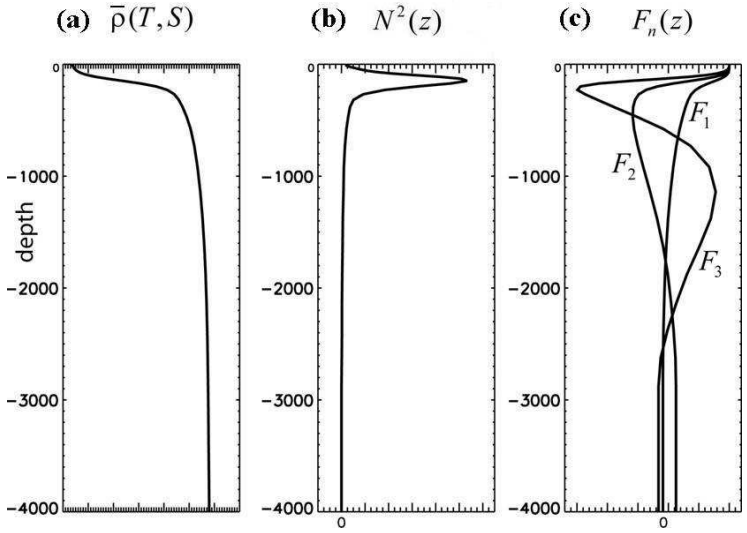

Figure 2.2**:** Baroclinic structure of the equatorial Pacific at the dateline, as a function of depth (m): (a) Mean density, (b) Brunt-Väisälä frequency, and (c) Vertical functions of the associated gravest ocean baroclinic modes. Fields are non-dimensional.

A mean density profile is computed at the dateline. This density profile and the vertical functions of the associated gravest baroclinic modes are shown in figure 2.2. The vertical mode for n=0 is called the barotropic mode because its vertical function is constant. It has a very large propagation speed c_n=2000 m.s^{-1} and describes notably the tidal response of the ocean, but is irrelevant for our problem (not shown). The modes for n>0 are the baroclinic modes, in which motion depends on depth. We focus on the gravest baroclinic modes (n=1, 2, 3). Each vertical function F_n is equal to unity at the surface, and its number of nodes (where F_n vanishes) is proportional to the order n. Its derivative is maximal from the upper ocean to the mean thermocline depth. Note that under the hypothesis of large scale density changes the vertical functions can also be expressed analytically using a Wentzel-Kramers-Brillouin (WKB) approximation (Chelton et al., 1998). From a dynamical perspective, the gravest baroclinic modes are sufficient to account

for large scale motion in the upper ocean, such as vertical movements of the equatorial thermocline for example. Higher baroclinic modes are however necessary to account for small scale variability such as in the ocean mixed-layer for example (Dewitte et al., 1999). Also a greater number of modes is necessary so that dynamical variables (pressure, currents…) vanish in the deep ocean (below 500 m approximately). Parameters associated to this baroclinic structure are shown in table 2.1. The gravest baroclinic modes have greatest phase speed c_n, greatest wind stress projection coefficients P_n, smallest vertical derivative $d_z F_n / N^2$ at the mean thermocline depth (150m), and smallest dynamical damping ε_n.

The representation of ocean dynamics with a baroclinic structure in the continuously stratified case shares some similarities with the layered representation. We discuss those similarities in appendix 1.

Baroclinic mode	1	2	3	4	5
Phase speed c_n ($m.s^{-1}$)	2.7	1. 6	1.1	0.8	0.5
Projection coefficient P_n (mm^{-1})	3.8	3.6	1.5	1	0.9
$d_z F_n / N^2$ at 150m ($m^{-1}.s^2$)	16.2	42	77.4	80.1	38
Dynamical damping $1/\varepsilon_n$ (mths)	30	23	18	15	13

Table 2.1: Baroclinic structure parameters.

2.1.4. Energy Budget

We propose the adaptation of an integrated ocean energy budget to the particular case of shallow water dynamics with a baroclinic structure. Brown and Fedorov (2010) propose an integrated, basin-wide ocean energy budget of the equatorial Pacific for application in observations, reanalyses and CGCM runs (see also Goddard and Philander, 2000; Fedorov, 2007; Brown and Fedorov, 2008; Brown et al., 2010). With this view, the interannual variability is described in terms of the balance between energy input from wind stress forcings (i.e. wind power) and changes in the storage of available potential energy. This integral approach has proven successful for intermodel comparison, and was recently applied to the equatorial Atlantic ocean (Burls et al., 2011).

This energy budget has also been derived for application in the simpler case of shallow-water dynamics with two layers (see appendix B of Brown and Fedorov, 2010). We follow a similar formalism, but in the case of shallow waters dynamics with a baroclinic structure. We consider shallow water dynamics from equations 2.13-2.15 in the long-wave approximation (i.e. the meridional momentum equation 2.14 is in geostrophic balance) and omit the contribution from meridional wind stress forcing. For each baroclinic mode we derive a local energy budget:

$$(\partial_t + 2\varepsilon_n) e_n + \rho_o (\partial_x u_n p_n + \partial_y u_n p_n) = P_n u_n \tau_x \tag{2.16}$$

$$e_n = 0.5 \rho_o (u_n^2 + p_n^2 / c_n^2) \tag{2.17}$$

The dissipation rate $2\varepsilon_n$ sums two dissipation rates that are identical in the equations of zonal and vertical momentum 2.13 and 2.15 respectively. When further averaging horizontally over the equatorial Pacific basin, we obtain a global energy budget, similar to the one of Brown and Fedorov (2010), which reads:

$$(\partial_t + 2\varepsilon_n)E_n = P_n W_n + \text{energy loss at boundaries} \quad (2.18)$$

$$E_n = 0.5\iint \rho_o (u_n^2 + p_n^2/c_n^2)dxdy \quad (2.19)$$

$$W_n = \iint u_n \tau_x dxdy \quad (2.20)$$

where E_n is available potential energy by depth meter ($J.m^{-1}$) and W_n is wind power (Watts). Available potential energy accounts for both kinetic and potential energy, although kinetic energy is secondary (Brown and Fedorov, 2010). Wind power accounts for the work of wind stress forcing. Total available potential energy and wind stress power can be reconstructed by summing the (orthogonal) contribution from each baroclinic modes and integrating vertically. This energy budget gives a simple quantification of the energy transfer rate from wind stress forcing to the ocean dynamics. It shows (cf. equation 2.18) that the gravest baroclinic modes are the ones that project more wind power (with transfer rate P_n) and that are less dissipated (with dissipation rate $2\varepsilon_n$). They are therefore the most relevant for the conversion and storage of available potential energy. This theoretical formalism might also be useful to quantify the baroclinic modes variability, as a perspective for future works.

2.1.5. Equatorial Waves

We recall the theory of equatorial waves that can describe the transient response of the equatorial Pacific at interannual timescale (see also Clarke, 2008, its chapter 3). Figure 2.3 shows a dispersion diagram (k for wavenumber and ω for frequency) of all equatorial waves that are solutions of the shallow water dynamics from equations 2.13-2.15. At large spatial and temporal scales that are relevant to ENSO (c.f. red square), relevant solutions are equatorial Kelvin and Rossby waves, which can be considered non dispersive. For each baroclinic mode, there is a single Kelvin wave and an infinite set of equatorial Rossby waves (ordered with index m). To derive those solutions in the long-wave approximation, the meridional momentum equation 2.14 is approximated to geostrophic balance, and we further omit the contribution from meridional wind stress forcing.

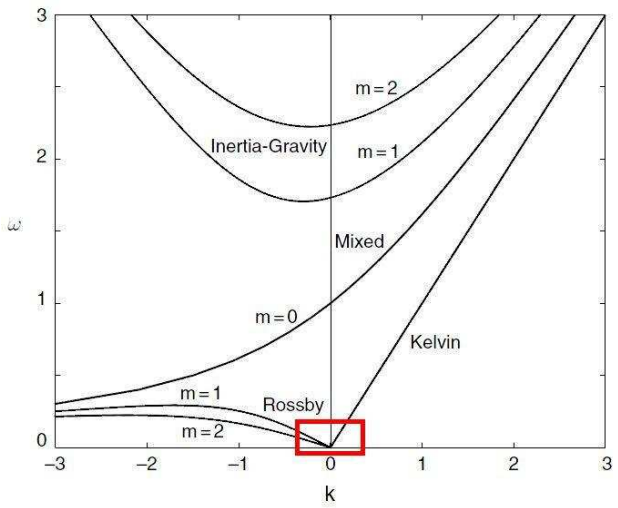

Figure 2.3: Dispersion relation of equatorial waves, as a function of the wavenumber k and frequency ω (adimensionalized by phase speed and Rossby radius). A single baroclinic mode is considered. m indicates the meridional order for the different types of equatorial waves. Only m=0,1,2 is shown (adapted from Clarke, 2008).

For each baroclinic mode n, the evolution for Kelvin wave $K_n(x, t)$ and Rossby waves $R_{nm}(x, t)$ reads

$$(\partial_t + \varepsilon_n) K_n + c_n \partial_x K_n = \frac{P_n F_K}{c_n} \tag{2.21}$$

$$(\partial_t + \varepsilon_n) R_{nm} - \frac{c_n}{(2m+1)} \partial_x R_{nm} = \frac{P_n F_{Rm}}{c_n} \tag{2.22}$$

$$F_K = \frac{< \tau_x \psi_0 >}{2\rho_o L_n} \tag{2.23}$$

$$F_{Rm} = \frac{m(m+1)}{2(2m+1)\rho_o L_n} \left[\frac{< \tau_x \psi_{m+1} >}{\sqrt{m+1}} - \frac{< \tau_x \psi_{m-1} >}{\sqrt{m}} \right] \tag{2.24}$$

where c_n is the phase speed, P_n is the wind stress forcing projection coefficient, $L_n = \sqrt{c_n/\beta}$ is the ocean Rossby radius, and ε_n is the dissipation rate. The Kelvin wave propagates eastward at speed c_n, while the Rossby wave of order m propagates westward at speed $c_n/(2m+1)$. The initial set of equations (2.13-2.15) has been projected on the meridional basis of Hermite functions ψ_m. Those functions are scaled by the ocean Rossby radius L_n, which reads $\psi_m(y/L_n)$ in equations 2.23 and 2.24. The Hermite functions are defined as

$$\psi_m(y) = \frac{\exp(-y^2/2) H_m(y)}{\sqrt{2^m m! \sqrt{\pi}}} \text{ with } H_m(y) = (-1)^m e^{y^2} d_y^m (e^{-y^2}) \tag{2.25}$$

and are orthogonals according to the scalar product

$$<> = \int_{-\infty}^{\infty} dy \tag{2.26}$$

If the system from equations 2.13-2.15 is truncated at the contribution from equatorial Kelvin and Rossby waves, zonal currents anomalies u_n and pressure anomalies p_n for each baroclinic mode are reconstructed as

$$\frac{u_n}{c_n} = K_n\psi_0 + \sum_{m=1}^{\infty} R_{nm}\left[\frac{\psi_{m+1}}{\sqrt{m+1}} - \frac{\psi_{m-1}}{\sqrt{m}}\right] \quad (2.27)$$

$$\frac{p_n}{c_n^2} = K_n\psi_0 + \sum_{m=1}^{\infty} R_{nm}\left[\frac{\psi_{m+1}}{\sqrt{m+1}} + \frac{\psi_{m-1}}{\sqrt{m}}\right] \quad (2.28)$$

where the number of Rossby wave m used in the truncature has to be determined. The meridional profiles of pressure and zonal current anomalies reconstructed from equatorial Kelvin and Rossby-1 (m=1) waves are shown in figure 2.4. For m even, Hermite functions are symmetrical, therefore the meridional profiles of Kelvin and Rossby-1 waves are symmetrical. The meridional extension is different for each baroclinic mode due to the ocean Rossby radius L_n. The reader is invited to refer to Clarke (2008, its chapter 3) for the reconstruction of other fields.

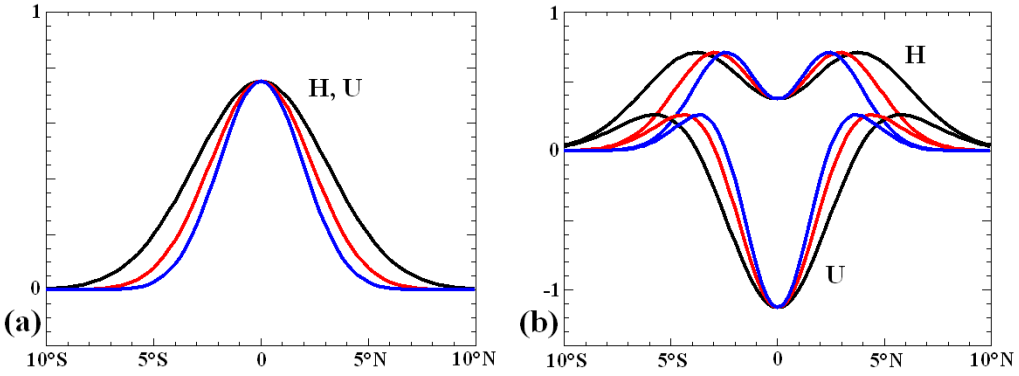

Figure 2.4**:** Non-dimensionnal meridional profiles of equatorial Kelvin waves (left) and Rossby waves (right), as a function of latitude (degrees north). The figure shows meridional profiles for the contribution to pressure (H, also height) and zonal currents (U), for the first (black), second (red) and third (blue) baroclinic mode.

The equatorial waves reflect at the eastern and western border of the equatorial Pacific. The equatorial Pacific extends approximately from 120°E (Indonesia-Australia) to 80°W (Peru-Ecuator), with a length around L=14 000 km. For the first baroclinic mode the Kelvin wave crosses the basin in around 2 months and the Rossby-1 wave in around 8 months. At the borders Kelvin waves are reflected into Rossby waves and inversely, which can be introduced through reflection coefficients as

$$K_n(0,t) = \sum_{m=1}^{\infty} r_{Rm} R_{nm}(0,t) \quad (2.29)$$

$$R_{nm}(L,t) = r_{Km}\ K_n(L,t) \quad (2.30)$$

where r_{Rm} is the reflection coefficient of Rossby-m wave into Kelvin wave at the western boundary (x=0), and r_{Km} is the reflection coefficient of Kelvin wave into Rossby-m wave at the eastern boundary (x=L). The

eastern boundary may be approximated into an infinite wall oriented meridionaly, with a no-slip condition. The western boundary is formed of many islands and is therefore gappy. It may be approximated as a condition of null normal flow. This reads

$$u(L,y,t)=0 \tag{2.31}$$

$$\int_{-\infty}^{\infty} u(0,y,t)dy = 0 \tag{2.32}$$

Under those approximations, reflection coefficients can be determined by recurrence on m odd (Boulanger and Menkes, 1995). In particular

$$r_{K1}=1,\ r_{K3}=\sqrt{3/2} \text{ and } r_{K5}=\sqrt{15/8} \text{ at the eastern boundary} \tag{2.33}$$

$$r_{R1}=1/2,\ r_{R3}=1/4\sqrt{6} \text{ and } r_{R5}=1/4\sqrt{30} \text{ at the western boundary} \tag{2.34}$$

Also it can be considered that since Kelvin waves are symmetrical meridionaly they only reflect into Rossby waves that are symmetrical (i.e. with m odd) and inversely. In practice, losses at boundaries are more complex than from this view and may be further parametrised (see Clarke, 2008, its chapter 4 for a discussion). At the eastern boundary a part of the equatorial Kelvin wave is not reflected and continues its propagation into coastal Kelvin waves along the American coast (both northward and southward). At the western boundary one may take into account the observed throughflow from the equatorial Pacific to the equatorial Indian ocean.

2.2. Derivation of the Oceanic Recharge-Discharge Modes

2.2.1. Article submitted to Journal of Physical Oceanography.

Based on previous elements of ocean dynamics, we propose a reduced ocean model (the TW model) that simulates the adjustment at basin scale of the equatorial Pacific. The model is presented in an article submitted to the revue Journal of Physical Oceanography (Thual et al., 2012d). A novel derivation is proposed that permits, using a minimum of approximations such as an asymptotic expansion at low-frequencies, to retrieve the dynamics of the Tilt and WWV modes that are associated to the recharge/discharge process of the equatorial thermocline.

Abstract: The dynamics of ENSO (El Niño Southern Oscillation) is largely associated to the interannual and basin-wide adjustment of the equatorial Pacific ocean. This ocean adjustment involves, among others, the faster propagation and reflection of equatorial long-waves forced by wind stress forcing. A novel derivation is proposed for the ocean component of the recharge/discharge model, which retains only the essential dynamics of these processes: gravest baroclinic modes, first equatorial long-waves, zonally-averaged wind stress forcing and low-frequency approximation. Model dynamics reduce to the so-called "Tilt" and "WWV" (Warm Water Volume) modes, corresponding respectively to a zonal sloping and a homogeneous shallowing/deepening of the equatorial thermocline. The Tilt mode adjusts instantly to wind stress forcing, while the WWV mode adjusts as a time-integrator. Main improvements as compared to previous studies are a simpler yet physical model derivation, which gives a representative dissipation rate of the WWV mode that accounts for both losses by friction and at boundaries, as well as an explicit sensitivity to wind stress curl. Despite its simplicity, the model forced by observed winds reproduces accurately the large-scale features of thermocline depth variability, giving further evidence of the recharge/discharge process relevance.

A Recharge/Discharge Model of the Equatorial Pacific derived from Low-Frequency Approximation of First Equatorial Long-Waves Dynamics

Sulian Thual (1), Boris Dewitte (1), Nadia Ayoub (1) and Olivier Thual (2)

(1) Laboratoire d'Etude en Géophysique et Océanographie Spatiale, Toulouse, France
(2) Université de Toulouse; INPT, UPS; IMFT, F-31400 Toulouse, France
(3) CNRS; IMFT, F-31400 Toulouse, France

Submitted to *Journal of Physical Oceanography*
21/08/2012

Abstract

The dynamics of ENSO (El Niño Southern Oscillation) is largely associated to the interannual and basin-wide adjustment of the equatorial Pacific ocean. This ocean adjustment involves, among others, the faster propagation and reflection of equatorial long-waves forced by wind stress forcing. A novel derivation is proposed for the ocean component of the recharge/discharge model, which retains only the essential dynamics of these processes: gravest baroclinic modes, first equatorial long-waves, zonally-averaged wind stress forcing and low-frequency approximation. Model dynamics reduce to the so-called “Tilt” and “WWV” (Warm Water Volume) modes, corresponding respectively to a zonal sloping and a homogeneous shallowing/deepening of the equatorial thermocline. The Tilt mode adjusts instantly to wind stress forcing, while the WWV mode adjusts as a time-integrator. Main improvements as compared to previous studies are a simpler yet physical model derivation, which gives a representative dissipation rate of the WWV mode that accounts for both losses by friction and at boundaries, as well as an explicit sensitivity to wind stress curl. Despite its simplicity, the model forced by observed winds reproduces accurately the large-scale features of thermocline depth variability, giving further evidence of the recharge/discharge process relevance.

1. Introduction

The ENSO (El Niño Southern Oscillation) is the most energetic climate fluctuation known on Earth after the seasonal cycle, with dramatic ecological and social impacts. Its dynamics is largely associated to the slow and basin-wide ocean adjustment of the equatorial Pacific (*Cane and Zebiak*, 1985; *Neelin et al.*, 1998). In ENSO theory, this ocean adjustment may drive a phase reversal from El Niño to La Niña and inversely, through the propagation and reflection of equatorial waves (*Suarez and Schopf*, 1988) or the recharge/discharge of the equatorial heat content (*Jin*, 1997a; b). This ocean adjustment involves considerable energy exchanges through variations of the equatorial thermocline depth (*Fedorov*, 2007; *Brown and Fedorov*, 2010), and explains the relatively high predictability of ENSO (*Meinen and McPhaden*, 2000; *McPhaden,* 2012).

The slow ocean adjustment of the equatorial Pacific has been described in previous studies with different degrees of complexity (e.g. *Jin*, 1997a; b; *Fedorov*, 2010; *Clarke*, 2010). A common feature of those studies is the consideration of a low-frequency approximation, i.e. of a slow adjustment that integrates, on an interannual timescale, faster processes of the equatorial Pacific ocean. *Jin* (1997a) has illustrated the major recharge/discharge paradigm of ENSO in a conceptual model, where ocean dynamics is averaged and discretized into a western and eastern box of the equatorial Pacific, and where, in the low-frequency approximation, the propagation time of equatorial Kelvin waves is omitted. *Jin* (1997b) has further derived a stripped-down coupled model with a synthetic representation of equatorial wave dynamics, exhibiting in the low-frequency approximation an ENSO regime with essential physics from *Jin* (1997a). *Fedorov* (2010) has considered the low-frequency approximation in order to expand the solutions of ocean shallow-water equations into power series. This allows describing ENSO with a rigorous and rich integro-differential equation, which encompasses both paradigms from *Suarez and Schopf* (1988) and from *Jin* (1997a; b).

At interannual timescale, the thermocline adjustment to wind stress forcing can be described by the evolution of two zonal modes of basin scale, the so-called “Tilt” and “WWV” (Warm Water Volume) modes (*Meinen and McPhaden,* 2000; *Clarke et al.*, 2007; *Clarke*, 2010). The Tilt and WWV modes can be statistically inferred from the first and second EOF modes of observed thermocline depth anomalies, as shown in figure 1 (from *Clarke et al.*, 2007). They consist respectively in a zonal tilting and a homogeneous shallowing/deepening of the equatorial thermocline. The associated timeseries show that the Tilt and WWV modes are in phase respectively with SST and time-integrated SST anomalies. Since, at interannual timescale, SST anomalies are almost in phase with wind stress anomalies, the Tilt mode adjusts instantly to the wind stress forcing, while the WWV mode adjusts as a time-integrator. Those modes are encountered (though not named) in the recharge/discharge model of *Jin* (1997a; b) that relates on a synthetic representation of equatorial wave dynamics. *Clarke* (2010) has further confirmed and documented that those modes can arise, in the low-frequency

approximation, from the faster propagation and reflection of equatorial waves. The evolution of the WWV mode is, however, also controlled by additional processes than the recharge/discharge process of the equatorial Pacific ocean (*Meinen and McPhaden*, 2000; *Clarke et al.*, 2007; *Bosc and Delcroix*, 2008; *Lengaigne et al.*, 2011).

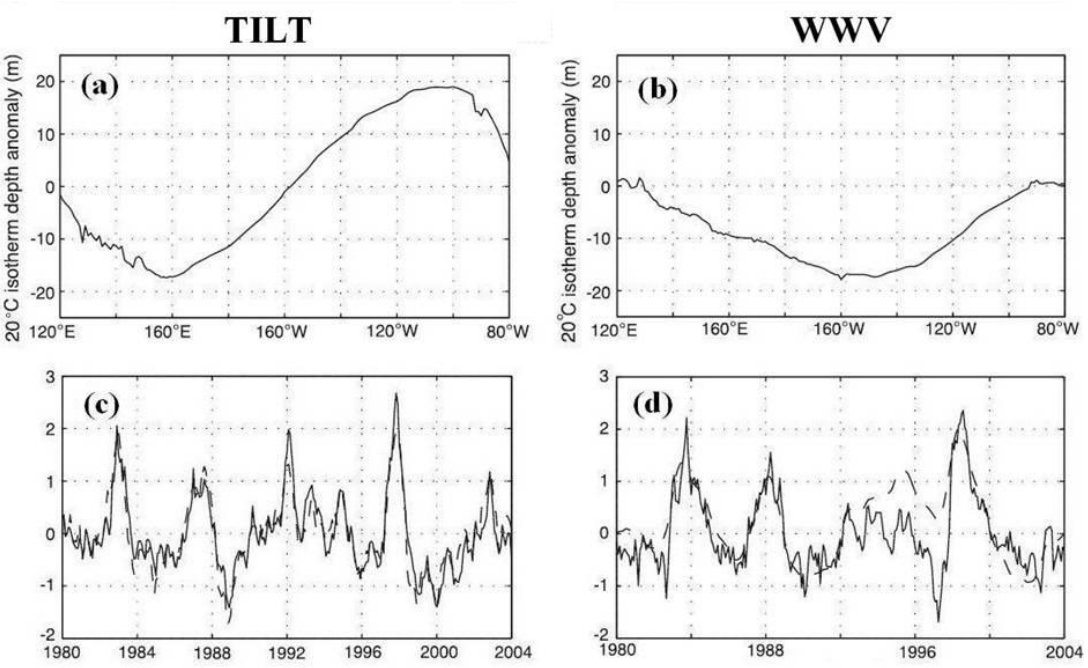

Figure 1: (a) First EOF (51% of variance) of 20°C isotherm depth anomaly (m) in the equatorial Pacific (5°N-5°S) and (c) corresponding first principal component (solid line). The dashed curve in (c) is the Niño-3.4 SSTA timeserie (c=0.93). (b) Second EOF (35% of variance) and (d) the corresponding second principal component (solid line). The dashed curve in (d) is the time-integrated Niño-3.4 SSTA timeserie. All timeseries are normalised at variance=0.5 (from *Clarke et al.*, 2007).

In this article, we derive a novel recharge/discharge model that reunites and extends some essential results of those studies dealing with the slow and basin-wide adjustment of the equatorial Pacific ocean. The model dynamics are similar to the one of *Jin* (1997a; b), though with a different derivation as we take advantage of an algebraic expansion in Fourier space similar to *Fedorov* (2010). The thermocline variability reduces to a Tilt and a WWV mode similar to *Jin* (1997a; b; *Clarke,* 2010), with additionally an explicit sensitivity to wind stress curl as already suggested by *Clarke et al.* (2007) and *Fedorov* (2010). For clarity, the model will be denoted hereafter as TW model (for "Tilt and WWV" model).

The article is organised as follows: section 2 presents shallow water equations in the long-wave approximation that are considered as a starting point to derive the TW model. Section 3 presents solutions from those shallow water equations in the case without wind stress forcing. Section 4 derives the TW model from the shallow water equations of section 2, in the low-frequency approximation and in the case of a realistic wind stress forcing. Section 5 interprets the TW model dynamics in terms of a

Tilt and WWV mode. Section 6 validates the TW model dynamics with observations. Section 7 is a discussion followed by concluding remarks.

2. Shallow waters dynamics

We consider linearized shallow-water dynamics in the equatorial Pacific ocean. We derive solutions in the long-wave approximation, where meridional momentum is supposed to be in geostrophic balance and where we omit the contribution from meridional wind stress forcing (see *Clarke*, 2008, its chapter 3). The system is truncated at the three gravest baroclinic modes (n=1, 2, 3) as in *Dewitte* (2000), and is further truncated at the equatorial Kelvin and first order Rossby wave (hereafter Rossby-1) as in *Thual et al.* (2011). Parameters of the ocean baroclinic structure are taken from *Thual et al.* (2011) (its table 1). For each baroclinic mode n, the system evolution reads:

$$(\partial_t + \varepsilon_n) K_n + c_n \partial_x K_n = c_n F_{K-n}, \qquad (1)$$

$$(\partial_t + \varepsilon_n) R_n - c_n \partial_x R_n / 3 = c_n F_{R-n}, \qquad (2)$$

$$F_{K-n} = P_n \frac{\int_{-\infty}^{+\infty} \tau \varphi_0 dy}{2\rho l_n {c_n}^2}, \qquad (3)$$

$$F_{R-n} = P_n \frac{\int_{-\infty}^{+\infty} (\tau \varphi_2 / \sqrt{2}) dy - \int_{-\infty}^{+\infty} \tau \varphi_0 dy}{3\rho l_n {c_n}^2}, \qquad (4)$$

where, for each baroclinic mode n, K_n is Kelvin wave amplitude, R_n is Rossby-1 wave amplitude, and $F_{K\text{-}n}$ and $F_{R\text{-}n}$ are projections of zonal wind stress anomalies τ. ε_n is a friction coefficient, c_n is the phase speed of Kelvin waves, and P_n is a projection coefficient. $\varphi_0=\psi_0(y/l_n)$ and $\varphi_2=\psi_2(y/l_n)$ are respectively the zero order and second order Hermite functions, ψ_0 and ψ_2, scaled by the oceanic Rossby radius $l_n=\sqrt{c_n/\beta}$ (normalisation of Hermite functions is the one from *Clarke*, 2008). β is the beta-plane parameter and ρ is the ocean density. Equatorial waves reflect at the western boundary (x=0) and eastern boundary (x=L) of the equatorial Pacific. This reads, for each baroclinic mode n:

$$K_n(0,t) = \gamma R_n(0,t), \qquad (5)$$

$$R_n(L,t) = \eta K_n(L,t), \qquad (6)$$

where γ and η are reflection coefficients, and L is the basin length (~18 000 km) that extends from 120°E to 80°W. We can reconstruct total thermocline depth anomalies H by summing the contribution of each baroclinic mode n, which reads:

$$H = \sum_n h_n \text{ , with } h_n / (s_n c_n^2) = (K_n + R_n)\varphi_0 + R_n \varphi_2 / \sqrt{2}, \qquad (7)$$

where the scaling factor $s_n=d_z V_n/N^2$ is estimated at the mean thermocline depth, d_z is vertical derivative, V_n is the vertical profile of the baroclinic mode n, and N is the Brunt-Väisälä frequency.

Hereafter, we will solve the system of equations (1-6) independently for each baroclinic mode and omit the subscript *n* for simplicity.

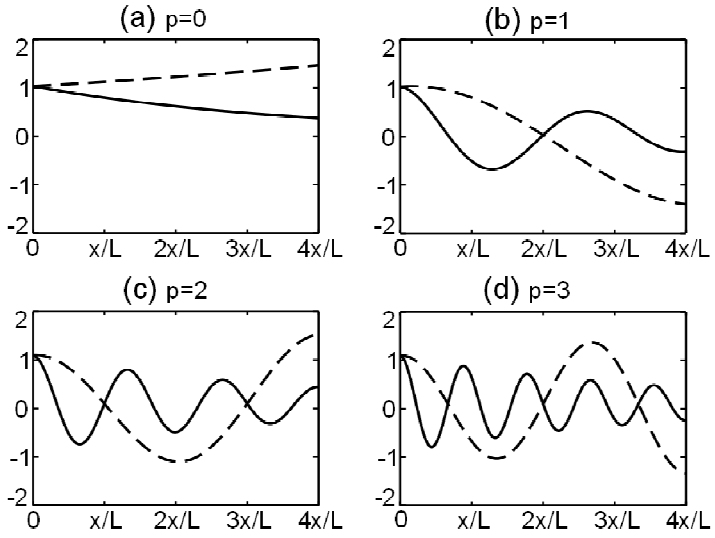

Figure 2: Solutions of equatorial Kelvin waves (dashed line) and Rossby-1 waves (thick line) without wind stress forcing, at t=0 and as a function of longitude x non-dimensionalized by the basin length L. (a) p=0, (b) p=1, (c) p=2, and (d) p=3. For a better visualisation, x extends to four times the basin length L. We choose A_p=1, B_p=1, γ=0.7 and η=1.

3. Solutions without wind stress forcing

At first, we solve the system of shallow-water equations (1-6) in the case of null wind stress forcing. Those solutions are shown for posterior comparison with the solutions of equations (1-6) that will be presented in the following sections in the case of non null wind stress forcing and in the low-frequency approximation. The elementary solutions of the linear system read:

$$K = \sum_p A_p \exp\left[-\sigma t - (\varepsilon - \sigma)x/c + ik_p(x - ct)\right], \qquad (8)$$

$$R = \sum_p B_p \exp\left[-\sigma t + 3(\varepsilon - \sigma)x/c - ik_p(3x + ct)\right], \qquad (9)$$

$$\sigma = \varepsilon - \ln(\gamma\eta)c/4L, \qquad (10)$$

$$k_p = -p\pi/4L, \qquad (11)$$

where p is an arbitrary integer, and A_p and B_p are arbitrary constants satisfying boundary conditions. Figure 2 shows the spatial structure of the four first solutions (p=0, 1, 2, 3). Similar modes have been described by *Jin* (1997b, its equation 2.7) and *Jin* (2001) and designated as free ocean adjustment modes. They can be illustrated by the standing oscillations of an elastic beam with two free boundary conditions. Those solutions are however not valid for high values of p, for which the small zonal scales are in contradiction with the long-wave approximation. The dissipation rate σ in equation (10) accounts for losses by both friction ε and boundary reflections, and is identical for all solutions that are

indexed by p. Losses from boundary reflections arise from the fact that, over each round-trip of the equatorial waves that lasts $4L/c$, the signal is multiplied by $\gamma\eta<1$. The dissipation rate σ is of particular interest, because it will be encountered in the asymptotic solutions of equations (1-6) presented in the following sections in the case of non null wind stress forcing and in the low-frequency approximation.

4. Low-frequency approximation

We consider a low-frequency approximation (*Jin*, 1997b; *Fedorov*, 2010; *Clarke*, 2010) to derive the TW model from the system of equations (1-6) in the case of non null wind stress forcing. The low-frequency approximation is also an approximation of small dissipations for the large scales and timescales under consideration (smaller scales, not described in the model, can be dissipated more strongly). Both the system oscillation frequencies ω and the friction coefficient ε are supposed to be small compared to the frequency $c/4L$ of a round-trip of equatorial waves across the basin. This reads $\omega<<c/4L$ and $\varepsilon<<c/4L$. Losses at boundaries are also supposed to be small, which reads $\gamma\sim1$ and $\eta\sim1$ and also implies that $-\ln(\gamma\eta)<<1$. Usually, a condition of null zonal current at the eastern boundary reads $\eta=1$, and a condition of null zonal mass flow at the western boundary reads $\gamma=0.5$, among additional reflection coefficients for higher order Rossby waves that are here omitted (see *Boulanger and Menkes*, 1995, beware that normalisation of Hermite functions is here different). The validity of the present asymptotic expansion may however extend up to such values, as will be shown in the following sections. Finally, in order to obtain simple solutions similar to *Jin* (1997a), we neglect the zonal dependency of wind stress forcing and rather consider the average of this signal over the entire basin. We suppose that, in the TW model, the intensity of wind stress forcing reads $F_K=f_K/L$ and $F_R=f_R/L$, where the zonally integrated wind stress projections f_K and f_R are estimated from observations as:

$$f_K = \int_0^L F_K dx \text{ and } f_R = \int_0^L F_R dx \,. \qquad (12)$$

We now present the derivation of the TW model. We focus on the steady response to a given wind stress forcing that oscillates at the low frequencies $\omega<<c/4L$. We consider the time-Fourier transform of equations (1-6) and perform an algebraic expansion similar to the one of *Fedorov* (2010), using $\omega<<c/4L$, $\varepsilon<<c/4L$ and $-\ln(\gamma\eta)<<1$. The slow time asymptotic analysis will then recovered by replacing the term $-i\omega$ by ∂_t, where i is the complex number. For each ω, the solution of equations (1-6) in the Fourier space reads:

$$K = A(x)\exp(-rx)\,, \qquad (13)$$

$$R = B(x)\exp(3rx)\,, \qquad (14)$$

$$r = (-i\omega+\varepsilon)/c\,, \qquad (15)$$

$$A(x) = \int_0^x F_K \exp(rs)ds + \gamma B_0 \ , \qquad (16)$$

$$B(x) = -\int_0^x 3F_R \exp(-3rs)ds + B_0 \ , \qquad (17)$$

$$B_0 = \frac{1}{1-\exp(\ln(\gamma\eta)-4rL)}\left[\int_0^L 3F_R \exp(-3rs)ds + \eta \exp(-4rL)\int_0^L F_K \exp(rs)ds\right], \quad (18)$$

where $B_0=B(0)$. The low-frequency approximation implies that $4rL<<1$ and that $-\ln(\gamma\eta)<<1$. This permits to simplify the system of equation (13-18). We use the approximation $\exp(a)\sim 1+a$, where $a<<1$ is for example $a=rx$, $a=-3rx$, $a=4rL$ or $a=\ln(\gamma\eta)-4rL$. We also use the approximation of zonally-independent wind stress forcing that reads $F_K = f_K/L$ and $F_R=f_R/L$. Taking the inverse Fourier transform and coming back to the notation $K(x,t)$ and $R(x,t)$ for the amplitude of Kelvin and Rossby-1 waves, the evolution of equatorial waves now reads:

$$K = 0.75(f_K - f_R)x/L - \ln(\gamma\eta)B_0 x/4L + B_0 , \qquad (19)$$

$$R = 0.75(f_K - f_R)x/L + 3\ln(\gamma\eta)B_0 x/4L + B_0 , \qquad (20)$$

$$(\partial_t + \sigma)B_0 = 0.25(f_K + 3f_R)c/L , \qquad (21)$$

$$\sigma = \varepsilon - \ln(\gamma\eta)c/4L . \qquad (22)$$

5. TW model

From the system of equations (19-22) and equation (7), we reconstruct thermocline depth anomalies for the baroclinic mode considered (we omit the *n* notation). This reads:

$$h/(sc^2) = \left[h_{WWV}\varphi_0 + g_{WWV}\varphi_2/\sqrt{2}\right] + (x/L)\left[h_{TILT}\varphi_0 + g_{TILT}\varphi_2/\sqrt{2}\right] \qquad (23)$$

where h_{WWV}, g_{WWV}, h_{TILT} and g_{TILT} are scalar functions of time that are deduced from equations (19-22) and that depend on the baroclinic mode considered. Equation (23) shows that thermocline depth anomalies are divided into a zonal mean component (i.e. that does not depend on x) and a sloping component (i.e. increasing/decreasing linearly with x). The zonal mean component is at the first order of the asymptotic expansion while the sloping component is at the second order ($h_{TILT}<<h_{WWV}$ and $g_{TILT}<<g_{WWV}$). We must however retain it because it accounts for the spatial variability of the model. As authorized by the asymptotic expansion, we further choose to remove the zonal mean component at the second order, since it is the spatial structure of the first order. This modifies equation (23) into:

$$h/(sc^2) = \left[h_{WWV}\varphi_0 + g_{WWV}\varphi_2/\sqrt{2}\right] + (x/L - 0.5)\left[h_{TILT}\varphi_0 + g_{TILT}\varphi_2/\sqrt{2}\right] \qquad (24)$$

We denote respectively the second and first term in the right-hand side of equation (24) the "Tilt mode" and "WWV mode" to be consistent with names from *Clarke* (2010). h_{TILT} and g_{TILT} are the intensity of the Tilt mode respectively on the zero and second order Hermite (scaled) function, φ_0 and φ_2. h_{WWV} and g_{WWV} are the intensity of the WWV mode respectively on φ_0 and φ_2.

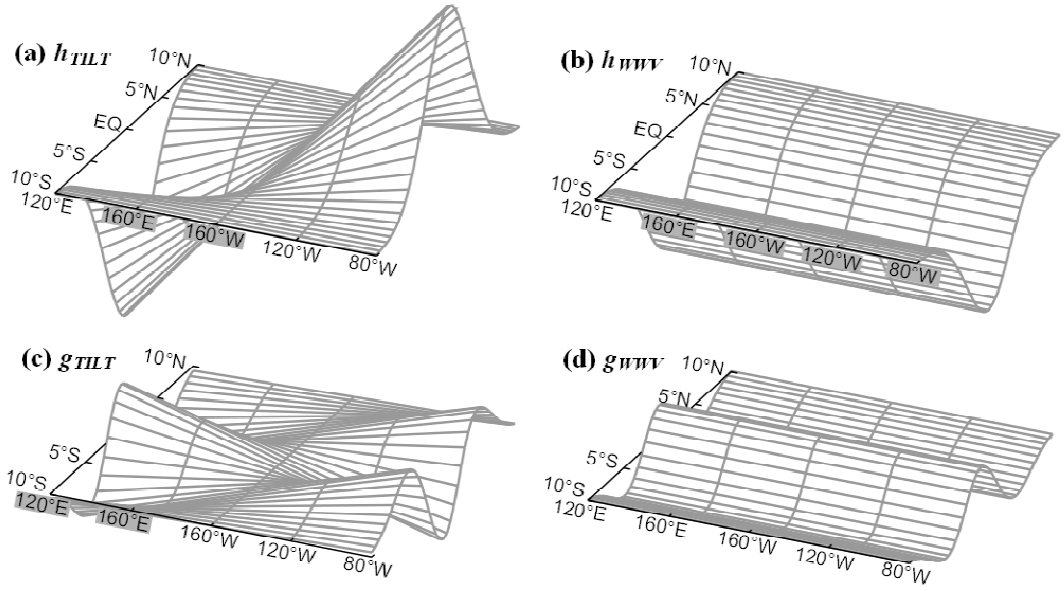

Figure 3: Spatial structure of thermocline depth anomalies from the TW model, non-dimensional and as a function of longitude and latitude, for (a) the Tilt mode and (b) the WWV mode on the zero order Hermite function φ_0, and for (c) the Tilt mode and (d) the WWV mode on the second order Hermite function φ_2. The amplitude of spatial structure in (a), (b), (c), and (d) is given respectively by the scalar functions of time h_{TILT}, h_{WWV}, g_{TILT}, and g_{WWV} (with g_{TILT}=0.5h_{TILT} and g_{WWV}=0.5h_{WWV}). We consider contribution from the gravest ocean baroclinic mode (n=1).

The Tilt and WWV mode dynamics are similar to the dynamics of the ocean component from *Jin* (1997a) with regards to spatial and temporal dependency. The spatial structure of the Tilt and WWV modes is illustrated in figure 3. For each baroclinic mode, the spatial structure is similar, only with a different meridional extension given by the corresponding oceanic Rossby radius (not shown). The Tilt mode consists in a zonal slope of thermocline depth anomalies, while the WWV mode is constant zonally. The simple expression of the Tilt mode (increasing/decreasing linearly with x) arises from our approximation of zonally-independent with stress forcing. In addition, the null zonal mean component of the Tilt mode (which we have chosen to remove) is consistent with the near null zonal mean component on the first EOF of observed thermocline depth anomalies (cf Figure 1.a). As deduced from equations (7) and (19-23), the temporal evolution of the Tilt and WWV modes reads:

$$h_{TILT} = 1.5(f_K - f_R) + 0.25\ln(\gamma\eta)h_{WWV}, \qquad (25)$$

$$(\partial_t + \sigma)h_{WWV} = 0.5(f_K + 3f_R)c/L, \qquad (26)$$

where we choose to neglect the second term from the right-hand side of equation (25), which is small in practice when the model is forced by observed winds. In addition, g_{TILT}=0.5h_{TILT} and g_{WWV}=0.5h_{WWV}. Therefore, the Tilt mode adjusts instantly to wind stress forcing, while the WWV mode adjusts as a time-integrator with dissipation rate σ. Note that wind stress forcing is, like the Tilt mode, at the second order of the asymptotic expansion. Consistently with *Jin* (1997a; b) and *Clarke* (2010), the

WWV mode arises explicitly from the propagation and reflection of equatorial waves that is not in phase with wind stress forcing. Model dynamics are similar to the ocean component from *Jin* (1997a; b), even though the overall WWV adjustment is slightly more complex because it sums up the contribution of the WWV mode from each baroclinic mode with different dissipation rate. However, the asymptotic expansion in the low-frequency approximation permits, here, to obtain a dissipation rate σ of the WWV mode that is the same than the one of solutions without wind stress forcing (equations (8-11)). This appears to be more representative because the WWV mode is obtained from a linear composition of those solutions. In addition, as compared to *Jin* (1997b, its equation 5.8) the dissipation rate σ further takes into account losses by friction ε.

We note that the WWV mode adjusts explicitly to wind stress curl, as already suggested by *Clarke et al.* (2007) and *Fedorov* (2010). Using the property of Hermite function derivatives (e.g. *Clarke*, 2008, its chapter 3) that

$$l\, d_y \varphi_1 = -\varphi_2 + \varphi_0 / \sqrt{2} \qquad (27)$$

and combining equation (3), (4), and (12), we can rewrite equation (26) into:

$$(\partial_t + \sigma) h_{WWV} = 0.5 f_{CURL} c / L \,, \qquad (28)$$

$$f_{CURL} = P \frac{\int_{-\infty}^{+\infty}\int_{0}^{L} (\partial_y \tau)\, \varphi_1 dxdy}{\sqrt{2}\, \rho c^2} \,, \qquad (29)$$

where $f_{CURL}=f_K+3f_R$ is the zonally integrated projection of wind stress curl on $\varphi_1=\psi_1(y/l)$ that is the first order Hermite function ψ_1 scaled by the corresponding oceanic Rossby radius l. As compared to previous studies, we also note that f_{CURL} can be estimated directly from observations without hypothesis on the shape of wind stress forcing.

6. TW Model Validation

In this section, we validate the TW model from the previous sections with observations from the SODA reanalysis (*Carton and Giese*, 2008) over the period 1958-2007. Figure 4 shows the evolution of thermocline depth anomalies in the equatorial Pacific, from the SODA reanalysis (figure 4.a), the shallow-water equations (1-6) forced by SODA winds (figure 4.b), and the TW model forced by SODA winds (figure 4.c). First, the shallow water equations (1-6) reproduce the thermocline depth variability with overall a good accuracy, indicating that our initial truncature of ocean dynamics (at the Kelvin and Rossby-1 waves and at the three gravest baroclinic modes) is appropriate. As compared to those shallow-water equations, the TW model further considers the low-frequency approximation. Due to its simpler spatial structure, the TW model reproduces accurately only the large scales of thermocline depth variability. Its solutions are also slightly in advance, probably due to the low-

frequency approximation that neglects the propagation time of equatorial long-waves for the adjustment of the Tilt mode.

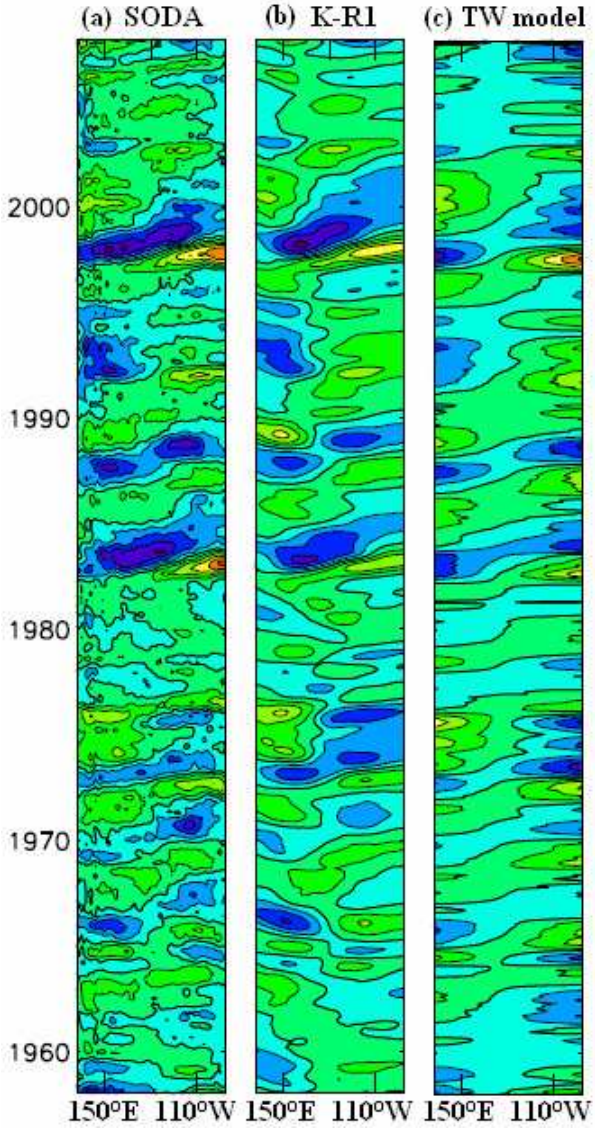

Figure 4: Hovmoller of thermocline depth anomalies (average 5°N-5°S) for (a) the SODA reanalysis, (b) the shallow water equations (1-6) forced by SODA winds, and (c) the TW model forced by SODA winds (see text). Contouring step is 10m and thick line (from blue to green) is zero-contour. Timeseries of thermocline and wind stress forcing were detrended and smoothed at 6 months, with time mean removed.

In order to validate the division of solutions into a Tilt and a WWV mode, we define a Tilt mode index I_{TILT} and a WWV mode index I_{WWV}. They read $I_{TILT} = (I_E - I_W)/2$ and $I_{WWV} = (I_E + I_W)/2$, where I_E and I_W are averages of thermocline depth anomalies H, respectively within 160°W-80°W and 120°E-160°W, and within 5°N-5°S. The Tilt mode index, I_{TILT}, measures the zonal tilting of the thermocline. The WWV mode index, I_{WWV}, measures the zonal mean of thermocline depth, and is also the conventional WWV index (*Meinen and McPhaden*, 2000). Figure 5 shows evolution of the Tilt and WWV mode indexes I_{TILT} and I_{WWV}, which are estimated from the SODA reanalysis (black) and from

the TW model forced by SODA winds (red). To compute figure 5, we choose values of reflection coefficients γ=0.7 and η=1 in the TW model that permit to better match observations (same values are also used in figure 4). Note that, while we have used an approximation of small losses by friction and at boundaries to expand model solutions, those solutions may still remain valid for stronger losses (e.g. for γ=0.7 and η=1). Results from the TW model are in overall agreement with observations (correlation is respectively 0.89 and 0.73 for I_{TILT} and I_{WWV}), despite the model simplicity (see also *Fedorov*, 2010, its figure 9, for a similar diagnostic).

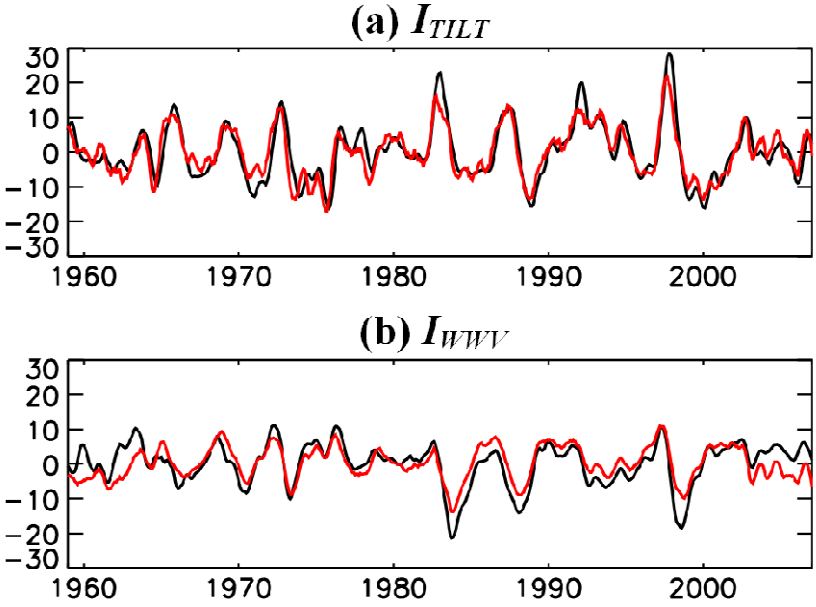

Figure 5: Timeseries of (a) Tilt mode index I_{TILT} and (b) WWV mode index I_{WWV} measured in the SODA reanalysis (black) and in the TW model forced by SODA winds (red). Units are meters. Correlation between timeseries is 0.89 in (a) and 0.73 in (b). Timeseries of thermocline and wind stress forcing were detrended and smoothed at 6 months, with time mean removed.

7. Conclusions

We have derived and validated a recharge/discharge model of the equatorial Pacific ocean (the TW model) based on shallow-water equations truncated at the contribution of the gravest baroclinic modes and first equatorial long-waves. Despite its simplicity, the model is non-heuristic. It catches the essential dynamics thanks to an asymptotic expansion in which the frequencies and the dissipations, both in the basin and at the boundaries, are small.

The TW model dynamics are similar to the ocean component from *Jin* (1997a; b), with slight improvements that consist in a representative dissipation rate σ of the WWV mode that accounts for both losses by friction and at boundaries, as well as an explicit sensitivity to wind stress curl. It would be interesting to explore whether those improvements may lead to new considerations in the broad range of applications that has been allowed by the simplicity and versatility of the recharge/discharge

model from *Jin* (1997a; b). This includes, among others: coupling to mixed-layer thermodynamics and atmosphere thermodynamics to invoke ENSO-oscillations (*Jin*, 1997a; b; *An and Jin*, 2001; *Clarke et al.*, 2007; *Fedorov*, 2010, where the phase lag of the WWV mode depending on σ is the essential feature for understanding the phase transition between El Niño and La Niña events), analytical sensitivity of ENSO to mean state feedbacks (*Jin et al.*, 2006, where the dissipation rate σ was omitted, but may be included as a further feedback term), analytical sensitivity of ENSO to ocean stratification (which is numerical in *Dewitte*, 2000; *Thual et al.*, 2011), and recharge/discharge process in the equatorial Indian and Atlantic oceans (*Jansen et al.*, 2009).

It may be interesting to assess whether the decrease in the lag between SST and WWV anomalies observed after 2000 (*McPhaden,* 2012) may be accounted for by the TW model. Considering that the SST anomalies are in phase with wind stress forcing, then, according to the TW model, changes in this lag may arise from changes in the dissipation rate $\sigma=\varepsilon-\ln(\gamma\eta)c/4L$ of the WWV mode, and would therefore be related to the background mean state. This possibility however calls for better estimating friction coefficients ε and boundary reflection coefficients γ and η, for which there is a great uncertainty in respective values (e.g. *Boulanger and Menkes*, 1995; *Fedorov*, 2007).

The TW model energetics share some similarities with the energy budget from *Fedorov* (2007, its appendix B) that is derived in the case of two-layer shallow water dynamics. In this energy budget, available potential energy E integrated over the basin adjusts to wind stress power W integrated over the basin as $(\partial_t + 2\varepsilon)E = W + B$, where ε is the friction coefficient of shallow water equations, and B is an implicit term corresponding to losses at boundaries. Locally, one can assume that available potential energy e only depends on thermocline depth anomalies H as $e=g^*H^2/2$, where g^* is the reduced gravity constant. For comparison, we may derive a similar expression of available potential energy e in the TW model directly from thermocline depth anomalies (equation 24-26), even though the expression of e is in reality more complex as we work with ocean baroclinic modes. With this view, available potential energy E integrated over the basin depends on a summed-up contribution from the Tilt and WWV modes. Assuming that, for the WWV mode contribution, H is a monochromatic function of frequency with dissipation rate $\sigma=\varepsilon-\ln(\gamma\eta)c/4L$, then the dissipation rate of associated available potential energy is 2σ. This is in agreement with the dissipation rate 2ε of available potential energy E from *Fedorov* (2007), though the dissipation rate 2σ further makes explicit energy losses at boundaries B that result from the reflection of equatorial waves. The available potential energy E in the TW model also results from the contribution of the Tilt mode, which is in phase with wind stress forcing and which is therefore incompatible with the dissipation rate 2ε from *Fedorov* (2007). *Brown and Fedorov* (2010) however stressed that the available potential energy E is largely a measure of the observed zonal slope of the equatorial thermocline, which we may traduce as the intensity of the Tilt mode. This counter-intuitive result calls for further understanding of the relation between the Tilt and WWV modes and ocean energetics.

While a main advantage of the TW model is its simplicity and versatility, it may as well be extended in order to better simulate the thermocline response to wind stress forcing. Main discrepancies with the observed thermocline response (cf figure 4 and 5) may arise from the following issues:

1) The zonal structure of the Tilt and WWV modes in observations of thermocline depth anomalies is more complex than in the TW model. Figure 1 shows that the Tilt mode has a zonal slope that is maximal in the central Pacific where zonal wind stress forcing is maximal. The WWV mode is also maximal in the central Pacific, probably for the same reason. To account for this, one may consider that wind stress forcing is non-null only over a restricted domain, for which the model derivation remains similar (e.g. from ¼ to ¾ of the basin length as in *An and Jin*, 2001). More radically, the approximation of zonally-independent wind stress forcing (that permits to obtain a Tilt mode increasing/decreasing linearly with longitude) may be relaxed.

2) The TW model is truncated at the gravest baroclinic modes and first equatorial long-waves. We have also derived an alternate version the TW model that considers shallow water dynamics with two ocean layers, which is somewhat equivalent to considering a single ocean baroclinic mode (setup is from *Jin*, 1997b). This alternate version exhibits a weaker thermocline depth variability that would call for modified parameter tunings in order to better fit to observations (not shown). This appears to come to the fact that it lacks the contribution from higher-order baroclinic modes that helps trapping more momentum flux from wind stress forcing (*Dewitte*, 2000; *Thual et al.*, 2011). Furthermore, the sensitivity to the truncature of equatorial long-waves should have to be explored, though this would require to derivate more complex solutions where higher orders of Rossby waves are considered (e.g. *Jin*, 2001; *Clarke*, 2010).

3) Additional processes that control the evolution of the WWV mode are not accounted for in the TW model. They are, among others, adiabatic processes such as interior mass transport and mass transport across the western boundary (*Meinen and McPhaden*, 2000; *Clarke et al.*, 2007; *Bosc and Delcroix*, 2008), as well as diabatic processes such as diathermal mass transport and solar forcing that reaches the equatorial thermocline (*Lengaigne et al.*, 2011). Further model parameterization might allow accounting for those processes.

References

An, S.-I., and F.-F. Jin (2001), Collective Role of Thermocline and Zonal Advective Feedbacks in the ENSO Mode, *Journal of Climate*, *14*(16), 3421–3432.

Bosc, C., and T. Delcroix (2008), Observed equatorial Rossby waves and ENSO-related warm water volume changes in the equatorial Pacific Ocean, *J. Geophys. Res.*, *113*, 14 PP., doi:200810.1029/2007JC004613.

Boulanger, J.-P., and C. Menkes (1995), Propagation and reflection of long equatorial waves in the Pacific Ocean during the 1992–1993 El Niño, *J. Geophys. Res.*, *100*(C12), PP. 25,041–25,059, doi:199510.1029/95JC02956.

Brown, J. N., and A. V. Fedorov (2010), How Much Energy Is Transferred from the Winds to the Thermocline on ENSO Time Scales?, *Journal of Climate*, *23*(6), 1563–1580, doi:10.1175/2009JCLI2914.1.

Cane, M. A., and S. E. Zebiak (1985), A Theory for El Niño and the Southern Oscillation, *Science*, *228*(4703), 1085–1087, doi:10.1126/science.228.4703.1085.

Carton, J. A., and B. S. Giese (2008), A Reanalysis of Ocean Climate Using Simple Ocean Data Assimilation (SODA), *Monthly Weather Review*, *136*(8), 2999–3017, doi:10.1175/2007MWR1978.1.

Clarke, A. J. (2008), *An introduction to the dynamics of El Niño and the southern oscillation*, Academic Press, 324 pp.

Clarke, A. J. (2010), Analytical Theory for the Quasi-Steady and Low-Frequency Equatorial Ocean Response to Wind Forcing: The "Tilt" and "Warm Water Volume" Modes, *Journal of Physical Oceanography*, *40*(1), 121–137.

Clarke, A. J., S. Van Gorder, and G. Colantuono (2007), Wind Stress Curl and ENSO Discharge/Recharge in the Equatorial Pacific, *Journal of Physical Oceanography*, *37*(4), 1077–1091, doi:10.1175/JPO3035.1.

Dewitte, B. (2000), Sensitivity of an Intermediate Ocean–Atmosphere Coupled Model of the Tropical Pacific to Its Oceanic Vertical Structure, *Journal of Climate*, *13*(13), 2363–2388, doi:10.1175/1520-0442(2000)013<2363:SOAIOA>2.0.CO;2.

Fedorov, A. V. (2007), Net energy dissipation rates in the tropical ocean and ENSO dynamics, *Journal of climate*, *20*(6), 1108–1117.

Fedorov, A. V. (2010), Ocean Response to Wind Variations, Warm Water Volume, and Simple Models of ENSO in the Low-Frequency Approximation, *Journal of Climate*, *23*(14), 3855–3873, doi:10.1175/2010JCLI3044.1.

Jansen, M. F., D. Dommenget, and N. Keenlyside (2009), Tropical Atmosphere–Ocean Interactions in a Conceptual Framework, *Journal of Climate*, *22*(3), 550–567, doi:10.1175/2008JCLI2243.1.

Jin, F.-F. (1997a), An Equatorial Ocean Recharge Paradigm for ENSO. Part I: Conceptual Model, *Journal of the Atmospheric Sciences*, *54*(7), 811–829.

Jin, F.-F. (1997b), An Equatorial Ocean Recharge Paradigm for ENSO. Part II: A Stripped-Down Coupled Model, *Journal of the Atmospheric Sciences*, *54*(7), 830–847, doi:10.1175/1520-0469(1997)054<0830:AEORPF>2.0.CO;2.

Jin, F.-F. (2001), Low-frequency modes of tropical ocean dynamics, *Journal of climate*, *14*(18), 3874–3881.

Jin, F.-F., S. T. Kim, and L. Bejarano (2006), A coupled-stability index for ENSO, *Geophys. Res. Lett.*, *33*, 5 PP., doi:200610.1029/2006GL027221.

Lengaigne, M., U. Hausmann, G. Madec, C. Menkes, J. Vialard, and J. M. Molines (2011), Mechanisms controlling warm water volume interannual variations in the equatorial Pacific: diabatic versus adiabatic processes, *Climate Dynamics*, doi:10.1007/s00382-011-1051-z.

McPhaden, M. J. (2012), A 21st Century Shift in the Relationship between ENSO SST and Warm Water Volume Anomalies, *Geophys. Res. Lett.*, doi:10.1029/2012GL051826.

Meinen, C. S., and M. J. McPhaden (2000), Observations of Warm Water Volume Changes in the Equatorial Pacific and Their Relationship to El Niño and La Niña, *Journal of Climate*, *13*(20), 3551–3559.

Neelin, J. D., D. S. Battisti, A. C. Hirst, F.-F. Jin, Y. Wakata, T. Yamagata, and S. E. Zebiak (1998), ENSO theory, *Journal of Geophysical Research*, *103*(C7), 14261–14290.

Suarez, M. J., and P. S. Schopf (1988), A Delayed Action Oscillator for ENSO, *Journal of the Atmospheric Sciences*, *45*(21), 3283–3287.

Thual, S., B. Dewitte, S.-I. An, and N. Ayoub (2011), Sensitivity of ENSO to Stratification in a Recharge–Discharge Conceptual Model, *Journal of Climate*, *24*(16), 4332–4349.

2.2.2. Supplementary Materials

The ocean adjustment to wind stress forcing described in the previous section (i.e. in Thual et al., 2012d) is sensitive to the relative contribution of each baroclinic mode, which shows a different evolution of the Tilt and WWV modes. Noteworthy, the dissipation rate of the WWV mode for each baroclinic mode n is $\sigma_n=\varepsilon_n-\ln(\gamma\eta)c_n/4L$. The sensitivity of σ_n to the baroclinic mode considered is shown in figure 2.5.a, where values are taken from table 2.1. The dissipation rate accounts for both losses by Rayleigh friction ε_n and by boundary reflections $\zeta_n=-\ln(\gamma\eta)c_n/4L$. The dissipation rate by Rayleigh friction $\varepsilon_{\mathbf{n}}$ increases with higher baroclinic modes. Note that the exact value of $\varepsilon_{\mathbf{n}}$ is arguable, and that it may also be parameterized differently than from a Rayleigh friction (McCreary, 1981; Gent et al., 1983; Picaut et al., 1993). The dissipation rate from boundary reflections ζ_n is proportional to the basin crossing time of equatorial waves $c_n/4L$, because each crossing multiplies the signal by $\gamma\eta<1$. Because higher baroclinic modes have a slower phase speed $c_{\mathbf{n}}$, they result in weaker losses from boundary reflections. Losses however depends on the boundary reflection coefficients γ and η, which account for several processes at the western and eastern boundaries and which exact values are therefore arguable (Boulanger and Menkes, 1995; Jin, 1997b; Dewitte et al., 2003). We set $\gamma\eta$=0.6, 0.8 or 1 in figure 2.5.a to show this sensitivity.

Our results suggest that the contribution of the gravest baroclinic modes is dominant for the ocean adjustment at basin scale and at interannual timescale. This is because they have greatest projection coefficient P_n and smallest dissipation rate σ_n for the evolution of the WWV mode (figure 2.5.b). Under similar considerations, we have shown in previous section 2.1.4 that the gravest baroclinic modes are also the most relevant for the storage of available potential energy. Those considerations may justify in particular a truncature at the contribution from the three gravest baroclinic modes, as will be done in the following chapters. The same truncature is considered in the model of Dewitte (2000) and other related studies. Because our work in several following chapters is an extension of those studies, it is also convenient to consider, whenever possible, similar hypotheses. In the following chapters, we will see that the sensitivity to the ocean baroclinic structure can however be more complex when considering that the ocean and atmosphere are coupled, which is another central feature of the ENSO.

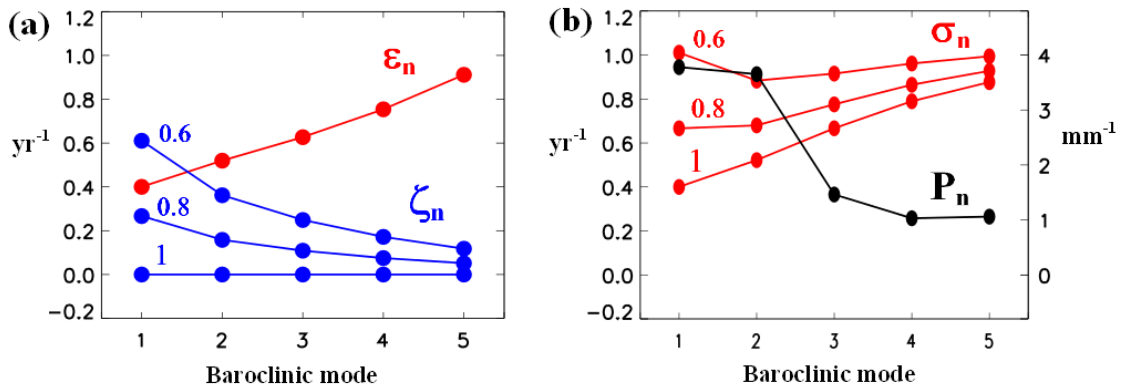

Figure 2.5: (a) Contributions ε_n (red) and ζ_n=-ln($\gamma\eta$)c_n/4L (blue) to the dissipation rate σ_n, in yr^{-1} and as a function of the baroclinic mode n. Losses at boundaries ζ_n are shown for three values of reflection coefficient product, $\gamma\eta$=0.6, 0.8 or 1. (b) Dissipation rate σ_n (red, yr^{-1}) and wind stress projection coefficient P_n (mm^{-1}) as a function of the baroclinic mode n. Dissipation rate σ_n is shown for three values of the reflection coefficient product, $\gamma\eta$=0.6, 0.8 or 1.

Chapter

3. Coupled Dynamics

This chapter is dedicated to the study of coupled ocean-atmosphere dynamics in the equatorial Pacific. We recall at first notions on mixed-layer thermodynamics and atmospheric dynamics that are relevant to ENSO. A reduced coupled model (the AC model for Absolute and Convective model) is proposed, that is truncated meridionaly to the first ocean and atmosphere equatorial waves and that has a zonal infinite domain (i.e. no boundary reflections). The AC model considers contributions from the first ocean and atmosphere baroclinic modes and retains the dominant thermodynamic processes of the oceanic mixed-layer. The temporal stability of this model evidences some of the leading coupled instabilities of the equatorial Pacific system. Those instabilities are of large spatial scale (approximately the basin length), of interannual timescale and are of coupled nature between the ocean and atmosphere.

The diagnostic of absolute/convective instability is further introduced, which proposes an alternative view on the stability problem. This diagnostic assesses whether small perturbations localized in space and time (e.g. random wind disturbances) lead to instabilities that develop in-place or propagate away from the perturbed region. It may identify different ENSO formation mechanisms, where the role of boundary reflections is either central or secondary. Such diagnostic permits to discuss key features of coupled instabilities that are implicitly considered in ENSO models. The possibility that ENSO develops, in the absolutely unstable regime, without involving boundary reflections is of particular interest, because it is in contradiction with common theories. An article is included that presents main results. Supplementary materials are also provided, where we compute the temporal stability of the AC model with contributions from the three gravest ocean baroclinic modes.

3.1. Background

3.1.1. Mixed Layer Thermodynamics

We recall at first elements of mixed-layer thermodynamics that are relevant for ENSO. We derive an equation for the evolution of mixed-layer temperature anomalies following Dijkstra (2006). The upper ocean is generally well-mixed up to a depth of 50m. The temperature in this mixed layer changes due to air-sea interaction, exchange processes with deeper layers and advection. Under the approximation that the temperature is vertically homogeneous over the layer, one can integrate the heat balance equation which results in an equation for the mixed-layer temperature. The evolution of temperature T reads

$$\partial_t T + u\partial_x T + v\partial_y T = K_H\,(\partial_x^2 T + \partial_y^2 T) + \frac{Q_{oa} - Q_b}{\rho_o C_p H_m} \tag{3.1}$$

where u and v are respectively zonal and meridional currents integrated in the mixed layer, ρ_o is the ocean density, h_{mix} is the mixed layer depth (considered constant), Q_{oa} is the ocean-atmosphere heat flux, Q_b is the heat flux at the bottom of the mixed layer, C_p is a heat capacity constant, and K_H is a dissipation constant. The ocean-atmosphere heat flux may be parametrised into a linear damping relatively to an equilibrium temperature, and a similar approach may be adopted for dissipative processes. It may be assumed that the heat flux at the bottom of the mixed layer is attributed essentially to vertical advective processes, whereas diffusive processes are secondary. It is therefore parametrised as

$$\frac{Q_b}{\rho C_p H_m} = wG_z \text{ with } G_z = \frac{T - T_{SUB}}{h_{mix}} \tag{3.2}$$

where w and T_{SUB} are respectively vertical current and temperature at the base of the mixed layer, and G_z defines a vertical gradient of temperature at the base of the mixed layer. We linearise the heat budget from equation 3.1 around a mean state at equilibrium. For simplicity we keep previous notations for anomalies while an over-bar denotes a mean state average. The linearised heat budget reads

$$(\partial_t + \varepsilon_T)T + (u\partial_x \overline{T} + v\partial_y \overline{T} + w\overline{G_z}) + (\bar{u}\partial_x T + \bar{v}\partial_y T + \bar{w}G_z) = 0 \tag{3.3}$$

where ε_T is a collective linear damping accounting for ocean-atmosphere heat flux and dissipative processes..Temperature anomalies at the base of the mixed layer T_{SUB} may be related directly to thermocline depth anomalies h through an empirical efficiency factor, which reads $T_{SUB} = \gamma h$ (An and Jin, 2001). This assumes a direct relation between heating at the base of the mixed layer and the vertical displacements of the isotherms within the well stratified waters. The efficiency factor is in practice computed from a linear regression. For simplicity we retain only a few dominant terms of the heat budget from equation 3.3, which now reads

$$\partial_t T = F^{D}T + F^{ZA}u + F^{T}h \tag{3.4}$$

with $F^{D} = -(\varepsilon_T + \overline{w}/h_{mix})$, $F^{ZA} = -\partial_x \overline{T}$ and $F^{T} = \overline{w}\gamma/h_{mix}$ that are respectively coefficients of the damping feedback, the zonal advective feedback and the thermocline feedback (An and Jin, 2001, An and Jin, 2000; Fedorov and Philander, 2001). Those feedbacks are illustrated in figure 3.1. The damping feedback (usually negative) accounts collectively for the adjustment time of the mixed layer through dissipative processes, ocean-atmosphere heat flux adjustment and the mean upwelling. The zonal advective feedback accounts for the zonal heat advection by anomalous zonal current in a mean zonal gradient of temperature, which is the case at large scale in the equatorial Pacific where western waters are warmer than eastern waters. The thermocline feedback accounts for vertical heat advection of temperature anomalies by the mean upwelling, where temperature anomalies are related to thermocline vertical displacements.

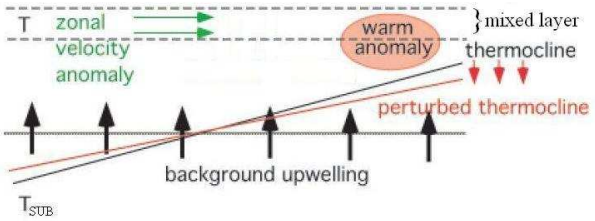

Figure 3.1: Sketch of the thermocline feedback (red arrows) and the zonal advective feedback (green arrows) (adapted from Dijkstra, 2006).

3.1.2. Atmosphere Dynamics

We recall elements of atmosphere dynamics that are relevant to the interannual variability of the equatorial Pacific. For the large scales under consideration, a simple Gill model may describe the deterministic response of the atmosphere (Gill, 1980). Note that this large scale dynamics is different from the high frequency and stochastic dynamics that is encountered in the central Pacific, and for which additional processes are considered (Wang and Xie, 1998).

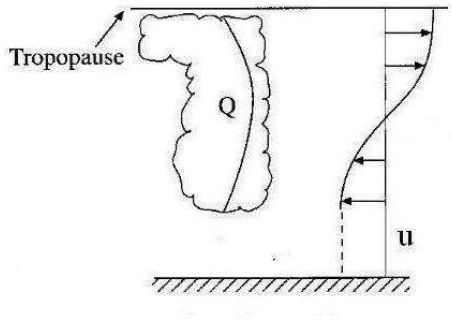

Figure 3.2: Sketch of the Gill Model (adapted from Battisti et al., 1999).

The Gill model is illustrated in figure 3.2. It describes the response of the entire troposphere (the first 10 km) to deep convection, where the latent heat flux at the top of the troposphere (the tropopause) is the forcing term. It considers simple shallow water dynamics, similar to the ocean, but where the adjustment time of the atmosphere (~a few days) is neglected. In particular, it is assumed that the atmospheric response is dominated by the first gravest baroclinic mode, confined to the troposphere (see Clarke, 2008, its Chapter 9). Because the first baroclinic mode changes sign between the bottom and top of the troposphere, zonal advection is inverted (for example horizontal convergence in lower layers results in horizontal divergence in upper layers). The Gill model reads

$$\varepsilon u - \beta y v + \partial_x (gh) = 0 \tag{3.5}$$

$$\beta y u + \partial_y (gh) = 0 \tag{3.6}$$

$$\varepsilon (gh) + c_a^2 (\partial_x u + \partial_y v) = -Q \tag{3.7}$$

where β is the beta-plane parameter, g the gravity constant, u and v are respectively zonal and meridional velocity averaged through the lower layer, h is height anomalies at the tropopause, c_a is the atmospheric wave speed (that is estimated from the troposphere thickness and stratification), and ε is a thermal and mechanical dissipation rate (chosen identical in equations 3.5 and 3.7 to simplify the analytical treatment). Q is the latent heat flux at the top of the troposphere, which results from both evaporation and convection and which may be related empirically to SST anomalies. The model then gives the low level winds, which act as a forcing term for the ocean dynamics through friction at the ocean-atmosphere interface.

An alternative to the Gill model that is worth mentioning is the Lindzen-Nigam model (Lindzen and Nigam, 1987). The Lindzen-Nigam model describes the response of the atmospheric boundary layer (the first 1 km) to horizontal gradients of surface pressure that are related to horizontal SST gradients. Although quite different with regard to the physical processes under consideration, the Lindzen-Nigam model can be put in a similar form to the one of the Gill model following the variable change proposed by Neelin (1989). This facilitates the analytical treatment, though model parameters are different. Both models follow shallow water dynamics with two layers (i.e. a single atmosphere baroclinic mode). Discrepancies between both models are discussed in Battisti et al. (1999) and An (2011). Also a modified version of the Gill model is used in the model from Zebiak and Cane (1987), with a further parametrisation of atmospheric convergence in the lower layers.

It is possible to consider atmospheric equatorial waves as solutions of the Gill model (or alternatively the Lindzen-Nigam model), following a similar formalism than for the ocean (see chapter 2). Equatorial Kelvin and Rossby waves in the long-wave approximation are relevant to describe the atmosphere adjustment at large spatial and temporal scales that are relevant to ENSO (see also Clarke, 2008, its chapter 6). The Rossby radius of atmospheric equatorial waves is however larger than the Rossby radius of oceanic equatorial waves, as shown in figure 3.3. This truncated representation of the atmosphere will be considered in the following section.

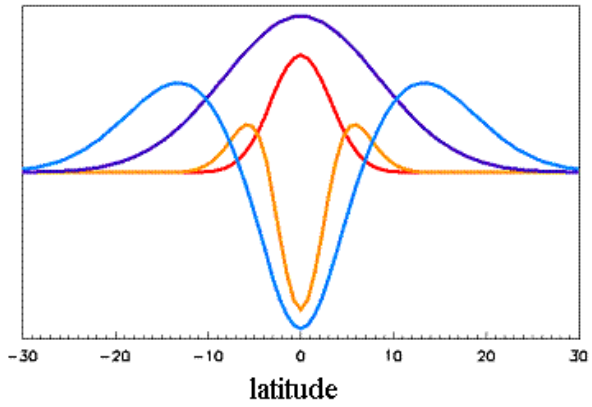

Figure 3.3 Non-dimensional meridional profiles of ocean and atmosphere equatorial waves, as a function of latitude (degree north). Contribution to zonal currents is shown for the ocean Kelvin wave (red), the ocean Rossby wave (orange), the atmosphere Kelvin wave (blue), and the atmosphere Rossby wave (cyan).

3.2. Absolute or Convective Nature of ENSO Instabilities

3.2.1. Article Published in Q. J. R. Meteorol. Soc.

Based on previous elements of ocean dynamics, atmosphere dynamics and mixed-layer thermodynamics, we propose a reduced coupled model (the AC model) that identifies dominant coupled instabilities of the equatorial Pacific. The model is presented in an article published in the revue Quarterly Journal of the Royal Meteorological Society (Thual et al., 2012a). The article further introduces the diagnostic of absolute/convective instability, which proposes an alternative view at the stability problem in the equatorial Pacific. It permits to discuss certain features of coupled instabilities that are related to the more general understanding of ENSO formation mechanisms.

Abstract: The El Niño–Southern Oscillation (ENSO) is driven by ocean–atmosphere interactions in the equatorial Pacific, and this variability is often attributed to coupled modes that are evidenced by the temporal stability analysis of anomaly models. Here, the further diagnostic of absolute/convective instability is considered, which assesses whether small perturbations localized in space and time (e.g. random wind disturbances) lead to instabilities that develop in-place or propagate away from the perturbed region. It is shown that boundary conditions play a secondary role for this approach and that the development of large-scale wave packets in the equatorial Pacific basin is possible, as in the case of an infinite domain. As an illustration, two simple coupled models are diagnosed that rely either on thermocline processes or zonal advective processes. The model with thermocline processes is ‘absolutely unstable’ and therefore develops intrinsic oscillations, while the model with zonal advective processes is ‘convectively unstable’ and therefore acts as a noise amplifier. The identification of the two instability regimes may characterize different ENSO formation mechanisms as a response to random wind disturbances. For the absolutely unstable regime, a standing ENSO-like oscillation can develop in the equatorial Pacific without involving boundary reflections, while for the convectively unstable regime boundary reflections are essential.

RMetS
Royal Meteorological Society

Absolute or convective instability in the equatorial Pacific and implications for ENSO

Sulian Thual,[a] Olivier Thual[b,c]* and Boris Dewitte[a]
[a]*Laboratoire d'Etude en Géophysique et Océanographie Spatiale, Toulouse, France*
[b]*Université de Toulouse; INPT, UPS; IMFT, Toulouse, France*
[c]*CNRS; IMFT, Toulouse, France*

*Correspondence to: O. Thual, IMFT, Allée C. Soula, Toulouse 31400, France. E-mail: thual@imft.fr

The El Niño–Southern Oscillation (ENSO) is driven by ocean–atmosphere interactions in the equatorial Pacific, and this variability is often attributed to coupled modes that are evidenced by the temporal stability analysis of anomaly models. Here, the further diagnostic of absolute/convective instability is considered, which assesses whether small perturbations localized in space and time (e.g. random wind disturbances) lead to instabilities that develop in-place or propagate away from the perturbed region. It is shown that boundary conditions play a secondary role for this approach and that the development of large-scale wave packets in the equatorial Pacific basin is possible, as in the case of an infinite domain. As an illustration, two simple coupled models are diagnosed that rely either on thermocline processes or zonal advective processes. The model with thermocline processes is 'absolutely unstable' and therefore develops intrinsic oscillations, while the model with zonal advective processes is 'convectively unstable' and therefore acts as a noise amplifier. The identification of the two instability regimes may characterize different ENSO formation mechanisms as a response to random wind disturbances. For the absolutely unstable regime, a standing ENSO-like oscillation can develop in the equatorial Pacific without involving boundary reflections, while for the convectively unstable regime boundary reflections are essential. Copyright © 2012 Royal Meteorological Society

Key Words: ENSO; equatorial Pacific; interannual variability; absolute instability; wave packets; conceptual models

Received 5 February 2012; Revised 9 May 2012; Accepted 23 May 2012; Published online in Wiley Online Library

Citation: Thual S, Thual O, Dewitte B. 2012. Absolute or convective instability in the equatorial Pacific and implications for ENSO. *Q. J. R. Meteorol. Soc.* DOI:10.1002/qj.1988

1. Introduction

A hierarchy of models of increasing complexity simulate the interannual variability of the equatorial Pacific with a particular focus on the forecast of El Niño/La Niña events and, more generally, explain the main features of the El Niño–Southern Oscillation (hereafter ENSO). In those models, the development of anomalies is mainly attributed to interactions between the ocean and the atmosphere. The studies of temporal instabilities exhibited by those models have led to the emergence of the theory of coupled modes (Neelin *et al.*, 1998). It also provides a fruitful view for the interpretation of observations and coupled general circulation models.

The temporal stability analysis of models has allowed the identification of various types of coupled modes of the equatorial Pacific. They are usually classified depending on the physical processes involved. A large number of studies distinguish two families of coupled modes either based on thermocline processes or zonal advective processes in the ocean (Hirst, 1986; Bejarano and Jin, 2008; Thual *et al.*, 2011). An and Jin (2001) and Fedorov and Philander

(2001) further suggest that the relative strength of those two processes can lead to different regimes of the ENSO in terms of amplitude, frequency and propagation. Other relevant coupled modes have been evidenced that rely solely on the interaction between the atmosphere and the oceanic mixed layer (Wang and Xie, 1998; Dommenget, 2010). Asymptotic limits for the adjustment time of each of the coupled system components are also important. Neelin (1991) distinguishes the coupled modes where the adjustment time of sea-surface temperature (SST) is fast compared to the adjustment time of the ocean dynamics (the fast-SST regime) and inversely (the fast-wave regime). Furthermore, within this line of studies, it is usually assumed that a 'fast atmosphere' adjusts immediately to SST. Although the reflections at the eastern and western boundaries are usually considered in coupled models, some noticeable studies identify coupled modes without boundary conditions (Hirst, 1986; Wang and Weisberg, 1996; Weisberg and Wang, 1997; Wang and Xie, 1998; Pontaud and Thual, 1995, 1998).

A further approach to temporal stability analysis is the diagnostic of absolute/convective instability. So far, this approach has not been considered for the identification of coupled modes in the equatorial Pacific. The diagnostic of absolute/convective instability originates from plasma physics (Briggs, 1964) and has been further developed in fluid mechanics. A review of the method is given in Huerre and Monkewitz (1990), a discussion on its practical implementation in Suslov (2006), and a few applications in geophysical fluid dynamics stability problems are listed in Pedlosky (2012). The diagnostic assesses whether small perturbations localized in space and time lead to instabilities that develop in-place or propagate away from the perturbed region. Absolutely unstable systems develop intrinsic oscillations in the perturbed region: they act as 'oscillators' with intrinsic dynamics. Convectively unstable systems amplify but disperse the external perturbations: they act as 'noise amplifiers' with extrinsic dynamics.

In most ENSO theories, boundary reflections are essential for the system to oscillate, as they provide the necessary negative feedback for the transition from a warm (El Niño) phase to a cold (La Niña) phase and inversely (Suarez and Schopf, 1988; Jin, 1997; Picaut *et al.*, 1997). Those theories consider coupled modes that are solutions of a system with prescribed boundary conditions. Absolute or convective instabilities are of a different nature, although they are not incompatible with the presence of boundary conditions. They are described in terms of wave packets, which result from the superposition of a continuum of modes that are solutions of a linear system in an infinite domain. When further considering boundary conditions, the reflected components simply superpose in a linear framework. The diagnostic of absolute/convective instability depicts whether the stationary component decays or develops into a standing oscillation, independently of the reflected components.

The diagnostic may characterize different ENSO formation mechanisms as a response to random disturbances, e.g. westerly winds bursts (Harrison and Vecchi, 1997). Different scenarios can be expected depending on the stability of the equatorial Pacific system (Philander and Fedorov, 2003; Kleeman, 2008; Kessler, 2002). If the system is strongly damped, the ENSO has to be only a direct response to random wind disturbances, but this hypothesis is unlikely. If the system is unstable enough, it may be self-regulated by internal nonlinear processes, such as overlapping resonance with the seasonal cycle (Jin *et al.*, 1994) or mean state rectification by the heat budget asymmetry (Timmermann *et al.*, 2003). The diagnostic presented here applies in the intermediate case of a slightly unstable system. As stressed by Neelin *et al.* (1998), for such a system the ENSO is weakly nonlinear, in the sense that dominant spatial and temporal scales of variability are determined by the leading coupled mode(s) issued from linear stability. Random wind disturbances are not necessary to maintain the variability but still act as a trigger of specific events, through small perturbations that are amplified by the coupled system in the form of wave packets. As a response to random wind disturbances, in the absolutely unstable regime an ENSO cycle can develop as a standing oscillation, while in the convectively unstable regime an ENSO cycle may still develop but only if boundary reflections are involved.

In this article, the approach is illustrated by diagnosing two simple coupled models of the equatorial Pacific that differ in the thermodynamic processes considered. We aim at evaluating, among those processes, those that lead either to an absolute or to a convective regime. The models are presented in section 2. Section 3 is dedicated to a temporal stability analysis of the models as a consistency check with previous studies. In section 4 we diagnose the models in terms of absolute/convective instability. Section 5 is a discussion, followed by concluding remarks.

2. Coupled system

We consider a shallow-water model for the ocean in the long-wave approximation and in an infinite domain. This system is projected on the meridional basis of 'oceanic' Hermite functions (with oceanic Rossby radius $\sqrt{c_o/\beta}$) and truncated at the Kelvin and first Rossby equatorial wave components, $K(x,t)$ and $R(x,t)$. Those depend on longitude and time through

$$\begin{aligned}(\partial_t + \varepsilon_o)K + c_o\partial_x K &= P_K(\tau_x),\\ (\partial_t + \varepsilon_o)R - \frac{c_o}{3}\,\partial_x R &= P_R(\tau_x),\end{aligned} \tag{1}$$

where ε_o is the dynamical damping, c_o is the phase speed of the oceanic Kelvin waves, $\tau_x(x,y,t)$ is the field of zonal wind stress anomalies (N m^{-2}) and P_K and P_R are projection operators on the oceanic Hermite functions. The parameter values are those from Thual *et al.* (2011) when considering only the contribution from the first baroclinic mode of the ocean. The approach is similar for the atmosphere. We consider a Gill-type shallow-water model in the long-wave approximation (Gill, 1980). The system is projected on the meridional basis of 'atmospheric' Hermite functions (with atmospheric Rossby radius $\sqrt{c_a/\beta}$) and truncated at the Kelvin and first Rossby equatorial wave components, $k(x,t)$ and $r(x,t)$. Those depend on longitude and time through

$$\begin{aligned}\varepsilon_a k + c_a\,\partial_x k &= P_k(\,T),\\ \varepsilon_a r - \frac{c_a}{3}\,\partial_x r &= P_r(\,T),\end{aligned} \tag{2}$$

where ε_a is the atmospheric dynamical damping, c_a is the phase speed of the atmospheric Kelvin waves, $T(x,y,t)$ is the field of SST anomalies and P_k and P_r are projection operators on the atmospheric Hermite functions. The parameter values

are those from Hirst (1986). The adjustment time of the atmosphere (a few days) is neglected compared to the one of the ocean (a few months). Finally, we consider a linearized mixed-layer thermodynamic model for SST anomalies T and retain only the dominant thermodynamic processes, namely the feedbacks due to damping, zonal advection and thermocline depth anomalies:

$$(\partial_t + \varepsilon_T)T = f_H H + f_U U, \tag{3}$$

where ε_T is the thermodynamic damping and f_H and f_U are constant coefficients. Model parameters are derived from Thual *et al.* (2011), where further considering constant and representative values of the thermocline feedback efficiency factor ($\gamma = 0.1^\circ\text{C m}^{-1}$) and the mean SST zonal gradient ($\partial_x T = -10^\circ\text{C}/L$, where L is the basin length of 17 000 km). $H(x, y, t)$ and $U(x, y, t)$ are fields of thermocline depth anomalies (m) and zonal current anomalies (m s^{-1}) respectively, which can be reconstructed from K and R using the oceanic Hermite functions. Similarly, $\tau_x(x, y, t)$ can be reconstructed from k and r using the atmospheric Hermite functions if assuming, as in Hirst (1986), that wind stress is proportional to wind speed. In order to eliminate the variables τ_x, T, H and U we project and combine the oceanic, atmospheric and thermodynamic equations. We obtain a linear system of four variables K, R, k, r that depend on longitude and time:

$$\begin{aligned}
&(\partial_t + \varepsilon_o)K + c_o \partial_x K = M_{Kk} k + M_{Kr} r,\\
&(\partial_t + \varepsilon_o)R - \frac{c_o}{3}\partial_x R = M_{Rk} k + M_{Rr} r,\\
&(\partial_t + \varepsilon_T)\left(k + \frac{c_a}{\varepsilon_a}\partial_x k\right) = M_{kK} K + M_{kR} R,\\
&(\partial_t + \varepsilon_T)\left(r - \frac{c_a}{3\,\varepsilon_a}\partial_x r\right) = M_{rK} K + M_{rR} R,
\end{aligned} \tag{4}$$

where M_{Kk}, M_{Kr}, M_{Rk}, M_{Rr}, M_{kK}, M_{kR}, M_{rK} and M_{rR} are constant coefficients. Interestingly, the phase speed resulting from the combined atmosphere and thermodynamics $\varepsilon_T c_a/\varepsilon_a \sim$ 2 m s^{-1} is close to the phase speed of the ocean model $c_o \sim$ 3 m s^{-1}. The resulting damping $\varepsilon_T \sim$ (35 day)$^{-1}$ is, however, much stronger than for the ocean model ε_o = (2.5 year)$^{-1}$.

We consider two variants of this coupled system, which differ by the thermodynamic processes involved. The distinction between thermocline and zonal advective processes has already been adopted in various studies of the equatorial Pacific coupled modes, as it leads to two families of coupled modes that have different properties and that are both relevant for interpreting the interannual variability. We consider a first model (hereafter H-model) where only thermocline processes are considered ($f_U = 0$), and a second model (hereafter U-model) where only zonal advective processes are considered ($f_H = 0$). Note that we also implemented a third model where both processes are considered, which is not documented here since the main conclusions are similar to those of the H-model. For numerical applications, ε_o = (30 month)$^{-1}$, c_o = 2.8 m s^{-1}, ε_a = (2.3 day)$^{-1}$, c_a = 30 m s^{-1}, and ε_T = (35.7day)$^{-1}$. In both models, $M_{Kk} = -6.0, M_{Kr} = 8.4, M_{Rk} = 2.3$, and $M_{Rr} = -3.9$ (numerical values are given in year^{-1}). In the H-model $M_{kK} = 32.1, M_{kR} = 45.3, M_{rK} = 12.5$, and $M_{rR} = 21.1$. In the U-model $M_{kK} = 16.8, M_{kR} = -9.9, M_{rK} = 6.6$ and $M_{rR} = -2.1$.

3. Temporal stability analysis

We search for one-dimensional vector fields $\boldsymbol{X}(x, t) = [K, R, k, r]$ that are solutions of the coupled system of the previous section. Since the system is real, linear and homogeneous in an infinite domain, one can consider complex solutions of the form $\boldsymbol{X} = \boldsymbol{X}_0 \exp[i(kx - \omega t)]$, where $k = k_r + ik_i$ and $\omega = \omega_r + i\omega_i$ are respectively the complex wave number and frequency (i is the imaginary number). Non-trivial solutions are obtained when a couple (k, ω) satisfies the generalized dispersion relation $D(k, \omega) = 0$, which is obtained through the transformations $\partial_x = ik$ and $\partial_t = -i\omega$ followed by a kernel analysis of the resulting algebraic system. The temporal stability consists, for a determined real wave number k_r, in evaluating the complex roots ω of the dispersion relation $D(k_r, \omega) = 0$. As a preliminary step to the diagnostic of absolute/convective instability, we comment here on the temporal stability analysis of each model as a consistency check with previous studies.

The temporal stability of the H-model is shown in Figure 1. At large wave number, the modes are identical to the uncoupled case, with an 'oceanic Kelvin coupled mode' (yellow) and an 'oceanic Rossby coupled mode' (green) that propagate at speed c_o and $-c_o/3$ respectively ($c_o \sim$ 3 m s^{-1}) and that are slightly damped ($\omega_i \sim -1$ year^{-1}), as well as two 'atmospheric coupled modes' (cyan and blue) that do not propagate and that are strongly damped ($\omega_i \sim -10$ year^{-1}). For a decreasing wave number, one of the atmospheric coupled modes (blue) eventually becomes unstable. Neelin (1991) named this type of unstable mode the 'slow SST mode', where the ocean dynamics adjustment is fast compared to the SST adjustment. This slow SST mode propagates eastward for $k_r \sim 0.2$ (1000 km)$^{-1}$ and westward for $k_r < 0.1$ (1000 km)$^{-1}$, and has maximal amplitude on the atmospheric Kelvin wave (not shown). The temporal stability of the U-model is shown in Figure 2. In this model the oceanic Kelvin coupled mode (yellow) and the second atmospheric coupled mode (cyan) are similar to those of the H-model. However, the slow SST mode (blue) remains damped and the oceanic Rossby coupled mode (green) is slightly unstable. This oceanic Rossby coupled mode propagates westward as in the uncoupled case, and

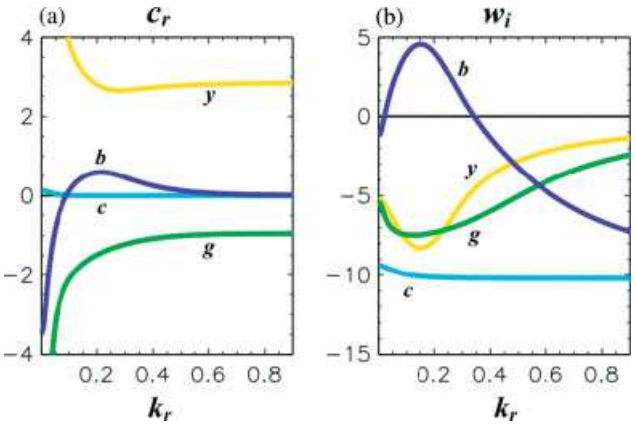

Figure 1. Temporal stability of the H-model. Results are shown for the four mode solution of the dispersion relation, which are identified by colours (yellow, green, cyan, blue). (a) Phase speed $c_r = \omega_r/k_r$ (m s^{-1}) as a function of the real wave number k_r (unit is (1000 km)$^{-1}$). For comparison, the equatorial Pacific length is 17 000 km, which corresponds to a wave number around 0.4 (1000 km)$^{-1}$. (b) Growth rate ω_i (year^{-1}) as a function of k_r. This figure is available in colour online at wileyonlinelibrary.com/journal/qj

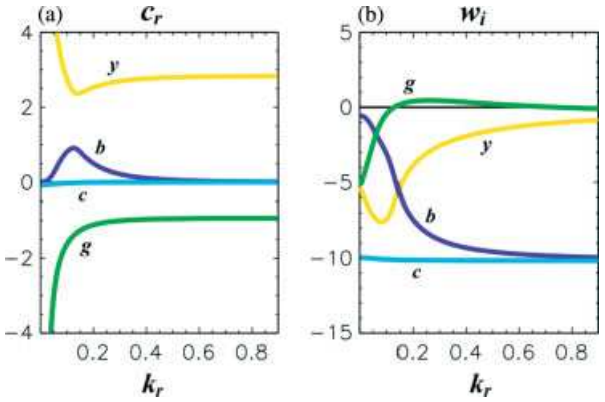

Figure 2. Same as Figure 1 but for the U-model. This figure is available in colour online at wileyonlinelibrary.com/journal/qj

has maximal amplitude on the oceanic Rossby wave (not shown). As in Hirst (1986), we have tested the case with an opposite mean SST gradient ($f_U < 0$), which leads to an opposite direction of propagation, i.e. a slightly unstable oceanic Kelvin coupled mode (not shown). The results agree overall with Hirst (1986, their Figures 7 and 13), Wang and Weisberg (1996, their Figure 1) and Wang and Xie (1998, their Figure 9).

The results from Hirst (1986, their Figure 20), however, exhibit great sensitivity to the number of Hermite functions retained for the meridional truncation. As a further test, we recomputed the temporal stability of the H-model and U-model when increasing the number of meridional components in both the ocean and atmosphere (only odd, i.e. symmetrical Rossby components, were considered). We find that this only slightly modifies the behaviour of the most unstable modes (not shown). We believe that this interesting property of our system is due to the use of an adapted Hermite basis for the atmosphere (with atmospheric Rossby radius), different from the Hermite basis used for the ocean (with oceanic Rossby radius). In Hirst (1986), the Hermite basis of the ocean is used to project the entire system, therefore a large number of meridional modes are necessary to represent the larger meridional scale of the atmosphere.

In the infinite domain considered here, the above temporal stability analysis can be used to describe wave packets made of the superposition of a continuum of modes with wave numbers close to a given real value k_r. Such wave packets propagate at group velocity $\partial\omega_r/\partial k_r$. One can compute the growth rate ω_i of the wave packets propagating at zero group velocity and document their temporal growth or decay at a given location. However, such a consideration must be extended with the study of 'generalized wave packets' built with a continuum of complex wave numbers, i.e. waves with both a wave number k_r and a spatial growth rate $-k_i$. Indeed, the most unstable of the generalized wave packets with zero group velocity will provide the local response of the system to a localized perturbation. This analysis is formalized through the diagnostic of absolute/convective instability described and applied to our models in the next section.

4. Absolute or convective instability

We introduce the diagnostic of absolute/convective instability following Huerre and Monkewitz (1990) and apply it to the models described in the previous sections. Such a diagnostic is relevant only for systems that are linearly unstable. This is the case for the H-model and the U-model, where the temporal analysis evidences the unstable slow SST mode and the slightly unstable oceanic Rossby coupled mode respectively (see section 3). For such a system, we aim at evaluating the system response $G(x, t)$ to a pulse in space and time, which is a solution of

$$D(-i\partial_x, i\partial_t)G(x,t) = \delta(x)\delta(t),$$

where $D(k, \omega)$ is the dispersion relation of the system, i is the complex number and δ is the Dirac function. For this problem, G is the Green function, which can be computed through integration in the complex space as

$$G(x,t) = \frac{1}{(2\pi)^2}\iint \frac{\exp(i(kx-\omega t))}{D(\omega,k)}\mathrm{d}\omega\,\mathrm{d}k,$$

where ω and k are complex. We suppose for simplicity that the dispersion relation admits a single root $\omega(k)$ (the demonstration can be extended to the case of multiple roots), and we use the residual method to integrate over the path $\omega(k)$:

$$G(x,t) = \frac{-i}{2\pi}\int_{-\infty}^{+\infty} \frac{\exp(i(kx-\omega t))}{\partial_\omega D(\omega,k)}\,\mathrm{d}k,$$

where $t \geq 0$. We consider solutions over a ray path at constant (and real) velocity V (m s^{-1}), verifying $x = Vt$. For large t, we can approximate asymptotically the integral with the steepest-descent method, provided we find a saddle point of the complex function $\rho(k) = i[kV - \omega(k)]$, i.e. a complex root k_0 of $(\mathrm{d}\rho/\mathrm{d}k)(k_0) = 0$. If such a root exists, the asymptotic expansion for large t reads

$$G(Vt,t) \sim -\exp(i\pi/4)(2\pi\, t\, d_k^2\omega)^{-1/2}\frac{\exp(\rho)}{\partial_\omega D},$$

where the right member is taken at $k_0 = k_{0r} + i\ k_{0i}$ and at the corresponding $\omega_0 = \omega_{0r} + i\ \omega_{0i}$. This shows that the response is a 'generalized wave packet' of wavelength $2\pi/k_{0r}$ and spatial growth rate $-k_{0i}$ that travels at speed $V = (\mathrm{d}\omega/\mathrm{d}k)(k_0)$ with a temporal growth rate equal to $Re[\rho(k_0)]$. If multiple roots exist, the behaviour is dominated by the most unstable root.

Such behaviour is overlooked in particular for $V = 0$, to distinguish between the absolutely unstable and convectively unstable regimes. If for $V = 0$ the temporal growth rate $Re[\rho(k_0)]$ is positive (which reads $\omega_{0i} > 0$), then the system is said to be absolutely unstable, meaning that an unstable generalized wave packet develops in the perturbed region. If for $V = 0$ the temporal growth rate is negative, it is said to be convectively unstable. Such a system has to be at least unstable for one non-null value of V, because it is nevertheless linearly unstable according to temporal stability. Supposing that such an unstable generalized wave packet develops, then, in the meantime, it propagates away at non-null speed V from the perturbed region and is evacuated at a large time-scale. Therefore, in the perturbed region the signal is dispersed and decays, similarly to the linearly stable regime.

In general, searching the saddle points of the system can require an important practical implementation, especially if

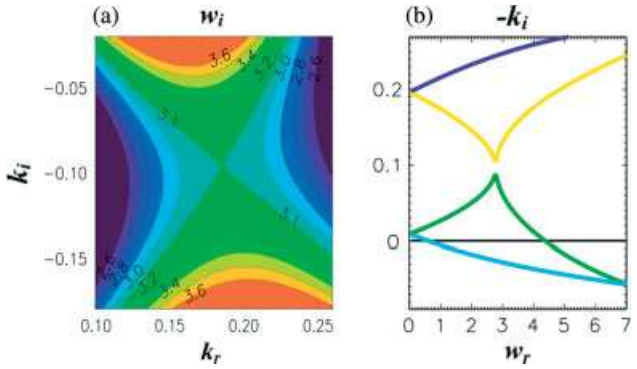

Figure 3. Saddle point detection for the H-model. (a) Imaginary frequency ω_i (year^{-1}) as a function of the real wave number k_r (X-axis, unit is (1000 km)$^{-1}$) and the imaginary wave number k_i (Y-axis, unit is (1000 km)$^{-1}$). The saddle point is found at the intersection of the isocontours for $\omega_{0i} \sim 3.1$ year^{-1}. (b) Imaginary wave number$-k_i$ (unit is (1000 km)$^{-1}$) as a function of the real frequency ω_r (year^{-1}) and for $\omega_i = \omega_{0i}$. The saddle point is found at the intersection of two roots $k(\omega)$. This figure is available in colour online at wileyonlinelibrary.com/journal/qj

automation is required (Suslov, 2006). The coupled system considered here, with four variables, is, however, rather simple thanks to the system truncation at the first meridional Hermite functions. We use a graphical method for the detection of saddle points, which is illustrated in Figure 3 for the H-model. At first, the saddle points for $V = 0$ are detected in the wave number complex space (k_r, k_i) at the intersections of the isocontours of the imaginary frequency ω_i (Figure 3(a)). At least one saddle point must be detected. The system is absolutely unstable provided that the most unstable saddle point verifies $\omega_{0i} > 0$ (ω_{0i} is the absolute growth rate). Also one can easily show that ω_{0i} is always inferior or equal to the maximal growth rate from the temporal stability. As stressed by Huerre and Monkewitz (1990), for the absolute instability to be assessed the most unstable saddle point must also satisfy the Briggs (1964) criterion: such a saddle point must be at the intersection ($\omega = \omega_0$) of two roots $k(\omega)$ that originate from the upper and lower parts of the k-plan ($k_i > 0$ and $k_i < 0$) when increasing ω_i. We have checked that this was the case (Figure 3(b)).

We have found that the H-model is absolutely unstable, while the U-model is convectively unstable. For the H-model the absolute growth rate is $\omega_{0i} = 3.1$ year^{-1} and the absolute frequency is $\omega_{0r} = 2.8$ year^{-1} (period is $2\pi/\omega_{0r} \sim 2.2$ years). This is consistent with contemporary ENSO characteristics (i.e. a maintained oscillation with a period of 2 to 7 years). The associated saddle point is found at $k_{0i} \sim -0.1$ (1000 km)$^{-1}$ and $k_{0r} \sim 0.2$ (1000 km)$^{-1}$ (i.e. a wavelength $2\pi/k_{0r} \sim 30\,000$km, which is about twice the equatorial Pacific basin length). The oscillation therefore occurs at a basin scale. For the U-model there are no unstable ($\omega_{0i} > 0$) roots, therefore the system is convectively unstable.

As a consistency test, we simulated numerically the impulse response of both models, and the results are illustrated in Figure 4. In good agreement with the diagnostic of absolute/convective instability, for the H-model, which is absolutely unstable, the amplitude of the response grows in-place of the initial perturbation, while for the U-model, which is convectively unstable, the amplitude decays.

We also investigated results as a function of the intensity of the thermodynamic feedback considered (either thermocline or zonal advective feedback). In both models, we found a first transition from the linearly stable regime to the convectively unstable regime when increasing the intensity from zero, followed by a second transition from the convectively unstable regime to the absolutely unstable regime. In the H-model, the first transition occurs at around 14% of the reference value of f_H and the second transition at around 16%. It is therefore unlikely that the H-model sustains a convective regime within such a narrow range of parameter values. In the U-model the first transition occurs at around 50% of the reference value of f_U and the second transition at around 130%. Therefore the U-model is preferentially in the convective regime. When the U-model is in the absolute regime ($f_U \sim$ 130% to 200% of its reference value), however, it sustains a high-frequency oscillation ($2\pi/\omega_{0r} \sim 0.9$ year) that is only slightly unstable ($\omega_{0i} < 1.3$ year^{-1}).

5. Discussion

In this article we have considered a simple coupled system of the equatorial Pacific in an infinite domain, using shallow-water dynamics for both the ocean and atmosphere in the long-wave approximation and truncating at the Kelvin and first-meridional Rossby waves. Two variants of the coupled system were considered, which differ by the thermodynamic processes controlling the variations in SST. At first, the models were diagnosed in terms of temporal stability. In agreement with previous studies,

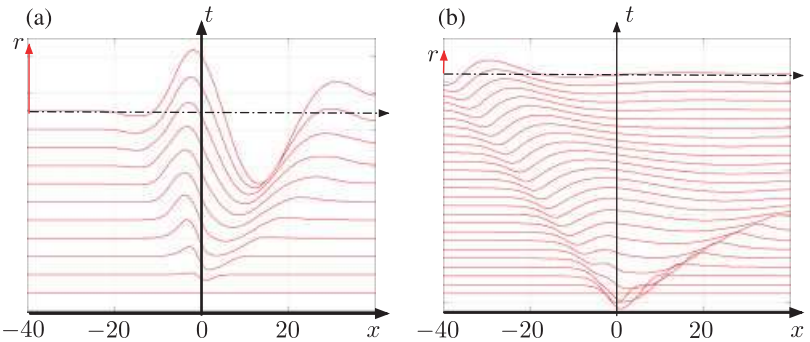

Figure 4. Response to an initial and localized perturbation. The atmospheric Kelvin profile is initialized with a Gaussian shape of 1000 km root mean square centred at $x = 0$. The amplitude of the atmospheric Rossby profile $r(x, t)$ is represented as a function of x (unit is 1000 km) as t increases by steps of 20 days. For comparison, the equatorial Pacific basin length is about 17 000 km. (a) Absolute instability for the H-model: the amplitude grows in-place of the initial perturbation (time increases up to 200 days). (b) Convective instability for the U-model: the amplitude decays in-place of the initial perturbation (time increases up to 500 days). This figure is available in colour online at wileyonlinelibrary.com/journal/qj

the model with thermocline processes (H-model) shows an unstable slow SST mode, while the model with zonal advective processes (U-model) shows a slightly unstable oceanic Rossby coupled mode. Then, the models were diagnosed in terms of absolute/convective instability. Within a representative range of parameters values, the H-model is absolutely unstable and the U-model is convectively unstable.

In the H-model, spatial and temporal scales of the absolute instability are consistent with contemporary ENSO characteristics, namely a basin-scale interannual oscillation. This suggests that a standing ENSO-like oscillation can develop in the equatorial Pacific without involving boundary reflections. Here, the ENSO develops on a continuum of coupled modes that can be viewed as 'generalized wave packets', which are considered in an infinite domain and that are not inhibited by the addition of boundary conditions. In most ENSO theories, the dynamics are rather described by coupled modes that are temporal 'basin modes', which are quantified as they satisfy boundary conditions (e.g. as the harmonics of a vibrating string). Temporal basin modes were not considered here, but they can coexist with the generalized wave packets in a linear framework. However, generalized wave packets cannot be constructed as a continuum of temporal basin modes because their asymptotic behaviour for large time is in $\exp(\rho\, t)/\sqrt{t}$. In the case of an absolutely unstable system, generalized wave packets may be at least as important for ENSO formation as temporal basin modes. In the case of a convectively unstable system, only temporal basin modes may develop an ENSO oscillation, therefore basin parameters (its geometry and reflection coefficients) should be important.

There is an ongoing discussion on whether ENSO is a series of events triggered by random wind disturbances or a self-sustained natural mode of the coupled ocean–atmosphere. The diagnostic presented here, within the assumed hypothesis, may eventually provide material for this discussion. It is assumed here that the interannual variability results from the linear amplification of random wind disturbances, which leads to different ENSO formation mechanisms depending on the regime of the equatorial Pacific system. The regime (absolutely unstable, convectively unstable or linearly stable) may change depending on the mean state, and therefore it would be fundamental to map transitions as a function of the many mean state parameters.

So far, we have considered local modes where the mean state is constant or varies very slowly in space as compared to the wavelength of the problem. The diagnostic of absolute/convective instability may, however, be different when considering various regions as a whole, with different properties. Such a diagnostic for inhomogeneous systems in space requires the concept of global modes (Huerre and Monkewitz, 1990). Since the equatorial Pacific shows an important zonal contrast in its mean state parameters, it would be interesting to consider global modes where this contrast is taken into account. The equatorial Pacific can be schematically divided into the Eastern Pacific (Niño3 region: 150°W–90°W, 5°S–5°N) dominated by thermocline processes and the Central Pacific (Niño4 region: 150°E–150°W, 5°S–5°N) dominated by zonal advective processes (An and Jin, 2001). According to our results (where only the thermocline process leads to the absolute regime) an intrinsic oscillation should develop preferentially in the Eastern Pacific, while in the Central Pacific the flow should be in large part controlled by the features of the random wind disturbances. This, however, assumes that the Eastern and Central Pacific are independent.

There is also the possibility that changes in the leading processes over the equatorial Pacific modify the areas of convective/absolute instability from one El Niño event to another and, consequently, the location of peak SST anomalies. For example, focus has been given recently to a new type of El Niño with peak SST anomalies in the Central Pacific, called 'Modoki' El Niño, 'Warm Pool' or 'Central Pacific' El Niño (Ashok *et al.*, 2007; Kao and Yu, 2009; Yeh *et al.*, 2009; Dewitte *et al.*, 2011). Kug *et al.* (2009) noted that this type of event is related to stronger zonal advective and atmospheric damping processes, while the conventional 'Cold Tongue' event with peak anomalies in the Eastern Pacific is more related to thermocline processes. For this type of event, the discharge process of the equatorial heat content is not efficient enough to trigger the reversal from the warm to the cold phase, which suggests a secondary role of boundary reflections. This questions to what extent the 'Central Pacific' El Niño may be accounted for by the absolute regime documented in this study.

Acknowledgements

S. Thual has been supported by CNRS and Conseil Régional Midi-Pyrénées under contract No. 022009. The authors would like to thank Professors Nick Hall, Soon-Il An and Sang-Wook Yeh for fruitful discussions, as well as the two anonymous reviewers.

References

An S-I, Jin F-F. 2001. Collective role of thermocline and zonal advective feedbacks in the ENSO Mode. *J. Climate* **14**: 3421–3432.

Ashok K, Behera SK, Rao SA, Weng H, Yamagata T. 2007. El Niño Modoki and its possible teleconnection. *J. Geophys. Res.* **112**: C11007, DOI: 10.1029/2006JC003798.

Bejarano L, Jin F-F. 2008. Coexistence of equatorial coupled modes of ENSO. *J. Climate* **21**: 3051–3067.

Briggs R. 1964. *Electron–Stream Interaction with Plasmas*. MIT Press: Cambridge, MA.

Dewitte B, Choi J, An S-I, Thual S. 2011. Vertical structure variability and equatorial waves during central Pacific and eastern Pacific El Niños in a coupled general circulation model. *Clim. Dynam.* **38**: 2275–2289.

Dommenget D. 2010. The slab ocean El Niño. *Geophys. Res. Lett.* **37**: L20701, DOI: 10.1029/2010GL044888.

Fedorov AV, Philander SG. 2001. A stability analysis of tropical ocean–atmosphere interactions: bridging measurements and theory for El Niño. *J. Climate* **14**: 3086–3101.

Gill AE. 1980. Some simple solutions for heat-induced tropical circulation. *Q. J. R. Meteorol. Soc.* **106**: 447–462.

Harrison DE, Vecchi GA. 1997. Westerly wind events in the tropical Pacific, 1986–95. *J. Climate* **10**: 3131–3156.

Hirst AC. 1986. Unstable and damped equatorial modes in simple coupled ocean–atmosphere models. *J. Atmos. Sci.* **43**: 606–632.

Huerre P, Monkewitz PA. 1990. Local and global instabilities in spatially developing flows. *Annu. Rev. Fluid Mech.* **22**: 473–537.

Jin F-F. 1997. An equatorial ocean recharge paradigm for ENSO. Part I: Conceptual model. *J. Atmos. Sci.* **54**: 811–829.

Jin F-F, Neelin JD, Ghil M. 1994. El Nino on the Devil's Staircase: annual subharmonic steps to chaos. *Science* **264**: 70–72.

Kao H-Y, Yu J-Y. 2009. Contrasting Eastern-Pacific and Central-Pacific types of ENSO. *J. Climate* **22**: 615–632.

Kessler WS. 2002. Is ENSO a cycle or a series of events? *Geophys. Res. Lett.* **29**: 2125, DOI: 10.1029/2002GL015924.

Kleeman R. 2008. Stochastic theories for the irregularity of ENSO. *Phil. Trans. R. Soc. A* **366**: 2509–2524.

Kug J-S, Jin F-F, An S-I. 2009. Two types of El Niño events: Cold Tongue El Niño and Warm Pool El Niño. *J. Climate* **22**: 1499–1515.

Neelin JD. 1991. The slow sea surface temperature mode and the fast-wave limit: analytic theory for tropical interannual oscillations and experiments in a hybrid coupled model. *J. Atmos. Sci.* **48**: 584–606.

Neelin JD, Battisti DS, Hirst AC, Jin F-F, Wakata Y, Yamagata T, Zebiak SE. 1998. ENSO theory. *J. Geophys. Res.* **103**(C7): 14261–14290.
Pedlosky J. 2012. Instability theory for the oceans and atmosphere. http://www.whoi.edu/profile.do?id=jpedlosky
Philander SG, Fedorov A. 2003. Is El Niño sporadic or cyclic? *Annu. Rev. Earth Planet. Sci.* **31**: 579–594.
Picaut J, Masia F, du Penhoat Y. 1997. An advective-reflective conceptual model for the oscillatory nature of the ENSO. *Science* **277**: 663–666.
Pontaud M, Thual O. 1995. Some effects of a mean zonal thermocline gradient on planetary equatorial waves. *Ann. Geophys.* **13**: 1223–1228.
Pontaud M, Thual O. 1998. Coupled process for equatorial Pacific interannual variability. *Q. J. R. Meteorol. Soc.* **124**: 527–555.
Suarez MJ, Schopf PS. 1988. A delayed action oscillator for ENSO. *J. Atmos. Sci.* **45**: 3283–3287.
Suslov SA. 2006. Numerical aspects of searching convective/absolute instability transition. *J. Comput. Phys.* **212**: 188–217.
Thual S, Dewitte B, An S-I, Ayoub N. 2011. Sensitivity of ENSO to stratification in a recharge–discharge conceptual model. *J. Climate* **24**: 4332–4349.
Timmermann A, Jin F-F, Abshagen J. 2003. A nonlinear theory for El Niño bursting. *J. Atmos. Sci.* **60**: 152–165.
Wang B, Xie X. 1998. Coupled modes of the warm pool climate system. Part I: The role of air–sea interaction in maintaining Madden–Julian oscillation. *J. Climate* **11**: 2116–2135.
Wang C, Weisberg RH. 1996. Stability of equatorial modes in a simplified coupled ocean–atmosphere model. *J. Climate* **9**: 3132–3148.
Weisberg RH, Wang C. 1997. A western Pacific oscillator paradigm for the El Niño–Southern Oscillation. *Geophys. Res. Lett.* **24**: 779–782.
Yeh S-W, Kug J-S, Dewitte B, Kwon M-H, Kirtman BP, Jin F-F. 2009. El Nino in a changing climate. *Nature* **461**: 511–514.

3.2.2. Supplementary Materials

Additional sensitivity tests have been performed with the AC model from the previous article, and are recalled briefly. We removed the cross term $\partial_x\partial_t$ in the equation that combines thermodynamics and atmosphere dynamics, which simplifies the system into two equations of characteristics and leads to a similar temporal stability except at small scales. We computed the spatial stability of the AC model and compared it to temporal stability using standard techniques, which evidences discrepancies only at large scales. Finally, we computed temporal stability with alternatively a Lindzen-Nigam atmosphere and parameters taken from An (2011), which presents only damped modes.

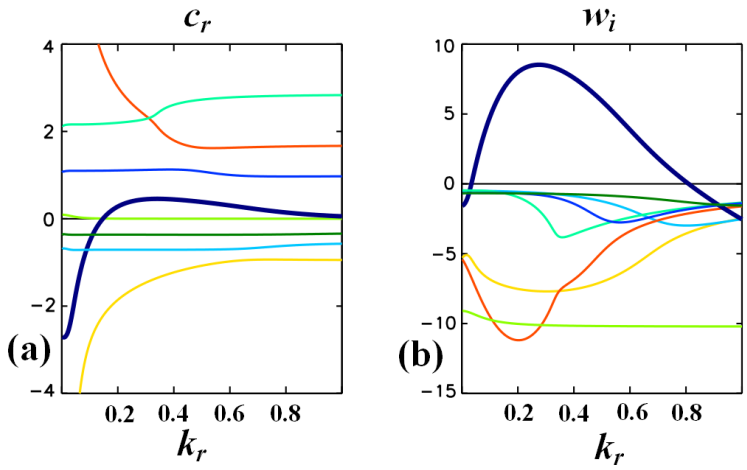

Figure 3.4: Temporal stability of the AC model whith thermocline processes, when considering contributions of the three gravest ocean baroclinic modes. (a) Phase speed $c_r = \omega_r/k_r$ (m.s^{-1}) as a function of the real wavenumber k_r (units is (1000 km)$^{-1}$). (b) Growth rate ω_i as a function of k_r. The system admits eight eigenmodes, each represented by different colors. The slow SST mode is in thick blue line.

We compute the temporal stability of the AC model (with thermocline processes only) when considering the contribution from the three gravest ocean baroclinic modes. This is shown in figure 3.4. We focus in particular on the slow SST mode (thick blue line), which is the leading coupled instability in term of growth rate. As compared to a single baroclinic mode ocean (see previous article, it figure 1), the slow SST mode has a greater growth rate, which extends to higher values of the wavenumber k_r, but keeps a similar phase speed. The increased growth rate is most likely related to an increased thermocline retroaction. The similar phase speed is most likely because, for the slow SST mode, the ocean dynamics adjustment is much faster than the thermodynamic adjustment (which is the so-called fast wave limit, Neelin, 1991). It is therefore rather the thermodynamic adjustment that sets the phase speed. This illustrates how the contribution of the higher baroclinic modes may modify the characteristics of coupled instabilities. Note also that, because with three baroclinic modes the number of system variables is increased, carrying a diagnostic of absolute/convective instability would require more complex and automated methods (Suslov, 2006).

Chapter

4. A Reduced ENSO Model

In this chapter, we design and document the dynamics of a reduced strip model reproducing ENSO-like oscillations, the TD model (for Thual and Dewitte model). It is inspired from previous studies but additionnaly takes into account the three gravest baroclinic modes of a continuously stratified ocean. The background stratification of the equatorial Pacific ocean may modify in particular the ocean baroclinic structure, and so the relative contribution of the gravest baroclinic modes to the ocean dynamics. This feature is critical for the ocean adjustment to wind stress forcing at interannual timescale, as discussed in chapter 2. The sensitivity of ENSO to the background stratification has already been documented in previous studies, from observations or numerical simulations. We extend those studies by adopting a different approach, where the sensitivity to the background stratification is studied in a conceptual framework. The temporal stability of the TD model gives the main characteristics (growth rate, frequency, spatial structure) of the simulated ENSO mode. We document how those characteristics may vary with changes in the background ocean stratification. The stratification modifies in particular the projection of wind stress forcing onto the gravest ocean baroclinic modes, and as such their contributions to the ocean dynamics. We find that an increased stratification (i.e. increased contribution from the second and third baroclinic modes) leads to a more unstable and low frequency ENSO mode in the model. An article presenting main results is included. Supplementary materials are also provided, where we document the design of the statistical atmosphere that is used in the TD model.

In a short second part, we discuss limitations arising from the statistical estimation of the thermocline feedback, which is commonly used in reduced models of ENSO such as the TD model. We show that this estimation can be misleading in the central Pacific due to the dominant zonal advective feedback. This calls for a modified estimation of the thermocline feedback, which would have to be based on more dynamical considerations. The latter may be crucial for the representation of ENSO in reduced to intermediate complexity models, because the thermocline feedback is one of the major thermodynamic processes that control characteristics of the ENSO.

4.1. Sensitivity of ENSO to Ocean Stratification

4.1.1. Article Published in Journal of Climate

We insert an article that documents the stability of a reduced strip model reproducing ENSO-like oscillations (TD model for Thual and Dewitte model). This article has been published in Journal of Climate (Thual et al., 2011). The TD model is strongly inspired by the strip model of An and Jin (2001), but considers an ocean baroclinic structure instead of two-layers shallow water dynamics (cf. chapter 2). This accounts for peculiarities of the background stratification different than the mean thermocline depth. An increased stratification (i.e. increased contribution from the second and third baroclinic modes) leads to a more unstable and low frequency ENSO mode. Sensitivity to the thermocline and zonal advective feedback is also documented.

Abstract: El Niño–Southern Oscillation (ENSO) is driven by large-scale ocean–atmosphere interactions in the equatorial Pacific and is sensitive to change in the mean state. Whereas conceptual models of ENSO usually consider the depth of the thermocline to be influential on the stability of ENSO, the observed changes in the depth of the 20°C isotherm are rather weak, on the order of approximately 5 m over the last decades. Conversely, changes in stratification that affects both the intensity and sharpness of the thermocline can be pronounced. Here, the two-strip conceptual model of An and Jin is extended to include three parameters (i.e., the contribution of the first three baroclinic modes) that account for the main characteristics of the mean thermocline vertical structure. A stability analysis of the model is carried out that indicates that the model sustains a lower-frequency ENSO mode when the high-order baroclinic modes (M2 and M3) are considered. The sensitivity of the model solution to the coupling efficiency further indicates that, in the weak coupling regime, the model allows for several ocean basin modes at low frequency. The latter can eventually merge into a low-frequency and unstable mode representative of ENSO as the coupling efficiency increases. Also, higher baroclinic modes project more energy onto the ocean dynamics for the same input of wind forcing. Therefore, in this study's model, a shallower, yet more intense mean thermocline may still sustain a strong (i.e., unstable) and low-frequency ENSO mode. Sensitivity tests to the strength of the two dominant feedbacks (thermocline vs zonal advection) indicate that the presence of high-order baroclinic modes favors the bifurcation from a low-frequency regime to a higher-frequency regime when the zonal advective feedback is enhanced. It is suggested that the proposed formalism can be used to interpret and measure the sensitivity of coupled general circulation models to climate change.

.

Sensitivity of ENSO to Stratification in a Recharge–Discharge Conceptual Model

SULIAN THUAL AND BORIS DEWITTE

Laboratoire d'Etudes en Géophysique et Océanographie Spatiale, Toulouse, France, and Instituto Geofisico del Peru, Lima, Peru

SOON-IL AN

Department of Atmospheric Sciences, Yonsei University, Seoul, South Korea

NADIA AYOUB

Laboratoire d'Etude en Géophysique et Océanographie Spatiale, Toulouse, France

(Manuscript received 18 October 2010, in final form 1 March 2011)

ABSTRACT

El Niño–Southern Oscillation (ENSO) is driven by large-scale ocean–atmosphere interactions in the equatorial Pacific and is sensitive to change in the mean state. Whereas conceptual models of ENSO usually consider the depth of the thermocline to be influential on the stability of ENSO, the observed changes in the depth of the 20°C isotherm are rather weak, on the order of approximately 5 m over the last decades. Conversely, change in stratification that affects both the intensity and sharpness of the thermocline can be pronounced. Here, the two-strip conceptual model of An and Jin is extended to include three parameters (i.e., the contribution of the first three baroclinic modes) that account for the main characteristics of the mean thermocline vertical structure.

A stability analysis of the model is carried out that indicates that the model sustains a lower ENSO mode when the high-order baroclinic modes (M2 and M3) are considered. The sensitivity of the model solution to the coupling efficiency further indicates that, in the weak coupling regime, the model allows for several ocean basin modes at low frequency. The latter can eventually merge into a low-frequency and unstable mode representative of ENSO as the coupling efficiency increases. Also, higher baroclinic modes project more energy onto the ocean dynamics for the same input of wind forcing. Therefore, in this study's model, a shallower, yet more intense mean thermocline may still sustain a strong (i.e., unstable) and low-frequency ENSO mode. Sensitivity tests to the strength of the two dominant feedbacks (thermocline vs zonal advection) indicate that the presence of high-order baroclinic modes favors the bifurcation from a low-frequency regime to a higher-frequency regime when the zonal advective feedback is enhanced.

It is suggested that the proposed formalism can be used to interpret and measure the sensitivity of coupled general circulation models to climate change.

1. Introduction

El Niño–Southern Oscillation (ENSO), the well-known climate fluctuation, is driven by large-scale ocean–atmosphere interactions in the equatorial Pacific. It has dramatic impacts in many regions surrounding the Pacific Ocean. In recent decades, many efforts have been dedicated to the observation and modeling of ENSO. In particular, the Tropical Ocean and Global Atmosphere (TOGA) program (McPhaden et al. 1998) has led to the development of a wide variety of models and paradigms that allowed improving our understanding of this phenomenon (Neelin et al. 1998). From the early work of Bjerknes (1969), who first observed positive ocean–atmosphere feedbacks leading to El Niño (and oppositely to La Niña) growth, various ENSO theories were proposed that consider negative oceanic feedbacks associated with the decay and phase transition of such events. Those negative oceanic feedbacks were based on,

Corresponding author address: Sulian Thual, Laboratoire d'Etudes en Géophysique et Océanographie Spatiale, 14 Av. Edouard Belin, 31400 Toulouse, France.
E-mail: sulian.thual@gmail.com

DOI: 10.1175/2011JCLI4148.1

among others, the delayed effect of planetary equatorial wave propagation on SST anomalies (Battisti and Hirst 1989; Schopf and Suarez 1988) and/or on the oceanic heat transfer from the equatorial region toward the off-equatorial regions and vice versa [cf. recharge–discharge oscillator of Jin (1997a,b)]. The oscillatory nature of ENSO could therefore be linked to the coupled nature of the equatorial ocean–atmosphere system, in which the ocean provides the memory of the system. In a simplified framework, this has been addressed through the theorical formalism of basinwide coupled instabilities (Neelin et al. 1994), which permits the exploration of the phase space of the ENSO mode. In particular, this approach permitted establishing that ENSO (characterized here by a growth rate and an oscillation frequency) is very sensitive to the characteristics of the oceanic mean state (An and Jin 2000; An and Wang 2000; Fedorov and Philander 2001). The latter actually controls the relative strength of the dominant feedbacks in the tropical Pacific—namely, the thermocline feedback, which relates the thermocline depth anomalies to SST anomalies [dominant in the Niño-3 region (5°S–5°N, 150°–90°W)]; and the zonal advective feedback, which designates the rate of SST changes along the equator as mostly controlled by anomalous zonal advection of mean SST [dominant in the Niño-4 region (5°S–5°N, 150°E–150°W)]. This conceptual view has been particularly fruitful for interpreting more complex systems (Mechoso et al. 2003), which include the coupled general circulation models (CGCMs) of the Coupled Model Intercomparison Project phase 3 (CMIP3) (Meehl et al. 2007), and their sensitivity to change in mean state. In particular, the diversity of the mean state characteristics in these models goes along with a wide range of ENSO dynamics (Van Oldenborgh et al. 2005; Guilyardi 2006; Belmadani et al. 2010). For instance, in these models, a cooler SST mean state tends to be associated with a larger (reduced) contribution of the zonal advective (thermocline) feedback strength (Belmadani et al. 2010). Changes in ENSO variability in recent decades (Yeh et al. 2009; Lee and McPhaden 2010) also suggest that a warmer state may influence the ENSO dynamics through the change in the balance between the two feedbacks. However, the diversity of the sensitivity of models to the increase in greenhouse gases (An et al. 2008; Yeh et al. 2010) makes it difficult to identify which parameter change of the mean state is critical. An et al. (2008) show that the change in the vertical contrast—that is, the change in difference between the subsurface temperature and SST—turns out to be more influential on ENSO than changes in the mean SST itself. This indicates that the vertical ocean stratification is a key parameter for understanding the sensivity of ENSO to global warming (Yeh et al. 2010).

In linear conceptual models of ENSO [Jin 1997b; An and Jin 2001, the two-strip Jin model (JN model); Fedorov and Philander 2001)], three parameters usually define the mean state: 1) the mean upwelling; 2) the mean zonal SST gradient across the equatorial Pacific; and 3) the mean thermocline depth, which constrains the wave dynamics. Although the mean thermocline depth (as inferred from the depth of the 20°C isotherm) determines to some extent the characteristics of the mean stratification, paradoxically, observations and oceanic reanalyses reveal a small change in the mean thermocline depth at decadal-to-interdecadal time scales (Wang and An 2001; Dewitte et al. 2009). Conversely, change in stratification in the vicinity of the thermocline can be significant, reflecting the rich vertical structure variability of the equatorial Pacific (Dewitte et al. 1999; Moon et al. 2004). In particular, a slight flattening thermocline, as experienced after the 1970s, is associated with an increased stratification in the central equatorial Pacific that corresponds to a 1.4°C decrease at 150 m, 180° (cf. Fig. 1 of Dewitte et al. 2009). In CGCMs, increased stratification may actually lead to an ENSO amplitude rise, although the thermocline flattens and thus reduces the Bjerknes feedback (Dewitte et al. 2007). Although the change in ENSO may result from a rectified effect by the change in mean state (Jin et al. 2003; Rodgers et al. 2004; Dewitte et al. 2007), it has been argued that the stability of ENSO may be altered in a warmer climate, meaning that the balance between the thermocline and zonal advective feedbacks is modified (Yeh et al. 2009; Collins et al. 2010). Before addressing the climate change problem, it seems necessary to first better understand the sensitivity of ENSO to the representation of the thermocline in a linear framework. This is the objective of this paper, which builds upon the works by Jin (1997b) and An and Jin (2001) to document the stability of ENSO in a more realistic framework. In particular, it proposes an extension of the Jin two-strip model, which takes into account the peculiarities of the equatorial Pacific thermocline—namely, its depth, thickness (e.g., sharpness), and intensity—which had not been considered explicitly in the original Jin model. The latter are introduced in the model in the form of the contribution of the first three baroclinic mode structure functions. In that sense the model can be considered as a reduced and linearized version of the model by Dewitte (2000), in the same manner that the Jin two-strip model is a reduced and linearized version of the model by Zebiak and Cane (1987). The background motivation of this study is to provide a theoretical framework within the linear approximation for the understanding of the impact of climate change on ENSO.

The paper is organized as follows: section 2 provides a description of the model. Section 3 is dedicated to a

stability analysis of the model and documents the sensitivity of the ENSO mode to several key parameters accounting for the mean state change. Section 4 is a discussion followed by concluding remarks.

2. Model description

The model used in this study is called the Thual–Dewitte (TD) model. It can be viewed as an extension of Jin's (1997b) two-strip model. It is based on similar physics, except that it has a refined representation of the mean thermocline through the consideration of several baroclinic modes (instead of one mode in the Jin model). It is thus composed of six equatorial strips extending from 125°E to 80°W for the oceanic component. Like the Jin model, only one equatorial strip is considered for the mixed layer model, and a statistical relationship is considered for the atmosphere. Also, the TD model can be considered as a reduced and linearized version of the model by Dewitte (2000), in the same manner the Jin two-strip model is a reduced and linearized version of the model by Zebiak and Cane (1987). This implies that nonlinear advection is omitted in the formulation of the model and that entrainment temperature is symmetrical and linear with respect to thermocline depth anomalies. The TD model also does not consider a seasonally varying mean state, unlike the Dewitte (2000) model. Finally, the Dewitte (2000) model considers an infinite number of meridional Rossby modes, whereas the TD model considers only the first meridional Rossby mode. All model parameters were derived from the Simple Ocean Data Assimilation (SODA) reanalysis over the period 1958–2007 (Carton and Giese 2008), and anomalies are considered with respect to the mean over this period. The following details each component of the model.

a. Ocean dynamics

We consider an ocean at rest in hydrostatic balance with a reference state that is described by the mean density ρ_0 and Brunt–Väisälä frequency N^2. The Brunt–Väisälä frequency (or mean buoyancy) is proportional to the vertical gradient of density and therefore defines various characteristics of the mean thermocline, such as its depth (being the depth where N^2 is maximal), thickness, for example, sharpness (being the vertical extension of the N^2 profile around the mean thermocline depth), and intensity (being the value of N^2 at the mean thermocline depth). Although the mean stratification in the equatorial Pacific exhibits important zonal variations, here a mean buoyancy vertical profile $N^2(z)$ typical of the central Pacific (170°–120°W) is chosen because the linear formalism cannot easily account for the zonal changes in stratification. Note that the central Pacific (170°–120°W) is the area that mostly controls ocean dynamics in our model, as the wind stress forcing is maximal in such an area. For clarity, $N^2(z)$ will be referred to as the mean stratification. From $N^2(z)$, a basis of vertical functions F_n with associated speed c_n can be derived assuming the separation into horizontal and vertical variables as follows:

$$\left(u, v, \frac{p}{\rho_0}, \frac{X_z}{\rho_0}, \frac{Y_z}{\rho_0}\right)(x,y,z,t) = \sum_{n=1}^{\infty} (u_n, v_n, p_n, X_n, Y_n)(x,y,t)F_n(z),$$

where (u, v) are the anomalies of zonal and meridionnal currents, respectively; p is the pressure; and (X_z, Y_z) are the zonal and meridionnal wind stress vertical derivatives, respectively. The ocean dynamics thus reduce to an equation of evolution for each vertical mode on the equatorial β plane as shown:

$$\begin{aligned} &\partial_t u_n - y\beta v_n = -\partial_x p_n + X_n \\ &\partial_t v_n + y\beta u_n = -\partial_y p_n + Y_n \\ &\partial_t p_n + c_n^2(\partial_x u_n + \partial_y v_n) = 0. \end{aligned} \tag{1}$$

In this paper, the focus is on the long wavelength–low-frequency equatorial waves (Kelvin and Rossby waves), which are nondispersive. The meridional momentum equation is thus approximated by the geostrophic balance, and therefore the meridional wind stress contribution is neglected. The system (1) can be projected onto the basis of the theoretical meridionnal functions associated with an infinitely unbounded ocean (Cane and Sarachik 1976), and the contribution of the baroclinic modes to zonal currents and pressure reads as follows:

$$\frac{u_n}{c_n}(x,y,t) = q_{n0}(x,t)\psi_0(y_n) + \sum_{m=1}^{\infty} q_{nm}(x,t)\left[\frac{\psi_{m+1}(y_n)}{\sqrt{m+1}} - \frac{\psi_{m-1}(y_n)}{\sqrt{m}}\right] \quad \text{and}$$

$$\frac{p_n}{c_n^2}(x,y,t) = q_{n0}(x,t)\psi_0(y_n) + \sum_{m=1}^{\infty} q_{nm}(x,t)\left[\frac{\psi_{m+1}(y_n)}{\sqrt{m+1}} + \frac{\psi_{m-1}(y_n)}{\sqrt{m}}\right],$$

with $y_n = y\sqrt{\beta/c_n}$. The q_{n0} and q_{nm} are the projection of the nth baroclinic mode on the Kelvin and mth meridional Rossby wave structures, respectively, and the ψ_m terms are the Hermite functions. A differential equation for the ocean dynamics can then be written for each baroclinic mode n:

$$(\partial_t + \varepsilon_n) q_{n0} + c_n \partial_x q_{n0} = \frac{\langle X_n, \psi_0(y_n)\rangle}{2 c_n L_n} \quad \text{and} \quad (2)$$

$$(\partial_t + \varepsilon_n) q_{nm} - \frac{c_n}{(2m+1)} \partial_x q_{nm} = \frac{m(m+1)}{2 c_n L_n (2m+1)} \left[\frac{\langle X_n, \psi_{m+1}(y_n)\rangle}{\sqrt{m+1}} - \frac{\langle X_n, \psi_{m-1}(y_n)\rangle}{\sqrt{m}} \right],$$

where we use $L_n = \sqrt{c_n/\beta}$ and $\langle X_n, \psi_m(y)\rangle = \int_{-\infty}^{\infty} X_n \psi_m dy$.

In the absence of wind forcing, the first equation ($m = 0$) accounts for the free eastward propagation of Kelvin equatorial waves with phase speed c_n, while the second equation ($m > 0$) accounts for the free westward propagation of Rossby waves with phase speed $-c_n/(2m + 1)$. Odd (even) Rossby waves have a meridional symetric (asymetric) structure. A damping is introduced as a Rayleigh-type friction with e-folding rate ε_n for each vertical mode following Dewitte (2000). Furthermore, a perfect reflection of the waves at the meridional boundaries is considered that leads to an explicit formulation of the reflection efficiencies (Boulanger and Menkes 1995). For simplicity, the reflection efficiency depends only on the horizontal modes m. We assume an infinitely extended wall in the north–south direction for the eastern boundary x_E and a no mass flow condition for the western boundary x_W. Therefore, the theorical values of reflection efficiency in the case of a Kelvin wave ($m = 0$) and the first meridional-mode Rossby wave ($m = 1$) can be derived as

$$q_{n0}(x_W, t) = 0.5 q_{n1}(x_W, t) \quad \text{and} \quad q_{n1}(x_E, t) = q_{n0}(x_E, t),$$

where we use the conditions $u = 0$ at x_E and $\int_{-\infty}^{\infty} u\, dy = 0$ at x_W.

A constant mixed layer depth of 50 m is assumed, and for each vertical mode a projection coefficient P_n is introduced. By taking H_0 the ocean bottom depth, we have

$$X_n = \frac{P_n}{\rho_0} \tau_x \quad \text{and} \quad P_n = \frac{\int_{h_{\text{mix}}}^{0} F_n\, dz}{h_{\text{mix}} \int_{H_0}^{0} F_n^2\, dz},$$

where $\sum_{n=0}^{\infty} P_n = 1/h_{\text{mix}}$, τ_x is the zonal wind stress anomalies, and h_{mix} is the mixed layer depth.

Therefore, by considering n vertical modes and m horizontal orders, the ocean dynamics can be depicted by $n \times m$ strips of variables q_{nm}. In our model, we consider the contribution of the first three vertical baroclinic modes ($n = 1, 2, 3$). These modes are the most energetic propagating modes in the equatorial Pacific that best describe the wave dynamics (Dewitte et al. 1999, 2009). As in Kang and An (1998), only the contribution of the Kelvin and first-meridional Rossby waves ($m = 0, 1$) are taken into account, considering that they explain a large amount of variance of the baroclinic modes (Dewitte et al. 1999, 2003). Therefore, the ocean dynamics is depicted by six strips of variables q_{nm}. The use of several baroclinic modes introduces slower-propagating waves and therefore lower frequencies in the model. One could alternatively increase m instead of n to introduce slower-propagating Rossby waves (at speed $-c_n/(2m + 1)$); however, it would keep the propagation speed of the Kelvin waves (at speed c_n) unchanged, and the introduced Rossby waves would be dissipated relatively quickly because of their slower phase speed (shorter wavelength). The parameters of the ocean model are summarized in Table 1. A more detailed description of the ocean dynamics formalism used in this article can be found in Clarke (2008).

TABLE 1. Ocean model parameters.

	Baroclinic mode		
	1	2	3
c_n (m s^{-1})	2.7	1.6	1.1
P_n (m m^{-1})	3.8	3.6	1.5
$d_z F_n / N^2$ (m^{-1} s^2)	16.2	42.0	77.4
ε_T (month^{-1})	1/30	1/23	1/18

b. Atmospheric component

A statistical relationship between SST anomalies along the equator T_E and τ_x between 11°S and 11°N is used to build the atmospheric model. Here SST anomalies along the equator are calculated from a meridional average between 1°S and 1°N and therefore depend only on longitude and time. The statistical relationship is derived from the singular value decomposition (SVD) (Bretherton et al. 1992) between T_E and τ_x of the SODA data during 1958–2007, which leads to the modes $e_k(x)$ and $f_k(x, y)$ associated to the time series α_k and β_k, such that

$$T_E(x,t) = \sum_k \alpha_k(t) e_k(x) \quad \text{and}$$

$$\tau_x(x,y,t) = \sum_k \beta_k(t) f_k(x,y).$$

We retain the first two SVD modes ($k = 1, 2$) that account for 66% and 15% of the covariance, respectively. The first (second) SVD mode accounts for 70% (28%) of the total variance for the SST and 31% (30%) of the wind stress. The first SVD mode captures a remote interaction between eastern positive SST anomalies and

central positive wind stress anomalies, while the second SVD mode captures a more local and delayed interaction between central positive SST anomalies and positive (negative) wind stress anomalies slightly west (east) of the SST anomalies (not shown). Therefore, in our model the atmospheric relationship reduces to

$$\tau_x(x,y,t) = \mu \sum_{k=1}^{2} C_k^{\mathrm{SVD}} \alpha_k^{\mathrm{SVD}}(t) f_k(x,y),$$

where C_k^{SVD} is a regression coefficient defined as $\langle \alpha_k \beta_k \rangle / \langle \alpha_k^2 \rangle$, where the angle brackets here denote the time average over the entire length of the used sample, 1958–2007; and α_k^{SVD} at a given time is derived by projecting SST anomalies onto the SST eigenvector e_k. The atmospheric relationship is somewhat similar to the one of An and Jin (2000), but it is based on a SVD rather than an empirical orthogonal function (EOF) decomposition. As in An and Jin (2000) and other comparable studies, a coupling coefficient (or efficiency) μ is introduced to explore the sensitivity of the coupled instabilities to the strength of the air–sea interaction; $\mu = 1$ corresponds to realistic ocean–atmosphere coupling at interannual time scale. Here, the projection of wind stress forcing patterns (f_1 and f_2) on the equatorial waves meridional profiles is only slightly dependent on the baroclinic mode order (not shown). This is consistent with the fact that the atmospheric Rossby radius is much larger than the oceanic Rossby radius L_n of the gravest baroclinic modes (assuming that the zonal wind stress anomalies along the equator can be fitted to a Gaussian profile in the meridional direction). This implies that the forcing term of the right-hand side of (2) in section 2a can be approximated by $P_n(F_K/c_n)$ and $P_n(F_R/c_n)$ for the Kelvin and first-Rossby equation, respectively, where F_K and F_R are longitudinal profiles independent of the baroclinic mode order that is considered.

c. Mixed layer model

An equatorial strip is used for the thermodynamic equation controlling the rate of SST anomaly changes. The formulation is identical to An and Jin (2001), but here the equatorial strip extends from 1°S to 1°N. The T_E anomalies, thermocline depth anomalies h_E, and zonal surface currents anomalies u_E are averaged in the equatorial strip and therefore depend only on longitude and time. For T_E, we have

$$\partial_t T_E = F^D T_E + F^T h_E + F^{\mathrm{ZA}} u_E, \qquad (3)$$

where

$$F^D = -\left(\varepsilon_T + \frac{\overline{w}}{h_{\mathrm{mix}}}\right), \quad F^T = \frac{\overline{w}}{h_{\mathrm{mix}}}\gamma(x), \quad \text{and}$$
$$F^{\mathrm{ZA}} = -\partial_x \overline{T}(x).$$

Here ε_T is a thermodynamical damping coefficient of 125 days^{-1}, $\overline{w}$ is the mean upwelling, h_{mix} is constant (=50 m), γ is an efficiency factor associated with the vertical thermal advection, and $\partial_x \overline{T}$ is the mean zonal gradient of SST along the equatorial Pacific. We derive h_E and u_E from ocean dynamics (see section 2a). Following Dewitte (2000), h_E and u_E are estimated as

$$h_E(x,t) = \sum_{n=1}^{3} \langle p_n \rangle \left(\frac{d_z F_n}{N^2}\right) \overline{h} \quad \text{and}$$
$$u_E(x,t) = \sum_{n=1}^{3} \langle u_n \rangle F_n(0)$$

with $F_n(0) = 1$. The angle brackets denote a meridional average in the equatorial strip and $\overline{h}$ is the mean depth of the equatorial thermocline. The first, second, and third terms on the right-hand side of (3) correspond to the damping feedback, thermocline feedback (FT), and zonal advective feedback (FZA), respectively, in the equatorial strip. The thermocline feedback accounts for the anomalous advection of subsurface temperature anomalies by the mean upwelling, while the zonal advective feedback represents the anomalous advection of mean SST by zonal currents. Thus, FT and FZA depend on the characteristics of the mean state of the equatorial Pacific. The values of those parameters are derived from SODA. They are plotted in Fig. 1 in a nondimensionnal form to ease the comparison with previous studies. To derive $\overline{w}$ (mean vertical velocity), the linear model of Dewitte (2000) is forced by the mean climatological wind stress from SODA with wave parameters derived from the vertical model decomposition of the mean stratification of SODA (see Table 1). From this model a mean upwelling of $\overline{w} = 0.99$ m day^{-1} is estimated by zonal averaging over the domain 140°–90°W. We use an empirical function connecting h (defined as the depth of the 20°C isotherm) and the subsurface temperature T_{SUB} (the temperature at h_{mix}) as $T_{\mathrm{SUB}} = A \tanh(Bh)$ (Zebiak and Cane 1987; Battisti and Hirst 1989), where the coefficients A and B are estimated by the least squares method from the SODA data. After the linearization of the derivative dT_{SUB}/dh, the efficiency factor for the thermocline feedback is thus $\gamma(x) = A(x)B(x)$. Such a formulation is different from An and Jin (2000), who further introduce a constant coefficient as $\gamma = AB \cosh^{-2}(Bh_0)$, where $h_0 = 70$ m. However $\gamma(x)$ is around 0.15°C m^{-1} in the eastern Pacific, which is in

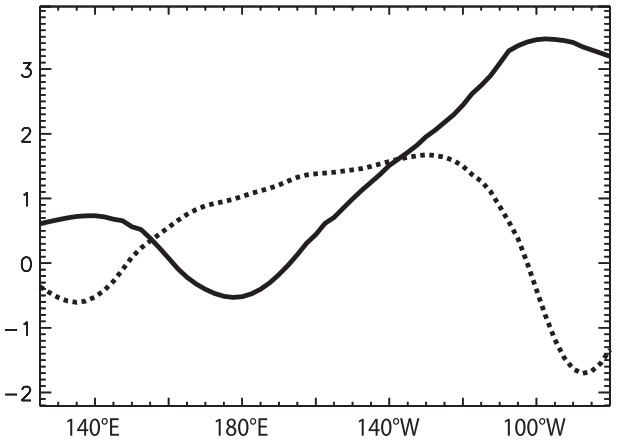

FIG. 1. Zonal profiles of FT (solid line) and FZA (dotted line). FT is adimensionalized by $HL/D_T c_1$ and FZA by L/D_T, where H = 150 m, L is the basin width (m) ranging from 125°E to 80°W, D_T = 7.5°C, and c_1 is the speed of the first baroclinic mode (m s^{-1}).

good agreement with the obtained values in An and Jin (2000). A Savitsky–Golay filter (Savitzky and Golay 1964) is used to smooth the thermocline feedback profile and to calculate the derivative $\partial_x \overline{T}$ in the zonal advective feedback term.

3. Stability analysis of the simulated ENSO

A stability analysis of the TD model is performed and the results are analyzed in this section. Because the mean stratification influences both the mean circulation and the variability, its impact on the ENSO mode cannot be inferred in a straightforward way. Here, we focus on interpretating the model's behavior in light of previous comparable theoretical studies, as well as depict the model's sensitivity to the mean stratification. First, for a fixed mean stratification, we document the dependency of the ENSO mode to the strength of the ocean–atmosphere coupling, as in previous comparable studies (sections 3a–c). Then we document the dependency of the ENSO mode to the projection of wind stress forcing on the different baroclinic modes (section 3d). Finally, we document the dependency of the ENSO mode to the relative strength of the thermodynamical feedbacks (section 3e).

a. Frequency and growth rate

The solutions of the TD model are calculated numerically. It consists of seeking the eigenvectors and eigenvalues of the Jacobian matrix built from the linear differential equations described above (see section 2), where the vector (q_{nm}, T_E) is the unknown of our system. The eigenvalues provide the growth rate and frequencies of the leading coupled modes. They are plotted in Fig. 2 for different values of μ, ranging from 0 to 1.5. Only the eigenmodes with a growth rate greater than -1.8 yr^{-1} and a frequency less than 1.5 yr^{-1} are plotted. The results indicate that the TD model is able to sustain a variety of oscillatory and stationary modes that can be stable (negative growth rate) or unstable (positive growth rate).

In the uncoupled case ($\mu = 0$), the oscillating eigenmodes consist of ocean basin modes (OBMs). In our model with no ocean–atmosphere interaction ($\mu = 0$), each baroclinic mode is independent of the others (there is no mode interference) and has associated Kelvin and Rossby-1 waves, which propagate freely at speeds c_n and $c_n/3$, respectively. Therefore, each baroclinic mode produces an ocean basin mode of its own, whose frequency is consistent with the time for a Kelvin wave and a Rossby-1 wave to reflect and travel across the basin [the frequency is $(L/c_n + 3L/c_n)^{-1}$, where L is the length of the basin]. The ocean basin mode frequency is 1.2, 0.73, and 0.5 yr^{-1} (see Table 1) for the first, second, and third baroclinic modes (M1–M3), respectively. In Fig. 2, we identify OBM1, OBM2, and OBM3 (at $\mu = 0$), which are associated with the baroclinic modes M1, M2, and M3, respectively. Two other ocean basin modes can be observed in Fig. 2 in the uncoupled case (marked by asterisks), whose frequencies (1.46 and 1 yr^{-1}) are the double of the frequency of OBM2 and OBM3 (0.73 and 0.5 yr^{-1}, respectively). These solutions are generally associated with large zonal wavenumbers, which are difficult to relate to some aspects of the observed variability in the equatorial Pacific. They also remain secondary for the stability of the system in term of growth rate.

We now focus on the system's behavior in the coupled case ($\mu > 0$). Here, the baroclinic modes are no longer independent because of ocean–atmosphere interaction, and therefore the eigenmodes take into account the contribution of every baroclinic mode. For each μ, the leading eigenmode of the system is defined as the eigenmode with maximal growth rate. With an increasing coupling coefficient, the leading eigenmode switches from a nonoscillatory damped mode ($\mu \leq 0.3$) to an oscillatory eigenmode ($0.3 \leq \mu \leq 1.3$) before breaking into two nonoscillatory unstable modes ($\mu > 1.3$, not shown). Such behavior is similar to the one observed in the Jin two-strip model (An and Jin 2001), although for a different range of μ. Our focus is on the range of values for coupling efficiency where the leading eigenmode is oscillatory ($0.3 \leq \mu \leq 1.3$), which we define as the ENSO mode of our model. In Fig. 2, the ENSO mode is approximately in the range of frequency and growth rate of 0.05 to 0.5 and -1 to 0.8 yr^{-1}, respectively. The frequency and growth rate of the ENSO mode are further

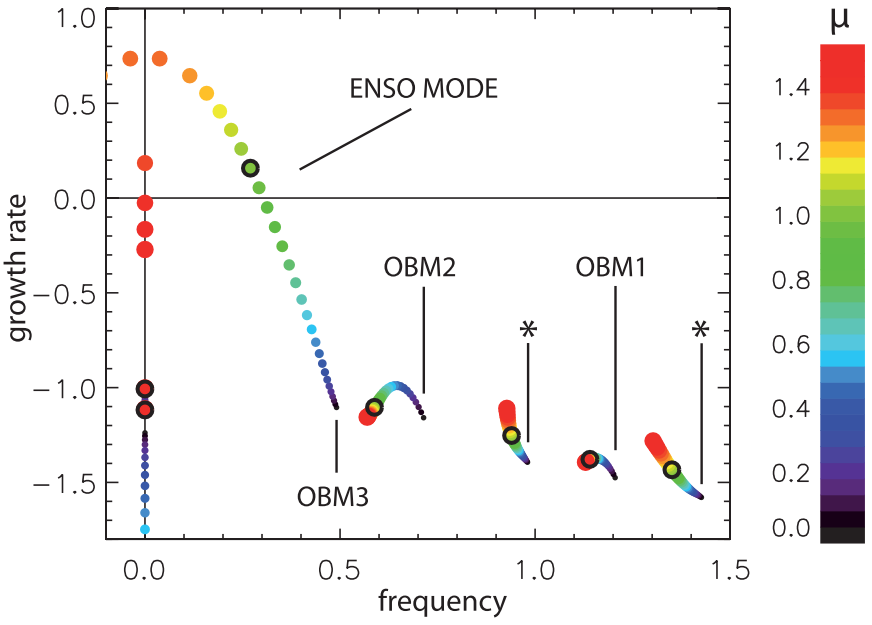

FIG. 2. Plot of eigenvalues of the TD model. Axes are frequency (yr^{-1}) and growth rate (yr^{-1}). We represent μ with increasing dot size as well as with color value (right scale), ranging from 0 to 1.5. For a coupling equal to unity, eigenvalues are overcontoured in black thick-lined open circles. Five ocean basin modes from the uncoupled case are identified (marked by OBM1, OBM2, OBM3, or an asterisk) as well as the ENSO mode in the coupled case (see text). The plot is symetric along the *y* axis, as all complex (i.e., oscillating) eigenvalues of the system come with their corresponding complex conjugate.

displayed in Fig. 3 as a function of μ ($0.3 \leq \mu \leq 1.3$). For $\mu = 1$, the ENSO mode is unstable with a period of approximately 3.7 yr, which is consistent with the contemporary ENSO characteristics (Trenberth and Stepaniak 2001) and the dominant frequency of the ENSO mode in the Dewitte's (2000) model (namely, 3.3 yr). In the following sections, we further analyze the spatial characteristics (eigenfunctions) of the ENSO mode of our model and its sensitivity to μ.

b. *Structure of the ENSO mode*

In this section, we analyze the eigenfunctions of the ENSO mode of our model. They are presented for the SST, thermocline depth *H*, and zonal current *U* anomalies of the model's equatorial strip in Fig. 4 for a value of coupling efficiency $\mu = 1$. In such representation, all eigenfunctions are sinusoidal. All fields are dominated by a standing ENSO oscillation for a period of 3.7 yr. The warm phase is associated with positive SST that departs from the central Pacific (160°W) and propagates both eastward and westward. West of 160°E, the SST is of opposite sign because of the cooling effect of the zonal advective feedback in this region (cf. Fig. 1). Along the equator, analytical Kelvin (Rossby-1) wave solutions have a contribution that is larger on *H* (*U*) (Cane and Sarachik 1976). Figure 4 indeed suggests that the transition from warm to cold phase is ensured by Rossby-1 wave reflections at the western boundary (with positive *U*) into Kelvin waves (with negative *H*),

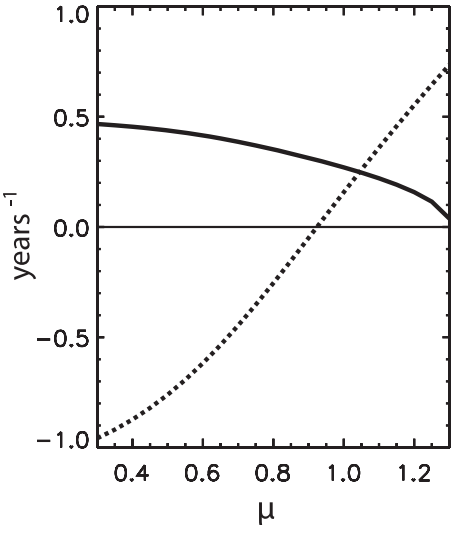

FIG. 3. Dependence of the eigenvalues of the leading eigenmode (ENSO mode) on the relative μ. Solid curve is frequency (yr^{-1}); dotted curve is growth rate (yr^{-1}). The parameters are as in Fig. 2, but μ ranges from 0.3 to 1.3.

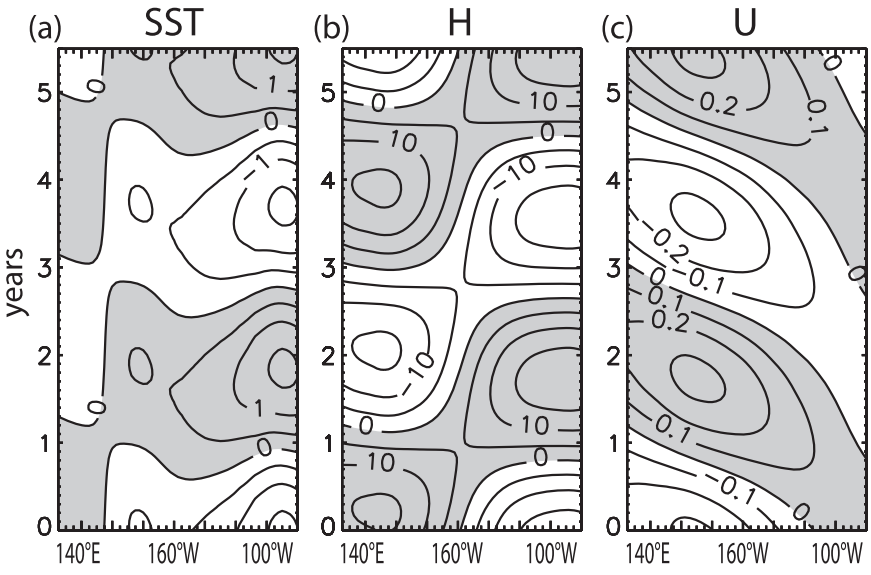

FIG. 4. Time–longitude plots of (a) SST anomalies (°C), (b) thermocline depth anomalies (m) and (c) zonal current anomalies (m s^{-1}) along the equator for the ENSO mode at $\mu = 1$ (see text). The contour interval is 0.5°C for the SST, 5 m for H, and 0.1 m s^{-1} for U. Shading is for positive values.

consistent with the delayed oscillator theory (Schopf and Suarez 1988). Features relevant to the recharge–discharge theory (Jin 1997a,b) are also observed, which result from oceanic wave adjustment in the model: the warm water volume (WWV) (or zonal average of H) is maximal at the beginning of the warm phase (when H is positive all along the equator), thus leading the El Niño signal in the east by approximately a quarter of a period.

The characteristics of the ENSO mode in the TD model can be interpreted in light of the coupled instability theory, in which the H mode (U mode) refers to the instabilities arising from a dominant thermocline feedback (zonal advective feedback) process. The H mode and the U mode impact on SST can be observed in Fig. 4, where they are responsible for the eastward SST anomaly propagation from 160° to 90°W and the westward SST anomaly propagation from 160°W to 125°E, respectively. Here, the H mode is dominant, which produces maximal SST in the eastern Pacific. The feedback mechanisms of the two instabilities (the H mode and the U mode) are different in many ways. The H mode, associated with the thermocline feedback, arises from the merging of a damped SST mode and ocean adjustment mode (An and Jin 2001). Such a mode was originally discussed as the delayed oscillator mode by Schopf and Suarez (1988). The zonal advective feedback produces the U mode by destabilizing the gravest ocean basin mode (An and Jin 2001). It is related to the SST mode introduced by Neelin et al. (1994). Jin and An (1999) further demonstrated that both instabilities are dynamically linked via the geostrophic balance between the upper-ocean zonal current and the meridional gradient of the thermocline. In our model, because the geostrophic balance is not considered explicitly, the dynamical coexistence of the two instabilities has to emerge through a different process.

Our results indicate that the TD model is able to simulate a realistic ENSO mode at $\mu = 1$ that is consistent with former theoretical studies (Jin 1997a,b; An and Jin 2001). Figure 4 can be compared to Fig. 8 of An and Jin (2001), which shows the results of the stability analysis of their model [model parameters are derived from the National Centers for Environmental Prediction (NCEP) oceanic reanalysis covering the period from January 1980 to December 1995]. Although the TD model and the Jin model are based on a different formalism for ocean dynamics, the eigenmodes characteristics are comparable. The TD model, however, produces more intense SST anomalies in the east because of a stronger thermocline feedback. The sensitivity of the TD model to μ is depicted in the next section.

c. Sensitivity to coupling coefficient

In the following, as a first step, we document the sensitivity of the dynamical adjustment of the model to μ. Figure 5 presents the eigenvectors amplitude of SST, H, and U for the ENSO mode as a function of longitude and μ ($0.3 \leq \mu \leq 1.3$). The results indicate that the TD

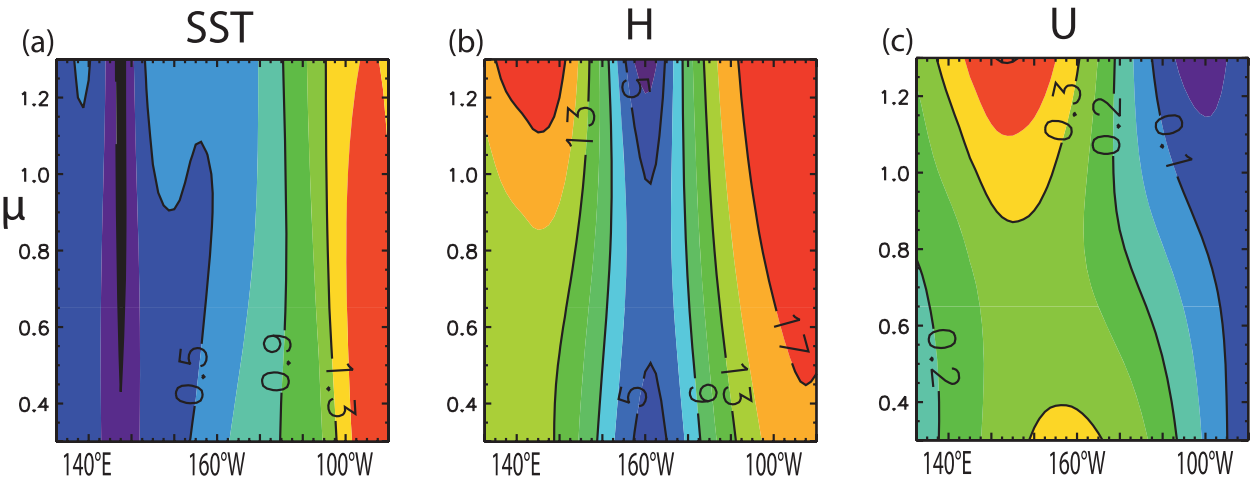

FIG. 5. Eigenvector amplitude as a function of longitude and μ for the ENSO mode. We consider the anomalies of (a) SST (°C), (b) H (m), and (c) U (m s^{-1}). The contour interval is 0.2°C for the SST, 2 m for H, and 0.05 m s^{-1} for U.

model sustains distinct regimes depending on the coupling coefficient. The amplitude of SST is maximal in the eastern Pacific and shows little sensitivity to the coupling coefficient. The amplitude of H increases with the coupling coefficient in both the eastern and western Pacific. The amplitude of U, however, shows a different sensitivity, with strong zonal currents in the central Pacific for both a small coupling coefficient ($\mu \sim 0.3$) and a strong coupling coefficient ($\mu \sim 1.3$). First, for a small coupling coefficient ($\mu \sim 0.3$), the ENSO mode is very close to OBM3 from the uncoupled case (see Fig. 2). As a result the model produces relatively strong zonal currents ($U \geq 0.3$ m s^{-1}) in the central Pacific, which is identical to the feature of an ocean basin mode (An 2005). Second, for a large coupling coefficient ($\mu \sim 1.3$), the ENSO mode has a period that is very large compared to the time delays induced by the propagation of equatorial Kelvin and Rossby-1 waves (see section 3a). Therefore, there is no apparent zonal propagation on the dynamical fields U and H (not shown). This absence of zonal propagations leads to an increase of U in the central Pacific through the contribution of Rossby-1 waves, which are locally forced by the atmosphere. This peculiar behavior of the system with a strong coupling coefficient is in contrast to the behavior of the Jin model which produces strong zonal currents only for a small coupling coefficient [see Fig. 5 of An (2005) for a comparison]. It is attributed to different ocean dynamics adjustments in the Jin model and the TD model. The Jin model assumes a geostrophic balance between the equatorial and the off-equatorial strips as well as a locally wind-driven component to derive zonal current anomalies along the equator (Jin and An 1999), whereas in the TD model zonal current anomalies are derived explicitly from the Kelvin and Rossby-1 wave contributions. Therefore, differences between the two models originate mostly from their sensitivity to μ. In particular, for a similar value of the coupling coefficient, the TD model sustains a lower-frequency ENSO mode than the Jin model, which is mainly attributable to the contribution of higher-order baroclinic modes. Details of the differences in sensitivity to μ of the TD model and the Jin model are provided in the appendix.

We now investigate the role of vertical structure variability in the model, documenting the dynamical adjustment with regard to the contribution of the baroclinic modes.

d. *Role of baroclinic modes*

Considering the importance of high-order baroclinic modes ($n = 2, 3$) in setting the sensitivity of eigenmodes to the coupling efficiency described above, in this section we detail their specific role in the transition phase between leading instabilities and in setting the characteristic time scales of variability of the ENSO mode. The eigenvectors' amplitude of H and U for M1–M3 is displayed in Fig. 6 as a function of longitude and μ ($0.3 \leq \mu \leq 1.3$). Each baroclinic mode exhibits maximum amplitude for H in the eastern and western Pacific and maximum amplitude for U in the central Pacific. Interestingly, differences arise regarding the baroclinic modes' sensitivity to coupling. For a small coupling coefficient ($0.3 \leq \mu \leq 0.8$), the amplitude of M3 (for U and H) is dominant because the ENSO mode is close to OBM3 (see Fig. 2), which has a dominant amplitude on M3 (not shown). However, for a large coupling coefficient ($0.8 \leq \mu \leq 1.3$), M2 is dominant both in terms of U and H. Interestingly, the amplitude of M1 remains

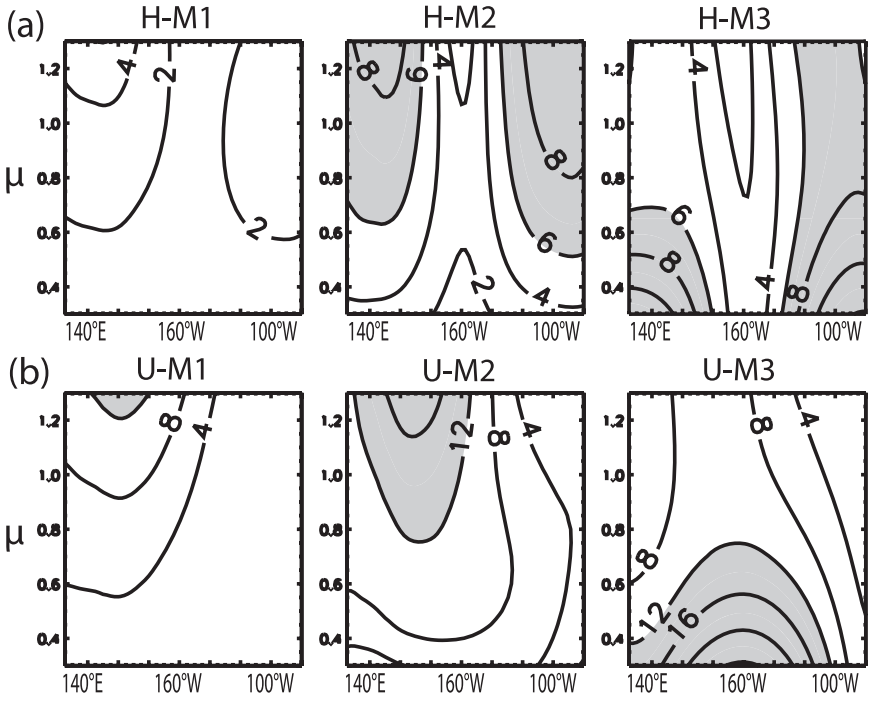

FIG. 6. (a) As in Fig. 5b, but for the contribution of the baroclinic modes to H anomalies (m). (left to right) Contribution of the first, second, and third baroclinic modes is contoured with a 2-m interval. Shading is for values greater than 6 m. (b) As in Fig. 5c, but for the contribution of the baroclinic modes to U anomalies (cm s^{-1}) contoured with a 4 cm s^{-1} interval. Shading is for values greater than 12 cm s^{-1}.

overall secondary compared to the other baroclinic modes. This illustrates the importance of higher baroclinic modes in setting the characteristics of the ENSO mode in our model. First, although wind stress forcing projects similarly onto the first two baroclinic modes ($P_1 \sim P_2$, see Table 1), M2 is overall the main contributor to the ENSO mode. Second, when varying μ, the baroclinic mode contribution is modified through change in the nature of the ENSO mode from an ocean basin mode regime to a strong coupling regime (see section 3c).

It is also worth investigating the inverse problem, which consists of determining how changes in the baroclinic mode contribution only may alter the nature of the leading eigenmode. To document such sensitivity, the solution of the TD model is sought for a wide range of values of the projection of wind stress forcing on each baroclinic mode P_n while the other parameters derived from the mean stratification remain constant. We introduce a new varying sensitivity parameter δ while μ is kept constant ($\mu = 1$). In such a test, the wind stress projection coefficients (see section 2a) vary as $P_1(1 - \delta)$, $P_2(1 + \delta/2)$, and $P_3(1 + \delta/2)$ for the baroclinic modes M1, M2, and M3, respectively. At $\delta = -2$ ($\delta = 1$), the wind stress projects solely on M1 (M2 and M3) while we roughly conserve the wind stress energy input, defined here as the sum of $P_1 + P_2 + P_3$. It is worth noting here that M1 ($n = 1$) accounts for the density difference between the upper layer and the bottom ocean, and therefore it mostly represents the mean thermocline depth, whereas higher-order baroclinic modes M2 and M3 ($n = 2, 3$) stand for the mean thermocline sharpness and intensity (Dewitte et al. 2007, 2009). Simply put, a deeper thermocline tends to increase the first baroclinic mode contribution, while a sharper and more intense thermocline leads to an increased contribution of the second and third baroclinic modes. A stability analysis is then performed for each value of δ in the range ($-1.5 \leq \delta \leq 1$), and the frequency and growth rate of the solutions are presented in Fig. 7. For an increasing parameter δ (P_2 and P_3 favored over P_1), the ENSO mode is displaced toward a more unstable and low-frequency regime. For instance, a larger δ corresponds to a sharper and shallower thermocline, which will tend to trap more wind stress forcing in the surface layers because of the finer meridional scale of variability of the high-order baroclinic modes. Note that in our model, a larger δ is roughly equivalent to a larger μ in terms of the growth rate and frequency of the simulated ENSO mode (by

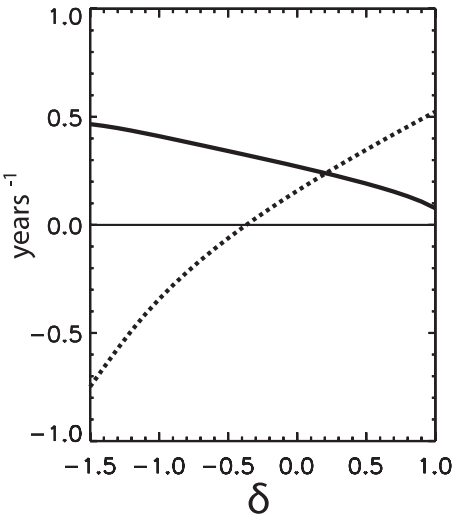

FIG. 7. Dependence of the eigenvalues of the ENSO mode on δ, where δ ranges from -1.5 to 1. The solid curve is frequency (yr^{-1}); the dotted curve is growth rate (yr^{-1}).

comparing Figs. 3 and 7). However, μ is arbitrary in our model, while δ can be related to the characteristics of the thermocline, and in that sense has a physical meaning.

This emphasizes the role of mean stratification in setting the stability characteristics of the ENSO mode.

e. Sensitivity to thermodynamical feedbacks

Changes in mean state associated with natural variability or climate change have the potential to impact the ENSO dynamics through changes in the main ENSO feedbacks (An and Jin 2001). In the TD model, the mean stratification $N^2(z)$ controls the wind stress forcing of ocean dynamics through the relative contribution of the baroclinic modes (see section 3d), but it also constrains some aspects of the mixed layer thermodynamics because it influences the strength of the thermocline feedback and the zonal advective feedback (see section 2c). For instance, mean upwelling conditions (which contribute to the thermocline feedback) depend on the characteristics of the mean thermocline. The more intense (i.e., thinner) or shallower the thermocline, the larger the $\overline{w}$ for the same input of wind stress forcing. Also, the dynamical relationship between changes in the thermocline depth and changes in the subsurface temperature at the base of the mixed layer, described by γ in the thermocline feedback (see section 2c), is sensitive to the mean stratification. A shallower thermocline leads to a stronger γ, which is observed, for example, in the eastern equatorial Pacific in comparison to the central equatorial Pacific (see Fig. 1). Furthermore, a more intense thermocline leads to a stronger γ, as subsurface temperature anomalies become more sensitive to the vertical displacements of the isopycnes. Conversely, the sensitivity of the zonal advective feedback to the mean stratification is not straightforward. However, the mean zonal gradient of SST $\partial_x \overline{T}$ (see section 2c) is related to ocean–atmosphere heat flux adjustments, which are also constrained by the mean stratification characteristics.

In this section, we introduce the new sensitivity parameter α, which controls the ratio of the FZA over the FT in the SST equation

$$\partial_t T_E = F^D T_E + (1-\alpha)F^T h_E + (1+\alpha)F^{ZA} u_E \quad \text{with} \quad -1 \le \alpha \le 1.$$

The mean stratification influences the relative strength of the zonal advective and thermocline feedbacks, thus the α parameter. However, we assume that α has a different effect on the ENSO mode than the other parameters (c_n, P_n, F_n) characterizing the mean stratification because it influences the ENSO mode through the modification of the mixed layer thermodynamics instead of the ocean dynamics. Therefore, we assume that α can be modified to explore the phase space of the ENSO mode in the model while the other parameters (c_n, P_n, F_n) remain fixed. Note also that this parameter has already been used to explore various regimes of the Jin model in previous studies (An and Jin 2000, 2001; An 2005). For $\alpha = -1$, only the thermocline feedback is at work, while for $\alpha = 1$, the rate of SST changes is mainly controlled by the zonal advective feedback. The case $\alpha = 0$ corresponds to the reference run described previously. We choose to work with the two parameters (α, μ) to explore the phase space of the ENSO mode as a function of the strength of the ENSO feedbacks. The analysis is similar to the one by An (2005) but in a multibaroclinic mode context.

The results of the stability analysis of the model in terms of growth rate and frequency are presented in Fig. 8 for different values of α and μ. High-frequency eigenmodes (>0.75 yr^{-1}) are not contoured, as they remain secondary for the stability of the system in term of growth rate. In Fig. 8 we identify two types of eigenmodes called EG2 and EG3. By definition, the eigenmodes of EG2 (EG3) depart in the uncoupled case from the OBM2 (OBM3) (see section 3a). With an increasing μ, the eigenmodes of EG3 are eventually displaced toward a low-frequency regime, while the eigenmodes of EG2 keep a somewhat similar frequency in the range of 0.55–0.73 yr^{-1}. This has implications for the stability of the ENSO mode of our model, defined here as the leading oscillating eigenmode of the system (see section 3a). For a negative α (FT favored), the ENSO mode belongs to EG3 and the stability is very similar to the previous case (Fig. 2).

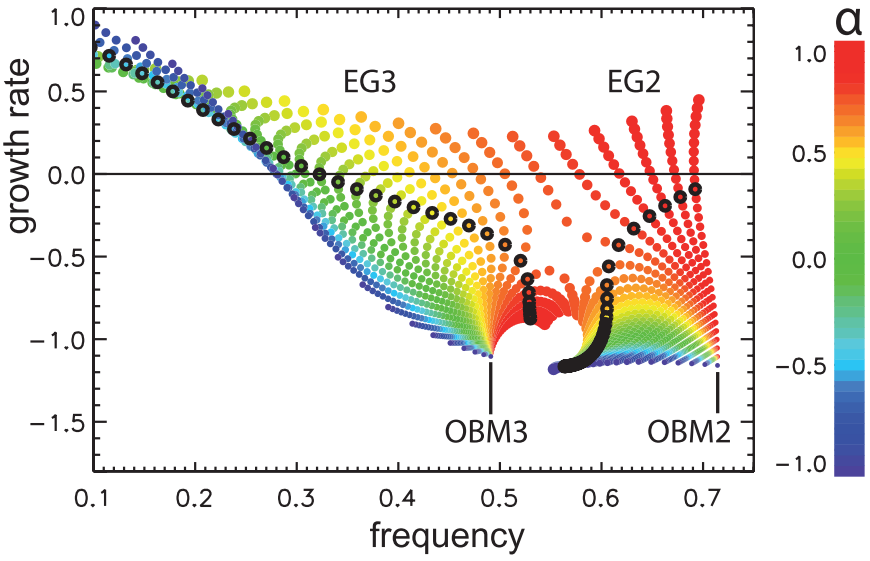

FIG. 8. Plot of eigenvalues of the TD model with sensitivity to μ and α. Axes are frequency (yr^{-1}) and growth rate (yr^{-1}). We represent μ ($0 \le \mu \le 1.5$) with increasing dot size and α value ($-1 \le \alpha \le 1$) with color (right scale). For a coupling equal to unity, eigenvalues are overcontoured by black thick-lined open circles. OBM2 and OBM3 from the uncoupled case are identified as well as EG2 and EG3 (see text). The plot is symetric along the *y* axis, as all complex (i.e., oscillating) eigenvalues of the system come with their corresponding complex conjugate.

However, for strong positive values of α ($\alpha \ge 0.7$), the ENSO mode eventually switches (bifurcates) from EG3 to EG2 with significant changes of its growth rate and frequency. To better illustrate such a feature, the frequency and growth rate of the leading eigenmode (ENSO mode) are contoured in Fig. 9 as a function of α and μ. Here, the ENSO mode is alternatively in EG3 or in EG2, or is nonoscillating (NO, not contoured). The transition between EG3 and EG2 is marked by a slight jump in frequency and a local minimum of growth rate. Near such a transition, the second leading eigenmode has a similar growth rate compared to the first one (not shown); therefore, the system has two favored frequencies (around 0.5 and 0.6 yr^{-1}). It is worth noting that the ENSO mode can even switch to EG1 for very strong (hypothetical) coupling values and $\alpha \sim 1$ (not shown). The representation in Fig. 9 gives insight into the system's sensitivity to both α and μ. When α decreases (FT favored), the leading eigenmode is displaced toward a more unstable and low-frequency regime. For α near unity (FZA favored), the system's frequency remains close to the frequency of OBM2 (0.73 yr^{-1}), independent of the value of the coupling efficiency parameter. Such a result is in agreement with An (2005), who suggests that the *H* mode (see section 3b) induced by the thermocline feedback is much more sensitive to μ than the *U* mode induced by the zonal advective feedback.

In the following, we focus on the spatial structure of the ENSO mode in the phase space (α, μ). The localization of SST anomalies depends mostly on α and very little on μ, with a favored thermocline (zonal advective) feedback producing maximal SST anomalies in the eastern (central) Pacific (not shown). Also, when α increases so does the amplitude of *H* and *U* while the thermocline pivot (defined here as the longitude of the minimum amplitude of *H* along the equator) is progressively displaced to the west, from 145°W at $\alpha = -1$ to 175°E at $\alpha = 1$ (not shown). These changes reflect changes in the WWV anomalies, which characterize the delayed response of the ocean with respect to the atmosphere in the coupled system (Meinen and McPhaden 2000). Here, the WWV anomaliess are defined as the zonal and meridional average of *H* in the equatorial strip of the model (1°N–1°S, 125°E–80°W). The amplitude of the WWV anomalies is displayed in Fig. 10a as a function of α and μ. When the ENSO mode is displaced toward a low-frequency regime (see also Fig. 9), the amplitude of the WWV anomalies decreases and the *H* anomalies reduce to a zonal seasaw mode or ''tilt'' mode, consistent with Clarke (2010). This is illustrated by the phase difference of *H* between the eastern Pacific (90°W) and the western Pacific (180°) (gray dashed lines on Fig. 10a). At low frequencies, the eastern and western Pacific are almost in phase opposition (180°), which leads to weak WWV anomalies. Also, the WWV anomalies are

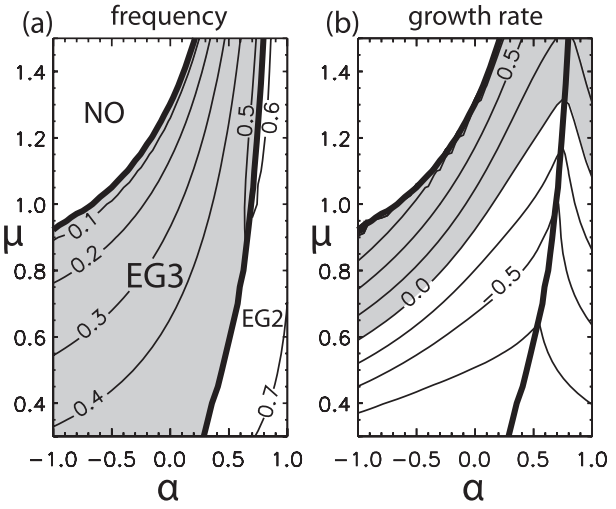

FIG. 9. (a) Frequency (yr^{-1}) of the first leading eigenmode (ENSO mode) as a function of α and μ. Contour interval is 0.1 yr^{-1}. Thick black lines separate areas NO, EG3, and EG2 (see text). NO eigenmodes are not represented. Shading is for eigenmodes in the area EG3. (b) Growth rate (yr^{-1}) of the first leading eigenmode. Contour interval is 0.25 yr^{-1}. Thick black lines separate areas NO, EG3, and EG2. Shading is for positive values.

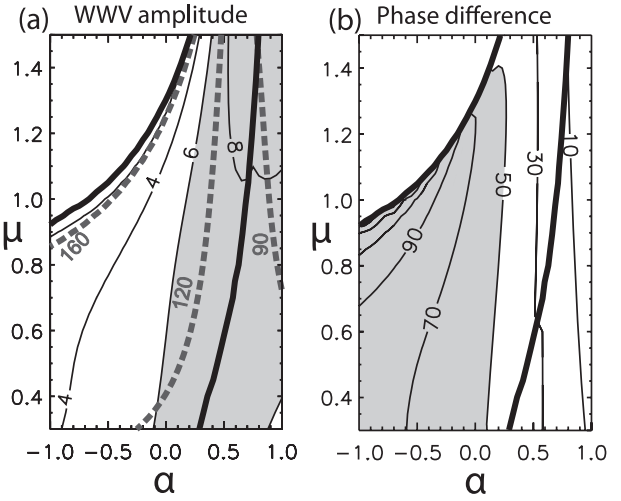

FIG. 10. (a) Amplitude of WWV anomalies (m) as a function of α and μ, defined here as the zonal average of H anomalies in the equatorial strip (1°N–1°S, 125°E–80°W). Contour interval is 2 m. Thick black lines separate areas NO, EG3, and EG2 as defined in Fig. 9. Shading is for values greater than 6 m. Phase difference of H anomalies between the eastern Pacific (90°W) and the central Pacific (180°) is overplotted in thick gray dashed lines (°). (b) Phase difference (°) between Niño-3 SST anomalies and WWV anomalies as a function of α and μ. Niño-3 SST is defined here as the average of SST anomalies in the region 1°N–1°S, 150°–90°W. A positive phase difference is for WWV anomalies leading the Niño-3 SST anomalies. Shading is for values greater than 50°.

related to the recharge–discharge mechanism proposed by Jin (1997a). Jin's (1997a) simple model for ENSO is based on two linear first-order ordinary differential equations for eastern SST and heat content (~WWV) anomalies. Therefore, in this model the WWV anomalies lead the eastern SST anomalies by a quarter of a period (90°) [see also Burgers et al. (2005) for a similar approach]. The phase difference between the eastern SST and WWV anomalies is contoured in Fig. 10b as a function of α and μ for the TD model. When the thermocline feedback is favored ($\alpha \sim -1$), the TD model reproduces the recharge–discharge mechanism of Jin (1997a) with a phase difference between SST and WWV anomalies close to 90°. However, when the zonal advective feedback is favored ($\alpha \sim 1$), the WWV and eastern SST anomalies are almost in phase, indicating that the recharge–discharge mechanism of Jin (1997a) is not at work. It is also interesting to note from Fig. 10a that when the recharge–discharge mechanism is operating in the TD model ($\alpha \sim -1$), the amplitude of the WWV anomalies is smaller than when the recharge–discharge mechanism is not operating ($\alpha \sim 1$).

Considering the sensivity of the recharge–discharge mechanism in the TD model to α, it is worth investigating how M1–M3 contribute to the WWV anomalies. For each baroclinic mode, the WWV anomalies (WWV_n for $n = 1, 2, 3$) were estimated and analyzed (not shown), where the total WWV anomalies result from $WWV = WWV_1 + WWV_2 + WWV_3$. The results indicate that first, WWV_1 leads WWV_2, consistent with the faster oceanic adjustment time scale associated with M1 compared to M2. For the same reason, WWV_2 leads WWV_3. Second, on average in the (α, μ) phase space, the second baroclinic mode mostly contributes to the total WWV anomalies (by almost 40%). As a result, the total WWV anomalies tend to be in phase with WWV_2.

4. Discussion and conclusions

In this study, we propose an extension of the Jin two-strip model (Jin 1997b; An and Jin 2001) that includes the dominant characteristics of the vertical structure variability of the ocean stratification, in order to explore the sensitivity of the ENSO mode to change in mean stratification. While conceptual ENSO models usually rely on shallow-water dynamics in a two-layer framework, here we test to what extent the characteristics of mean stratification can impact the ENSO mode considering the contribution of the first three baroclinic modes. As with Jin (1997a,b), the model solution consists of a mode that shares many characteristics with the observed ENSO in terms of frequency and stability. Both elements of the recharge–discharge theory and the delayed oscillator theory are observed in the model, which result from oceanic wave adjustment. As in An

and Jin (2001), the stability of the ENSO mode depends on μ, which controls the coupling efficiency between the ocean and the atmosphere. In the standard case ($\mu = 1$), the dominant mode is unstable and oscillates at a period of 3.7 yr, which is consistent with the contemporary ENSO characteristics (Trenberth and Stepaniak 2001). Interestingly, for a similar value of the coupling coefficient, the TD model sustains a lower-frequency ENSO mode than in the Jin model that is mainly attributable to the longer oceanic adjustment time scales associated with the contribution of the higher-order baroclinic modes ($n = 2, 3$) in the TD model.

In the model the contribution of each baroclinic mode to the thermocline depth and zonal current anomalies is sensitive to the coupling coefficient. For the intermediary range of values of the coupling coefficient, the system is dominated by the contribution of the second baroclinic mode, while the contribution of the first baroclinic mode remains secondary. As with Dewitte (2000), this stresses the role of the second baroclinic mode in setting the variability time scales and stability characteristics of the ENSO mode. At weak coupling, however, the system is dominated by the contribution of the third baroclinic mode. Also, in a hypothetical case where the projection of wind stress forcing is accounted for essentially through higher-order baroclinic modes, the ENSO mode is displaced toward a more unstable and low-frequency regime. The latter suggests that a shallower, yet more intense mean thermocline may still sustain a strong (e.g., unstable) and low-frequency ENSO mode. We further introduce the sensitivity parameter α, which controls the ratio of the thermodynamical feedbacks in our model, namely, the thermocline and zonal advective feedbacks. Depending on the value of α, the system can produce different El Niño events with either the eastern or the central SST anomalies in the case of a favored thermocline or zonal advective feedback, respectively. For a favored zonal advective feedback, the frequency exhibits little sensivity to the coupling coefficient, as mentioned in An (2005). For a favored thermocline feedback, the recharge–discharge mechanism is at work with the second baroclinic mode controlling (in terms of phase and magnitude) the WWV anomalies.

Within certain ranges of parameters in our model, the consideration of high-order vertical modes allows for the existence of several ocean basin modes, which permits the bifurcation behaviors of the solution within the interannual frequency band. Thus, several leading modes with similar growth rate but a different frequency can coexist. This is consistent with the wide spectrum of ENSO variability. It suggests that the spreading of ENSO variability in the frequency domain may be explained to some extent within the linear formalism through the consideration of the peculiarities of the ocean stratification, without invoking chaotic behavior or nonlinear processes (Timmermann et al. 2003).

We now review a few limitations of our approach. Considering the critical role of high-order baroclinic modes in setting the ENSO mode characteristics and its sensitivity to μ, one may wonder about the implication of truncating to the first three baroclinic modes. Figure 11a shows the ENSO mode as simulated by the TD model in terms of frequency and growth rate, depending on the number of baroclinic modes considered, from 1 to 5. For $n = 3$ the results are identical to Fig. 2. As more baroclinic modes are considered, more energy is added to the system; therefore, the ENSO mode is slightly displaced toward a more unstable and low-frequency regime. Interestingly, the stability is quite singular in the case of $n = 1$, in which the ENSO mode remains in a high-frequency and strongly damped regime. The latter stresses the importance of higher baroclinic modes ($n \geq 1$) for energy balance and dynamical adjustement of the tropical Pacific system (see also the appendix). However, for $n \geq 4$, the higher-order modes' contribution is essentially trapped in the upper layer and corresponds to the locally forced variability (Dewitte et al. 1999); therefore their representation may be inaccurate within the simple formalism of the TD model. Alternatively, the variability for $n \geq 4$ can be taken into account considering a simple frictional equation (Blumenthal and Cane 1989) forced by $\tau_f = (1/h_{\text{mix}} - \sum_{i=1}^{3} P_i)\tau_x$ (where P_i is the wind projection coefficient for the baroclinic mode i and h_{mix} is the mixed layer depth), which represents the part of the wind stress forcing that does not project onto the gravest baroclinic modes (here, the first three baroclinic modes). This leads to an estimation of zonal Ekman currents as shown:

$$u_{\text{ECK}} = \frac{1}{\rho_0 \, e_{\text{ECK}}} \left(\frac{1}{h_{\text{mix}}} - \sum_{n=1}^{3} P_n \right) \tau_x ,$$

where ρ_0 is the mean density, e_{ECK} is a damping rate coefficient of 1.5 days^{-1}, and τ_x is the zonal wind stress anomalies. For the sake of simplicity, Ekman currents were not considered in this study. Considering them in the model does not lead to qualitative changes of the results (not shown), which indicates that only the baroclinic modes having clear propagating characteristics ($n = 1, 2, 3$) are relevant here. Similarily, one may wonder what is the implication of truncating to the first Rossby wave ($m = 1$) in the TD model. An experiment is performed in which the contribution from the third and fifth Rossby waves ($m = 3, 5$) is added to the model, and the results are displayed in Fig. 11b. Note that the Rossby waves for $m = 2, 4$ are meridionally

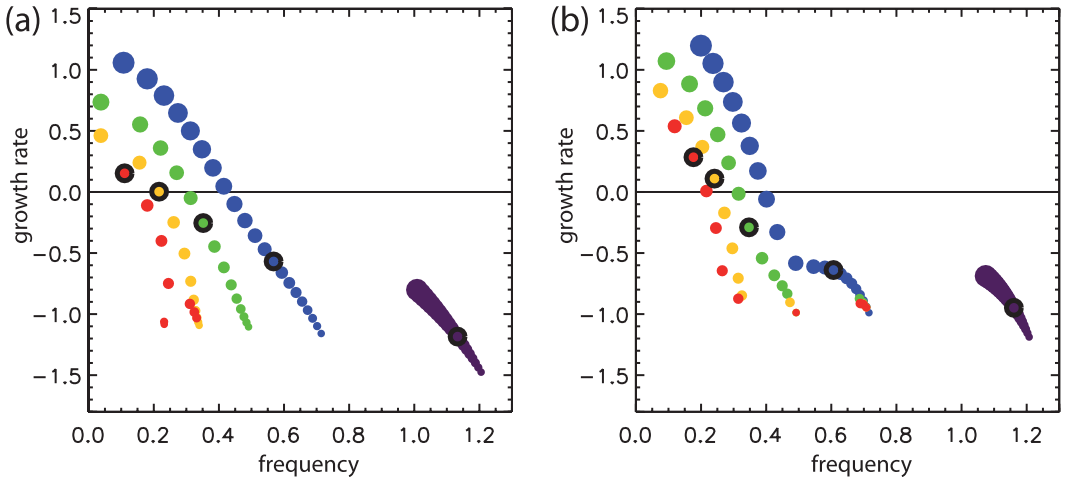

FIG. 11. (a) Plot of eigenvalues for the ENSO mode with sensitivity to n considered in the model, namely, $n = 1$ (purple), $n = 2$ (blue), $n = 3$ (green), $n = 4$ (yellow), and $n = 5$ (red). Axes are frequency (yr^{-1}) and growth rate (yr^{-1}). ENSO mode is defined as the dominant oscillating eigenmode of the system. Here μ increases from 0 to 2 with an interval of 0.1. For $\mu = 0.8$, eigenvalues are overcontoured in black thick-lined open circles. (b) As in (a), but adding the contribution of the Rossby-3 and Rossby-5 equatorial waves ($m = 3$ and $m = 5$, see text) to the model.

asymmetrical and are therefore omitted. The contribution from Rossby-3 and Rossby-5 waves increases the strength of zonal advective processes in the TD model, and as a consequence it leads to a slight increase of the frequency of the ENSO mode (see section 3e). The results, however, suggest that the contribution from higher-order Rossby waves is not critical for the stability of the TD model.

Another limitation is associated with the representation of SST in the model that omits the meridional variability scales, because, like in the Jin model, only one equatorial strip for SST is considered. Considering that the first baroclinic mode extends more meridionally than the higher-order baroclinic modes (in terms of the Kelvin wave), this may somehow lead to a greater contribution of the first baroclinic mode to SST change in the equatorial band (5°N–5°S) than considered here. The consideration of two or more strips for SST off the equator would, however, require considering the contribution of meridional advection, which may burden the formalism proposed here. Also, specific coupling between baroclinic modes and the atmospheric (SVD) modes may be at work in the real word (Yeh et al. 2001), which stresses the sensivity of ENSO to the meridional scale of variability of SST. Further study is required to document this process in a more realistic framework.

As a last limitation, it is worth mentioning the simplicity of the formalism with regard to the realism of the thermocline in terms of its east–west contrast. The thermocline slope (deep in the central Pacific and shallow in the eastern Pacific) is not accounted for in our model, which considers a zonally uniform mean stratification. Because of modal dispersion, a greater contribution of higher baroclinic modes is expected in the eastern basin (Dewitte et al. 1999). Although such an effect could be taken into account within the linear formalism used here (cf. Busalacchi and Cane 1988), it is not clear to what extent it may modify the sensitivity of the model solution to the mean stratification characteristics documented here. This would deserve further study.

Despite these limitations, the model presented here may contain the appropriate physics to document the interaction between mean state changes and ENSO variability. Fedorov and Philander (2001) already showed that the depth of the mean thermocline can modify the ENSO characteristics (growth and frequency) and that with a realistic value for the thermocline depth, the ENSO mode can be significantly modified. Here, two other ingredients that depict the thermocline structure—namely, its sharpness and intensity—are considered in a similar theoretical framework. This has implications for the study of the ENSO modulation in the contemporary climate. In particular, the vertical stratification is expected to increase during the future greenhouse warming (An et al. 2008; Yeh et al. 2009), which tends to increase the higher-order baroclinic mode contributions (Dewitte et al. 2009). To what extent change in stratification associated with global warming can impact the balance between feedback processes is an issue of debate in the community. At this stage, it is interesting to note that most Intergovernmental Panel on Climate Change (IPCC)

models exhibit a high sensitivity to global warming with drastic change in stratification (Timmerman et al. 1999; An et al. 2008; Yeh et al. 2009, 2010). The extended version of the Jin model proposed here can provide a theoretical framework for interpreting such diversity in model behavior. This is the topic of future research.

Acknowledgments. S. Thual was supported by Centre National de la Recherche Scientifique (CNRS) and Conseil Régional Midi-Pyrénées, Contract 022009. S.-I. An was supported by Grant RACS 2010-2601 from the Korea Meteorological Administration Research and Development program. The two anonymous reviewers are thanked for their constructive comments.

APPENDIX

Sensitivity to the Coupling Coefficient: Comparison with the Jin Model

In this appendix we describe the differences in sensitivity to the coupling coefficient μ of the TD model and the Jin two-strip (JN) model (Jin 1997b; An and Jin 2001). Both models use similar ocean thermodynamics and statistics for the atmosphere; although, in the TD model, the sea surface temperature and wind stress anomalies are statistically related through singular value decomposition (SVD), rather than empirical orthogonal function (EOF) formalism as in An and Jin (2000). The two models mostly differ in their ocean dynamics. The Jin model assumes a geostrophic balance between the equatorial and the off-equatorial strips to derive zonal current anomalies along the equator, whereas in the TD model zonal current anomalies are derived explicitly from the Kelvin and Rossby-1 wave contributions. Also, the JN model proposes a collective view of the equatorial Rossby waves propagating at one-quarter (instead of one-third) of the Kelvin wave speed for the first baroclinic mode, as well as a reduced domain (140°E–90°W) compared to the TD model (125°E–80°W).

To ease the comparison between the two models, we introduce a reduced version of our model that considers only the contribution of the first vertical baroclinic mode ($n = 1$). Such a reduced model (TD-M1 model) serves as a benchmark for the comparison to the Jin model, because the ''one-mode'' approximation in our model is equivalent to consider shallow-water dynamics in a two-layered ocean. The same atmospheric and mixed layer models from sections 2b and 2c are used in the JN, TD, and TD-M1 models. For clarity, it is convenient to use the same fraction of the total wind stress forcing that is projected onto the baroclinic ocean in all three models.

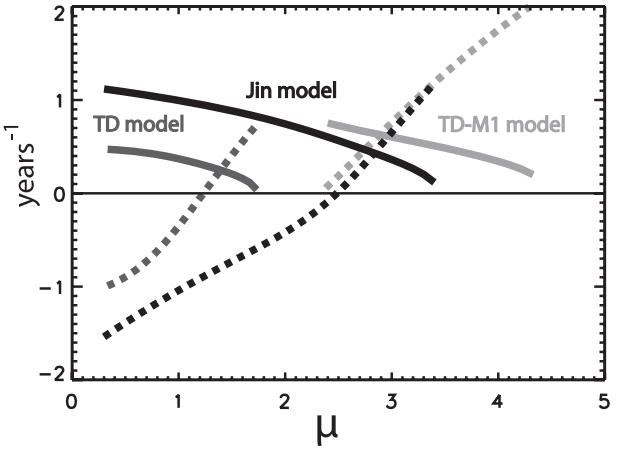

FIG. A1. Range of dependence of the eigenvalues of the ENSO mode to μ. Solid curve is frequency (yr^{-1}); dotted curve is growth rate (yr^{-1}). Results are presented for the TD model ($0.3 \leq \mu \leq 1.8$), the JN model ($0.3 \leq \mu \leq 3.5$), and the TD-M1 model ($2.3 \leq \mu \leq 4.3$). Eigenvalues are omitted for the coupling range where the ENSO mode is not oscillating. TD model and TD-M1 models are artificially modified to project the same amount of wind stress forcing on baroclinic motion as for the JN model (see text).

In the case of the TD model, the P_n coefficients give the fraction of wind stress forcing that is projected onto the corresponding vertical baroclinic modes, where the total fraction is expressed as $\sum_{n=0}^{\infty} P_n = 1/h_{\text{mix}}$. Therefore, the first, second, and third baroclinic modes project 19%, 18%, and 7%, respectively, of the total wind stress forcing and 44% in total (see Table 1). In the case of the JN model, which comprehends a single baroclinic mode and considers a mean thermocline depth at 150 m with a 50-m mixed layer depth, the momentum forcing that is projected onto the baroclinic ocean accounts for 33% of the total wind stress forcing. To compare the TD model and the TD-M1 model with the Jin model, the coupling efficiency is chosen so that wind stress forcing projecting onto the baroclinic ocean is adjusted to reach 33% of the total wind stress forcing, as in the JN model. The latter is achieved by adjusting/scaling the ocean–atmosphere coupling coefficient.

A stability analysis of the two models is performed for a set of values of μ. The eigenvalues of the ENSO mode (defined here as the dominant oscillating eigenmode of the system) are presented in Fig. A1 for the three models as a function of μ. To ease the comparison, eigenvalues are omitted for the range of values of coupling efficiency where the ENSO mode is not the leading eigenmode of the system. In all three models, the frequency (growth rate) of the ENSO mode continuously decreases (increases) with μ. Both the JN model and the TD-M1 sustain a low-frequency ENSO mode (with a frequency between 0.1 and 0.5 yr^{-1}) only when values of the

coupling efficiency are large ($2.5 \leq \mu \leq 3.5$). This suggests that the stability of the JN and TD-M1 models are somewhat similar, although the JN model also exhibits solutions at a lower value of the coupling efficiency ($\mu \leq 2.5$). For the intermediary range of value of the coupling efficiency ($\mu \sim 1$), the JN model sustains a high-frequency ENSO mode ($\sim 1\ \mathrm{yr}^{-1}$) because it has a fast oceanic adjustment time related to the phase speed of the first baroclinic mode ($c_1 = 2.7\ \mathrm{m\ s}^{-1}$). By comparison, the TD model sustains a lower-frequency ENSO mode ($\sim 0.4\ \mathrm{yr}^{-1}$) around $\mu \sim 1$ because higher baroclinic modes ($c_2 = 1.6\ \mathrm{m\ s}^{-1}$ and $c_3 = 1.1\ \mathrm{m\ s}^{-1}$) introduce longer oceanic adjustment time scales. A similar comparison is made in Dewitte (2000) but with an extended version of the Cane–Zebiak model. Nevertheless, the reason why the JN model and the Cane–Zebiak model simulate a proper time scale of ENSO is that the ENSO time scale can also be modified by the other model's parameters, such as the sensivity of entrainment temperature to the thermocline depth, for example (Dewitte and Perigaud 1996). Intermediate coupled models, such as the Cane–Zebiak model, and simple models, such as the JN model, and the TD model all relate to some point on an empirical formulation that best fits their needs to reproduce realistic ENSO characteristics. Most of the assumptions are usually made on the mixed layer thermodynamics, especially when nonlinearities are taken into account. Here, it is suggested that higher baroclinic mode contribution ($n = 2, 3$) introduces longer oceanic adjustment time scales, thus leading to larger and more realistic ENSO time scales (2–7 yr). This does not exclude the possibility to reduce the ocean dynamics to a single baroclinic mode for simplicity; however, if so, its characteristics should be representative of the whole baroclinic motion.

REFERENCES

An, S.-I., 2005: Relative roles of the equatorial upper ocean zonal current and thermocline in determining the timescale of the tropical climate system. *Theor. Appl. Climatol.,* **81,** 121–132.

——, and F.-F. Jin, 2000: An eigen analysis of the interdecadal changes in the structure and frequency of ENSO mode. *Geophys. Res. Lett.,* **27,** 2573–2576.

——, and B. Wang, 2000: Interdecadal change of the structure of the ENSO mode and its impact on the ENSO frequency. *J. Climate,* **13,** 2044–2055.

——, and F.-F. Jin, 2001: Collective role of thermocline and zonal advective feedbacks in the ENSO mode. *J. Climate,* **14,** 3421–3432.

——, J.-S. Kug, Y.-G. Ham, and I.-S. Kang, 2008: Successive modulation of ENSO to the future greenhouse warming. *J. Climate,* **21,** 3–21.

Battisti, D. S., and A. C. Hirst, 1989: Interannual variability in a tropical atmosphere–ocean model: Influence of the basic state, ocean geometry and nonlinearity. *J. Atmos. Sci.,* **46,** 1687–1712.

Belmadani, A., B. Dewitte, and S.-I. An, 2010: ENSO feedbacks and associated time scales of variability in a multimodel ensemble. *J. Climate,* **23,** 3181–3204.

Bjerknes, J., 1969: Atmospheric teleconnections from the equatorial Pacific. *Mon. Wea. Rev.,* **97,** 163–172.

Blumenthal, B., and M. A. Cane, 1989: Accounting for parameter uncertainties in model verification: An illustration with tropical sea surface temperature. *J. Phys. Oceanogr.,* **19,** 815–830.

Boulanger, J.-P., and C. Menkes, 1995: Propagation and reflection of long equatorial waves in the Pacific Ocean during the 1992–1993 El Niño. *J. Geophys. Res.,* **100** (C12), 25 041–25 059.

Bretherton, C. S., C. Smith, and M. Wallace, 1992: An intercomparison of methods for finding coupled patterns in climate data. *J. Climate,* **5,** 541–560.

Burgers, G., F.-F. Jin, and G. J. Van Oldenborgh, 2005: The simplest ENSO recharge oscillator. *Geophys. Res. Lett.,* **32,** L13706, doi:10.1029/2005GL022951.

Busalacchi, A. J., and M. A. Cane, 1988: The effect of varying stratification on low-frequency equatorial motions. *J. Phys. Oceanogr.,* **18,** 801–812.

Cane, M. A., and E. S. Sarachik, 1976: Forced baroclinic ocean motions. 1. Linear equatorial unbounded case. *J. Mar. Res.,* **34,** 629–665.

Carton, J. A., and B. S. Giese, 2008: A reanalysis of ocean climate using Simple Ocean Data Assimilation (SODA). *Mon. Wea. Rev.,* **136,** 2999–3017.

Clarke, A. J., 2008: *An Introduction to the Dynamics of El Nino & the Southern Oscillation*. Academic Press, 324 pp.

——, 2010: Analytical theory for the quasi-steady and low-frequency equatorial ocean response to wind forcing: The ''tilt'' and ''warm water volume'' modes. *J. Phys. Oceanogr.,* **40,** 121–137.

Collins, M., and Coauthors, 2010: The impact of global warming on the tropical Pacific Ocean and El Niño. *Nat. Geosci.,* **3,** 391–397.

Dewitte, B., 2000: Sensitivity of an intermediate ocean–atmosphere coupled model of the tropical Pacific to its oceanic vertical structure. *J. Climate,* **13,** 2363–2388.

——, and C. Perigaud, 1996: El Niño–La Niña events simulated with Cane and Zebiak's model and observed with satellite or in situ data. Part II: Model forced with observations. *J. Climate,* **9,** 1188–1207.

——, G. Reverdin, and C. Maes, 1999: Vertical structure of an OCGM simulation of the equatorial Pacific Ocean in 1985–94. *J. Phys. Oceanogr.,* **29,** 1542–1570.

——, S. Illig, L. Parent, Y. DuPenhoat, L. Gourdeau, and J. Verron, 2003: Tropical Pacific baroclinic mode contribution and associated long waves for the 1994–1999 period from an assimilation experiment with altimetric data. *J. Geophys. Res.,* **108,** 3121, doi:10.1029/2002JC001362.

——, S.-W. Yeh, B.-K. Moon, C. Cibot, and L. Terray, 2007: Rectification of ENSO variability in interdecadal changes in the equatorial background mean state in a CGCM simulation. *J. Climate,* **20,** 2002–2021.

——, S. Thual, S.-W. Yeh, S.-I. An, B.-K. Moon, and B. S. Giese, 2009: Low-frequency variability of temperature in the vicinity of the equatorial Pacific thermocline in SODA: Role of equatorial wave dynamics and ENSO asymmetry. *J. Climate,* **22,** 5783–5795.

Fedorov, A. V., and S. G. Philander, 2001: A stability analysis of tropical ocean–atmosphere interactions: Bridging measurements and theory for El Niño. *J. Climate,* **14,** 3086–3101.

Guilyardi, E., 2006: El Niño-mean state-seasonal cycle interactions in a multi-model ensemble. *Climate Dyn.,* **26,** 329–348.

Jin, F.-F., 1997a: An equatorial ocean recharge paradigm for ENSO. Part I: Conceptual model. *J. Atmos. Sci.,* **54,** 811–829.

——, 1997b: An equatorial ocean recharge paradigm for ENSO. Part II: A stripped-down coupled model. *J. Atmos. Sci.,* **54,** 830–847.

——, and S.-I. An, 1999: Thermocline and zonal advective feedbacks within the equatorial ocean recharge oscillator model for ENSO. *Geophys. Res. Lett.,* **26,** 2989–2992.

——, ——, A. Timmermann, and J. Zhao, 2003: Strong El Niño events and nonlinear dynamical heating. *Geophys. Res. Lett.,* **30,** 1120, doi:10.1029/2002GL016356.

Kang, I.-S., and S.-I. An, 1998: Kelvin and Rossby wave contributions to the SST oscillation of ENSO. *J. Climate,* **11,** 2461–2469.

Lee, T., and M. J. McPhaden, 2010: Increasing intensity of El Niño in the central-equatorial Pacific. *Geophys. Res. Lett.,* **37,** L14603, doi:10.1029/2010GL044007.

McPhaden, M. J., and Coauthors, 1998: The Tropical Ocean-Global Atmosphere observing system: A decade of progress. *J. Geophys. Res.,* **103,** 14 169–14 240.

Mechoso, C. R., J. D. Neelin, and J.-Y. Yu, 2003: Testing simple models of ENSO. *J. Atmos. Sci.,* **60,** 305–318.

Meehl, G. A., C. Covey, T. Delworth, M. Latif, B. McAvaney, J. F. B. Mitchell, R. J. Stouffer, and K. E. Taylor, 2007: The WCRP CMIP3 multimodel dataset: A new era in climate change research. *Bull. Amer. Meteor. Soc.,* **88,** 1383–1394.

Meinen, C. S., and M. J. McPhaden, 2000: Observations of warm water volume changes in the equatorial Pacific and their relationship to El Niño and La Niña. *J. Climate,* **13,** 3551–3559.

Moon, B.-K., S.-W. Yeh, B. Dewitte, J.-G. Jhun, I.-S. Kang, and B. P. Kirtman, 2004: Vertical structure variability in the equatorial Pacific before and after the Pacific climate shift of the 1970s. *Geophys. Res. Lett.,* **31,** L03203, doi:10.1029/2003GL018829.

Neelin, J. D., M. Latif, and F.-F. Jin, 1994: Dynamics of coupled ocean-atmosphere models: The tropical problem. *Annu. Rev. Fluid Mech.,* **26,** 617–659.

——, D. S. Battisti, A. C. Hirst, F.-F. Jin, Y. Wakata, T. Yamagata, and S. Zebiak, 1998: ENSO theory. *J. Geophys. Res.,* **103** (C7), 14 261–14 290.

Rodgers, K. B., P. Friederichs, and M. Latif, 2004: Tropical Pacific decadal variability and its relation to decadal modulations of ENSO. *J. Climate,* **17,** 3761–3774.

Savitzky, A., and M. J. E. Golay, 1964: Smoothing and differentiation of data by simplified least squares procedures. *Anal. Chem.,* **36,** 1627–1639.

Schopf, P. S., and M. J. Suarez, 1988: Vacillations in a coupled ocean–atmosphere model. *J. Atmos. Sci.,* **45,** 549–566.

Timmerman, A., J. Oberhuber, A. Bacher, M. Esch, M. Latif, and E. Roeckner, 1999: Increased El Niño frequency in a climate model forced by future greenhouse warming. *Nature,* **398,** 694–696.

——, F.-F. Jin, and J. Abshagen, 2003: A nonlinear theory for El Niño bursting. *J. Atmos. Sci.,* **60,** 152–165.

Trenberth, K. E., and D. P. Stepaniak, 2001: Indices of El Niño evolution. *J. Climate,* **14,** 1697–1701.

Van Oldenborgh, G. J., S. Y. Philip, and M. Collins, 2005: El Niño in a changing climate: A multi-model study. *Ocean Sci.,* **1,** 81–95.

Wang, B., and S.-I. An, 2001: Why the properties of El Niño changed during the late 1970s. *Geophys. Res. Lett.,* **28,** 3709–3712.

Yeh, S.-W., B. Dewitte, J.-G. Jhun, and I.-S. Kang, 2001: The characteristic oscillation induced by coupled processes between oceanic vertical modes and atmospheric modes in the tropical Pacific. *Geophys. Res. Lett.,* **28,** 2847–2850.

——, J.-S. Kug, B. Dewitte, M.-H. Kwon, B. P. Kirtman, and F.-F. Jin, 2009: El Niño in a changing climate. *Nature,* **461,** 511–514.

——, B. Dewitte, B. Young Yim, and Y. Noh, 2010: Role of the upper ocean structure in the response of ENSO-like SST variability to global warming. *Climate Dyn.,* **35,** 355–369, doi:10.1007/s00382-010-0849-4.

Zebiak, E., and M. A. Cane, 1987: A model El Niño–Southern Oscillation. *Mon. Wea. Rev.,* **115,** 2262–2278.

4.1.2. Supplementary Materials

We present supplementary material to the proposed article. A scalar version of the TD model is proposed in appendix 2. Its formulation is coarser yet more synthetic than the TD model, which permits to understand the essential recharge/discharge process that leads to an ENSO oscillation.

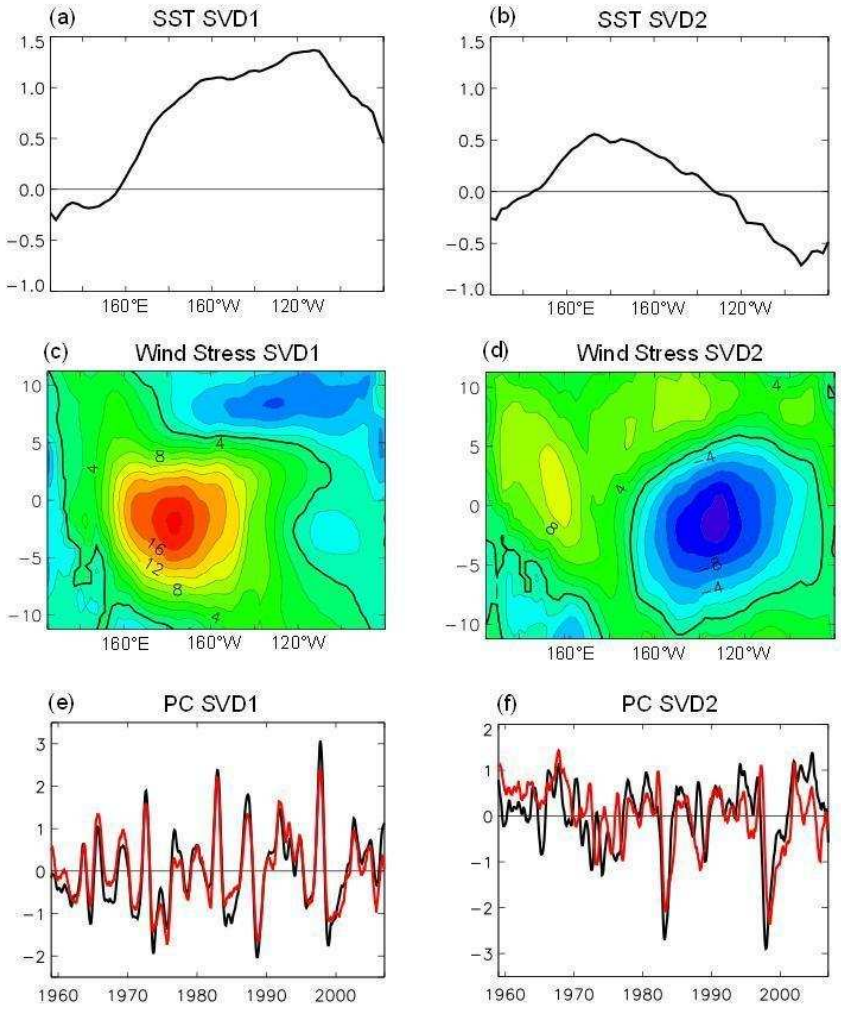

Figure 4.1: SST anomalies (°C) in the equatorial strip as a function of longitude, for (a) first (66% cov) and (b) second (14% cov) SVD mode between SST and wind stress anomalies. (c) and (d): Idem for wind stress anomalies (10^{-2}.dyn.cm^{-2}) as a function of longitude and latitude. Thick line indicates zero-contour. Fields are dimensionalised by standard deviation of associated timeseries. (e) and (f): Normalized and smoothed timeseries associated to (e) the first and (f) second SVD mode: SST (black) and wind stress anomalies (red).

Figure 4.1 shows the statistical atmosphere used in the TD model. A Singular Value Decomposition (SVD, see Bjornsson and Venegas, 1997) is computed between SST anomalies averaged in an equatorial strip 1°N-1°S and wind stress anomalies, from the SODA reanalysis (Carton and Giese, 2008). The SVD is truncated at the first two statistical modes. For the first SVD mode (66% cov), eastern SST anomalies force central zonal wind stress anomalies, which is the main feature of El Niño events. For the second SVD mode

(14% cov), central SST anomalies force both eastern and western wind stress anomalies. It is then supposed that wind stress anomalies adjust immediately to SST anomalies, which can be computed from a regression model between SVD modes. A similar approach is adopted in An and Jin (2001) and An and Jin (2000), which however consider rather EOF decompositions.

A statistical atmosphere is an interesting alternative to the Gill or Lindzen-Nigam atmosphere presented in chapter 3. It may account for additional features of atmosphere dynamics such as its non-linearities, as well as changes in atmospheric variability between the western and eastern Pacific. The statistical atmosphere is however less likely to allow for the zonal propagation of coupled instabilities (e.g. as in the AC model of chapter 3), because its response to SST anomalies remains basin-wide and is fixed spatially. An important care must also be taken when dealing with SVD (or EOF) modes of a statistical atmosphere, because they may not correspond to fully individual dynamics modes (Monahan et al., 2009). Note also that this statistical relation takes implicitly into account the direct (i.e. short timescale) feedback of the atmosphere on SST. This includes notably the heat flux feedback, accounting for a latent heat and a shortwave flux components (Lloyd et al., 2009). A slight limitation of the TD model is that those direct feedbacks, implicitely accounted for in the statistical atmosphere, are not taken into account in the mixed-layer thermodynamics controlling the evolution of SST, where only the main processes are retained.

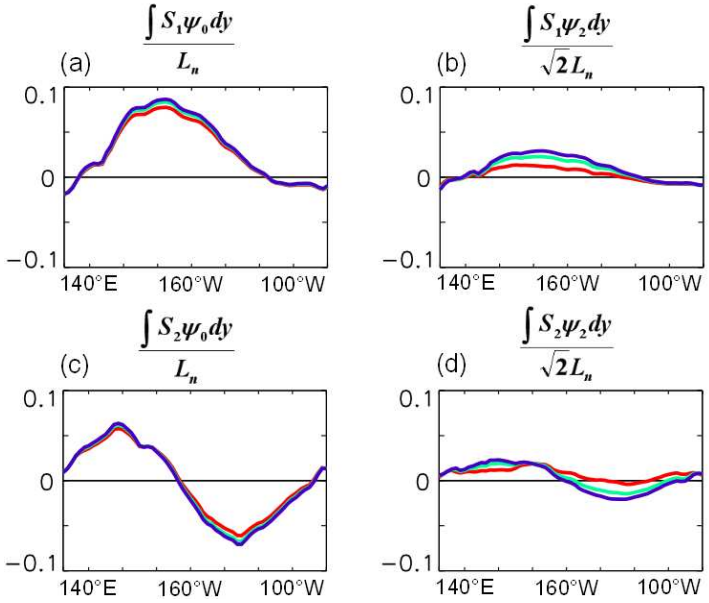

Figure 4.2**:** Meridional projection of the SVD modes from the statistical atmosphere on the zero and second order Hermite functions, as a function of longitude. (a) Projection of the first SVD mode (S_1, non-dimensional) on the zero order Hermite function ψ_0 with Rossby radius L_n from the associated baroclinic mode: n=1 (red), n=2 (green), n=3 (blue). (b) Projection of S_1 on the second order Hermite function ψ_2. (c) Projection of the second SVD mode S_2 on ψ_0. (d) Projection of S_2 on ψ_2.

Figure 4.2 shows the projection of the statistical atmosphere (first and second SVD modes) on the zero and second order Hermite functions with Rossby radius of the associated ocean baroclinic mode. The projection terms are almost independent on the baroclinic mode considered, which is consistent with the fact

that the atmospheric radius of wind stress anomalies is here much larger than the oceanic radius of each baroclinic mode (see also commentary at the end of section 2.b of the previous article).

4.2. Estimation of the thermocline feedback

In this section, we discuss some limitations related to the statistical estimation of the thermocline feedback efficiency. In the TD model, the efficiency factor γ (°C.m^{-1}) of the thermocline feedback is estimated from a regression between temperature anomalies at the base of the mixed layer (around 50m) and thermocline depth anomalies (see figure 1 of the article in this chapter). This statistical estimation can however be misleading in the central Pacific due to the dominant zonal advective feedback. Figure 4.3.a shows the correlation between temperature anomalies and thermocline depth anomalies (D_{20}), at the equator and as a function of longitude and depth. Focus is given on temperature T_{SUB} at the base of the mixed layer (around 50m). The correlation map suggests that the estimation of the efficiency factor γ from a regression is quite valid in the eastern equatorial Pacific, where the thermocline is shallow and therefore T_{SUB} and D_{20} are highly correlated. It is however more difficult to estimate γ in the central Pacific, where correlation lowers or even change sign which leads to an opposite thermocline feedback that is irrelevant. In the central Pacific, one has to disentangle the role of the zonal advective feedback that is the dominant process. Figure 4.3.b shows the correlation between temperature anomalies and anomalies of the position of the 28°C SST isotherm (X_{28}, deg lon). The 28°C isotherm is a proxy of the Warm Pool eastern edge, which separates well eastern cold waters from western warm waters (Delcroix et al., 2000). The correlation between T_{SUB} and X_{28} is positive from the central to eastern Pacific and negative in the western Pacific. This is because during El Niño events (and oppositely during La Niña events) the Warm Pool is advected eastward, which leads to a warming in the central to eastern Pacific and a cooling in the western Pacific through the zonal advective feedback.

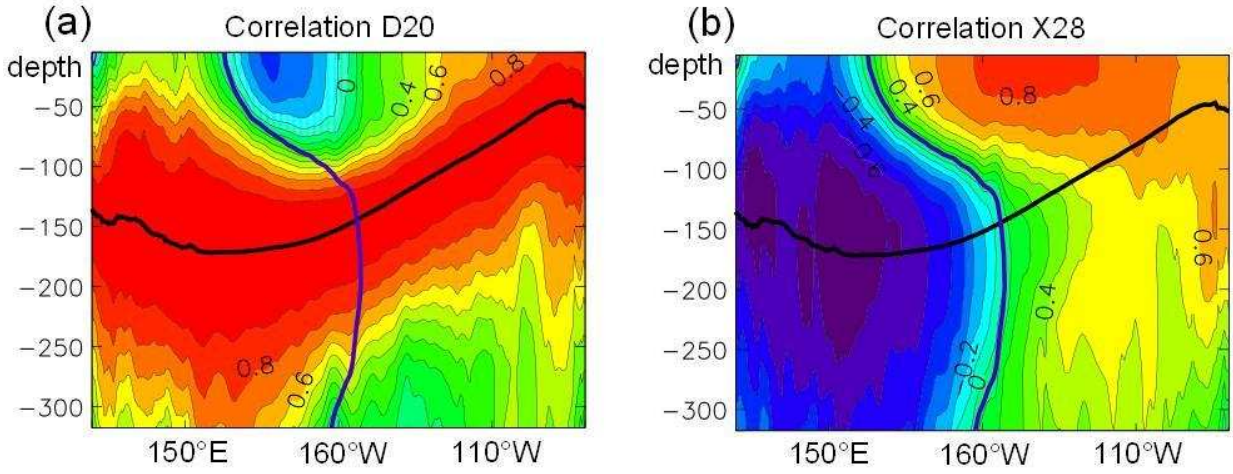

Figure 4.3: (a) Correlation of temperature anomalies at the equator (5°N-5°S) with D_{20} anomalies (20°C isotherm), as a function of longitude and depth (m). The mean thermocline is overplotted (black thick line), as well as the zero-contour of the first EOF mode of temperature anomalies (blue thick line). (b) Correlation of temperature anomalies with X_{28} anomalies (28°C SST isotherm).

To summarize, in the central Pacific region (150°E to 150°W) anomalies of temperature at the base of the mixed-layer are anticorrelated with thermocline depth anomalies, and in the meantime are correlated with anomalies of the position of the Warm Pool eastern edge. This particular feature is related to the chronology of El Niño and La Niña events. Zelle et al. (2004) already discussed such feature, but here we propose a different interpretation from the first EOF of temperature anomalies. The first EOF of temperature anomalies (hereafter EOF1, 59% cov) is shown in figure 4.4.a. Sign is inverted between surface and subsurface in the region 150°E-150°W (which leads to an anticorrelation when the field is reconstructed), and notably the zero-contour (thick blue line) matches the left edge of the area of anticorrelation from figure 4.3. EOF1 accounts for the zonal tilting of the equatorial thermocline, which results in opposite subsurface warming and cooling in the eastern and western Pacific. Figure 4.4.b shows that EOF1 also accounts for zonal currents in the central to eastern Pacific. In other words, EOF1 accounts for the simultaneous thermocline tilting and eastward displacement of the Warm Pool during El Niño events, and an opposite behaviour during La Niña events. In fact, anomalies of thermocline and zonal currents are to some extent dynamically linked through geostrophic balance near the equator (Jin and An, 1999; An and Jin, 2001). Because EOF1 accounts for 59% of total covariance, it may explain to a large extent the anticorrelation between temperature and thermocline depth anomalies observed in figure 4.3.a. In the region 150°E-150°W, the thermocline feedback from EOF1 alone should cool the surface waters, however the zonal advective feedback from EOF1 is positive and dominant therefore a warming rather occurs.

This may explain from a dynamical approach the anticorrelation between temperature anomalies at the base of the mixed layer and thermocline depth anomalies in the central Pacific. This anticorrelation can lead to a statistical estimation of the efficiency factor γ from the thermocline feedback that is misleading. Results call for a different estimation of the thermocline feedback which would have to be based on more

dynamical considerations. This may be crucial for the representation of ENSO in reduced to intermediate complexity models, because the thermocline feedback is one of the major thermodynamic processes that control characteristics of the ENSO. Those preliminary results have been reconsidered and extended in an article published recently, where it is further investigated mechanisms of changes in the thermocline feedback of the central Pacific over the recent decades (Dewitte et al., 2012).

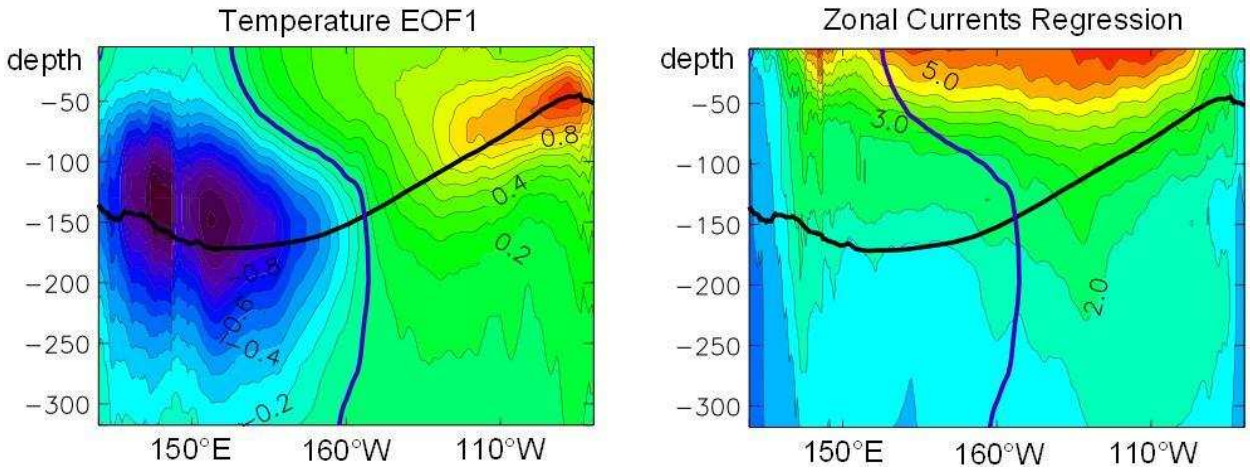

Figure 4.4: (a) First EOF (59% var) of temperature anomalies (°C) at the equator (5°N-5°S), as a function of longitude and depth (m). The mean thermocline is overplotted (black thick line), as well as the zero-contour of the first EOF mode of temperature (blue thick line). (b) Regression of Principal Components (i.e. timeserie) from the first EOF of temperature on zonal currents anomalies ($cm.s^{-1}$). Contours are dimensionalised by the timeserie standard deviation.

Chapter

5. Decadal Modulation

In this chapter, we document the relation between the decadal modulation of ENSO characteristics and the changes in the mean state of the equatorial Pacific. We use the TD model introduced in chapter 4 as a diagnostic tool. Its parameters are tuned from the SODA reanalysis, in order to compute values of the ENSO stability over the recent decades. We relate observed changes in stability to various ocean and atmosphere feedbacks during the climate shift of the 1970s. A particular focus is given on the role of ocean stratification that modifies the projection of wind stress forcing on the gravest ocean baroclinic modes. It is shown that the sensitivity of ENSO stability to this process is of an order of magnitude similar to the sensitivity to thermodynamic and atmospheric feedbacks. We extend the method to a preindustrial run from the GFDL model (300 years), which shows separable periods where changes in mean state are associated to changes in the occurrence of the type of El Niño event (either of type Eastern Pacific or Central Pacific), and which somewhat mimicks the changes in conditions after 2000. A submitted article is included that presents main results. Supplementary materials are proposed where model parameters are tuned from the GODAS reanalysis. We also discuss main limitations for the use of the TD model as a fully robust and reproductible diagnostic tool for ENSO stability.

The modelling of Central Pacific events in reduced models such as the TD model is also discussed. Noteworthy, the TD model simulates changes in stability of the mode associated to Eastern Pacific events, buth it does not simulate a dominant ENSO mode associated to Central Pacific events (this feature is also observed for background conditions from after 2000 in SODA and GODAS). This leads us to question to which extent the mechanisms of the Central Pacific El Niño may be accounted for in reduced models of this kind.

5.1. Modulation of ENSO over the Recent Decades

5.1.1. Decadal Changes in Ocean Stratification

We document how decadal changes in ocean stratification reflect on the ocean baroclinic structure. The ocean stratification (e.g. the Brunt-Väisälä frequency profile N^2) sets in particular the wind stress projection coefficients P_n of the ocean baroclinic structure (cf. chapter 2 and chapter 4). Figure 5.1 shows the regression of N^2 on wind stress projection coefficients P_n for the gravest ocean baroclinic modes (n=1, 2, 3), as a function of longitude and depth. This regression was obtained from the recently available SODA dataset that ranges from 1871 to 2008 (Giese and Ray, 2011). It illustrates the relationship between P_n and variations of ocean stratification at decadal timescale. In the central Pacific, regression is positive (negative) above (below) the mean thermocline depth. This indicates that P_n coefficients increase with a shallowing of the mean thermocline, which also corresponds to a more stratified ocean. P_n coefficients are also sensitive to the thermocline intensity and vertical extension, because they are deduced from the entire N^2 profile. In the eastern Pacific however the relation between P_1 and N^2 is inverted. This may be because the vertical scale of the first baroclinic mode is much greater than the mean thermocline depth, and therefore the first baroclinic mode is not representative of vertical motion at the mean thermocline depth. In fact, in the eastern Pacific thermocline motion is much more accounted for by the contribution from higher baroclinic modes (Dewitte, 2000).

Within the linear formalism of the TD model a single vertical profile N^2 is considered to compute P_n, which is representative of the central Pacific stratification (170°E-170°W, cf. chapter 2 and chapter 4). The evolution over the recent decades of coefficients P_n (n=1, 2, 3) from the central Pacific is shown in figure 5.2. The decadal variability is more pronounced on the higher baroclinic modes (P_2 and P_3) than on the first baroclinic mode (P_1) (Dewitte et al., 2007; 2009). The coefficients P_2 and P_3 show a strong increase after the 1970s as well as a strong decrease after 2000 (see also Lee et al. (2011) that documents the interannual variability of those parameters). From the proposed formalism of the TD model, we will investigate in the next sections how changes in ocean stratification may have influenced the observed changes in ENSO characteristics after the 1970s and after 2000.

As stressed in Thual et al. (2011), the ocean stratification may characterize both the baroclinic structure and thermodynamic feedbacks of the ocean mixed layer (e.g. thermocline and zonal advective feedbacks). In the following, we will however assume that those processes are well delineated: P_n coefficients reflect ocean stratification at large vertical scale (i.e. the entire vertical structure that includes the equatorial thermocline), while thermodynamic feedbacks may be sensitive to ocean stratification in the upper layers (i.e. below the ocean mixed-layer). We suppose that the influence of those processes on ENSO characteristics is separable. In the next sections, the ocean stratification will refer only to P_n coefficients.

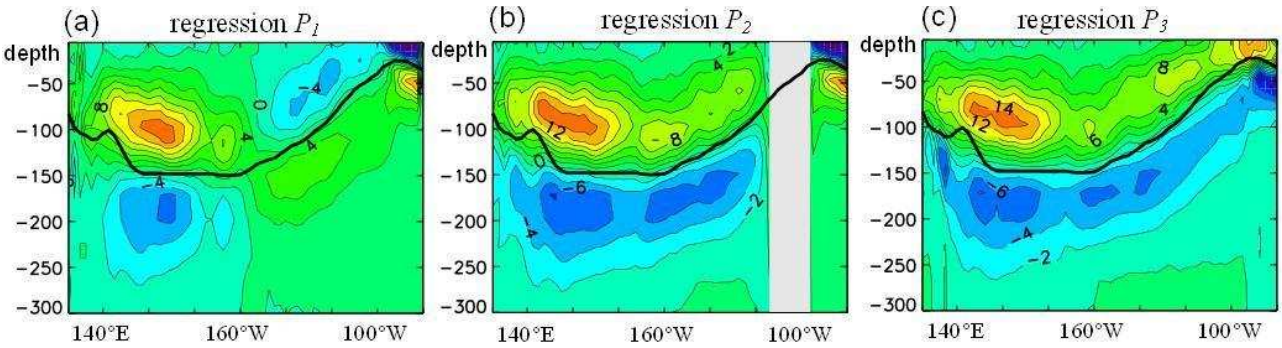

Figure 5.1**:** Regression of the Brunt-Väisälä frequency profile N^2 (10^{-2} mn^{-2}) on wind stress projection coefficients (a) P_1, (b) P_2, and (c) P_3, as a function of longitude and depth. Regressions are computed from a running mean (7-years) on SODA over 1871-2008 (Giese and Ray, 2011), where P_n depends on longitude. Regression values are multiplied by the standard deviation of P_n. Mean thermocline depth is overlaid (thick line) which is defined at maximal value of temporal average of N^2. The solver failed to compute the second baroclinic mode (P_2) within 110°W-90°W.

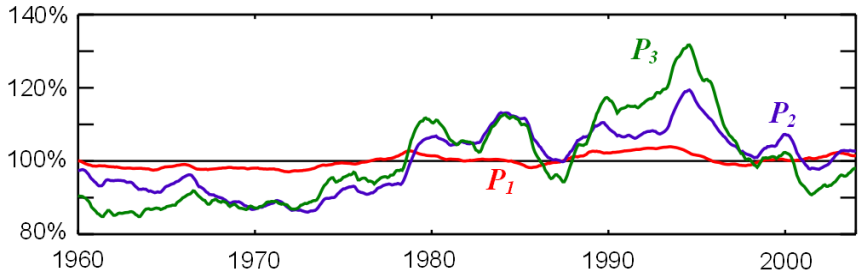

Figure 5.2**:** Running mean (7 years) of wind stress projection coefficients P_1 (red), P_2 (blue), and P_3 (green) from a density profile of the equatorial central Pacific (170°E-170°W). Values are expressed in percent of their average value over 1960-2008.

5.1.2. Article submitted to Journal of Climate

We include a submitted article that documents changes in background conditions and associated ENSO stability during the climate shift of the 1970s and after 2000. The article has been submitted to Journal of Climate (Thual et al., 2012c). It can be seen as an extension of the article presented in chapter 4. Changes in ENSO characteristics during the climate shift of the 1970s have already been documented, and it is interesting to compare results from the TD model with previous studies. Changes in ENSO characteristics after 2000 are also worth documenting, because they have been given significant focus recently (Lee and McPhaden, 2010; McPhaden, 2012) but have not been related to the background mean state from a stability approach.

Abstract: Changes in the mean circulation of the equatorial Pacific are partly related to the strong decadal modulation of the El-Niño Southern Oscillation (ENSO). This relationship is overlooked from the linear stability of a conceptual recharge/discharge model of the equatorial Pacific with parameters tuned from the observed mean state. Focus is given to change in the mean stratification of the upper-ocean that modifies the projection of wind stress forcing momentum onto the gravest ocean baroclinic modes. Whereas decadal changes in the mean thermocline depth are usually considered in conceptual ENSO models, decadal changes in mean stratification that accounts for the intensity and thickness of the mean thermocline are also shown to influence the simulated ENSO stability. Their influence on the simulated frequency and growth rate is comparable in intensity to the one of usual thermodynamic and atmospheric feedbacks, while they have here a secondary effect on the spatial structure and propagation of SST anomalies. This sensitivity is evidenced in particular for the climate shift of the 1970s in the SODA dataset, as well as in a pre-industrial simulation of the GFDL model showing stratification changes similar to the ones after 2000. Despite the limitations of the linear stability formalism, conclusions on the sensitivity to stratification may be extended to interpret the modulation and diversity of ENSO in observations and in global circulation models that have a refined representation of the oceanic vertical structure.

Influence of Recent Stratification Changes on ENSO stability in a Conceptual Model of the Equatorial Pacific

Sulian Thual (1), Boris Dewitte (1), Soon-Il An (2), Serena Illig (1) and Nadia Ayoub (1)

(1) Laboratoire d'Etude en Géophysique et Océanographie Spatiale, Toulouse, France

(2) Department of Atmospheric Sciences, Yonsei University, Seoul, South Korea

Submitted to *Journal of Climate*

21/06/2012

Revised

11/11/2012

Abstract

Changes in the mean circulation of the equatorial Pacific are partly related to the strong decadal modulation of the El-Niño Southern Oscillation (ENSO). This relationship is overlooked from the linear stability of a conceptual recharge/discharge model of the equatorial Pacific with parameters tuned from the observed mean state. Focus is given to change in the mean stratification of the upper-ocean that modifies the projection of wind stress forcing momentum onto the gravest ocean baroclinic modes. Whereas decadal changes in the mean thermocline depth are usually considered in conceptual ENSO models, decadal changes in mean stratification that accounts for the intensity and thickness of the mean thermocline are also shown to influence the simulated ENSO stability. Their influence on the simulated frequency and growth rate is comparable in intensity to the one of usual thermodynamic and atmospheric feedbacks, while they have here a secondary effect on the spatial structure and propagation of SST anomalies. This sensitivity is evidenced in particular for the climate shift of the 1970s in the SODA dataset, as well as in a pre-industrial simulation of the GFDL model showing stratification changes similar to the ones after 2000. Despite the limitations of the linear stability formalism, conclusions on the sensitivity to stratification may be extended to interpret the modulation and diversity of ENSO in observations and in global circulation models that have a refined representation of the oceanic vertical structure.

1. Introduction

The El-Niño Southern Oscillation (ENSO) is a natural mode of variability of the equatorial Pacific that experiences a strong modulation of its characteristics at decadal to inter-decadal timescales. For example, after the 1970s, ENSO characteristics were modified towards less frequent and stronger events, with additionally a tendency towards more eastward propagating SST anomalies (Wang and Wang 1996; An et al. 2006). ENSO characteristics also changed dramatically over the recent decades, with an increased occurrence of Central Pacific El Niño events characterized by maximal SST anomalies in the central Pacific, in opposition to the more described Eastern Pacific El Niño events (Ashok et al. 2007; Kug et al. 2009; Lee and McPhaden 2010). In addition, the amplitude and phase-lag of the recharge/discharge process (Jin 1997a; b) associated to the equatorial Pacific thermocline weakened after 2000, suggesting also changes in the mechanisms and predictability of ENSO (McPhaden 2012). The modulation of ENSO characteristics remains a critical issue for the scientific community, as it continuously challenges established theoretical understanding of ENSO properties as well as the reliability of forecasting systems (Kirtman and Schopf 1998; Neelin et al. 1998; McPhaden 2012).

A non-resolved issue regarding the ENSO modulation is its relation to the changes in the mean circulation of the equatorial Pacific, and in particular those associated to changes in the mean stratification. Figure 1a shows changes in mean temperatures at the equator after the climate shift of the 1970s, evidencing a shallowing of the equatorial mean thermocline as well as a vertical stratification increase, with a 0.2°C warming in surface and a 1.8°C cooling in subsurface (Moon et al. 2004; Dewitte et al. 2009). Despite the relatively short record, changes in the mean state were also observed after 2000 (figure 1b), with a strengthening of the equatorial Pacific Warm Pool associated to a slight deepening of the equatorial mean thermocline, a 0.2°C warming in surface and a 1.2°C warming in subsurface. One established understanding of the ENSO is that it is a near-neutral mode of oscillation that arises from a destabilization of the equatorial Pacific mean circulation rather than from external forcing alone (Neelin et al. 1998; Philander and Fedorov 2003). Therefore, although the ENSO modulation in observations and simulations is related to many aspects of the climatic system, such as decadal modes of variability, ENSO asymmetry, seasonal cycle interaction, or random fluctuations (Jin et al. 1994; Jin 2001; Rodgers et al. 2004; Seager et al. 2004), some of its characteristics have been clearly shown to be related to changes in the destabilized background mean state (Fedorov and Philander 2001; An and Jin 2001; Sun and Zhang 2006; Choi et al. 2011). This relation is also of particular interest in a context of global warming, for which climate projections by coupled general circulation models (hereafter CGCMs) overall agree on a modification towards a warmer mean state of the equatorial Pacific, but overall disagree on an increase or decrease of ENSO activity (Guilyardi et al. 2009). Those models indeed simulate their own mean state with a large and complex set of compensating ENSO feedbacks, among which a critical challenge is to identify which feedbacks are most influential on the simulated ENSO modulation (Collins et al. 2010; Kim and Jin 2010; Belmadani et al. 2010).

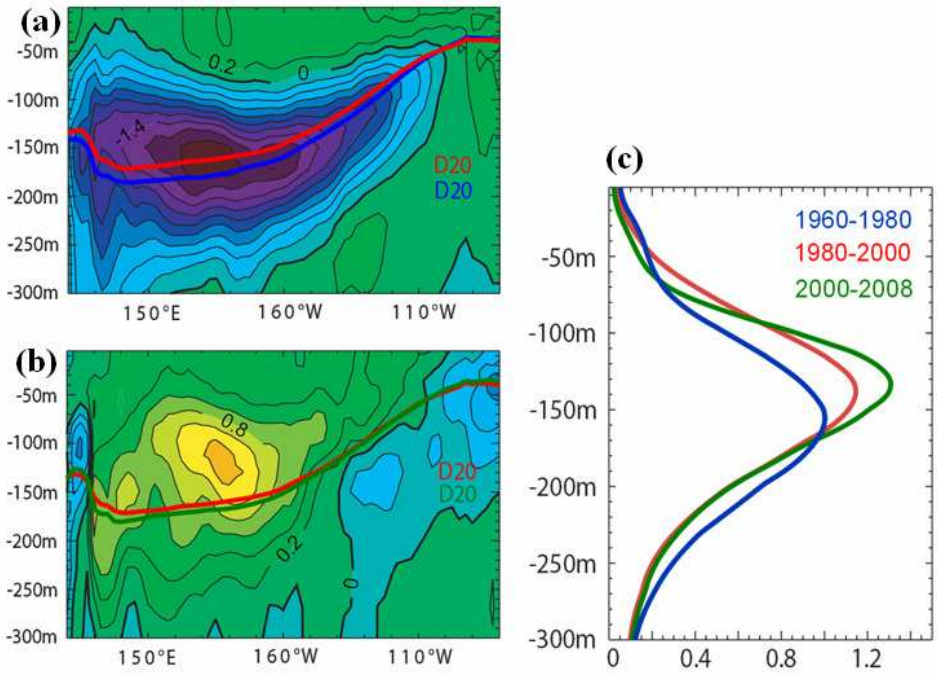

Figure 1: Mean temperature difference (a) 1980-2000 minus 1960-1980 and (b) 2000-2008 minus 1980-2000, in the SODA reanalysis, at the equator and as a function of longitude and depth. Contour interval is 0.2°C. The mean 20°C isotherm (D20) is superimposed for 1960-1980 (blue), 1980-2000 (red), and 2000-2008 (green). (c) Brunt-Väisälä frequency N^2 (min^{-2}, averaged within 170°E-170°W) as a function of depth for each period. Changes are significant at the 99% level from a Student t-test assuming unequal variance, except in the first 50 meters (at depth 110m) for the climate shift of the 1970s (the mean state change of 2000).

Among the various mean state feedbacks (i.e. parameters) that may be influential on the ENSO modulation, this article focuses in particular on the upper-ocean stratification of the equatorial Pacific. Figure 1c shows changes in the Brunt-Väisälä frequency profile N^2, which is proportional to the vertical gradient of density (i.e. buoyancy or stratification), for the climate shift of the 1970s and for the mean conditions after 2000. It evidences changes in both the thermocline depth (defined where N^2 is maximal) and "sharpness" (i.e. amplitude and vertical extension of N^2). To account for the sensitivity of ENSO to this particular parameter, a refined representation of the ocean vertical structure is necessary, which may be achieved by considering the gravest baroclinic modes of the continuously stratified ocean (Dewitte 2000; Moon et al. 2004; Dewitte et al. 2007; 2009; Thual et al. 2011). One critical aspect that will be overlooked here is how decadal changes in the thermocline shape (i.e. stratification) may modify the projection of wind stress forcing onto the gravest ocean baroclinic modes, and to which extent this may be influent on ENSO.

This sensitivity is accounted for in the recharge/discharge conceptual model from Thual et al. (2011) (hereafter TD2011). In this anomaly model the mean state is prescribed and controls the linear stability of the so-called ENSO mode, i.e. its oscillation frequency, growth rate and spatial structure. Such types of reduced to intermediate models that focus on fundamental oscillation mechanisms have been successful to interpret several aspects of ENSO modulation (An and Jin 2000; An and Wang 2000; Fedorov and Philander 2001; An and Jin 2001). They have also allowed for synthetic inter-comparison of most influential ENSO feedbacks in

observations and CGCM simulations, with for example the Bjerknes index (Jin et al. 2006; Kim and Jin 2010) that is build from the linear stability of the recharge/discharge model of Jin (1997a). In the line of those former studies, the TD model has been shown to reproduce the linear stability, driving mechanisms and main parameter sensitivity of the ENSO (TD2011). Its peculiarity is, however, its particular sensitivity to the upper-ocean stratification, which is not taken into account in former reduced models with a two-layer ocean.

This article therefore extends the study from TD2011, where here the sensitivity of the simulated ENSO stability to upper-ocean stratification is assessed for realistic cases of mean state changes such as the climate shift of the 1970s in the SODA reanalysis (Carton and Giese 2008), as well as in a pre-industrial simulation of the GFDL_CM2.1 model (Wittenberg et al. 2006) showing stratification changes similar to the ones after 2000. The article is organized as follows: Section 2 recalls the main characteristics of the TD model. Section 3 documents mean state and stability changes during the climate shift of the 1970s. Section 4 documents the mean state and stability changes in the GFDL model, with considerations also extended to a panel of other pre-industrial CGCM simulations. Section 5 is a discussion followed by concluding remarks.

2. Method

In this section, we briefly recall the main characteristics and formalism of the TD model, which is used for linear stability analysis through tuning of its parameters from the observed mean state. The reader is also invited to refer to TD2011 for more details. We also describe briefly the pre-industrial datasets that will be used in section 3 and 4.

2.1 The TD model

The TD model is a linear model of the equatorial Pacific that considers the evolution of anomalies with respect to a prescribed mean state. It solves the first equatorial waves for the three gravest baroclinic modes of a continuously stratified ocean (derived from the Boussinesq approximation). This reads, for each baroclinic mode n (n=1,2,3):

$$(\partial_t + \varepsilon_n) K_n + c_n \partial_x K_n = \frac{P_n \int_{-\infty}^{+\infty} \tau_x \psi_0 dy}{2 \rho_o L_n c_n} , \qquad (1)$$

$$(\partial_t + \varepsilon_n) R_n - (c_n / 3) \partial_x R_n = \frac{P_n \int_{-\infty}^{+\infty} \left(\tau_x \psi_2 / \sqrt{2} - \tau_x \psi_0 \right) dy}{3 \rho_o L_n c_n} , \qquad (2)$$

with also conditions of reflection at the eastern and western boundaries (not shown). τ_x is zonal wind stress forcing anomalies and ρ_0 is ocean mean density. For each baroclinic mode n, K_n and R_n are respectively the amplitude of the Kelvin and first Rossby wave, c_n is the phase speed of Kelvin waves. $\psi_0=\phi_0(y/L_n)$ and

$\psi_2=\phi_2(y/L_n)$ where ϕ_0 and ϕ_2 are the zero and second order Hermite functions respectively, $L_n=\sqrt{c_n/\beta}$ is the ocean Rossby radius and β is the beta-plane parameter. The contributions from all equatorial waves and baroclinic modes are solved and then summed-up to reconstruct both thermocline and zonal current anomalies (see TD2011).

The efficiency of transfer of mechanical work from wind stress forcing to ocean motion is set by projection coefficients P_n, which are computed for the three gravest ocean baroclinic modes (n=1,2,3) as

$$P_n = \frac{1}{\int_H^0 {F_n}^2 dz} \qquad (3)$$

where H is the ocean bottom depth, and F_n is the vertical function associated to the baroclinic mode n. The vertical functions F_n (and therefore the P_n coefficients) are computed from the Brunt-Väisälä frequency N^2 of the ocean, i.e. the buoyancy or stratification profile. N^2 is averaged in the central Pacific (170°E-170°W), where decadal variability is most marked (Dewitte 2000, see also figure 1). Figure 2 shows variations in the P_n coefficients estimated from the SODA reanalysis, with marked decadal variations over the recent decades that reach up to 20% of their nominal values and that are anti-correlated with variations in the central Pacific mean thermocline depth. Noteworthy changes in P_1 are weak while P_2 and P_3 capture the essential stratification variability at decadal timescales (Dewitte et al. 2007).

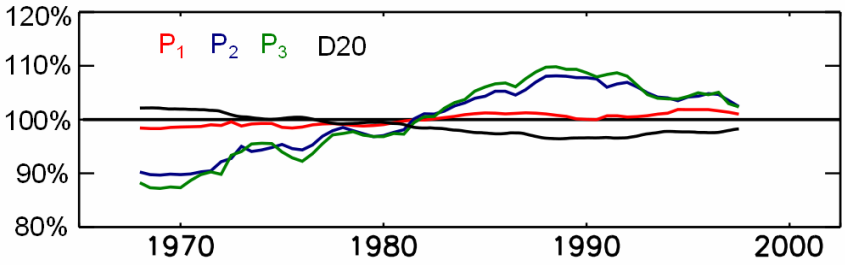

Figure 2: Running mean (20 years) of projection coefficients P_1 (red), P_2 (blue) and P_3 (green), and mean thermocline depth D20 (black, averaged in area Niño4), in percent of their mean value over 1958-2008 in the SODA reanalysis.

In addition, the TD model considers dominant processes of oceanic mixed-layer thermodynamics that control the evolution of sea surface temperature anomalies in an equatorial strip, consisting in a zonal advective feedback F_U, thermocline feedback F_H and damping feedback F_W. It further considers coupling to a statistical atmosphere that relates zonal wind stress anomalies to SST anomalies, with two responses μ_1 and μ_2 build from the two first modes of a Singular Value Decomposition (66 and 15% of covariance respectively). This reads

$$\partial_t T = F_W T + F_H h + F_U u \qquad (4)$$

$$\tau_x = \mu_1(T) + \mu_2(T) \qquad (5)$$

where T, h, u, and τ_x are respectively anomalies of SST, thermocline depth, zonal currents, and zonal wind stress forcing.

2.2 SODA and CGCMs

In this article, the TD model parameters are tuned from the Simple Ocean Data Assimilation (SODA) reanalysis version 1.2.6 (Carton and Giese 2008) and from various CGCM simulations derived from the CMIP3 (Coupled Model Intercomparison Phase 3) archive. For the CGCMs, the pre-industrial simulations are used, namely for which the concentration of greenhouse gases is fixed to estimates from 1850, which makes it appropriate for studying the physical mechanisms of natural climate variability. The simulations are listed in table 1. They correspond to the models selected in Belmadani et al. (2010), except for the BCCR-BCM2.0 model. They span around 150 years except for the GFDL_CM2.1 model for which we consider a longer pre-industrial simulation of 300 years (Wittenberg et al. 2006). This later simulation has been extensively analysed in recent studies (Kug et al. 2010; Choi et al. 2011; Dewitte et al. 2012a) due to the ability of the GFDL model to simulate an alternation of periods with increased occurrence of Central Pacific or Eastern Pacific El Niño events.

3. Climate shift of the 1970s

In this section, we compute the stability of the TD model which parameters are tuned from the varying mean state of the SODA reanalysis spanning 1958-2008 (Carton and Giese 2008). Only a reduced set of the TD model parameters are tuned from this varying mean state, while remaining parameters are estimated over the entire SODA record as in TD2011. For the ocean, only the P_n coefficients are tuned, because they show the most marked decadal variations among parameters from equations (1-2) (Dewitte et al. 2007). For mixed-layer thermodynamics (equation 4), the zonal advective feedback F_U is scaled by mean SST difference between 150°W-90°W and 120°E-180°E (An and Jin 2000). The thermocline feedback F_H is scaled by mean difference between SST and subsurface temperature (0 to 100m) over 150°W-90°W (An et al. 2008). The damping feedback F_W is scaled by the intensity of mean zonal wind stress over 150°W-90°W (which controls the mean upwelling intensity). Finally, the statistical atmosphere responses μ_1 and μ_2 (equation 5) are scaled by the correlation of timeseries from their respective SVD modes, whereas those SVD modes are computed over the entire SODA record.

The TD model is linear with respect to initial conditions, and, for a given set of model parameters, its eigenmodes (eigenvectors and eigenvalues) are computed from a linear stability analysis (see for example TD2011, its figure 2). As in TD2011, the so-called ENSO mode is defined as the eigenmode with maximum growth rate. The model also exhibits various secondary eigenmodes, but they remain here significantly more damped (with growth rate around -1.5 yr^{-1}) and are therefore not considered.

Figure 3 shows the linear stability of the simulated ENSO mode, namely its period and growth rate, as a function of the position and length of the window interval used to tune model parameters (P_n, F_U, F_H, F_W, μ_1, μ_2) from the varying mean state of the SODA reanalysis. This tests the significance of mean state and stability changes with respect to shorter-term climatic fluctuations. Specific events of the interannual variability (e.g. El

Niño 1983, 1992, 1998) may result in spurious stability shifts for short window intervals, as seen on associated diagonal rays (see for example the white dashed lines for the effect of the 1983 El Niño). Stability changes for window intervals shorter than 10 years are obviously spurious (cf red horizontal line), and are shown here only for illustration purpose, while stability changes become more clearly separable from interannual variability for longer window intervals (~20 years). This notably reveals the difficulty, due to the short record, to evidence changes in stability after 2000, despite the observations that some ENSO properties have been changing with notably an increased occurrence of Central Pacific El Niño events (Lee and McPhaden 2010; McPhaden 2012). The relation between the mean circulation and the occurrence of the Central Pacific El Niño will be considered in a following section based on the analysis of a pre-industrial CGCM simulation than spans a sufficient period to reach statistical confidence. Here the main feature of the SODA record is rather the climate shift of the 1970s, which consists in an increase in period and growth rate after 1980 and that is separable from interannual fluctuations for a window interval around 20 years.

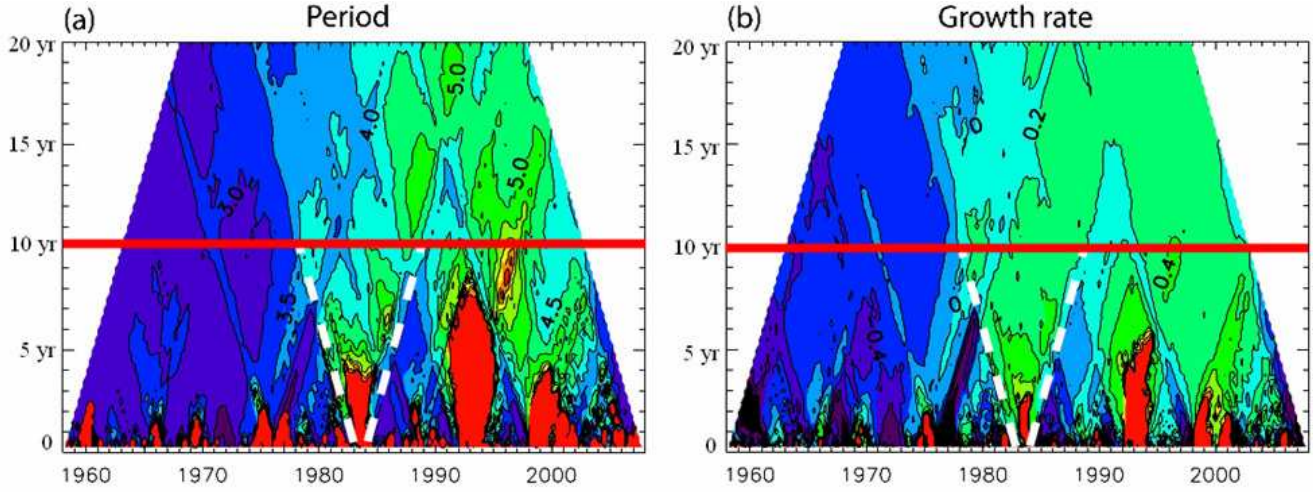

Figure 3: (a) Period (yr) and (b) Growth rate (yr^{-1}) of the simulated ENSO mode, as a function of the window center (X-axis, years) and window length (Y-axis, years) used for the tuning of the TD model parameters from the SODA reanalysis. For the period (growth rate), contour increases from blue to red with a step of 0.5 years (0.2 yr^{-1}) and values superior to 7 years (1.2 yr^{-1}) are not contoured. Stability changes for short window intervals (<10 years, cf. red horizontal line) are spurious, and may result from specific El Niño events (e.g. white dashed lines for El Niño 1983).

Changes in stability for the climate shift of the 1970s are further shown in figure 4. Here the TD model parameters are tuned from either the window interval 1960-1980 (blue) or 1980-2000 (red). Despite the TD model simplicity, the simulated increase in frequency and growth rate after 1980 is qualitatively consistent with the decrease (increase) in ENSO occurrence (amplitude) from the observed record (Wang and Wang 1996; An and Jin 2000). This corresponds to modified scaling of model parameters after 1980, on P_1 (+3%), P_2 (+25%), P_3 (+18%) for the upper-ocean stratification, F_U (-5%), F_H (+18%) and F_W (-11%) for mixed-layer thermodynamics, μ_1 (+1%) and μ_2 (+66%) for the statistical atmosphere. Noteworthy changes are weak for P_1 but marked for P_2 and P_3 (see also figure 2). Changes in parameters of mixed-layer thermodynamics are in qualitative agreement with An and Jin (2000), while the increase in atmospheric response μ_2 somewhat reflects the eastward shift of the zonal wind stress with respect to the SST anomalies after 1980 (An and Wang 2000).

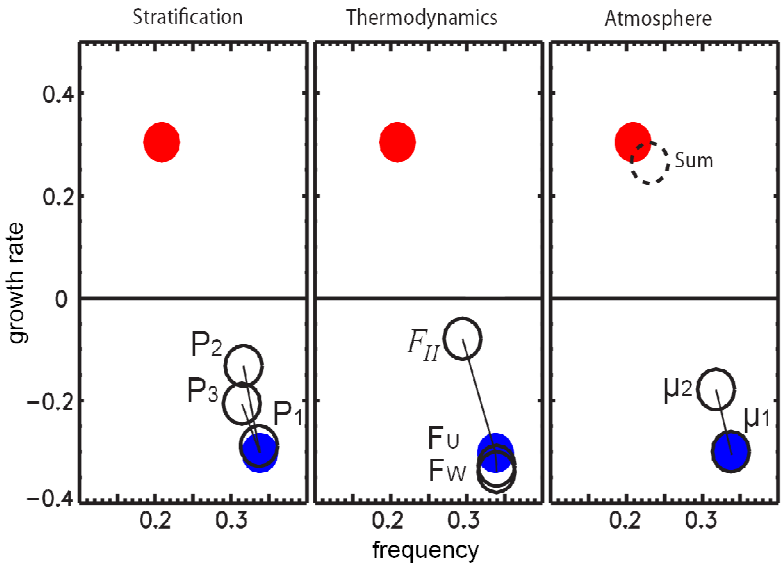

Figure 4: Frequency (yr^{-1}) and growth rate (yr^{-1}) of the ENSO mode simulated by the TD model, for the climate shift of the 1970s. Stability values are shown for tuning from the SODA record from either the window interval 1960-1980 (blue) or 1980-2000 (red). The open black circles are obtained by tuning individually each parameter from 1980-2000 with other parameters tuned from 1960-1980. The "sum point" (black open dashed circle) sums all stability changes from individual parameter changes.

As an attempt to quantify the sensitivity to each model parameter, the model stability is recomputed with tuning from 1960-1980 except for a single parameter tuned from 1980-2000 (black open circles in figure 4). This reveals the contribution of each parameter to the total change in stability, and as so its relative influence on the ENSO stability. The influence of P_1 for example is much weaker than the one of P_2 and P_3. The influence of mixed-layer thermodynamic processes has already been depicted in An and Jin (2000), though the latter study did not disentangle the relative influence of the thermocline and zonal advective feedbacks. Here it appears that the thermocline feedback F_H is most influential, at least in our model. In addition, the atmospheric response μ_2 leads to moderate changes in stability. As a consistency check, we also compute the sum of each stability changes from single parameter changes (black open dashed circle). It approximately matches the stability from 1980-2000 (red), which validates our hypothesis of stability changes depending linearly on parameter changes. In conclusion, a main result from figure 4 is that the influence of stratification parameters (P_2 and P_3) onto the ENSO stability is comparable in magnitude to the one of mixed-layer thermodynamics and atmosphere parameters. This indicates that sensitivity to stratification parameters P_n also needs to be taken into account.

Figure 5 shows the spatial structure of SST and thermocline depth anomalies reconstructed from the eigenvectors of the ENSO modes of figure 4 (where the tuning of the TD model is either from 1960-1980 or 1980-2000 periods). They remain similar after 1980 except for the increased period of oscillation, and there is in particular no significant changes in SST propagation like in the observed record (An et al. 2006). This limitation may arise from the model statistical atmosphere (build from two SVD modes) that may constrain too much the location of the center of action of wind stress anomalies, and therefore limit the zonal propagation of

coupled instabilities. Such limitation could be overcome by further considering higher SVD modes, or alternatively a dynamical atmosphere (Neelin et al. 1998; Fedorov and Philander 2001), but is out of the scope of this article. The TD model however simulates a spatially fixed recharge/discharge process (Jin 1997a; b) that is qualitatively representative of ENSO. This is seen from maximal SST anomalies in the eastern Pacific in phase with a sea-saw pattern of thermocline depth anomalies and out of phase with the equatorial heat content as seen from the thermocline depth anomalies having the same sign all along the equator. We also note from the zero-contours (dashed lines) that the contribution of each baroclinic mode to thermocline depth anomalies follows a similar recharge/discharge process, though with a slight delay on higher baroclinic modes.

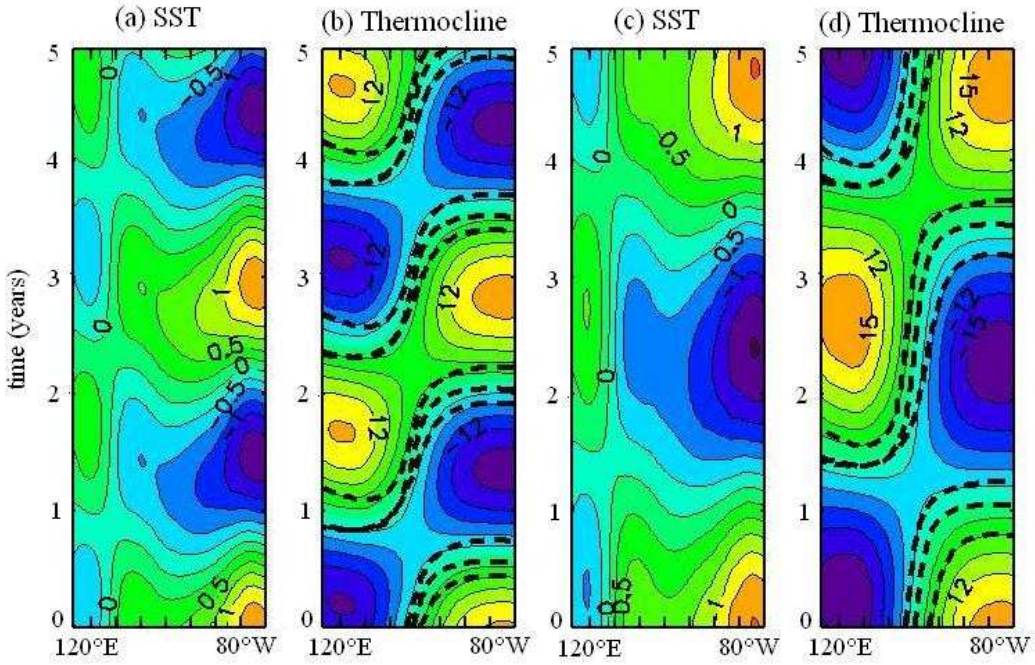

Figure 5: (a) Temperature and (b) thermocline depth anomalies, as a function of longitude and time, reconstructed from the ENSO mode eigenvector of 1960-1980 with growth rate omitted. (c) Temperature and (d) thermocline depth anomalies from the ENSO mode eigenvector of 1980-2000. Contouring step is 0.25°C (3m) for temperature (thermocline depth) anomalies. Black dashed lines in (b) and (d) are the zero-contours for the contribution of the three gravest baroclinic modes (n=1,2,3) to thermocline depth anomalies.

The increased stratification after 1980 modifies the frequency and growth rate of the simulated ENSO mode (cf. figure 4), but has little impact on its spatial structure (cf. figure 5). From equations (1-2), it appears that the increased stratification (P_n coefficients) enhances the intensity of the thermocline response, because for a same atmospheric forcing the ocean baroclinic modes trap more momentum (Dewitte 2000). This somewhat increases the intensity of ocean/atmosphere coupling and as so modifies the simulated growth rate and frequency (Jin 1997a; An and Jin 2001). There is also a slight decrease in the simulated amplitude of heat content (Warm Water Volume) anomalies after 1980, which is due to a slight increase in the phase between heat content and SST anomalies (not shown). A similar result was found in TD2011 (its figure 10) when increasing directly the intensity of ocean/atmosphere coupling, which has been interpreted in terms of change in the regime of oscillation rather than only in the direct thermocline response to wind stress forcing.

4. Decadal changes in stratification and ENSO stability

Because the SODA reanalysis only allows to address sensitivity to stratification during the climate shift of the 1970s, in the section we also analyse various CGCM simulations that grasp some aspects of the ENSO modulation (Lin 2007). As a first step, we perform a stability analysis similar to the one of the previous section with the TD model tuned from the mean state outputs of a pre-industrial simulation of the GFDL_CM2.1 model (Wittenberg et al. 2006). While the SODA record is too short after 2000 such that changes in stability may be disentangled from interannual fluctuations (cf. figure 3), the GFDL simulation offers the opportunity to study qualitatively similar changes over a longer time record, at least with respect to the ENSO modulation and mean stratification (Kug et al. 2010; Choi et al. 2011; Dewitte et al. 2012a).

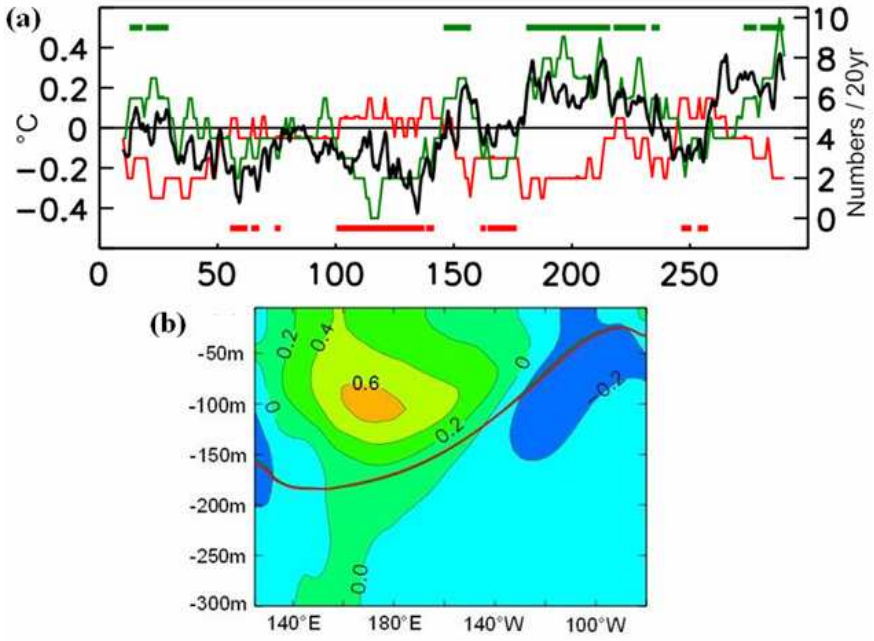

Figure 6: (a) Decadal variability and decadal modulation of ENSO in the GFDL_CM2.1 simulation, as a function of time (X-axis, yr). Green (red) thin line indicates twenty-year frequency of CP (EP) events, in numbers by 20 years (right Y-axis). Black line indicates twenty-year running mean of SST averaged within Niño4m region, in °C (left X-axis). Green (red) horizontal thick lines in the top (bottom) indicate period intervals used to compute the warm (cold) mean state. Adapted from Kug et al. (2010) and Choi et al. (2011)). (b) Temperature differences at the equator between the warm and cold mean state, as a function of longitude and depth. Contour interval is 0.2°C. The 20°C isotherm depth is drawn for the warm (green) and cold (red) mean state.

Figure 6a shows the decadal variability and ENSO modulation of the GFDL simulation. The GFDL model simulates an alternation of periods of increased occurrence of Central Pacific (CP) and Eastern Pacific (EP) El Niño events. Following Kug et al. (2010) and Choi et al. (2011), CP and EP events are defined from a 0.5°C threshold value of SST anomalies during NDJ respectively in areas Niño4m and Niño3m. Those areas are defined by shifting by 20° westward the usual areas Niño4 and Niño3 due to the westward shift of variability in the GFDL simulation. Figure 6 evidences that at decadal timescale the occurrence of CP events (thin green line)

is anticorrelated (c=-0.6) with the one of EP events (thin red line), and is further correlated (c=0.7) to variations of central Pacific mean SST (black line). Similarly to Choi et al. (2011), we define a warm (cold) mean state that is averaged over all period intervals where deviation of central Pacific mean SST is superior (inferior) to 0.5°C (-0.5°C) as compared to the full record. This threshold value is lower than +-1°C in Choi et al. (2011) because here the simulation is shorter (300 years instead of 500). The period intervals used for averaging are shown in figure 6a for the warm mean state (thick green horizontal lines, in top) and the cold mean state (thick red horizontal lines, in bottom). Figure 6b shows temperature differences between the defined warm state and the cold state. Interestingly, it consists in a strengthening of the equatorial Pacific warm pool similar to the one observed after 2000 on the shorter SODA record (cf. figure 1). In this sense the transition from the cold state (with higher occurrence of EP events) to the warm state (with higher occurrence of CP events) in the GFDL simulation is qualitatively similar to the transition after 2000 in the SODA record.

The TD model parameters are tuned from either the warm mean state or the cold mean state of the GFDL simulation. We use a similar method than in the previous section, by first computing a reference state from the full GFDL record and then by tuning a reduced set of parameters. This corresponds to modified scaling of model parameters from the cold to the warm mean state, on P_1 (+1%), P_2 (-9%), P_3 (-25%) for the upper-ocean stratification, F_U (+4%), F_H (-7%) and F_W (+4%) for mixed-layer thermodynamics, μ_1 (+5%) and μ_2 (+2%) for the statistical atmosphere. In addition, because in the GFDL simulation the variability is shifted westward by around 20 degrees, averages are shifted accordingly to compute variations in P_n, F_H, F_U, and F_W. Changes in mean state parameters are qualitatively consistent with Choi et al. (2011), where the warm mean state is associated to a reduced thermocline feedback (F_H), an enhanced damping feedback due to enhanced easterlies (F_W), and a slightly increased atmospheric response to SST anomalies (μ_1 and μ_2).

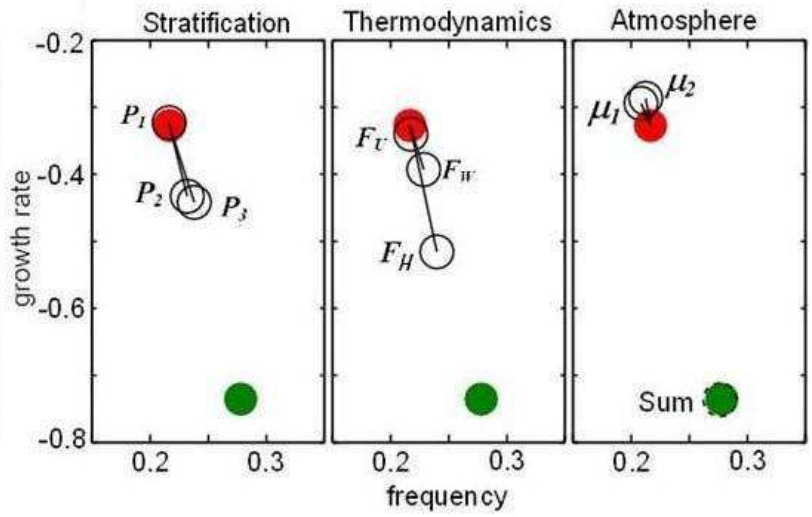

Figure 7: Frequency (yr^{-1}) and growth rate (yr^{-1}) of the ENSO mode simulated by the TD model, with parameters tuned from the warm mean state (green) or the cold mean state (red) of the GFDL_CM2.1 simulation. The open black circles are obtained by tuning individually each parameter from the cold mean state with other parameters tuned from the warm mean state. The "sum point" (black open dashed circle) sums all stability changes from individual parameter changes.

Changes in stability are shown in figure 7, where the TD model is tuned from either the warm mean state (red) or the cold mean state (green) of the GFDL simulation. The TD model simulates a more stable and high frequency ENSO mode for the warm mean state. Like for the climate shift of the 1970s in the SODA record (figure 4), changes in stability are mostly controlled by the thermocline feedback (F_H,) and stratification parameters P_2 and P_3. Again, a main conclusion is that the influence of stratification parameters (P_2 and P_3) onto the ENSO stability is comparable in magnitude to the one of mixed-layer thermodynamics and atmosphere parameters. This also extends results from Choi et al. (2011) where linear stability was not assessed.

Like for the climate shift of the 1970s (cf. figure 5), the TD model here simulates a spatially fixed recharge/discharge process with maximal SST anomalies in the eastern Pacific, which is representative of EP events (not shown). For a warmer mean state (with decreased stratification) this eigenmode is more damped, which is qualitatively consistent with the decreased occurrence of EP events. There is however no leading eigenmode associated to CP events, at least with maximal SST anomalies in the central Pacific. Indeed, to our knowledge there are at this time no studies of reduced models such as the TD model that clearly identify an eigenmode representative of CP events. This limitation will be discussed in the concluding section of this article.

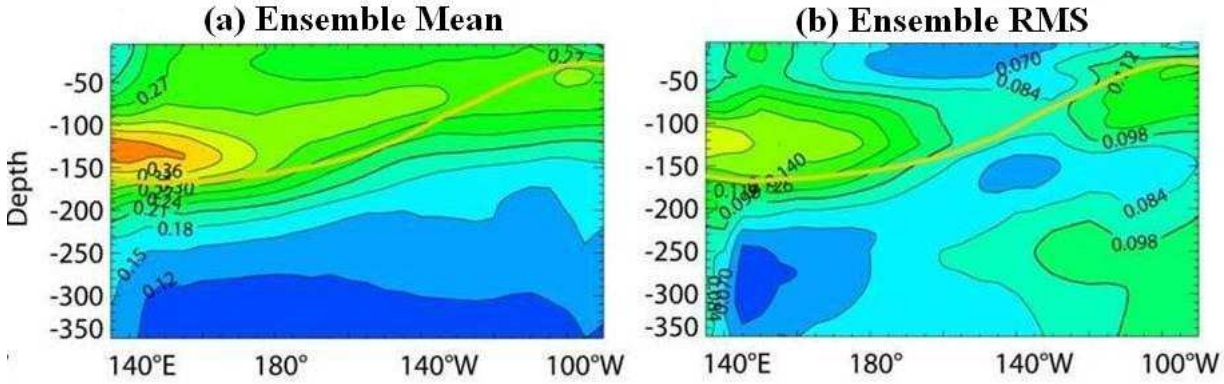

Figure 8: (a) Ensemble mean and (b) ensemble dispersion, among the panel of fifteen CGCM simulations, of the mean state temperature variability (°C, defined as standard deviation of the 10 years running mean). Results are shown at the equator as a function of longitude and depth. The ensemble mean thermocline depth is superimposed (yellow thick line).

The relation between ENSO modulation and the mean stratification is further considered in a panel of pre-industrial simulations of various CGCMs from the CMIP3 archive (see section 2.2). Like the GFDL_CM2.1 model (included in the panel), these models simulate their own mean state with a refined representation of the ocean vertical structure allowed by their relatively high vertical resolution. Figure 8 shows the mean state temperature variability among the ensemble of model simulations. From the ensemble mean in figure 8a, it appears that mean state variability is most pronounced just above the equatorial thermocline and in the central to western Pacific, which is similar to the previously described mean state changes of the SODA reanalysis (cf. figure 1) and the GFDL_CM2.1 simulation (cf. figure 7). The ensemble dispersion in figure 8b further shows that this region is also where CGCMs mostly disagree on the intensity of mean state variability.

Those considerations may be extended to the P_n coefficients, which mean state variability shows a significant ensemble mean (1.0%, 3.2%, and 6.9% with respect to nominal value for P_1, P_2 and P_3 respectively) and ensemble dispersion (0.3%, 1.5%, and 3.4% with respect to nominal value for P_1, P_2 and P_3 respectively).

Model	P1	P2	P3	D20
MIUB_ECHO_G	-0.53	0.81	0.82	-0.54
CNRM_CM3	-0.49	0.78	0.75	-0.75
GFDL_CM2_1	-0.47	0.60	0.72	-0.57
MPI_ECHAM5	0.46	0.62	0.62	-0.70
INMCM3_0	0.10	0.62	0.61	-0.71
CSIRO_MK3_0	-0.29	0.57	0.64	-0.36
GFDL_CM2_0	-0.40	0.46	0.73	-0.33
CSIRO_MK3_5	-0.32	0.54	0.47	-0.21
UKMO_HADCM3	-0.19	0.46	0.53	-0.44
FGOALSrun1	-0.03	0.64	0.28	-0.39
MRI_CGCM2_3_2A	-0.25	0.36	0.32	-0.54
NCAR_CCSM3_0	-0.52	0.18	0.42	0.00
IPSL_CM4	-0.21	0.03	0.52	0.28
INGV_ECHAM4	0.18	-0.03	0.30	0.07
UKMO_HADGEM1	-0.24	-0.20	0.02	0.22

Table 1: Correlation, among the panel of fifteen CGCM simulations, between the 20-years running standard deviation of Niño3-SST anomalies (i.e. the index N3Var like in Rodgers et al. 2004), and the 20-years running mean of P_1, P_2, P_3 (averaged within 170°E-170°W) and D20 (mean thermocline depth averaged in area Niño4). Models are ordered by decreasing correlation on P_2 and P_3. All timeseries were detrended.

We also consider, in the panel of CGCM simulations, the relation between the decadal variability of mean stratification and the simulated ENSO modulation. Table 1 shows correlations between the variations in the P_n coefficients and in the index N3Var of ENSO modulation (defined here as the running standard deviation of Niño3-SST anomalies). Interestingly, various models (up-most in table 1) show a significant correlation (c>0.6) for both P_2 and P_3. Meanwhile, variations in P_1 are rather weakly anticorrelated with the ENSO modulation, as is also the case for the mean thermocline depth of the central Pacific. Nevertheless, results from the SODA and GFDL_CM2.1 suggest that P_2 and P_3 are most influent on ENSO stability. In all models the index N4Var (for Niño4-SST anomalies) is strongly correlated with N3Var (c>0.7), which therefore does not permit in those relatively short records (~150 years) a clear separation between periods of increased occurrence of EP or CP events. It is however interesting to note that the CNRM_CM3, GFDL_CM2.1 and INCM3_0 (but not UKM0-HADGCM.1) are among the models showing greatest correlations between stratification changes and the ENSO modulation, while they are in the meantime the ones where the relative intensity of CP and EP events is best represented (Yu and Kim 2010). In conclusion, the decadal variability of mean stratification in the central Pacific (P_n coefficients) appears to be a robust feature of the panel of CGCM simulations, which is significantly correlated to the ENSO modulation in some models, while in the meantime there are significant discrepancies among models with respect to the intensity of such variability.

5. Summary and discussion

A recharge/discharge conceptual model has been used to document changes in the mean state and stratification of the equatorial Pacific as well as the associated changes in ENSO stability. This relation has been overlooked for the climate shift of the 1970s in the SODA reanalysis as well as in a pre-industrial simulation of the GFDL_CM2.1 model showing stratification changes similar to the ones after 2000. Considerations on the relation between stratification changes and ENSO modulation were also extended to a panel of other pre-industrial simulations of coupled global circulation models (CGCMs).

Sensitivity tests have been considered for the relative influence of various mean state parameters onto the ENSO stability rather than for one type of parameter alone (see also Jin et al. 2006; Kim and Jin 2010). As compared to previous sensitivity studies, the conceptual model used here (Thual et al. 2011) also considers dynamics of the gravest baroclinic modes of the continuously stratified ocean rather than two-layer shallow-water dynamics, which further allows considering peculiarities of the mean thermocline structure (thickness, intensity and overall shape) and its changes. Results from the SODA reanalysis and the GFDL simulation confirm the significant sensitivity of ENSO stability to decadal changes in the ocean stratification parameters (P_n) that control the efficiency of transfer of work from wind stress forcing to ocean motion. In addition, such sensitivity is comparable in magnitude to the one of usual thermodynamic and atmospheric parameters. This also complements previous studies where the sensitivity to stratification has been assessed through direct numerical simulation (Moon et al. 2004; Dewitte et al. 2007; 2009).

The evidenced sensitivity is, however, limited to the model representation of ENSO dynamics, and the means by which mean state feedbacks are estimated. The reduced model is indeed too simple to account for all the many features of ENSO modulation. It successfully simulates a dominant oscillating eigenmode, qualitatively representative of ENSO oscillations, where the main process is a recharge/discharge on the equatorial thermocline (Jin 1997a; b). However, due to its statistical parameterization of the atmospheric response, the model favors standing SST modes rather than propagating SST modes like in the observed record (An et al. 2006). For this reason, its sensitivity to ocean stratification is mostly on the frequency and growth rate of the simulated eigenmode. In particular, for realistic parameter range (e.g. as derived from the GFDL_CM2.1 simulation) the reduced model does not simulate an eigenmode representative of Central Pacific (CP) El Niño events. Indeed, to our knowledge there are at this time no studies of reduced models such as the one proposed here that clearly identify an eigenmode representative of CP events. Accounting for this may involve additional parameter tunings (e.g. on the thermocline feedback which estimation can be misleading in the central Pacific, cf. Dewitte et al. 2012b) or additional mechanisms, including non linear ones (Philip and van Oldenborgh 2009). Kug et al. (2010) for example suggested from composites of the GFDL_CM2.1 simulation that the CP El Niño might be representative of a damped westward propagating mode of SST anomalies, involving mainly atmospheric processes. In addition, we may wonder if the CP El Niño can be accounted for by either modifications of the leading eigenmode (Fedorov and Philander 2001) or rather as a secondary eigenmode competing in term of growth rate with the leading eigenmode (Bejarano and Jin 2008).

One general and critical challenge for reduced ENSO models is to account, at the same time, for both a more refined representation of the observed processes as well as a more synthetic view at the most influential ones. This suggests two complementary perspectives for future works on sensitivity to ocean stratification. First, we may further refine the representation of ocean stratification in the reduced model, for example by considering the contribution of higher ocean baroclinic modes (Thual et al. 2011) or by accounting for zonal stratification changes (Busalacchi and Cane 1988). Second, it would be interesting to provide a more synthetic view at the sensitivity to ocean stratification in order to easier CGCM inter-comparison. For example, the linear stability of the proposed reduced model shares many characteristics with the Bjerknes index (Jin et al. 2006; Kim and Jin 2010), such as a recharge/discharge process with fixed spatial structure, as well a growth rate of the simulated ENSO depending linearly on the contribution of various mean state feedbacks. Therefore it may be interesting to assess sensitivity to ocean stratification within this synthetic and versatile framework, though the consideration of the gravest ocean baroclinic modes would render the derivation of the Bjernkes index more complex.

In conclusion, our results call for considering stratification changes in order to interpret more aspects of the modulation and diversity of ENSO in observations (e.g. for the climate shift of the 1970s) and in CGCMs that have a refined representation of the ocean vertical structure. Notably, the diversity of ENSO variability in CGCMs goes along with significant model dispersion in terms of mean stratification and its low-frequency variability (e.g. figure 8 and table 1 for the CMIP3 archive). This is also likely to have implications for the CGCM responses to global warming (Guilyardi et al. 2009) where mean stratification is expected to increase significantly. It is proposed here to include in the metrics for the evaluation of the CGCMs one related to ocean stratification. The formalism and results proposed in this study may provide material for elaborating such metric, which is plan for future work.

References:

An, S., and F. Jin, 2000: An eigen analysis of the interdecadal changes in the structure and frequency of ENSO mode. *Geophysical Research Letters*, **27**, 2573.

An, S.-I., and B. Wang, 2000: Interdecadal Change of the Structure of the ENSO Mode and Its Impact on the ENSO Frequency. *Journal of Climate*, **13**, 2044–2055.

An, S.-I., and F.-F. Jin, 2001: Collective Role of Thermocline and Zonal Advective Feedbacks in the ENSO Mode. *Journal of Climate*, **14**, 3421–3432.

An, S.-I., Z. Ye, and W. W. Hsieh, 2006: Changes in the leading ENSO modes associated with the late 1970s climate shift: Role of surface zonal current. *Geophys. Res. Lett.*, **33**, L14609, doi:10.1029/2006GL026604.

An, S.-I., J.-S. Kug, Y.-G. Ham, and I.-S. Kang, 2008: Successive Modulation of ENSO to the Future Greenhouse Warming. *Journal of Climate*, **21**, 3–21, doi:10.1175/2007JCLI1500.1.

Ashok, K., S. K. Behera, S. A. Rao, H. Weng, and T. Yamagata, 2007: El Niño Modoki and its possible teleconnection. *J. Geophys. Res.*, **112**.

Bejarano, L., and F.-F. Jin, 2008: Coexistence of Equatorial Coupled Modes of ENSO. *Journal of Climate*, **21**, 3051–3067.

Belmadani, A., B. Dewitte, and S.-I. An, 2010: ENSO Feedbacks and Associated Time Scales of Variability in a Multimodel Ensemble. *Journal of Climate*, **23**, 3181–3204, doi:10.1175/2010JCLI2830.1.

Busalacchi, A. J., and M. A. Cane, 1988: The Effect of Varying Stratification on Low-Frequency Equatorial Motions. *Journal of Physical Oceanography*, **18**, 801–812, doi:10.1175/1520-0485(1988)018<0801:TEOVSO>2.0.CO;2.

Carton, J. A., and B. S. Giese, 2008: A Reanalysis of Ocean Climate Using Simple Ocean Data Assimilation (SODA). *Monthly Weather Review*, **136**, 2999–3017, doi:10.1175/2007MWR1978.1.

Choi, J., S.-I. An, J.-S. Kug, and S.-W. Yeh, 2011: The role of mean state on changes in El Niño's flavor. *Climate Dynamics*, **37**, 1205–1215, doi:10.1007/s00382-010-0912-1.

Collins, M. and Coauthors, 2010: The impact of global warming on the tropical Pacific Ocean and El Ni[ntilde]o. *Nature Geoscience*, **3**, 391–397, doi:10.1038/ngeo868.

Dewitte, B., 2000: Sensitivity of an Intermediate Ocean–Atmosphere Coupled Model of the Tropical Pacific to Its Oceanic Vertical Structure. *Journal of Climate*, **13**, 2363–2388, doi:10.1175/1520-0442(2000)013<2363:SOAIOA>2.0.CO;2.

Dewitte, B., S.-W. Yeh, B.-K. Moon, C. Cibot, and L. Terray, 2007: Rectification of ENSO Variability by Interdecadal Changes in the Equatorial Background Mean State in a CGCM Simulation. *Journal of Climate*, **20**, 2002–2021, doi:10.1175/JCLI4110.1.

Dewitte, B., S. Thual, S.-W. Yeh, S.-I. An, B.-K. Moon, and B. S. Giese, 2009: Low-Frequency Variability of Temperature in the Vicinity of the Equatorial Pacific Thermocline in SODA: Role of Equatorial Wave Dynamics and ENSO Asymmetry. *Journal of Climate*, **22**, 5783–5795, doi:10.1175/2009JCLI2764.1.

Dewitte, B., J. Choi, S.-I. An, and S. Thual, 2012a: Vertical structure variability and equatorial waves during central Pacific and eastern Pacific El Niños in a coupled general circulation model. *Climate Dynamics*, **38**, 2275–2289.

Dewitte, B., S.-W. Yeh, and S. Thual, 2012b: Reinterpreting the thermocline feedback in the western-central equatorial Pacific and its relationship with the ENSO modulation. *Climate Dynamics*, doi:10.1007/s00382-012-1504-z.

Fedorov, A. V., and S. G. Philander, 2001: A Stability Analysis of Tropical Ocean–Atmosphere Interactions: Bridging Measurements and Theory for El Niño. *Journal of Climate*, **14**, 3086–3101.

Guilyardi, E., A. Wittenberg, A. Fedorov, M. Collins, C. Wang, A. Capotondi, G. J. van Oldenborgh, and T. Stockdale, 2009: Understanding El Niño in Ocean–Atmosphere General Circulation Models: Progress and Challenges. *Bulletin of the American Meteorological Society*, **90**, 325–340, doi:10.1175/2008BAMS2387.1.

Jin, F.-F., 1997a: An Equatorial Ocean Recharge Paradigm for ENSO. Part I: Conceptual Model. *Journal of the Atmospheric Sciences*, **54**, 811–829.

Jin, F.-F., 1997b: An Equatorial Ocean Recharge Paradigm for ENSO. Part II: A Stripped-Down Coupled Model. *Journal of the Atmospheric Sciences*, **54**, 830–847, doi:10.1175/1520-0469(1997)054<0830:AEORPF>2.0.CO;2.

Jin, F.-F., 2001: Low-frequency modes of tropical ocean dynamics. *Journal of climate*, **14**, 3874–3881.

Jin, F.-F., J. D. Neelin, and M. Ghil, 1994: El Nino on the Devil's Staircase: Annual Subharmonic Steps to Chaos. *Science*, **264**, 70–72.

Jin, F.-F., S. T. Kim, and L. Bejarano, 2006: A coupled-stability index for ENSO. *Geophys. Res. Lett.*, **33**, 5 PP., doi:200610.1029/2006GL027221.

Kim, S. T., and F.-F. Jin, 2010: An ENSO stability analysis. Part II: results from the twentieth and twenty-first century simulations of the CMIP3 models. *Climate Dynamics*, **36**, 1609–1627, doi:10.1007/s00382-010-0872-5.

Kirtman, B. P., and P. S. Schopf, 1998: Decadal Variability in ENSO Predictability and Prediction. *Journal of Climate*, **11**, 2804–2822, doi:10.1175/1520-0442(1998)011<2804:DVIEPA>2.0.CO;2.

Kug, J.-S., F.-F. Jin, and S.-I. An, 2009: Two Types of El Niño Events: Cold Tongue El Niño and Warm Pool El Niño. *Journal of Climate*, **22**, 1499–1515.

Kug, J.-S., J. Choi, S.-I. An, F.-F. Jin, and A. T. Wittenberg, 2010: Warm Pool and Cold Tongue El Nino Events as Simulated by the GFDL 2.1 Coupled GCM. *J. Clim.*, **23**, 1226–1239, doi:10.1175/2009JCLI3293.1.

Lee, T., and M. J. McPhaden, 2010: Increasing intensity of El Niño in the central-equatorial Pacific. *Geophys. Res. Lett.*, **37**, 5 PP., doi:201010.1029/2010GL044007.

Lin, J.-L., 2007: Interdecadal variability of ENSO in 21 IPCC AR4 coupled GCMs. *Geophys. Res. Lett.*, **34**, L12702, doi:10.1029/2006GL028937.

McPhaden, M. J., 2012: A 21st Century Shift in the Relationship between ENSO SST and Warm Water Volume Anomalies. *Geophys. Res. Lett.*, doi:10.1029/2012GL051826.

Moon, B.-K., S.-W. Yeh, B. Dewitte, J.-G. Jhun, I.-S. Kang, and B. P. Kirtman, 2004: Vertical structure variability in the equatorial Pacific before and after the Pacific climate shift of the 1970s. *Geophys. Res. Lett.*, **31**, 4 PP., doi:200410.1029/2003GL018829.

Neelin, J. D., D. S. Battisti, A. C. Hirst, F.-F. Jin, Y. Wakata, T. Yamagata, and S. E. Zebiak, 1998: ENSO theory. *Journal of Geophysical Research*, **103**, 14261–14290.

Philander, S. G., and A. Fedorov, 2003: Is El Niño sporadic or cyclic? *Annual Review of Earth and Planetary Sciences*, **31**, 579–594.

Philip, S., and G. J. van Oldenborgh, 2009: Significant Atmospheric Nonlinearities in the ENSO Cycle. *Journal of Climate*, **22**, 4014–4028, doi:10.1175/2009JCLI2716.1.

Rodgers, K. B., P. Friederichs, and M. Latif, 2004: Tropical Pacific Decadal Variability and Its Relation to Decadal Modulations of ENSO. *Journal of Climate*, **17**, 3761–3774, doi:10.1175/1520-0442(2004)017<3761:TPDVAI>2.0.CO;2.

Seager, R., A. R. Karspeck, M. A. Cane, Y. Kushnir, A. Giannini, A. Kaplan, B. Kerman, and J. Velez, 2004: Predicting Pacific decadal variability. *Geophysical monograph*, **147**, 105–120.

Sun, D.-Z., and T. Zhang, 2006: A regulatory effect of ENSO on the time-mean thermal stratification of the equatorial upper ocean. *Geophys. Res. Lett.*, **33**, 4 PP., doi:200610.1029/2005GL025296.

Thual, S., B. Dewitte, S.-I. An, and N. Ayoub, 2011: Sensitivity of ENSO to Stratification in a Recharge–Discharge Conceptual Model. *Journal of Climate*, **24**, 4332–4349.

Wang, B., and Y. Wang, 1996: Temporal Structure of the Southern Oscillation as Revealed by Waveform and Wavelet Analysis. *Journal of Climate*, **9**, 1586–1598, doi:10.1175/1520-0442(1996)009<1586:TSOTSO>2.0.CO;2.

Wittenberg, A. T., A. Rosati, N.-C. Lau, and J. J. Ploshay, 2006: GFDL's CM2 Global Coupled Climate Models. Part III: Tropical Pacific Climate and ENSO. *Journal of Climate*, **19**, 698–722, doi:10.1175/JCLI3631.1.

Yu, J.-Y., and S. T. Kim, 2010: Identification of Central-Pacific and Eastern-Pacific types of ENSO in CMIP3 models. *Geophys. Res. Lett.*, **37**, L15705, doi:10.1029/2010GL044082.

5.1.3. Supplementary Materials

We provide supplementary materials to the previous submitted article. In appendix 3, we propose a statistical relationship built from the evolution of the TD model parameters and stability, which evidences certain features of the decadal modulation of ENSO characteristics.

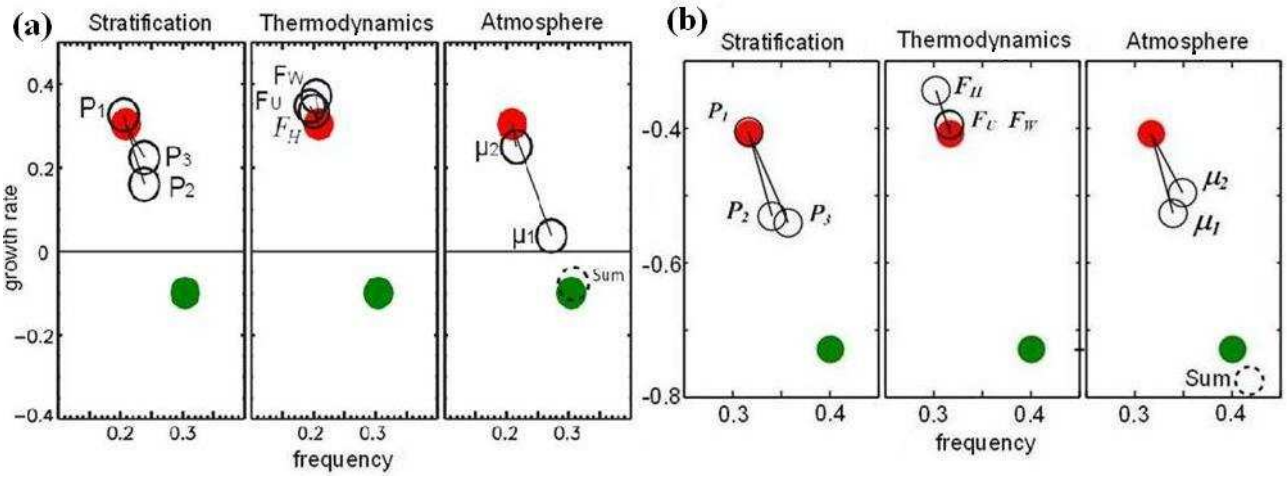

Figure 5.3: (a) Frequency (yr^{-1}) and growth rate (yr^{-1}) of the ENSO mode as simulated by the TD model with parameters tuned from the SODA reanalysis, for the period 1980-2000 (red) and 2000-2008 (green),. Stability values are shown when a single parameter is modified (black open circles) from period 1980-2000 to period 2000-2010. (b) Same as (a) but for parameters tuned from the GODAS reanalysis, for the period 1980-2000 (red) and 2000-2010 (green).

The change in ENSO stability after 2000 was not computed in the previous submitted article, due to the short record of the SODA dataset. This change in stability is nevertheless shown in figure 5.3. We also proceed to a consistency check based on the GODAS reanalysis (Behringer et al., 1998) that extends from 1980 to 2010. The method used to compute ENSO stability from GODAS is similar to the one for SODA: a reference state of the TD model is initially computed from an average over 1980-2010 (see Thual et al. 2011), then several mean state parameters are tuned from either the period 1980-2000 or 2000-2010 (see previous submitted article). Results are overall similar in each dataset: the TD model simulates an ENSO mode that is more damped and at higher frequency after 2000, and the sensitivity to the atmospheric feedbacks and to the stratification parameters is dominant. Note however that, due the short record of both datasets, it is not possible to determine wether the change in ENSO stability after 2000 is significant. Those results remain therefore subjective, but however suggest that the changes in stratification after 2000 might (potentially) have a significant impact on ENSO variability. This also complements an article that we have published recently, which documents change in baroclinic modes variability during Central Pacific El Niño events with a particular focus on conditions after 2000 (Dewitte et al., 2011).

We have also extended our analysis to a preindustrial run of the Kiev Climate model (KCM) (Park et al., 2009). Similarly to the GFDL, the KCM exhibits a decadal modulation of the occurrence of EP and CP

events (Yeh et al., 2011). We have investigated whether this modulation is associated to changes in the background mean state. We have separated periods of higher occurrence of EP and CP events following the classification from Yeh et al. (2011), and alternatively the classification from Choi et al. (2010). Those approaches however do not evidence that changes in the occurrence of the two types of El Niño events are associated to significant changes in background conditions. In particular, changes in thermal structure at the equator are too weak (~0.1°C maximum) to induce a significant change in ENSO stability. This suggests that the selection of the El Niño type has to arise from another process in the KCM. Yeh et al. (2011) shows for instance that changes in the background mean state do occur in the KCM but are significant only at higher latitudes. Those may impact the interannual variability of the equatorial Pacific through teleconnections, which should be investigated.

We have explored a vast amount of alternative TD model parametrizations (e.g. meridional truncature and average, proxy of thermocline and mixed-layer depth, mean upwelling estimation, idealised atmosphere, computation of atmospheric SVD modes over time) that are not detailed here for brievety. We have found overall significant discrepancies in results depending on the means by which the model is designed and the mean state feedbacks are computed. We must therefore advice that uncareful sensitivity tests to mean state feedbacks with the TD model can be misleading. As a perspective for future works, they are several limitations that should be overcome in order to use the TD model stability as a fully robust and reproductible diagnostic tool (e.g. for any dataset, and to assess sensitivity to any mean state feedback):

1.) The spatial structure of certain model parameters is too complex to explore sensitivity. This is the case for thermodynamic feedbacks that are estimated zonally in an equatorial strip (where the thermocline feedback estimation can further be misleading in the central Pacific, cf. chapter 4). It is also the case for the first SVD modes of the statistical atmosphere, which may not correspond to individual dynamical modes (Monahan et al., 2009) and whose sensitivity is therefore difficult to interpret. This is notably one of the reasons for which sensitivity tests in the previous submitted article were restricted to a limited set of parameters.

2.) The computation of a TD model reference state omits several processes associated to the mean state of the equatorial Pacific, and its associated stability may therefore be quite different from one dataset to another (e.g. in GODAS where the ENSO mode is much more damped than in SODA, cf. figure 5.3). While we may limit variations in mean state over time to a few representative parameters (e.g. P_1, P_2, P_3, F_H, F_U,, F_W,, μ_1, μ_2), a reference state however needs to be recomputed from one dataset to another. This limits the comparison between datasets.

3.) The sensitivity of the simulated ENSO stability may depend non-linearly on mean state feedbacks (cf. sum point in figure 5.3). Although sensitivity may for instance be non-linear in the real world, this burdens the intercomparison between sensitivity to each feedback.

Alternative stability diagnostics exist that overcome certain of those issues (Jin et al., 2006; Kim and Jin, 2010a; 2010b). The stability index from Jin et al. (2006) is built from the recharge/discharge model of

Jin, 1997a (its growth rate). Conditions are averaged in a western and eastern box of the equatorial Pacific, which removes the sensitivity to a complex spatial structure (though specific spatial structures may not be accounted for, for instance the one associated to Central Pacific El Niño events). Most ocean processes are retained, and several regression coefficients are introduced that relate the intensities of variations in each model variable. Those regression coefficients ensure in particular that the stability index is representative of the amplitude of ENSO in the associated dataset (e.g. Kim and Jin, 2010b, its figure 12). Finally, by omitting the damping rate of WWV anomalies that is small as compared to the damping rate of SST anomalies, the stability index (i.e. growth rate) depends linearly on mean state feedbacks (Burgers, 2005). Those further simplifications could be implemented in the TD model as a perspective for future works. The objective would be to obtain a framework similar to the one of Jin et al.(2006) that would additionally take into account the sensitivity to the background ocean stratification. A good starting point for this may be the scalar version of the TD model that is presented in appendix 2.

5.2. Central Pacific El Niño Events in Reduced Models

On the basis of results from the previous sections, we discuss how the TD model and reduced models in general may reproduce the mechanisms of Central Pacific El Niño events. In each dataset (SODA, GODAS, GFDL), the TD model reproduces an ENSO mode representative of EP events that is more damped when mean state parameters are representative of a stronger Warm Pool. The weakening of EP events is qualitatively consistent with the observed variability. The picture given by the stability of the TD model is however incomplete, because it fails to reproduce a dominant mode associated to CP events. In the following, we discuss strategies to overcome this issue.

An eigenmode simulated by the TD model that would be representative of CP events may have to be related to enhanced zonal advective processes rather than thermocline processes, according to conclusions from Kug et al. (2009). In the TD model, thermocline and zonal advective processes lead to competing modes in terms of growth rate (see also Fedorov and Philander 2001; Bejarano and Jin 2008), though they may also contribute collectively to a single ENSO mode in other models (An and Jin 2001). Figure 5.4 shows stability values of the TD model as a function of the relative strength of thermocline and zonal advective processes (this is also figure 8 from Thual et al. 2011). Enhanced zonal advective (thermocline) processes favour the mode EG2 (EG3). Figure 5.5 shows eigenvectors of the ENSO mode EG2 for enhanced zonal advective processes (α=0.9, see Thual et al. 2011). EG2 is associated to maximal SST anomalies in the central Pacific, and might therefore be a good candidate to account for CP events. It is, however, associated to strong thermocline depth anomalies that are not representative of CP events. The mis-representation of CP events may also be related to an underestimation of zonal advective processes in the TD model. Indeed, we found that changes in the intensity of the zonal advective feedback as induced from observations (SODA,

GODAS, GFDL) do not lead to significant changes in ENSO stability (cf. previous sections), suggesting that in the TD model the latter feedback is secondary. This is also the case for Ekman zonal currents (not shown).

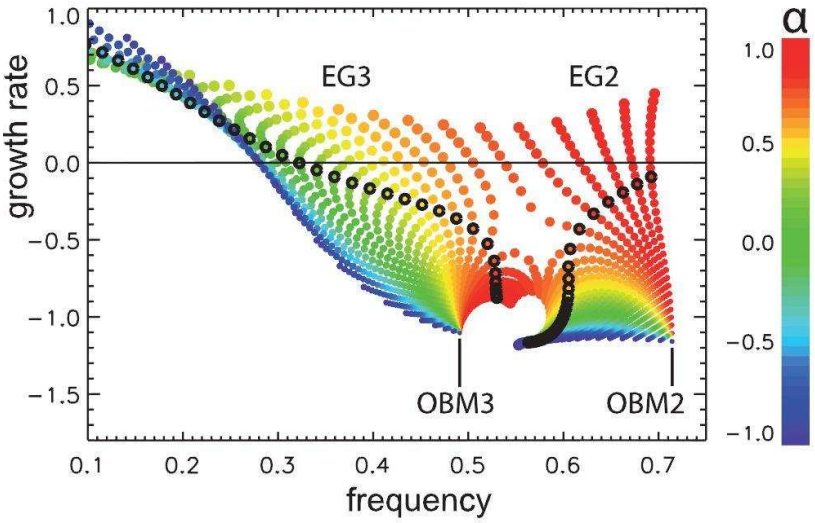

Figure 5.4: Plot of eigenvalues (frequency and growth rate, yr^{-1}) of the TD model with sensitivity to the ocean atmosphere coupling μ and the relative intensity of thermocline and zonal advective processes α. Nominal values are μ=1 and α=0. We represent μ with increasing dot size ($0 \leq \mu \leq 1.5$), and for μ=1 eigenvalues are contoured in black. We represent α with colors ($-1 \leq \alpha \leq 1$), where α=-1 (α=1) corresponds to dominant thermocline (zonal advective). OBM3 and OBM2 are ocean basin modes identified in the uncoupled case. EG3 and EG2 are two competing modes in terms of growth rate (from Thual et al. 2011).

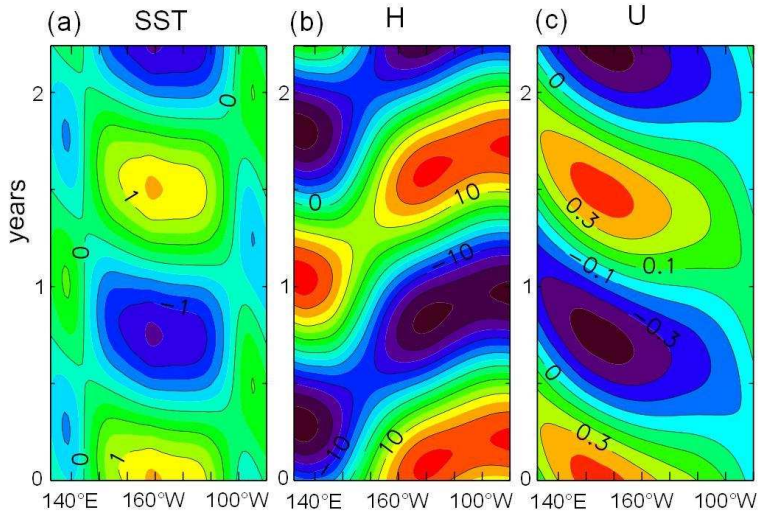

Figure 5.5: Time longitude plots of (a) SST anomalies (°C), (b) thermocline depth anomalies (m) and (c) zonal currents anomalies (m.s-1) for the ENSO mode EG2 simulated by the TD model, at μ=1 and α=0.9 (see Thual et al. 2011, its figure 4).

The role of boundary reflections during CP events may also be investigated. Figure 5.4 shows that the frequency of EG2 remains close to the one of an ocean basin mode (OBM2, see Thual et al. 2011). The eigenmode EG2 is controlled by the delay associated to the crossing and reflection of ocean equatorial waves across the equatorial Pacific, and is therefore strongly related to the presence of boundary reflections. This is consistent with our diagnostic from chapter 3, where we have found that representative values of zonal advective processes lead to an ENSO oscillation that is convectively unstable, and therefore relies to a large extent on boundary reflections. Alternatively, it could also be interesting to assess if the CP events are associated to an absolute instability, where on the contrary boundary reflections are secondary. This could be the case for enhanced zonal advective (or thermocline) processes in the central Pacific, or maybe for enhanced Ekman zonal currents (Kug et al. 2009, its figure 9) that have not been considered in Thual et al. (2012a). Those are two opposite views at the mechanisms of Central Pacific events, where the role of boundary reflections is either essential (for an ocean basin mode) or secondary (for an absolute instability). More generally, we may question whether CP events are associated to an oscillation paradigm that is different from the one(s) of EP events.

Chapter

6. Data Assimilation

In this chapter, we implement a method for the assimilation of sea level data in an already existing intermediate complexity model of the equatorial Pacific, the LODCA model (for Linear Ocean Dynamically Coupled to the Atmosphere). We begin this chapter by recalling elements of data assimilation. The assimilation method is an Ensemble Kalman Filter (EnKF), which describes model uncertainties with an ensemble of model realizations. We present the LODCA model as well as the tools that were developed during the thesis for the construction and implementation of the EnKF method.

The EnKF is implemented for a model configuration where the ocean is forced by wind stress forcings from the SODA reanalysis spanning 1958-2007. We design a perturbation method on the wind stress forcings where it is supposed that uncertainties arise from high frequency atmospheric variability. We document how this perturbation method permits the constraint of the model dynamics by pseudo-observations of sea level from the SODA reanalysis. We show that the major model constraint from sea level data is on the so-called Tilt and WWV modes that are associated to the recharge/discharge process of the equatorial thermocline. An alternative experiment is considered where pseudo-observations rather consist in two indexes measuring the intensity of the Tilt and WWV modes. This experiment leads to a similar predictive skill of sea surface temperature anomalies, which suggests that the constraint of the low-order model dynamics by sea level data is essential. A submitted article is included that presents main results. Supplementary materials are also provided.

6.1. Background

6.1.1. Minimisation Problem

In order to introduce main features of data assimilation methods, we start by presenting two minimisation problems, in the scalar case and the multi-dimensional case. Suppose that the true value of a scalar is x_t. This value is unknown, but we search a best estimate x_a of it given two estimates with known uncertainties. One estimate is a model realisation $x_b=x_t+\varepsilon_b$ with error ε_b. Another estimate is an observation realisation $y_o=Hx_t+\varepsilon_o$ with error ε_o. The observation is an indirect estimate of the scalar x_t, for which we introduce a linear observation operator H. We make the following hypotheses on errors ε_b and ε_o:

1) Errors are unbiased: $E(\varepsilon_b)=0$ and $E(\varepsilon_o)=0$, where E is the mean value (i.e. expected value).

2) Model and observation errors are uncorrelated: $E(\varepsilon_b\varepsilon_o)=0$

3) Errors are Gaussian with known variances: $E(\varepsilon_b^2)=\sigma_b^2$ and $E(\varepsilon_o^2)=\sigma_o^2$

The estimate x_a of the true state x_t has an error variance σ_a^2. We construct it as a linear combination $x_a(k)= k\, y_o/H+(1-k)x_b$, which implies $\sigma_a^2(k)= k^2\sigma_o^2/H^2+(1-k)^2\sigma_b^2$ where k has to be determined. We define the best estimate x_a as having minimal errors, which is found at k where σ_a is minimal. This implies that $k=H^2\sigma_b^2/(\sigma_o^2+ H^2\sigma_b^2)$. Another equivalent approach is to choose x_a with minimum distance to all estimates, which minimizes a quadratic cost function J that reads:

$$J(x)=\frac{1}{2}\frac{(x-x_b)^2}{\sigma_b^2}+\frac{1}{2}\frac{(Hx-y_o)^2}{\sigma_o^2} \qquad (6.1)$$

This minimisation problem is the elementary step for assimilation problems. In appendix 4, we propose an alternative probabilistic formulation. It is shown that x_a maximizes a probability function that accounts for both model and observation uncertainties. However, because the true state is unkown, this probability function has to be approximated.

We may generalize the minimisation problem to the multi-dimensional case. Suppose now that the true value of a field is $\mathbf{x_t}$. We search a best estimate $\mathbf{x_a}$ of it, given a model realisation $\mathbf{x_b}=\mathbf{x_t}+\boldsymbol{\varepsilon_b}$ and an observation realisation $\mathbf{y_o}=\mathbf{Hx_t}+\boldsymbol{\varepsilon_o}$. $\mathbf{H}$ is an observation operator, here linearised (i.e. a matrix). As previously, we suppose that errors are Gaussian, unbiased, and that model and observation errors are uncorrelated. They may however be correlations between model errors or between observations errors, for which we define a covariance matrix of model errors $\mathbf{B}=E(\boldsymbol{\varepsilon_b}\boldsymbol{\varepsilon_b}^T)$, and a covariance matrix of observation errors $\mathbf{R}=E(\boldsymbol{\varepsilon_o}\boldsymbol{\varepsilon_o}^T)$. The best estimate $\mathbf{x_a}$ has an associated covariance matrix of errors $\mathbf{A}=E(\boldsymbol{\varepsilon_a}\boldsymbol{\varepsilon_a}^T)$. As previously, the best estimate $\mathbf{x_a}$ minimizes a quadratic cost function J, which is generalised as

$$J(\mathbf{x})=\frac{1}{2}(\mathbf{x}-\mathbf{x_b})^T\mathbf{B}^{-1}(\mathbf{x}-\mathbf{x_b})+\frac{1}{2}(\mathbf{Hx}-\mathbf{y_o})^T\mathbf{R}^{-1}(\mathbf{Hx}-\mathbf{y_o}) \qquad (6.2)$$

The best estimate $\mathbf{x_a}$ is also the one that minimizes the trace of $\mathbf{A}$. In addition, $\mathbf{x_a}$ and $\mathbf{A}$ are expressed as

$$\mathbf{x_a} = \mathbf{x_b} + \mathbf{K}(\mathbf{y_o} - \mathbf{H}\mathbf{x_b}) \tag{6.3}$$

$$\mathbf{A} = \mathbf{B} - \mathbf{K}\mathbf{H}\mathbf{B} \tag{6.4}$$

$$\text{with } \mathbf{K} = \mathbf{B}\mathbf{H}^{\mathrm{T}}(\mathbf{H}\mathbf{B}\mathbf{H}^{\mathrm{T}} + \mathbf{R})^{-1} \tag{6.5}$$

For a little vocabulary, $\mathbf{K}$ is called the Kalman gain matrix, $\mathbf{y_o}$-$\mathbf{H}\mathbf{x_b}$ is called the innovation, $\mathbf{x_a}$–$\mathbf{x_b}$ is called the gain, where $\mathbf{x_b}$ is the background state and $\mathbf{x_a}$ is the analysed state. $\mathbf{x_a}$ is also called the Best Linear Unbiased Estimator (BLUE). By extension, the minimisation method is called the BLUE method (Gelb, 1974; Wunsch, 1996). The BLUE is the elementary step of most assimilation problems. The different extensions and implementations are discussed in the next section.

6.1.2. Assimilation Methods

A large variety of assimilation methods exist to treat the problem of estimation with known uncertainties, of which the minimisation problems presented in the previous section are a particular case. When working with both models and observations, the most common application is to replace a model background state $\mathbf{x_b}$ with an analysed state $\mathbf{x_a}$ that combines additional information from observations $\mathbf{y_o}$. Note however that the model correction is not necessarily restricted to the model state and can sometimes be extended to model forcings and parameters. Two families of methods exist to solve the minimisation problem for model states that evolve over time: sequential methods and variational (i.e. adjoint) methods. They are sketched in figure 6.1.

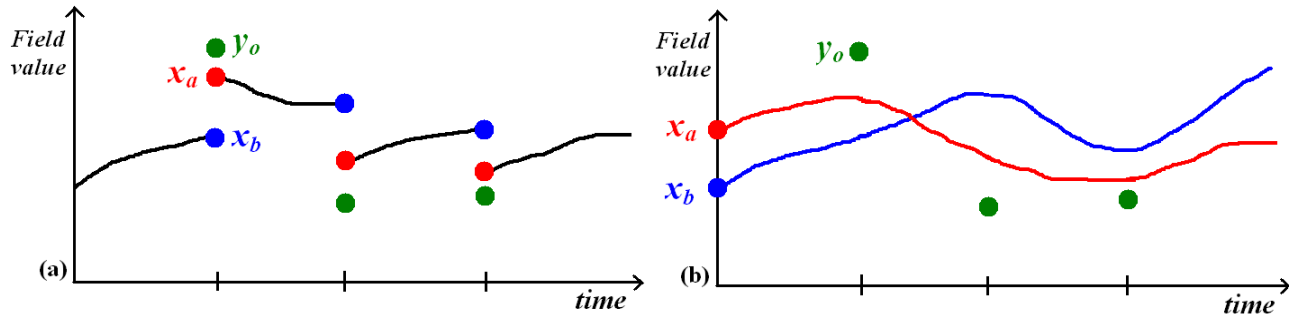

Figure 6.1: Sketch of (a) Sequential assimilation methods and (b) Variational assimilation methods. In this example we consider scalar values of the background state x_b (blue), analysed state x_a (red), and observations y_o (green). In sequential methods, x_b is corrected into x_a at each timestep where an observation y_o is available. In variational methods, x_b is an initial condition that is corrected into x_a such that its trajectory best matches posterior observations y_o.

Sequential assimilation methods consist in running the model and applying corrections sequentially, at timesteps where observations are available. The Linear Kalman Filter (LKF) method takes into account the evolution of the model and associated uncertainties over time (Kalman, 1960). At a timestep where observations are available, the BLUE is performed: the analysed state $\mathbf{x_a}$ replaces $\mathbf{x_b}$, and the analysed covariance matrix **A** replaces **B**. The model is then ran to compute $\mathbf{x_b}$ and **B** at the next timestep where observations are available. It is supposed that the model temporal evolution is linear, which reads:

$$\mathbf{x_b^{k+1}} = \mathbf{M^k}\,\mathbf{x_a^k} \tag{6.6}$$

$$\mathbf{B^{k+1}} = \mathbf{M^k}\,\mathbf{A^k}\,(\mathbf{M^k})^{\mathrm{T}} + \mathbf{Q^k} \tag{6.7}$$

where k denotes the timestep, and $\mathbf{M^k}$ is the model evolution operator. It is also possible to consider additional model errors arising from the temporal evolution, which are accounted for by the covariance matrix of errors $\mathbf{Q^k}$ (if $\mathbf{Q^k}$ is null, the model is said to be perfect). In the Extended Kalman filter (EKF) (Gelb, 1974), it is further assumed that the temporal evolution of the model state can be non-linear ($\mathbf{M^k}$ and **H** are no longer linearized in equations 6.3 and 6.6), while the evolution of model uncertainties however remains linear (all terms remain linearized in equations 6.4, 6.5 and 6.7). Finally, the Ensemble Kalman Filter (EnKF) describes statistics of uncertainties using a Monte Carlo approach (Evensen, 2003; 2007). This method will be presented in the next section. Sequential methods have been used extensively in ENSO models (Miller and Cane, 1989; Fischer et al., 1997; Cañizares et al., 2001; Sun et al., 2002; Tang and Hsieh, 2003; Kondrashov et al., 2008), with in particular several applications of the EnKF method (e.g. Ueno et al., 2004; Ham et al., 2009; Kug et al., 2010a; Zheng and Zhu, 2010).

For variational assimilation methods, the minimum of the cost function is searched while imposing some dynamical constraints related to the model temporal evolution. To a given initial background model state $\mathbf{x_b}$ is associated a first guess track given by the posterior temporal evolution of the model. This initial state is corrected into $\mathbf{x_a}$, such that the associated track best matches all posterior observations $\mathbf{y_o}$. The observation operator **H** (not necessarily linearized) includes the along-track model evolution such that $\mathbf{y_o}=\mathbf{H}(\mathbf{x_b})$. The search for a minimum $\mathbf{x_a}$ of the cost function J is performed by integrating the adjoint model and using a descent method (e.g. a conjugate gradient method) (Dimet and Talagrand, 1986; Wunsch, 1996). The 4DVAR method in particular has been extensively used by the meteorological community (Talagrand and Courtier, 1987; Courtier et al., 1994). There are also many applications to ENSO modelling and forecasting (e.g. Kleeman et al., 1995; Schneider et al., 1999; Bennett et al., 1998; 2000; Weaver et al., 2003).

6.1.3. Ensemble Kalman Filter

The Ensemble Kalman Filter (EnKF) is the assimilation method used in this thesis (Evensen, 2003; 2007). The EnKF is a sequential method in which uncertainties are described by a Monte Carlo approach, i.e.

an ensemble of realizations. It has gained popularity because of its simple formulation and relative ease of implementation. An essential advantage of the EnKF is that the ensemble of realizations directly provides the covariance matrix of model errors **B** and its associated temporal evolution. The background model state $\mathbf{x_b}$ is represented by an ensemble of N model realizations $\mathbf{x_b^i}$ where i=1,…, N. The observed state $\mathbf{y_o}$ is represented by an ensemble of N observation realizations $\mathbf{y_o^i}$ where i=1,…, N. The covariance matrix of model errors and of observation errors read respectively

$$\mathbf{B} = \mathrm{E}\left([\mathbf{x_b} - \mathrm{E}(\mathbf{x_b})][\mathbf{x_b} - \mathrm{E}(\mathbf{x_b})]^{\mathrm{T}}\right) \tag{6.8}$$

$$\mathbf{R} = \mathrm{E}\left([\mathbf{y_o} - \mathrm{E}(\mathbf{y_o})][\mathbf{y_o} - \mathrm{E}(\mathbf{y_o})]^{\mathrm{T}}\right) \tag{6.9}$$

where E denotes an average over the N realizations. The analysed model state $\mathbf{x_a}$ is represented by an ensemble of N model realizations $\mathbf{x_a^i}$ where i=1,…, N. It is computed during the analysis step as

$$\mathbf{x_a^i} = \mathbf{x_b^i} + \mathbf{K}(\mathbf{y_o^i} - \mathbf{H}\mathbf{x_b^i}) \text{, for i=1, …, N} \tag{6.10}$$

$$\text{with } \mathbf{K} = \mathbf{B}\mathbf{H}^{\mathrm{T}}(\mathbf{H}\mathbf{B}\mathbf{H}^{\mathrm{T}} + \mathbf{R})^{-1} \tag{6.11}$$

$$\text{and } \mathbf{A} = \mathrm{E}\left([\mathbf{x_a} - \mathrm{E}(\mathbf{x_a})][\mathbf{x_a} - \mathrm{E}(\mathbf{x_a})]^{\mathrm{T}}\right) \tag{6.12}$$

where **K** is the Kalman gain matrix, and **H** is the linearised observation operator. The temporal evolution of each model realization is then computed independently as

$$\mathbf{x_b^{i,k+1}} = \mathbf{M^k}(\mathbf{x_a^{i,k}}) + \mathbf{q^{i,k}} \text{ for i=1,…, N} \tag{6.13}$$

where k is the timestep, and $\mathbf{M^k}$ is the model evolution operator. For each model realization $\mathbf{q^{i,k}}$ has to be specified and accounts for (unbiased) errors arising from the model evolution.

6.2. Sea Level Data Assimilation in an Intermediate ENSO Model

6.2.1. Implementation

We present the LODCA model (for Linear Ocean Dynamically Coupled to the Atmosphere) (Dewitte, 2000), for which we implement the Ensemble Kalman Filter method. LODCA is an intermediate complexity model of the equatorial Pacific used for ENSO simulations and forecasts. It extends the model of Zebiak and Cane (1987) by considering the shallow-water dynamics of the gravest ocean baroclinic modes. It has been used to study from a modelling approach the relation between the ocean vertical structure characteristics and dynamics and the ENSO variability (e.g. Dewitte, 2000; Dewitte et al., 2007b; Belmadani et al., 2010), as well for ENSO forecasts (Dewitte et al., 2002). In addition, the TD model presented in chapters 4 and 5 can be seen as a reduced version of LODCA.

General elements on the various components of LODCA have already been introduced in previous chapters. LODCA is an anomaly model with a prescribed mean state climatology. It considers the evolution

of the three gravest baroclinic modes of a continuously stratified ocean, while the contribution of higher baroclinic modes is embedded in the form of mixed-layer shear currents (Blumenthal and Cane, 1989). As in the TD model, the baroclinic structure is constant over the equatorial Pacific, though the possibility to account for zonal stratification changes has been discussed in Dewitte et al. (1999) (see also Keenlyside and Kleeman, 2002). The LODCA model uses an explicit Euler scheme to compute the evolution over time of shallow-water ocean dynamics, which is permitted by a separation of eastward and westward propagating components (Cane and Patton, 1984). The atmospheric component is alternatively a Gill model (Gill, 1980) or a statistical atmosphere. As in Hirst (1986), a bulk formula is considered that relates wind stress anomalies to wind velocity in surface. The mixed-layer thermodynamics component is similar to the one from the model of Zebiak and Cane (1987), though LODCA uses a different parametrization of the thermocline feedback (Dewitte and Perigaud, 1996). Most thermodynamic processes are retained, and associated mean state parameters have an annual component. This permits notably to produce a mechanism of phase-locking to the seasonal cycle in LODCA, with El Niño/La Niña events peaking around December (Jin et al., 1994; Tziperman et al. 1994).

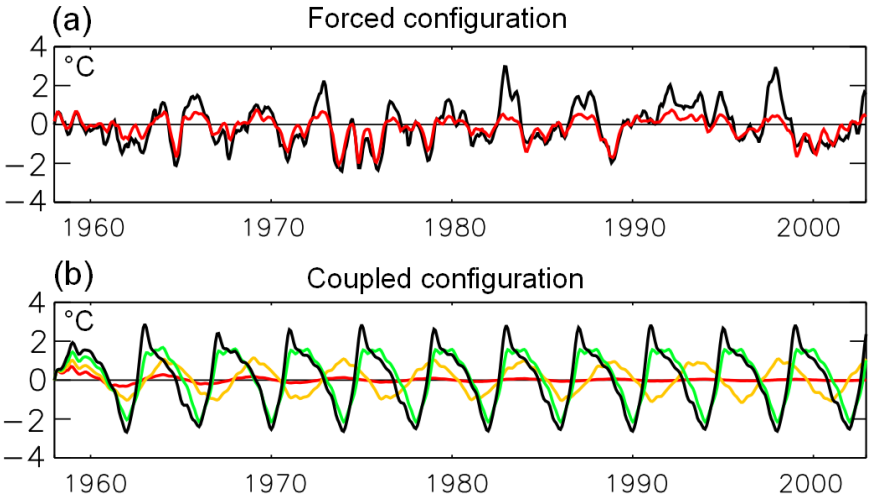

Figure 6.2: (a) Timeseries of Niño3-SST (black, °C) and Niño4-SST (red, °C) as simulated by the model in forced configuration. (b) Timeseries of Niño3-SST (°C) as simulated by the model in coupled configuration, for increasing values of the ocean-atmosphere coupling: 70% (red), 80% (yellow), 90% (green) and 100% (black) of its reference value.

LODCA can be run either in forced, nudged or coupled configuration. Figure 6.2 shows simulated SST anomalies in the forced and coupled configuration. In the forced configuration, observed wind stresses force the ocean component of the model. With this forcing alone, the model simulates an interannual variability that is close to the observed one. In the coupled configuration, the model evolves from an initial condition with no external forcing, and wind stresses are simulated by the atmospheric component. The nudged configuration is an intermediate case, where wind stresses are nudged between values from external forcings and values simulated by the atmospheric component. The nudging coefficient varies from the equator to higher latitudes (Dewitte et al. 2002), with an opposite latitudinal rate of change as compared to

Chen et al. (1997). ENSO forecasts are initialized in forced or nudged configuration, and ran in coupled configuration (Dewitte et al., 2002).

From Figure 6.2.b, we may hint the linear stability of LODCA in the coupled configuration. Visually, it appears that the LODCA model simulates a dominant ENSO eigenmode oscillating at a period of around 4 years. For a small value of the ocean-atmosphere coupling (orange), this ENSO mode is damped. For an increased value (black), the ENSO mode should become unstable, but anomalies have nevertheless a limited growth (to around 3°C), which results in a maintained (but non-sinusoidal) oscillation. We attribute this behaviour to the main model nonlinearity that is in the formulation of the thermocline feedback (Dewitte and Perigaud, 1996). The evolution of the field of SST anomalies T can be sketched as:

$$\partial_t T = F^D T + F^T \tanh\left(\frac{h - h_0}{\Delta}\right) \qquad (6.14)$$

where F^D is the damping feedback coefficent and F^T the thermocline feedback coefficient (we omit other feedbacks for brievity). h is the field of thermocline depth anomalies, and h_0 and Δ are reference values. Although the thermocline feedback (in tanh) is non-linear, we may linearise it around three asymptotical values of h in order to hint the model stability. For h near h_0 (tanh(x)~x), the thermocline feedback is proportional to h and the system is linearly unstable and oscillating. This leads to values of h and T increasing over time. For increasing values of h (tanh(x)~constant) and T, the damping feedback eventually overcomes the thermocline feedback in equation (6.14) and the system becomes linearly stable. This leads to values of h and T decreasing over time. The non-sinusoidal oscillation observed in figure 6.2.b is therefore marked by constant transitions from the linearly unstable regime (h and T small) to the linearly stable regime (h and T large). A quantitative stability analysis would be necessary to validate those elements, though it would be more complex to implement in a model of this complexity (Fedorov and Philander, 2001; MacMynowski and Tziperman, 2008).

Part of the student work during the thesis has consisted in implementing the EnKF method in the LODCA model. The constructed assimilation platform is written in Interactive Data Language (IDL). It executes the assimilation step in a fashion similar to Evensen (2003), runs the model LODCA (Fortran 70) and its forecasts. The architecture allows for various configurations (simple, perturbed or corrected runs, ensemble forecasts) and permits to easily modify or add model variables to the background or observation state. It builds on a vast personal IDL toolkit that includes pre-processing and post-processing tools. The platform and LODCA are light enough to be run on a personal laptop (with around one day needed to compute 50 years of ensemble simulation and 12 month forecasts, with 100 model realisations). An initial plateform has also been designed that uses the OpenPalm coupler (Buis et al., 2006). The OpenPalm coupler (now open source) is designed at the European Centre for Research and Advanced Training in Scientific Computation (CERFACS, Toulouse), which further provides useful training courses.

6.2.2. Article submitted to Ocean Dynamics

We insert a submitted article that documents certain aspects of the experiment of data assimilation in LODCA (Thual et al., 2012b). The assimilation method is recalled and is the one already described in the previous sections, where the LODCA model is forced by perturbed wind stress forcing and constrained by pseudo-observations of sea level anomalies from the SODA reanalysis over the last 50 years. We further show that the major model constraint is on the so-called Tilt and WWV modes that are associated to the recharge/discharge paradigm (see also chapter 2).

Abstract: A model of intermediate complexity of the equatorial Pacific implemented with an Ensemble Kalman Filter assimilation method is used to initialize retrospective forecasts of the El Niño Southern Oscillation (ENSO) over the period 1958-2007. The model is forced by winds and corrected by sea level pseudo-observations from the SODA reanalysis. We build a specific ensemble of model perturbations from the high-frequency component of atmospheric forcing, believed to be a main source of model errors. With this perturbation method, it is shown that the largest covariance of model errors is on the so-called Tilt and WWV modes of sea level, which are usually associated to the low-order and deterministic recharge/discharge process of the equatorial Pacific controlling ENSO oscillations. The constraint from sea level observations is therefore greatest on those modes, and permits to correct in particular the weak model amplitude of the WWV mode. As a consistency test, an alternative experiment is considered where the model is constrained only from observed sea level indexes quantifying the Tilt and WWV mode amplitudes, leading to a similar predictive skill. Results from this perturbation method suggest a central role on ENSO forecasts of the constraint of the low-order dynamics by the observed sea level.

Constraint of the Recharge/Discharge Process of an Intermediate Complexity Model of the Equatorial Pacific by Sea Level Data Assimilation

Sulian Thual (1), Nadia Ayoub (1) and Boris Dewitte (1)

(1) Laboratoire d'Etude en Géophysique et Océanographie Spatiale, Toulouse, France

Submitted to *Ocean Dynamics*

19/12/2012

Abstract

A model of intermediate complexity of the equatorial Pacific implemented with an Ensemble Kalman Filter assimilation method is used to initialize retrospective forecasts of the El Niño Southern Oscillation (ENSO) over the period 1958-2007. The model is forced by winds and corrected by sea level pseudo-observations from the SODA reanalysis. We build a specific ensemble of model perturbations from the high-frequency component of atmospheric forcing, believed to be a main source of model errors. With this perturbation method, it is shown that the largest covariance of model errors is on the so-called Tilt and WWV modes of sea level, which are usually associated to the low-order and deterministic recharge/discharge process of the equatorial Pacific controlling ENSO oscillations. The constraint from sea level observations is therefore greatest on those modes, and permits to correct in particular the weak model amplitude of the WWV mode. As a consistency test, an alternative experiment is considered where the model is constrained only from observed sea level indexes quantifying the Tilt and WWV mode amplitudes, leading to a similar predictive skill. Results from this perturbation method suggest a central role on ENSO forecasts of the constraint of the low-order dynamics by the observed sea level.

1. Introduction

A hierarchy of models of increasing complexity simulate the interannual variability of the equatorial Pacific with a particular focus on the forecast of the El Niño Southern-Oscillation (hereafter ENSO). Although those models show different levels of complexity, ranging from statistical models to hybrid models as well as fully physical models, they show overall a similar lead time of 6 to 12 months for which ENSO is predictable. This relatively important lead time is due to the deterministic and low-order dynamics of ENSO that is relatively well accounted for in all models, and is however limited due to partly stochastic variability in the equatorial Pacific that leads to an inherent predictability limit for the forecast of ENSO (Latif et al. 1998; Kirtman and Schopf 1998). Despite this inherent predictability limit, the advances in modelling strategies still leads to new improvements in ENSO forecasting (Chen et al. 2004; Chen and Cane 2008).

Main advances in modelling strategies are notably on assimilation methods, where the initialization of ENSO forecasts takes into account uncertainties in both models and available observations (e.g. Bennett et al. 1998; Sun et al. 2002; Zhang et al. 2005 ; Zheng et al. 2007). In the equatorial Pacific the intraseasonal atmospheric variability is partly stochastic (e.g. westerly wind-bursts) and can trigger specific El Niño/La Niña events (Moore and Kleeman 1999; Philander and Fedorov 2003; Kleeman 2008), which makes it a main natural source of model uncertainties. In addition, a large ensemble of observations is available for the correction of ENSO model uncertainties, which comprehends among other observed sea level, sea surface temperature, subsurface heat content, or surface wind stresses in the equatorial Pacific (McPhaden et al. 1998). A main issue for the building of assimilations methods is, however, in the choice of model uncertainties and observations that allow for relevant model corrections.

The low-order nature of ENSO dynamics may orient strategies for the building of assimilation methods. For example, in the equatorial Pacific the two leading statistical modes of covariance of thermocline depth anomalies are of basin scale. They are the so-called “Tilt mode” and the “Warm Water Volume mode” (Clarke 2010), which consist respectively in a zonal tilting and a homogeneous shallowing/deepening of the equatorial thermocline (see Meinen and McPhaden 2000, its figure 1). They have also a similar spatial structure on sea level anomalies due to the reduced gravity effect. In the recharge-discharge theory of Jin (1997), those modes form a lower-order system that illustrates the main oscillating characteristics of ENSO through the coupling to the atmosphere. In addition, the WWV mode, which adjusts slowly to wind stress forcing through meridional Sverdrup transport, is one of the main precursor of El Niño events (Meinen and McPhaden 2000; McPhaden 2012).

In this article, a model of intermediate complexity of the equatorial Pacific (Dewitte 2000) implemented with an Ensemble Kalman Filter assimilation method (Evensen 2003) is used to initialize retrospective ENSO forecasts over the period 1958-2007. The model is forced by winds and constrained by sea level observations from the SODA reanalysis (Carton and Giese 2008). We build specific model uncertainties from the high-frequency component of atmospheric forcing, and assess whether this perturbation method

allows for the correction of the Tilt and WWV mode associated to the equatorial thermocline variability. A main focus is therefore on the correction by sea level observations of the low-order and subsurface dynamics of the model, which is shown to be a main feature of the assimilation method and to be critical for the improvement of ENSO forecasts. The article is organised as follow: Section 2 presents the model, the observations and the assimilation method. Section 3 presents the construction of model uncertainties and the correction of the Tilt and WWV mode. Section 4 is dedicated to forecasting experiments. Section 5 is a discussion followed by concluding remarks.

2. Method

We use the intermediate complexity model of the equatorial Pacific from Dewitte (2000) for ENSO forecasting. In this anomaly model the mean state is prescribed. The ocean dynamics consists in linear and adiabatic shallow water dynamics on an equatorial beta-plane, described by the evolution of the three gravest ocean baroclinic modes (see also McCreary 1981; Keenlyside and Kleeman 2002). The thermodynamics of the ocean mixed-layer are similar to the one in Zebiak and Cane (1987) but uses a different parametrization for subsurface temperature. During the initialization step, the model is forced by observed wind stress anomalies, while during the forecasting step the model simulates wind stress anomalies from sea surface temperature anomalies using a statistical atmosphere. The reader is invited to refer to Dewitte (2000), Dewitte et al. (2002) and Yeh et al. (2001) for more details on the model. Also a reduced version of the model is documented in Thual et al. (2011).

The model is embedded with an Ensemble Kalman Filter (EnKF) assimilation method (Evensen 2003). The EnKF uses a Monte Carlo approach, i.e. an ensemble of model realizations (here $\boldsymbol{N}$=100) to account for model uncertainties. The generation of each model realization is made here from the perturbation of wind stress forcing, and is described in the next section. At a given time step and for one of the N model realizations, the model state is $\boldsymbol{x_b}=(h_1, h_2, h_3, u_1, u_2, u_3,)$ that depends on longitude and latitude, where h_n is the contribution from the baroclinic mode n (n=1, 2, 3) to thermocline depth anomalies (meters), and u_n the contribution to zonal currents anomalies (cm.s^{-1}). Sea level, thermocline depth and zonal current anomalies are reconstructed by summing the contribution of the three gravest baroclinic modes. In particular, for a given model state $\boldsymbol{x^b}$ the simulated sea level anomalies are given by $\mathbf{H}\boldsymbol{x^b}$, where $\mathbf{H}$ is a linear operator (see Dewitte 2000).

The model is corrected using sea level pseudo-observations from the SODA reanalysis over 1958-2007 (Carton and Giese 2008). As compared to regular observations, the SODA reanalysis provides full reconstructed maps of sea level data over the last 50 years, which permits to assess the model predictive skill over a large serie of El Niño/La Niña events. Following Evensen (2003), we consider N realizations of observations $\boldsymbol{y_o}$ that consist of monthly maps of sea level anomalies over the area 120°E-80°W and 20°N-20°S, and that are perturbed to account for observation uncertainties.

The analysis step of the EnKF is done at each month of the model simulation. It corrects each model realization $\boldsymbol{x_b}$ into $\boldsymbol{x_a}$ using $\boldsymbol{y_o}$, which reads

$$\boldsymbol{x}_a = \boldsymbol{x}_b + \mathbf{K}(\boldsymbol{y}_o - \mathbf{H}\boldsymbol{x}_b) \quad (1)$$

$$\mathbf{K} = \mathbf{B}\mathbf{H}^T(\mathbf{H}\mathbf{B}\mathbf{H}^T + \mathbf{R})^{-1} \quad (2)$$

$$\mathbf{B} = E\left([\boldsymbol{x}_b - E(\boldsymbol{x}_b)][\boldsymbol{x}_b - E(\boldsymbol{x}_b)]^T\right), \quad (3)$$

$$\mathbf{R} = E\left([\boldsymbol{y}_o - E(\boldsymbol{y}_o)][\boldsymbol{y}_o - E(\boldsymbol{y}_o)]^T\right), \quad (4)$$

where E denotes an average over the ensemble of realizations. **B** and **R** are respectively covariance matrix of model errors and observations errors. To compute the matrix inversion of equation (2), we follow the method of Evensen (2003) for large observation space.

3. Model uncertainties

We implement a specific perturbation method where model uncertainties arise from the high-frequency atmospheric component of wind stress forcing. Similarly to Kirtman and Schopf (1998), we compute a high-frequency timeserie of wind stress maps, which is obtained by removing the low-pass filtered component of wind stress maps from the SODA reanalysis (>9 months). We suppose that this high-frequency timeserie describes a stochastic process uncorrelated in time. Noteworthy its temporal distribution is nearly Gaussian (not shown). Then, at each month of the simulation of all *N* model realizations, we choose randomly an ensemble of *N* maps among all available maps of the high-frequency timeserie, which perturbs wind stress forcings (this is done posterior to the analyis step). Therefore, for each model realization the low frequency component of wind stress forcing is identical, while the high frequency component is stochastic and uncorrelated in time. In addition, in order to generate observation uncertainties, the monthly observations of sea level are perturbed with a white noise uncorrelated in space (**R** is diagonal), with an uniform variance ε_o chosen at a typical value of 4 cm^2.

We diagnose the nature of model uncertainties that are induced by this perturbation method. We compute the empirical orthogonal functions (EOFs) of the matrix $\mathbf{HBH^T}$ as $\mathbf{HBH^T=UWU^T}$, where **U** is a matrix of eigenvectors and **W** is a diagonal matrix of eigenvalues. Because here **R** is diagonal and uniform with variance ε_o, its projection on the basis of eigenvectors **U** is also a diagonal matrix with values ε_o. Therefore, we can express the gain in observation space, $\mathbf{H}(\boldsymbol{x}_a-\boldsymbol{x}_b)$, as a sum of independent contributions related to the innovation $\boldsymbol{y}_o-\mathbf{H}\boldsymbol{x}_b$, which reads:

$$\mathbf{H}(\boldsymbol{x}_a - \boldsymbol{x}_b) = \sum_{i=1}^{m} \boldsymbol{U}_i g_i \boldsymbol{U}_i^T (\boldsymbol{y}_o - \mathbf{H}\boldsymbol{x}_b) \quad (5)$$

$$\text{with } g_i = W_{ii}/(W_{ii} + \varepsilon_o) \quad (6)$$

where *m* is the dimension of observation space, and $\boldsymbol{U}_i$ is the i^{th} column of **U**. This sets an ensemble of orthogonal directions (or eigenvectors) $\boldsymbol{U}_i$ that correspond to different and independent model gains. Interestingly, the expression of g_i is similar to the one of the analysis step in the scalar case, where the variance of model errors is here replaced by the eigenvalue W_{ii} of matrix **W**. From equations (5-6), we may expect that

the model correction (i.e. gain) is maximal for directions i among which the innovation (i.e. the projection $\boldsymbol{U}_i^{\mathrm{T}}(\boldsymbol{y}_o-\mathbf{H}\boldsymbol{x}_b)$) is maximal, and for which g_i is maximal. Those are mot likely to be the first eigenvectors $\boldsymbol{U}_i$ (i.e. the first Ensemble-EOFs), because g_i is maximal for greatest eigenvalues W_{ii}. See also Stephenson and Doblas Reyes (2000), Echevin et al. (2000) and Auclair et al. (2003) for similar approaches, and note that because here **R** is diagonal and uniform the EOF decomposition is a particular case of Hénaff et al. (2009).

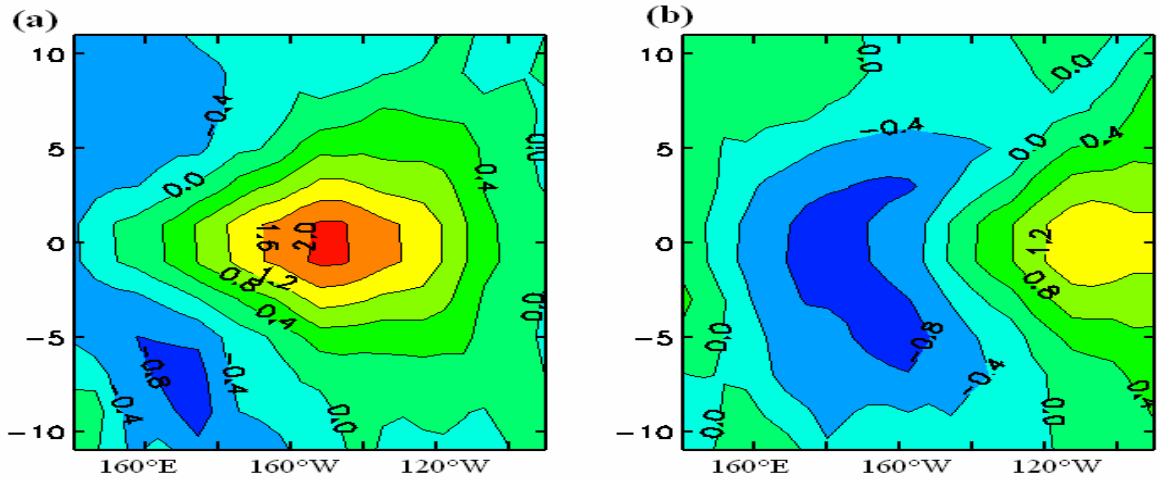

Figure 1: (a) Sea level anomalies from the first eigenvector of $\mathbf{HBH}^{\mathrm{T}}$ (19% var), or WWV-like mode, as a function of longitude and latitude, for the 15th of June 1997. The eigenvector is multiplied by the standard deviation of its associated principal component, such that units are cm. (b) Second eigenvector (12% var), or Tilt-like mode.

Figure 1 shows the first and second eigenvectors of $\mathbf{HBH}^{\mathrm{T}}$, respectively $\boldsymbol{U}_1$ and $\boldsymbol{U}_2$, at date June 1997 (prior to the major El Niño event of December 1997). Interestingly, those patterns of sea level anomalies are similar to the Tilt and WWV mode, which consist respectively in a zonal tilting (figure 1b) and a homogeneous shallowing/deepening (figure 1a) of equatorial sea level (see also Meinen and McPhaden 2000, its figure 1, on thermocline depth anomalies). This is consistent with the fact that the Tilt and WWV modes are leading modes of variability of the equatorial Pacific shallow-water sytem (e.g. as evidenced from linear stability, see Jin 2001 and Clarke 2010), and are therefore most likely to be disturbed by stochastic atmospheric forcing. In addition, because the perturbations from atmospheric high-frequency forcing are uncorrelated in time, and, because the shallow-water system is linear, the matrix $\mathbf{HBH}^{\mathrm{T}}$ is supposed to be constant over time. Indeed, the eigenvectors $\boldsymbol{U}_1$ and $\boldsymbol{U}_2$ show only slight variations over time that arise mostly from issues related to the undersampling of model uncertainties (because the ensemble size is limited) and the separation of $\mathbf{HBH}^{\mathrm{T}}$ into leading EOFs (Monahan et al. 2009).

Figure 2 shows the ensemble-correlation of model state variables with the leading EOFs from figure 1, computed among the ensemble of model realizations. This illustrates main model uncertainties on thermocline depth and zonal currents that are likely to be corrected from the observed sea level. Interestingly, main model uncertainties are spatially similar for the contribution of each baroclinic mode (except in term of amplitude which is not taken into account by the correlation). The spatial structure of the Tilt and WWV modes from figure 1 are retrieved on each baroclinic mode contribution to thermocline depth anomalies, due to the reduced

gravity effect (Dewitte 2000). In addition, uncertainties on the WWV (Tilt) mode are associated to uncertainties on zonal current all over the equator (in the eastern Pacific). This notably shows how the perturbation method permits, from the observed sea level, to correct the subsurface variability of the model. This correction would be impossible e.g. from direct linear interpolation (since **H** is non invertible).

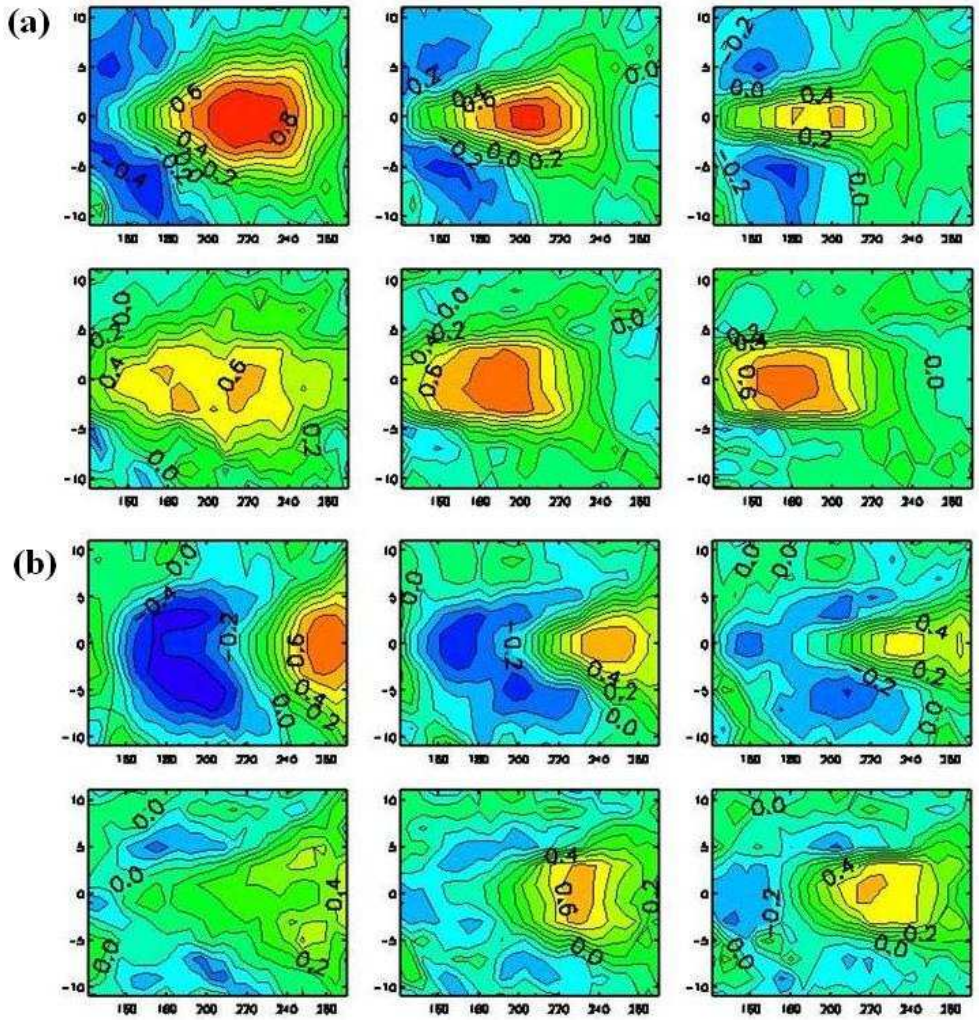

Figure 2: (a) Ensemble-Correlation, as a function of longitude (°E) and latitude (°N), of the first EOF from figure 1a (or WWV-like mode) with various model fields, such as baroclinic contribution to thermocline depth anomalies h_1, h_2, and h_3 (top row, from left to right), and baroclinic contribution to zonal current anomalies u_1, u_2, and u_3 (second row, from left to right). (b) Ensemble-Correlation of the second EOF from figure 1b (or Tilt-like mode), with model fields h_1, h_2, and h_3 (third row, from left to right) and u_1, u_2, and u_3 (bottom row, from left to right)

4. Forecast experiments

As a consistency check of results from the previous section, we perform various experiments of retrospective forecast over the period 1958-2007, namely RUN, EXP1 and EXP2. The experiment RUN is a single model realization without assimilation of sea level observations. The experiment EXP1 is the one described in the previous section, with assimilation of sea level observations. In the experiment EXP2, the

assimilation method is similar but observations from the SODA reanalysis consist only in two observed indexes of sea level, I_{TILT} and I_{WWV} (thus $\boldsymbol{y}_o$, **R** and **H** are different). Those are defined as $I_{TILT}=(I_E-I_W)/2$ and $I_{WWV}=(I_E+I_W)/2$, where I_E and I_W are respectively average of observed sea level anomalies over the Niño3 domain (150°W-90°W,5°N-5°S) and the Niño4 domain (150°E-150°W, 5°N-5°S). Each index is perturbed in order to account for observation uncertainties, with a representative variance ε_o=0.4 cm^2 (which is smaller than in EXP1 because the indexes are integrated quantities). The experiment EXP2 is a simplified setup as compared to EXP1, but is expected to lead to a similar correction of the Tilt and WWV mode in the model.

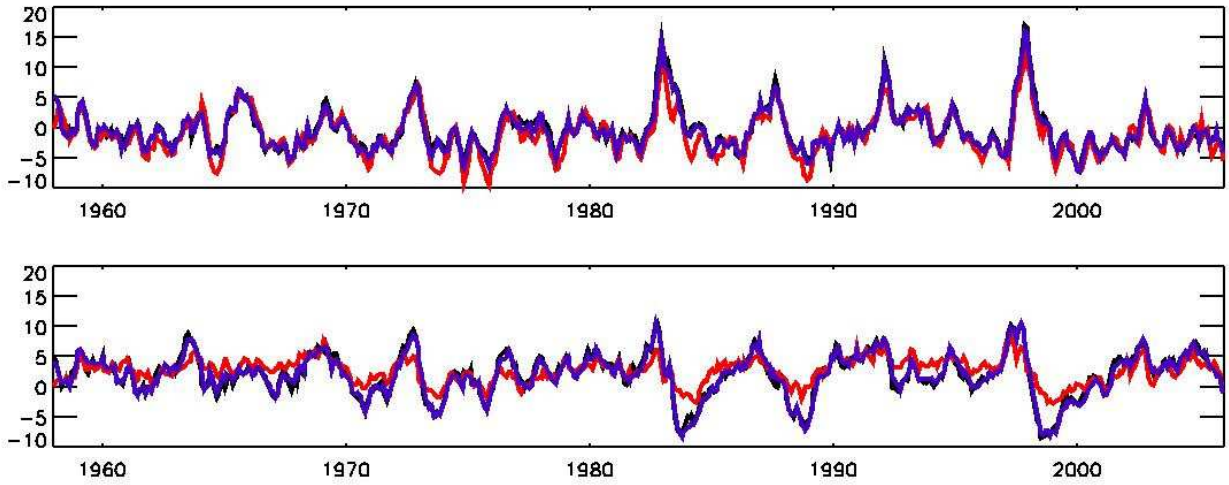

Figure 3: (a) Tilt mode index I_{TILT} of sea level anomalies (cm), as a function of time, as simulated in the experiment RUN (red), the experiment EXP1 (blue), and for observations from the SODA reanalysis (black). (b) Same as (a) for the WWV mode index I_{WWV}.

Figure 3 shows the simulated Tilt and WWV indexes for each experiment. Despite the lack of assimilation, the simulated Tilt mode in the experiment RUN (red, figure 3a) is in good agreement with the one from the SODA reanalysis (black, figure 3a), because in EXP1 the model is forced by observed winds. In EXP1 the model however simulates a WWV mode (red, figure 3b) that is too weak in amplitude as compared to observations (black, figure 3b), mostly during the discharge of equatorial of heat content (Jin 1997) that follows the major El Niño events of 1983, 1987 and 1998. This may arise from the shallow-water ocean component of the model that does not account for certain processes controlling the adjustment of the WWV mode (Clarke 2010; Lengaigne et al. 2011), as well as from its parameterization. In EXP1 (blue), the Tilt and WWV indexes are strongly corrected (cf previous section) and are therefore in strong agreement with observations. This strong agreement is also observed in EXP2 (not shown). Furthermore, in both EXP1 and EXP2 the ensemble dispersions of the Tilt and WWV mode show little variations over time (because **B** remains approximately constant, see previous section). During the analysis step of EXP1 (EXP2), the standard deviation of the Tilt index lowers from 0.63 to 0.28 cm (0.86 to 0.39 cm), while the standard deviation of the WWV index lowers from 0.58 to 0.31 cm (0.74 to 0.53 cm).

From the initialised states of RUN, EXP1 and EXP2, 12 months ensemble forecasts are ran in coupled mode. Figure 4 shows the predictive skill (correlation and RMSE) of each experiment, assessed on the Niño3-

SST index (average of sea surface temperature anomalies in 150°W-90°W, 5°N-5°S). This index is an independent variable as compared to sea level anomalies, though it is strongly correlated with the Tilt index I_{TILT} (c=0.89 in SODA) consistently with the recharge/discharge theory (Jin 1997). The experiment RUN without assimilation (blue) shows a predictive skill that is overall similar to other models of the TOGA era (Latif et al., 1998). Its correlation is better than the persistence of observations (black) for a lead time greater than 5 months, but it RMSE remains however greater. Both EXP1 (red) and EXP2 (green) show a slightly improved predictive skill as compared to RUN (blue), at all lead times. Most interestingly, the predictive skill is very similar in EXP1 and EXP2. We argue that this is because in both experiments there is a strong correction of the Tilt and WWV modes that are leading model uncertainties (cf figure 1). This suggests a central role on ENSO forecasts of the constraint of the low-order dynamics by the observed sea level.

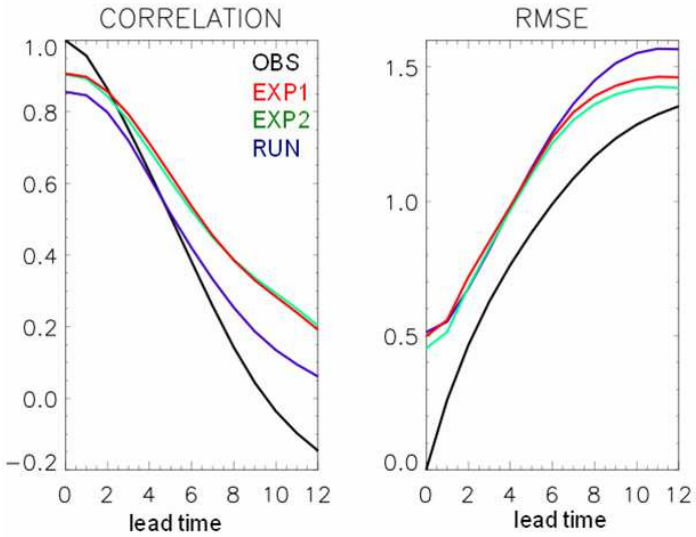

Figure 4: Predictive skill for the Niño3-SST index, over the period 1958-2007, as a function of the lead time (X-axis, in months). (a) Correlation with persistence of observed conditions (black), for the model without correction (blue), EXP1 (red) and EXP2 (green). (b) Same as (a) for Round Mean Square Errors (RMSE) in °C.

4. Discussion

An intermediate complexity model of the equatorial Pacific implemented with an Ensemble Kalman Filter assimilation method has been used to initialise El Niño retrospective forecasts over the period 1958-2007. We have built a specific ensemble of model perturbations from the high-frequency component of atmospheric forcing and quantified model constraint from observed sea level. We show that the major model constraint is on the so-called Tilt and WWV modes that are associated to the low-order and deterministic recharge/discharge process of the equatorial Pacific.

It has been argued in previous studies that in the equatorial Pacific the intraseasonal atmospheric variability (e.g. westerly wind-bursts) is a main source of uncertainties for the forecasting of ENSO events (Moore and Kleeman 1999; Philander and Fedorov 2003; Kleeman 2008). We have built a specific ensemble of model perturbations based on this assumption. From the analysis of the covariance matrix of model

uncertainties (Stephenson and Doblas Reyes 2000; Hénaff et al. 2009), an interesting result here is that such perturbation method leads to leading model uncertainties on the so-called Tilt and WWV modes of sea level anomalies. This is consistent with the fact that the Tilt and WWV modes are leading modes of variability of the equatorial Pacific shallow-water ocean (e.g. as evidenced from linear stability, Jin 2001; Clarke 2010), and are therefore most likely to be disturbed by stochastic atmospheric forcing. In other words, model uncertainties associated to this atmospheric stochastic variability have a low-order nature that is similar to the one of deterministic ENSO dynamics.

The Ensemble Kalman Filter assimilation method (Evensen 2003) implemented here permits the constraint of the model dynamics using observed sea level. Noteworthy, it solves a main issue that is to constraint the subsurface variability (here the contribution of the gravest ocean baroclinic modes) from the observed sea level in surface. Because the model is forced by observed winds, the simulated Tilt mode is quite realistic and requires no further corrections. The simulated WWV mode shows however a weak variability as compared to observations, especially during major El Niño events. This may arise from the shallow-water ocean component of the model that does not account for certain processes controlling the adjustment of the WWV mode (Clarke 2010; Lengaigne et al. 2011), as well as from its parameterization. The assimilation method permits to correct this feature. Based on those results, we have considered various retrospective forecast experiments spanning the period 1958-2007. We have shown in particular that coarse indexes of sea level observations, measuring only the amplitude of the Tilt and WWV mode, lead here to a similar ENSO predictive skill on SST anomalies. This suggests, in agreement with Chen and Cane (2008) and Latif et al. (1998), that the model predictive skill is at first order related to an accurate simulation of the low-order dynamics of ENSO. This also suggests that the most useful information from observed sea level is here the signal at basin scale.

Main conclusions from this article are of course restricted to the setup of the model and assimilation method. The predictive skill of the model is similar to the one of other models from the TOGA era (Latif et al., 1998), but would however benefit from an initialization with a coupled ocean-atmosphere rather than with prescribed atmospheric forcings (Dewitte et al. 2002; Chen et al. 2004). Despite the fact that the model setup and assimilation method may still be improved, conclusions on the leading role of the Tilt and WWV mode constraint are likely to be relevant to other experiments. Within a coupled framework, the atmospheric stochastic variability will rather perturb leading modes of variability that are coupled between the ocean and atmosphere, but which however also have a Tilt and WWV mode structure (Meinen and McPhaden 2000; Kleeman 2008). In addition, we may broaden the observations used for model correction, e.g. to sea surface temperatures or surface wind stresses (Zhang et al. 2005; Zheng et al. 2007). In this framework, the constraint of the recharge/discharge process from sea level observations will still be at work, but will require to consider additional covariance existing between uncertainties in the Tilt and WWV mode and other fields (Zheng and Zhu 2008).

References

Auclair, F., P. Marsaleix, and P. De Mey, 2003: Space-time structure and dynamics of the forecast error in a coastal circulation model of the Gulf of Lions. *Dynamics of Atmospheres and Oceans*, **36**, 309–346, doi:10.1016/S0377-0265(02)00068-4.

Bennett, A. F., B. S. Chua, D. E. Harrison, and M. J. McPhaden, 1998: Generalized Inversion of Tropical Atmosphere–Ocean Data and a Coupled Model of the Tropical Pacific. doi:10.1175/1520-0442(1998)011<1768:GIOTAO>2.0.CO;2. http://ir.library.oregonstate.edu/xmlui/handle/1957/27685 (Accessed May 23, 2012).

Carton, J. A., and B. S. Giese, 2008: A Reanalysis of Ocean Climate Using Simple Ocean Data Assimilation (SODA). *Monthly Weather Review*, **136**, 2999–3017, doi:10.1175/2007MWR1978.1.

Chen, D., and M. A. Cane, 2008: El Niño prediction and predictability. *Journal of Computational Physics*, **227**, 3625–3640, doi:10.1016/j.jcp.2007.05.014.

Chen, D., M. A. Cane, A. Kaplan, S. E. Zebiak, and D. Huang, 2004: Predictability of El Nino over the past 148 years. *Nature*, **428**, 733–736, doi:10.1038/nature02439.

Clarke, A. J., 2010: Analytical Theory for the Quasi-Steady and Low-Frequency Equatorial Ocean Response to Wind Forcing: The "Tilt" and "Warm Water Volume" Modes. *Journal of Physical Oceanography*, **40**, 121–137.

Dewitte, B., 2000: Sensitivity of an Intermediate Ocean–Atmosphere Coupled Model of the Tropical Pacific to Its Oceanic Vertical Structure. *Journal of Climate*, **13**, 2363–2388, doi:10.1175/1520-0442(2000)013<2363:SOAIOA>2.0.CO;2.

Dewitte, B., D. Gushchina, Y. duPenhoat, and S. Lakeev, 2002: On the importance of subsurface variability for ENSO simulation and prediction with intermediate coupled models of the Tropical Pacific: A case study for the 1997–1998 El Niño. *Geophys. Res. Lett.*, **29**, 5 PP., doi:200210.1029/2001GL014452.

Echevin, V., P. De Mey, and G. Evensen, 2000: Horizontal and Vertical Structure of the Representer Functions for Sea Surface Measurements in a Coastal Circulation Model. *Journal of Physical Oceanography*, **30**, 2627–2635, doi:10.1175/1520-0485(2000)030<2627:HAVSOT>2.0.CO;2.

Evensen, G., 2003: The Ensemble Kalman Filter: theoretical formulation and practical implementation. *Ocean Dynamics*, **53**, 343–367, doi:10.1007/s10236-003-0036-9.

Hénaff, M. L., P. D. Mey, and P. Marsaleix, 2009: Assessment of observational networks with the Representer Matrix Spectra method—application to a 3D coastal model of the Bay of Biscay. *Ocean Dynamics*, **59**, 3–20, doi:10.1007/s10236-008-0144-7.

Jin, F.-F., 1997: An Equatorial Ocean Recharge Paradigm for ENSO. Part I: Conceptual Model. *Journal of the Atmospheric Sciences*, **54**, 811–829.

Jin, F.-F., 2001: Low-frequency modes of tropical ocean dynamics. *Journal of climate*, **14**, 3874–3881.

Keenlyside, N., and R. Kleeman, 2002: Annual cycle of equatorial zonal currents in the Pacific. *J. Geophys. Res.*, **107**, 13 PP., doi:200210.1029/2000JC000711.

Kirtman, B. P., and P. S. Schopf, 1998: Decadal Variability in ENSO Predictability and Prediction. *Journal of Climate*, **11**, 2804–2822, doi:10.1175/1520-0442(1998)011<2804:DVIEPA>2.0.CO;2.

Kleeman, R., 2008: Stochastic theories for the irregularity of ENSO. *Philosophical Transactions of the Royal Society A: Mathematical, Physical and Engineering Sciences*, **366**, 2509 –2524.

Latif, M. and Coauthors, 1998: A review of the predictability and prediction of ENSO. *J. Geophys. Res.*, **103**, PP. 14,375–14,393, doi:199810.1029/97JC03413.

Lengaigne, M., U. Hausmann, G. Madec, C. Menkes, J. Vialard, and J. M. Molines, 2011: Mechanisms controlling warm water volume interannual variations in the equatorial Pacific: diabatic versus adiabatic processes. *Climate Dynamics*, doi:10.1007/s00382-011-1051-z.

McCreary, J. P., 1981: A Linear Stratified Ocean Model of the Equatorial Undercurrent. *Philosophical Transactions of the Royal Society of London. Series A, Mathematical and Physical Sciences*, **298**, 603–635.

McPhaden, M. J., 2012: A 21st Century Shift in the Relationship between ENSO SST and Warm Water Volume Anomalies. *Geophys. Res. Lett.*, doi:10.1029/2012GL051826.

McPhaden, M. J. and Coauthors, 1998: The Tropical Ocean-Global Atmosphere observing system: A decade of progress. *Journal of geophysical research*, **103**, 14169–14240.

Meinen, C. S., and M. J. McPhaden, 2000: Observations of Warm Water Volume Changes in the Equatorial Pacific and Their Relationship to El Niño and La Niña. *Journal of Climate*, **13**, 3551–3559.

Monahan, A. H., J. C. Fyfe, M. H. P. Ambaum, D. B. Stephenson, and G. R. North, 2009: Empirical Orthogonal Functions: The Medium is the Message. *Journal of Climate*, **22**, 6501–6514, doi:10.1175/2009JCLI3062.1.

Moore, A. M., and R. Kleeman, 1999: Stochastic Forcing of ENSO by the Intraseasonal Oscillation. *Journal of Climate*, **12**, 1199–1220, doi:10.1175/1520-0442(1999)012<1199:SFOEBT>2.0.CO;2.

Philander, S. G., and A. Fedorov, 2003: Is El Niño sporadic or cyclic? *Annual Review of Earth and Planetary Sciences*, **31**, 579–594.

Stephenson, D. B., and F. J. Doblas Reyes, 2000: Statistical methods for interpreting Monte Carlo ensemble forecasts. *Tellus A*, **52**, 300–322, doi:10.1034/j.1600-0870.2000.d01-5.x.

Sun, C., Z. Hao, M. Ghil, and J. D. Neelin, 2002: Data Assimilation for a Coupled Ocean–Atmosphere Model. Part I: Sequential State Estimation. *Monthly Weather Review*, **130**, 1073–1099, doi:10.1175/1520-0493(2002)130<1073:DAFACO>2.0.CO;2.

Thual, S., B. Dewitte, S.-I. An, and N. Ayoub, 2011: Sensitivity of ENSO to Stratification in a Recharge–Discharge Conceptual Model. *Journal of Climate*, **24**, 4332–4349.

Yeh, S., B. Dewitte, J. Jhun, and I. Kang, 2001: The characteristic oscillation induced by coupled processes between oceanic vertical modes and atmospheric modes in the tropical Pacific. *Geophys. Res. Lett.*, **28**, PP. 2847–2850, doi:200110.1029/2001GL012854.

Zebiak, S. E., and M. A. Cane, 1987: A model El Niño-Southern Oscillation. *Monthly weather review*, **115**, 2262–2278.

Zhang, R.-H., S. E. Zebiak, R. Kleeman, and N. Keenlyside, 2005: Retrospective El Niño Forecasts Using an Improved Intermediate Coupled Model. *Monthly Weather Review*, **133**, 2777–2802, doi:10.1175/MWR3000.1.

Zheng, F., and J. Zhu, 2008: Balanced multivariate model errors of an intermediate coupled model for ensemble Kalman filter data assimilation. *J. Geophys. Res.*, **113**, 16 PP., doi:200810.1029/2007JC004621.

Zheng, F., J. Zhu, and R.-H. Zhang, 2007: Impact of altimetry data on ENSO ensemble initializations and predictions. *Geophys. Res. Lett.*, **34**, 5 PP., doi:200710.1029/2007GL030451.

6.2.3. Supplementary Materials

We present supplementary materials to the submitted article proposed in this chapter. In appendix 5, we implement a parameter estimation method, where the model state is augmented such that parameters of the baroclinic structure can be estimated.

Figure 6.3 illustrates the construction of wind stress forcing perturbations. On interannual timescales, the atmospheric variability can be considered in approximate equilibrium with SST. On shorter timescales, however, the intense moist convection over the Warm Pool creates various atmospheric disturbances (e.g. westerly wind bursts, cf. Harrison and Vecchi, 1997) that may trigger ENSO events by destabilising slower modes of the equatorial Pacific coupled system. This high-frequency variability may be considered as a source of model uncertainty in LODCA, because it is partly stochastic and also because it is not accounted for by the model physics. Figure 6.3.a shows the high-frequency timeserie that is used to construct perturbation maps (of zonal and meridional wind stress anomalies) in the EnKF method. It is computed from SODA by removing the low-pass filtered component (>9 months) of the total signal. Noteworthy, figure 6.3.b shows that its temporal distribution is nearly Gaussian.

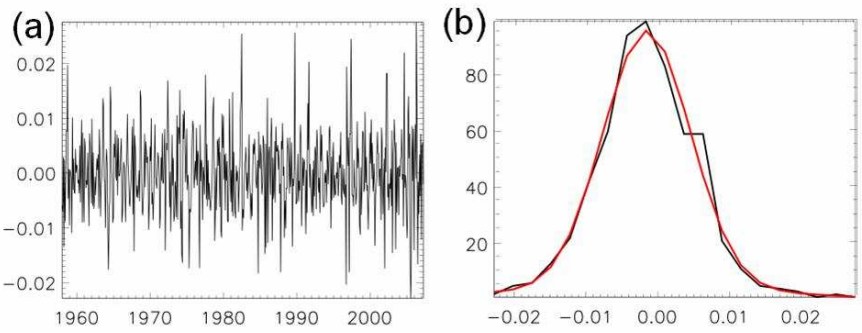

Figure 6.3**:** (a) High-frequency timeserie of zonal wind stress forcing ($N.m^{-2}$) averaged in the Niño4 domain (150°E-150°W, 5°N-5°S). (b) Corresponding histogram (20 steps) with fit of a Gaussian profile (red).

Figure 6.4 shows an ensemble run of LODCA whith perturbed wind stress forcings. The perturbation method leads to an ensemble dispersion that is almost constant over time, and that has a standard deviation of around 1°C for SST anomalies and 10m for thermocline depth anomalies. For strong SST anomalies the ensemble dispersion is however reduced (i.e. collapses), as seen for example during the El Niño events of 1982/83 and 1997/98. This is due to the formulation of the thermocline feedback in tanh that limits the growth of SST anomalies for strong values of thermocline depth anomalies (cf. section 6.2.1).

Another source of uncertainty that has not been considered here is that, because the equatorial Pacific system is partly nonlinear, dominant modes of variability may interact to generate a chaotic behaviour (Philander and Fedorov, 2003; Kleeman, 2008; Timmermann and Jin, 2008). In that case, the interannual variability may become very sensititive to initial conditions, thus limiting ENSO predictability. One interaction of this kind that has been given greatest focus is between the interannual modes of variability

and the annual cycle (Jin et al., 1994; Tziperman et al. 1994; Stein et al., 2011). This kind of interaction is however not observed in the LODCA model, which is only weakly non-linear and does not generate a chaotic behaviour.

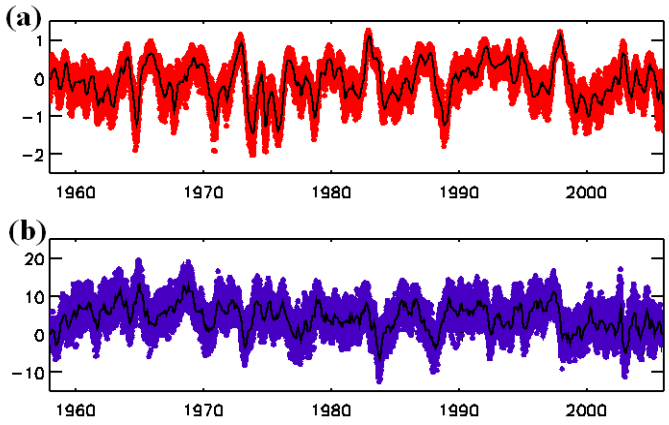

Figure 6.4: (a) Ensemble of model realizations (red) and ensemble mean (black) of Niño3 SSTA index (°C), for the model LODCA forced by perturbed winds. (b) Ensemble of model realizations (blue) and ensemble mean (black) of thermocline depth anomalies (m, average 150°E-90°W and 5°N-5°S).

We further illustrate the constraint of the model dynamics by the assimilation of sea level data in figure 6.5. Figure 6.5.a-c shows hovmullers of sea level anomalies for the experiment RUN, EXP1, and observations from the SODA reanalysis. The assimilation method improves in particular the representation on sea level anomalies during strong El Niño events such as the ones of 1983, 1987 and 1998. Those events are characterized by a strong zonal tilting at the peak phase (i.e. on the Tilt mode) and are followed by a basin-wide shallowing (i.e. on the WWV mode) in agreement with the recharge-discharge theory (Jin, 1997a). The model ensemble dispersion on sea level anomalies shows weak variations over time (cf. previous article), and shows furthermore weak variations over longitude (not shown). Its standard deviation decreases from 1.2 cm to 0.7 cm during the analysis step.

Figure 6.5.d-f shows the model constraint on integrated indexes of ocean variables that are independent from the sea level, such as sea surface temperatures (SST), thermocline depth (H) and zonal currents (U). As compared to the model without assimilation (blue), the model with assimilation (red) shows improvements that are weak on sea surface temperature and zonal currents. Those are indeed already well simulated by the model without assimilation that is forced by observed wind stresses from the SODA reanalysis. The model without assimilation however simulates a weak variability of the heat content (i.e. Warm Water Volume) as compared to observations (figure 6.5.e). The assimilation method permits to correct this feature. Note that the enhanced heat content variability leads to a slight overestimation of SST anomalies, especially during strong La Niña events (not shown). We may overcome this issue by constraining the model SST anomalies as well or by tuning parameters controlling the efficiency of the thermocline feedback (cf. chapter 4), in order to set an appropriate ratio between heat content and SST anomalies.

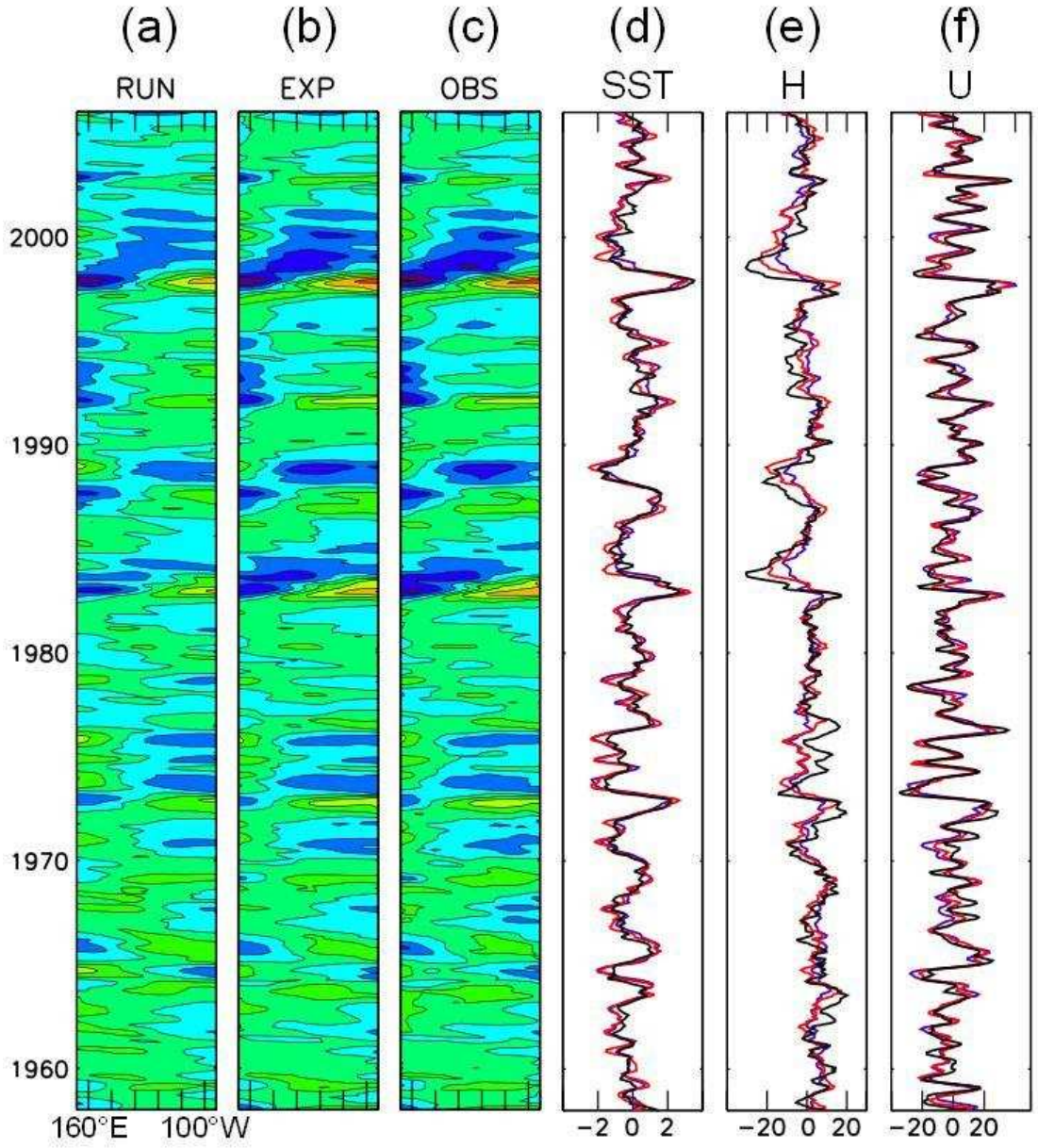

Figure 6.5: Hovmoller diagram of SLA (cm), as a function of longitude and time over the period 1958-2006. Results are shown for (a) the model run without assimilation RUN, (b) the ensemble average of model runs with assimilation EXP1, and (c) observations from the SODA reanalysis. Contours increase by 3°C, and from green to blue values become positive. Timeseries of (d) Niño3-SST anomalies (°C), (e) WWV anomalies (m, average 150°E-90°W), and (f) Niño-4 zonal current anomalies ($cm.s^{-1}$). Results are shown for the model run without assimilation (blue), the ensemble average of model runs with assimilation (red), and the SODA reanalysis (black).

Chapter

7. Conclusions and Perspectives

Version Francaise

Dans cette thèse nous avons abordé plusieurs thématique liées aux mécanismes, à la modulation et la prévision de l'Oscillation Australe El Niño (ENSO), sur la base d'une hiérarchie de modèles de complexité croissante, allant des modèles conceptuels à une méthode d'assimilation de données dans un modèle de complexité intermédiaire déjà existant. Afin de résumer les objectifs de notre démarche durant ces trois années de thèse, nous pouvons citer par exemple le leitmotiv de l'équipe de recherche de D. Neelin à UCLA : construire une hiérarchie de modèles de complexité toujours décroissante, ju*squ'à ce que l*e phénomène ait été distillé en ses éléments essentiels. Notre travail fournit un formalisme pour diagnostiquer la modulation des caractéristiques d'ENSO dans les observations, les prévisions et projections climatiques. Les résultats soutiennent la nécessité d'étendre la compréhension des mécanismes d'ENSO, afin de rendre compte de la diversité des régimes observés et d'améliorer les prévisions. En perspective pour des travaux futurs, nous pourrions également étendre notre formalisme pour étudier d'autres éléments essentiels du cycle ENSO tels que son irrégularité, son interaction avec le cycle saisonnier et ses non-linéarités.

Les thématiques suivantes ont étés abordées, que nous présentons par ordre d'apparence dans le manuscrit :

- Ch.2 : Le processus de recharge-décharge dans l'océan Pacifique équatorial.
- Ch.3 : Le rôle du couplage océan-atmosphère dans la formation d'ENSO.
- Ch.4 : La sensibilité d'ENSO à la stratification océanique.
- Ch.5 : Le rôle de l'état moyen sur la modulation décennale d'ENSO.
- Ch.6 : L'assimilation de données altimétriques dans les modèles d'ENSO.

Chapitre 2 : Dans les théories majeures d'ENSO, l'ajustement de l'océan équatorial à échelle de bassin permet l'oscillation entre phases El Niño et La Niña (Jin, 1997a). Cet ajustement consiste notamment en une évolution du contenu thermique équatorial (Warm Water Volume), qui intègre à échelle interannuelle la propagation et la réflexion des ondes océaniques équatoriales. Il a été décrit dans plusieurs études avec des degrés de complexité différents (e.g. Jin ,1997a; Clarke, 2010; Fedorov, 2010). Nous avons dérivé un modèle d'évolution du WWV (TW model) en nous appuyant sur ces études (Thual et al., 2012d). Les solutions décrivent de manière synthétique l'ajustement océanique à échelle de bassin, à travers l'évolution

d'un mode de Tilt (i.e. inclinaison zonale de la thermocline équatoriale) et d'un mode de WWV (i.e. approfondissement/soulèvement homogène de la thermocline équatoriale). Par rapport aux études précédentes, ces solutions simples sont obtenues avec un minimum d'approximations, telles qu'une projection de la dynamique sur les ondes équatoriales et une approximation des basses fréquences. Le formalisme simple de ce modèle pourrait être étendu et utilisé pour des applications pratiques. Nous avons également fourni un formalisme qui permet d'estimer, additionellement à l'ajustement de l'océan à échelle de bassin, le bilan d'énergie associé (Brown et Fedorov, 2010). Ce formalisme diffère des études précédentes car il considère les premiers modes baroclines d'un océan continûment stratifié. Nous suggérons pour une perspective de travaux futurs que ce bilan d'énergie pourrait également se révéler un outil intéressant pour interpréter la variabilité des modes baroclines de l'océan.

Chapitre 3 : L'interaction océan/atmosphere dans le Pacifique équatorial est un élément essentiel de la dynamique ENSO. Le formalisme des instabilités couplées a reçu une grande attention pour comprendre une telle interaction, car il permet d'identifier les échelles et processus dominants qui y sont associés (Neelin et al., 1998). Nous avons implémenté un diagnostic original (Huerre et Monkewitz, 1990) qui détermine par ailleurs la nature absolue ou convective des instabilités couplées. Nous avons montré dans un modèle couplé en milieu infini (AC model) que, pour un état moyen représentatif, les processus de thermocline induisent une instabilité absolue tandis que les processus d'advection zonale induisent une instabilité convective (Thual et al., 2012a). La troncature méridionale adaptée du modèle couplé que nous avons dérivé pourrait également être intéressante pour des utilisations pédagogiques, car elle permet de décrire les instabilités couplées avec un jeu réduit de variables. Le diagnostic d'instabilité absolue/convective permet de discuter le rôle de la variabilité stochastique de l'atmosphère et le rôle des réflexions aux frontières dans la formation d'ENSO, qui sont toujours en partie méconnus (e.g. Weisberg and Wang, 1997). Pour le régime absolument instable, une oscillation maintenue de type ENSO peut se développer dans le Pacifique équatorial sans impliquer de réflexions aux frontières, tandis que pour le régime convectivement instable les réflexions aux frontières sont essentielles. La possibilité qu'ENSO se développe sans impliquer de réflexions aux frontières devrait être explorée plus en détails, car elle est en contradiction avec les théories courantes. Nous pourrions implémenter le diagnostic en retenant des processus supplémentaires qui contrôlent la variabilité interannuelle du Pacifique équatorial (e.g. Wang et Xie, 1998). Par ailleurs, nous suggérons que perturber les réflexions aux frontières dans les modèles ENSO serait un sujet de grand intêret pour des travaux futurs, en raison des incertitudes importantes qui sont usuellement attribuées à ces réflexions (Boulanger et Menkes, 1995), et parce que ceci pourrait mettre en évidence une variabilité simulée qui serait qualitativement différente (e.g. de type absolument instable). Une application spécifique serait par exemple de perturber les réflexions aux frontières au cours du temps, afin de filtrer les instabilitées couplées qui dépendent fortement de réflexions aux frontières constantes.

Chapitre 4 : La dynamique du cycle ENSO est sensible aux caractéristiques de la stratification océanique dans le Pacifique équatorial. Cette sensibilité est intéressante à comprendre pour appréhender les

changements de dynamique d'ENSO dans un contexte de réchauffement climatique global, pour lequel les projections des modèles montrent une augmentation significative de la stratification océanique dans le Pacifique équatorial (Timmermann et al., 1999; An et al., 2008; DiNezio et al., 2009). La stratification océanique moyenne modifie en particulier la projection du forçage en vent sur les premiers modes baroclines de l'océan, et ainsi leurs contributions à la dynamique océanique (Dewitte et al., 1999; Dewitte, 2000; Yeh et al., 2001). Nous avons traité ce sujet dans un cadre conceptuel, où nous avons construit un modèle réduit couplé (TD model) qui retient la dynamique essentielle d'ENSO et prend en compte les premiers modes baroclines d'un océan continûment stratifié (Thual et al., 2011). A notre connaissance le TD model est le premier modèle qui détermine par une approche conceptuelle le rôle de la structure barocline océanique sur ENSO. L'espace des solutions du modèle a été exploré, indiquant un contrôle de la stabilité d'ENSO par les caractéristiques de la thermocline équatoriale. Nous avons montré en particulier qu'une stratification plus marquée (i.e. une augmentation de la contribution du second et troisième mode barocline) induit un régime ENSO plus instable et à plus basse fréquence. Ces résultats remettent en question les études de sensibilité qui ont consideré jusqu'ici la profondeur de thermocline équatoriale comme un paramètre influent sur la stabilité (e.g. Fedorov et Philander, 2001, leur figure 4). Dans ces études, une thermocline moins profonde induit un régime ENSO plus stable et à plus haute fréquence. Nous montrons ici que cette sensibilité peut s'avérer plus complexe, voire inverse : de manière générale une thermocline moins profonde est aussi associée à une augmentation de la stratification. Ceci peut induire, par le processus proposé précédemment, un régime ENSO qui est au contraire plus instable et à plus basse fréquence. Notre formalisme n'est pas forcément plus véridique, mais la divergence entre résultats suggère qu'il est nécéssaire de mieux prendre en compte les caractéristiques de la thermocline équatoriale. Ceci est aussi valable pour la rétroaction de thermocline sur les anomalies de SST. Nous avons mis en évidence certaines limitations provenant de l'estimation statistique de cette rétroaction (Zelle et al. 2004), qui peut s'avérer inappropriée dans le Pacifique central. Ces résultats appellent à une estimation différente de la retroaction de thermocline, notamment dans le Pacifique central, qui devrait être basée sur davantage de considérations dynamiques. Ces résultats préliminaires ont été reconsidérés et étendus dans un article que nous avons publié récemment (Dewitte et al., 2012).

Chapitre 5 : Le cycle ENSO montre une modulation décennale de ses caractéristiques qui est reliée en partie aux changements des rétroactions de l'état moyen du Pacifique équatorial (An et Jin, 2001; Fedorov et Philander, 2001). Plusieurs diagnostics permettent, dans un cadre linéaire, d'étudier cette relation (Jin et al., 2006). Ces diagnostics peuvent s'appliquer par exemple dans les observations, les réanalyses ou les projections climatiques. Ils permettent de comprendre comment l'état moyen module en partie la variabilité ENSO sur des échelles de temps décennales (An et Wang, 2000; An et Jin, 2000). Par ailleurs, il reste encore à déterminer les rétroactions qui seront les plus influentes pour le changement climatique à venir, afin de pouvoir se prononcer sur une amplification ou une réduction de l'activité ENSO (Collins et al., 2010). Nous avons utilisé un modèle réduit couplé (le TD model) pour diagnostiquer les rétroactions de l'état moyen et la stabilité ENSO associée au cours des dernières décennies. Nous avons montré que, pendant le shift

climatique de années 1970, la stratification moyenne de l'océan a inféré des changements de stabilité d'ENSO comparables en termes de magnitude aux changements inférés par les rétroactions atmosphériques et thermodynamiques (Thual et al., 2012c). Il serait toutefois nécéssaire de simplifier la représentation de certaines rétroactions de l'état moyen dans le TD model, qui est à l'heure actuelle encore complexe pour permettre un diagnostic entièrement robuste et reproductible. Nous avons également documenté la sensibilité à l'état moyen des évènements El Niño de type Pacifique Central (Ashok et al., 2007; Yeh et al., 2009), dans une simulation préindustrielle d'un CGCM (Kug et al. 2010b; Choi et al., 2010). Le TD model simule des changements de stabilité du mode associé aux évènements de type Pacifique Est, mais ne simule pas de mode dominant associé aux évènements de type Pacifique Central. Les mécanismes de ce dernier type d'évènement restent encore à être clairement identifiés. Les résultats de ce chapitre complémentent également un article que nous avons publié récemment, qui documente la variabilité des modes baroclines pendant les évènements CP (Dewitte et al., 2011).

Chapitre 6 : La simulation et la prévision d'ENSO sont des sujets de grand intérêt, pour lequels les méthodes d'assimilation qui prennent en compte les incertitudes des modèles et des observations peuvent fournir des améliorations significatives (Chen et Cane, 2008). Nous avons construit et implémenté un Filtre de Kalman d'Ensemble (Evensen, 2003) dans un modèle intermédiaire du Pacifique équatorial déjà existant (LODCA model, Dewitte, 2000). En nous basant sur certaines considérations théoriques (e.g. Kleeman, 2008), nous avons supposé que la variabilité atmosphérique aléatoire était la principale source d'incertitude dans le modèle (Thual et al., 2012b). Le modèle a été forcé par des vents perturbés et contraint par des réanalyses de niveaux de la mer, afin d'initialiser des prévisions rétrospectives sur les cinquante dernières années. Dans la continuité des autres chapitres, nous avons déterminé les apports de la méthode d'assimilation sur la dynamique réduite d'ENSO qui est simulée par le modèle. Nous avons montré que la contrainte majeure du modèle porte sur les modes de Tilt et de WWV qui sont associés au paradigme de recharge/décharge (Jin, 1997a; Meinen et McPhaden, 2000). La méthode d'assimilation permet de contraindre en particulier le contenu thermique équatorial (WWV) dont la variabilité est trop faible dans le modèle. L'implémentation de la méthode de Filtre de Kalman d'Ensemble dans le modèle de complexité intermédiaire est également un développement technique qui pourrait s'avérer utile pour des applications futures de simulation et de prévision d'ENSO. Une perspective intéressante serait l'initialisation du modèle en configuration couplée (Chen et Cane, 2008).

English Version

In this thesis we have assessed various topics related to the mechanisms, the modulation and the forecast of the El Niño Southern Oscillation (ENSO), on the basis of hierarchy of models of increasing complexity, from conceptual models to a data assimilation method in an already existing intermediate complexity model. To summarize the objectives of our approach during those three years of thesis, we may quote for example the leitmotiv from the research team of D. Neelin at UCLA: building a hierarchy of models of successively less complexity, until the phenomenon has been distilled down to it's essential elements. Our work provides a formalism to diagnose the modulation of ENSO characteristics in observations, climate projections and forecasts. Results support the need to extent the understanding of ENSO mechanisms, in order to account for the diversity of observed regimes and to improve forecasts. As a perspective for future work, we could also extend our formalism to other essential features of the ENSO cycle such as its irregularity, its interaction with the seasonal cycle and its non-linearities.

The following topics have been treated, which we present in order of appearance in the manuscript :

- Ch.2: The recharge-discharge process in the Pacific equatorial ocean.
- Ch.3: The role of the ocean-atmosphere coupling on ENSO formation.
- Ch.4: The sensitivity of ENSO to ocean stratification.
- Ch.5: The role of the mean state on the decadal modulation of ENSO.
- Ch.6: The assimilation of altimetric data in ENSO models.

Chapter 2: In major ENSO theories, the adjustment of the equatorial ocean at basin scale permits the oscillation between phases of El Niño and La Niña (Jin, 1997a). This adjustment consists notably in an evolution of the equatorial heat content (Warm Water Volume), which integrates at interannual timescale the propagation and reflection of ocean equatorial waves. It has been described in various studies with different degrees of complexity (e.g. Jin ,1997a; Clarke, 2010; Fedorov, 2010). We have derived a model for the evolution of the WWV (TW model) based on those studies (Thual et al., 2012d). Solutions describe synthetically the ocean adjustment at basin scale, through the evolution of a Tilt mode (i.e. zonal tilting of the equatorial thermocline) and a WWV mode (i.e. homogeneous deepening/shallowing of the equatorial thermocline). As compared to previous studies, those simple solutions are obtained with a minimum of approximations, such as a projection of the ocean dynamics on equatorial waves and a low-frequency approximation. The simple formulation of this model might be extended and used for practical applications. We have also provided a formalism that permits to estimate, additionally to the ocean adjustment at basin scale, its associated energy budget (Brown and Fedorov, 2010). This formalism differs from previous studies because it considers the first baroclinic modes of a continuously stratified ocean. We hint as a perspective for future work that this energy budget might also prove to be a useful tool to interpret the variability of ocean baroclinic modes.

Chapter 3: The ocean/atmosphere interaction in the equatorial Pacific is an essential feature of ENSO dynamics. The formalism of coupled instabilities has been given great focus to understand such interaction, because it permits to identify the leading scales and processes associated to it (Neelin et al., 1998). We have implemented an original diagnostic (Huerre and Monkewitz, 1990) that further assesses the absolute or convective nature of coupled instabilities. We have shown in a coupled model in the infinite domain (AC model) that, for a representative mean state, thermocline processes lead to an absolute instability while zonal advective processes lead to a convective instability (Thual et al., 2012a). The adapted meridional truncation of the coupled model that we have derived might also be interesting for pedagogic uses, because it permits to describe coupled instabilities with a reduced set of variables. The diagnostic of absolute/convective instability permits to discuss the role of atmospheric stochastic variability and the role of boundary reflections in the formation of ENSO, which are still partly unknown (e.g. Weisberg and Wang, 1997). For the absolutely unstable regime, a standing ENSO-like oscillation can develop in the equatorial Pacific without involving boundary reflections, while for the convectively unstable regime boundary reflections are essential. The possibility that ENSO develops without involving boundary reflections has to be further explored, because it is in contradiction with common theories. We may implement the diagnostic when retaining additionnel processes that control the interannual variability of the equatorial Pacific (e.g. Wang and Xie, 1998). Also, we hint that perturbing boundary reflections in ENSO models would be a topic of great interest in future works, due to the strong uncertainty that is usually attributed to these reflections (Boulanger and Menkes, 1995), and because this might evidence a simulated variability that is qualitatively different (e.g. of type absolutely unstable). A specific application would be for example to perturb boundary reflections over time, in order to filter coupled modes that rely strongly on constant boundary reflections.

Chapter 4: The dynamics of the ENSO cycle is sensitive to the characteristics of the ocean stratification over the equatorial Pacific. This sensitivity is interesting to understand in order to apprehend changes in ENSO dynamics in a context of global warming, for which model projections evidence a significant increase in ocean stratification over the equatorial Pacific (Timmermann et al., 1999; An et al., 2008; DiNezio et al., 2009). The background ocean stratification modifies in particular the projection of wind stress forcing onto the gravest ocean baroclinic modes, and as so their contributions to the ocean dynamics. We have treated this topic in a conceptual framework, where we have designed a reduced coupled model (TD model) that retains the essential ENSO dynamics and takes into account the gravest baroclinic modes of a continuously stratified ocean (Thual et al., 2011). To our knowledge the TD model is the first model assessing in a conceptual framework the role of the ocean baroclinic structure on ENSO. The space of model solutions has been explored, revealing a control on ENSO stability by characteristics of the equatorial thermocline. We have shown in particular that an increased stratification (i.e. increased contribution from the second and third baroclinic modes) leads to a more unstable and lower frequency ENSO regime. Those results question sensitivity studies that have considered so far the equatorial thermocline depth as an influent parameter on stability (e.g. Fedorov et Philander, 2001, their figure 4). In those studies, a shallower

thermocline leads to an ENSO regime that is more stable and at higher frequency. We show here that this sensitivity can be more complex, or even inverse: generally speaking, a shallower thermocline is associated to an increase in stratification. This can induce, by the process described previously, an ENSO regime that is on the contrary more unstable at lower frequency. Our formalism is not necessarily more veridic, but the divergence between results suggests that it is necessary to better account for characteristics of the equatorial thermocline. This also holds for the thermocline feedback on SST anomalies. We have stressed certain limitations arising from the statistical estimation of this retroaction (Zelle et al. 2004), which can be misleading in the central Pacific. Those results call for a different estimation of the thermocline feedback, notably in the central Pacific, which would have to be based on more dynamical considerations. Those preliminary results have been reconsidered and extended in an article that we have published recently (Dewitte et al., 2012).

Chapter 5: The ENSO cycle shows a decadal modulation of its characteristics that is related to some extent to changes in the retroactions of the equatorial Pacific mean state (An and Jin, 2001; Fedorov and Philander, 2001). Various diagnostics permit, in a linear framework, to study this relation (Jin et al., 2006). Those diagnostics can be used for example in observations, reanalyses or climate projections. They permit to understand how the mean state may modulates in part the ENSO variability on decadal timescales (An and Wang, 2000; An and Jin, 2000). In addition, there is still at this time the need to determine which feedbacks will be most influent for the future climate change, in order to give an opinion on an amplification or a reduction of the ENSO activity (Collins et al., 2010). We have used a reduced coupled model (the TD model) to diagnose changes in mean state feedbacks and associated ENSO stability over the recent decades. We have shown that, during the climate shift of the 1970s, the background ocean stratification inferred changes in ENSO stability similar in terms of magnitude to the changes inferred by atmospheric and thermodynamic feedbacks (Thual et al., 2012c). It would however be necessary to simplify the representation of certain mean state feedbacks in the TD model, which is at this time still complex to permit a fully robust and reproductible diagnostic. We have also documented the sensitivity to mean state of Central Pacific El Niño events (Ashok et al., 2007; Yeh et al., 2009) in a preindustrial CGCM run (Kug et al. 2010b; Choi et al., 2010). The TD model simulates changes in stability of the mode associated to Eastern Pacific events, but does not simulate a dominant mode associated to Central Pacific events. The mechanisms of the latter type of event still remain to be clearly identified. Results from this chapter also complement an article that we have published recently, which documents baroclinic modes variability during Central Pacific events (Dewitte et al., 2011).

Chapitre 6: The simulation and forecast of ENSO are topics of great interest, for which assimilation methods that account for uncertainties in models and observations can provide significant improvements (Chen and Cane, 2008). We have implemented an Ensemble Kalman Filter method (Evensen, 2003) in an already existing intermediate complexity model of the equatorial Pacific (LODCA model, Dewitte, 2000). Following certain theoretical considerations (e.g. Kleeman, 2008), we have supposed that random atmospheric variability was the main source of model uncertainty (Thual et al., 2012b). The model has been

forced by perturbed winds and constrained by reanalyses of sea level, in order to initialize retrospective forecasts over the last fifty years. In the continuity of the other chapters, we have assessed the improvements from the assimilation method on the low-order ENSO dynamics that is simulated by the model. We have shown that the major model constraint is on the so-called Tilt and WWV modes that are associated to the recharge/discharge paradigm (Jin, 1997a; Meinen and McPhaden, 2000). The assimilation method permits to constrain in particular the equatorial heat content (WWV) whose variability is too weak in the model. The implementation of the Ensemble Kalman Filter method in the intermediate complexity model is also a technical development that might prove useful for future applied ENSO simulations and forecasts. An interesting perspective would be the model intialization in coupled configuration (Chen and Cane, 2008).

Appendix

1. Comparison with a Layered Ocean Model

We discuss differences between the representation of ocean dynamics with a vertical structure that is either continuously stratified (i.e. density changes are continuous) or separated in layers (i.e. density changes are discontinuous) (Clarke, 2008). Both approaches are similar in the sense that they are both a singular value problem that describes ocean dynamics in a set of independent baroclinic modes. Figure A1.1 shows a representation of a shallow water model with two layers of different density (i.e. a single discontinuity at the interface). p_a is atmospheric pressure, ρ_1 and ρ_2 (with $\rho_1<\rho_2$) are upper and lower layer density respectively, $\bar{h}$ is mean thermocline depth, H is bottom depth, η is sea surface anomalies and h is thermocline depth anomalies. This representation can account at first order for vertical movements of the equatorial thermocline (defined at the separation between layers). For this layered model there are two possible motions, a barotropic mode and a single baroclinic mode. At the bottom depth the pressure reads

$$p(H) = p_a + \rho_1 g(\bar{h} + \eta - h) + \rho_2 g(H - \bar{h} + h) \qquad \text{(A1.1)}$$

The barotropic mode is independent of depth, therefore its contribution to pressure reads p_a at the bottom depth. Removing this contribution from equation A1.1, one finds that for the remaining baroclinic mode the sea surface and thermocline interface move in opposition, with $\eta = h(\rho_1 - \rho_2)/\rho_1$. The approach can be extended to the case of an ocean with n layers. A little combinatory gives the number of possible motions, which are different with respect to vertical directions of displacement (either upward or downward) of each of the n layers. For n layers moving in the same direction, one can form $n!/p!(n-p)!$ groups of p layers moving in opposite direction ($p \leq n$), then integration from p=0 to p=n gives 2^{2n} possible motions, from which all symmetrical motions are removed. There are therefore 2^{2n-1} possible motions (i.e. eigenvalues of the problem), which is also the number of baroclinic modes (plus the barotropic mode). The decomposition in a set of n layers is a degenerate case as compared to the baroclinic mode decomposition in the continuously stratified case, in the sense that the infinite set of modes collapses to a finite set of n modes. In this thesis, the term baroclinic structure refers to the continuously stratified case (though we have seen that baroclinic modes are also evidenced in the layered case).

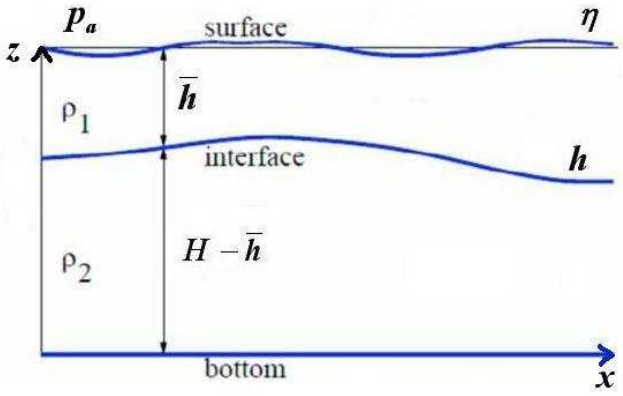

Figure A1.1: Schematics of a shallow-water model with two layers, as a function of longitude x and depth z (see text).

2. Scalar ENSO Model

We take the opportunity to mention the possibility to reduce the TD model (which is a zonal strip model) into a scalar model. A scalar model is coarser yet more synthetic than a strip model, which permits to understand the essential recharge/discharge process that leads to an ENSO oscillation (Jin, 1997a; Burgers, 2005). It may also be more adapted to diagnose ENSO stability and its sensitivity to background conditions in datasets (Jin et al., 2006; Kim and Jin, 2010a; Kim and Jin, 2010b, see discussion of Chapter 5). A limitation is however that because variability is averaged in specific regions of the equatorial Pacific, large differences in spatial patterns of ENSO may not be accounted for (Belmadani et al., 2010).

For the derivation of the scalar ENSO model, we may follow the leading assumptions from Jin (1997a), which proposes a scalar version of the strip model from Jin (1997b). We consider the ocean reduced model from chapter 2, where the thermocline depth adjustment is described by the evolution of the Tilt and WWV modes. The derivation of this ocean reduced model is different from Jin (1997a) because there is no discretisation of the ocean dynamics into a western and eastern box. We consider a thermodynamic equation for the evolution of SST. It is similar to TD2011, but we average SST in the eastern Pacific region (usually Niño3, 150°W-90°W, 5°N-5°S) and retain only the thermocline feedback F_H and damping feedback F_D. Finally, we assume as in Jin (1997a) that SST anomalies in the eastern Pacific region force wind stress anomalies over the entire basin. Without entering into details of the derivation, we can write the scalar model as

$$\partial_t T = F_D T + F_T h \text{, with } h = \sum_n h_{\Pi LTn} + h_{WWVn} \tag{A2.1}$$

$$\text{where } \sum_n h_{\Pi LTn} = \mu_{\Pi LT} T \tag{A2.2}$$

$$\text{and } (\partial_t + \sigma_n) h_{WWVn} = \mu_n T \tag{A2.3}$$

where T is SST anomalies. Thermocline depth anomalies h averaged in the eastern Pacific region results from the summed-contribution of the Tilt mode $h_{\Pi LTn}$ and h_{WWVn} mode on each baroclinic mode n. The Tilt mode adjusts immediately to wind stress forcing, and as so its summed-up contribution can be related to SST anomalies through a coupling coefficient $\mu_{\Pi LT}$. The WWV mode adjustment is different for each baroclinic mode, with dissipation rate σ_n (cf. chapter 2), and is related to SST anomalies through a coupling coefficient μ_n. The scalar model reduces to

$$\partial_t T = (F_D + \mu_{\Pi LT} F_T) T + F_T \sum_n h_{WWVn} \tag{A2.4}$$

$$\partial_t h_{WWVn} = -\sigma_n h_{WWVn} + \mu_n T \tag{A2.5}$$

The model invokes ENSO oscillations through a recharge/discharge process as in Jin (1997a). In the case of a single baroclinic mode (say n= 1), solutions can be found analytically. For the system to oscillate, it

must verify that $\Delta = (F_D + \mu_{\Pi LT} F_T + \sigma_1)^2 - 4F_T\mu_1$ is negative. The roots are therefore $s = (F_D + \mu_{\Pi LT} F_T - \sigma_1)/2 + i\sqrt{\Delta}/2$ and its complex conjugate, which real and imaginary part give respectively the growth rate and frequency of the system. For three baroclinic modes, they are three independent equations for the ocean dynamics.The growth rate and frequency may be computed as the roots of a matrix of dimension 4 by 4. We may alternatively derive independent oscillators for each baroclinic mode and use a perturbation method to represent the coupling between oscillators.

We may also suggest a specific setup of this model, in order to use it as a stability index similar to the one of Jin et al., 2006 (cf. discussion of chapter 5). We may suppose that the sensitivity to the background ocean stratification is critical only for the WWV adjustement. With this view, the damping rate of SST anomalies may be computed following Jin et al. (2006), while the WWV adjustment and its retroaction on SST anomalies may be computed from the contribution of the gravest baroclinic modes. This however implies that the damping rate of WWV anomalies cannot be omitted as is done in Jin et al. (2006). Such setup could be implemented as a perspective for future works.

3. Statistical Relationship between Mean State and Stability

As a last remark on the decadal modulation of ENSO variability, we propose a synthetic diagnostic that relates decadal changes in ENSO feedbacks and characteristics. This linear diagnostic on ENSO stability extends the one from chapter 5 to its limits, and as so remains exploratory: it is here fully assumed that, around a reference state, stability changes depend linearly on parameter changes. The diagnostic is based on a Singular Values Decomposition (SVD, see Bjornsson and Venegas, 1997) between parameter changes and stability changes of the TD model. It consists in first defining the "parameter vector" **P**=(P_1, P_2, P_3, μ_1, μ_2, F_U, F_H, F_W), which temporal evolution is estimated using a 7 years running mean. Using **P** in the TD model we compute frequency (F) and growth rate (G), then we define the "stability vector" **S**=(F,G). Both vectors are expressed in terms of anomaly with respect to their time-averaged value, which each component normalized by its standard deviation. The SVD leads to the modes that maximise the cross-correlation between **S** and **P**.

The diagnostic is applied over the recently available SODA dataset that extends from 1871 to 2008 (Giese and Ray, 2011). The first SVD mode accounts for 90% of cross-correlation. The associated eigenvectors are shown in figure A3.1a. They provide the dominant pattern of stability and parameter changes. Changes are strongly pronounced on the stratification parameters P_2 and P_3, the second atmospheric mode μ_2 and the thermocline feedback F_H. Those parameters are not necessarily most influent on stability when considered individually, but rather the direction of the associated eigenvector. Timeseries associated to the first SVD mode are shown in figure A3.1b. They evidence abrupt changes in mean state conditions and stability after the climate shift of the 1970s and after 2000, in agreement with results from chapter 5. Also, the decadal modulation is quite different before the 1960s, where there is a weak modulation and where both timeseries are in phase. Results may suggest that, before the 1960s, the first SVD mode evidences the internal variability of the ocean model used in SODA, which is only weakly constrained by the few observations available over this period. Those suggestions would however need to be further investigated.

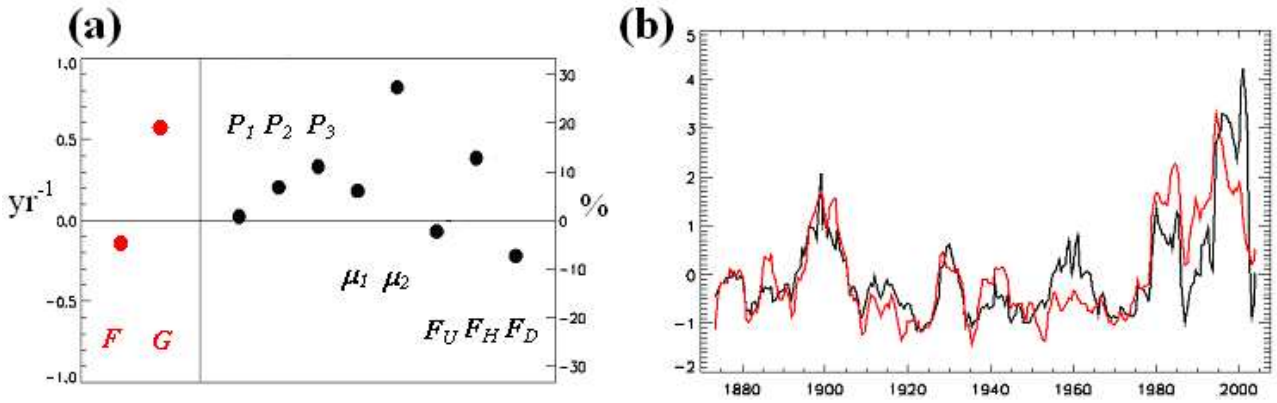

Figure A3.1: (a) Eigenvectors of the first SVD mode (90% cross-correlation) between the "stability vector" S and the "parameter vector" P. Components values of the eigenvectors are displayed in full circles along the X-axis (yr^{-1} for S, % of the reference value over 1870-2008 for P). (b) Normalised timeseries associated to S (red) and P (black).

4. Probabilistic Formulation in the Scalar Case

We reconsider the minimisation problem of chapter 6 with a probabilistic formulation in the scalar case. This formulation is an alternative to the Bayesian formulation that is based on the concept of joint probability. We propose a graphical method to understand how the best estimate is constructed. We search a best estimate x_a of a true state x_t given two estimates x_b and y_o with known uncertainties. This alternative approach is equivalent to finding a best estimate x_a that has minimum error variance, i.e. minimum distance to each estimate according to the cost function J. The model realisation x_b is one realisation of a random variable x, with associated probability density function (pdf) $f_x(x)$. As previously, f_x is Gaussian, centred on x_t and with error variance σ_b^2. The observation realisation y_o is one realisation of a random variable y, with associated pdf $f_y(y)$. f_y is Gaussian, centred on $y_t=Hx_t$ where H is an observation operator and with error variance σ_o^2. We suppose that model and observations errors are uncorrelated, therefore we can construct a joint pdf as $f_{xy}(x, y)= f_x(x)\, f_y(y)$, which reads

$$f_{xy}(x, y) = \frac{1}{2\pi\sigma_b\sigma_o}\exp\left[-\frac{1}{2}\frac{(x-x_t)^2}{\sigma_b^2}-\frac{1}{2}\frac{(y-y_t)^2}{\sigma_o^2}\right] \qquad \text{(A4.1)}$$

The joint pdf is shown in figure A4.1.a. They are only a restricted ensemble of couples of realisations (x, y) that are relevant to our problem. Those are the couples verifying y=Hx, for which model realisation and observation realisation are representative of a same random variable. We define this random variable as z, with associated pdf $f_z(z)=Cf_{xy}(z, Hz)$ that can be deduced graphically in figure A4.1.a over the straight line y=Hx. C is a normalization factor which ensure that the integral of the pdf $f_z(z)$ is equal to one. A realization of the random variable z is the estimate of our problem, which combines estimates from both model and observations (i.e. realisations of x and y). The maximum of f_z is found at $z=x_t$ (with $Hz=y_t$), which is also the maximum of f_{xy}. The pdf f_z is Gaussian, and its variance is as $\sigma_z^2=\sigma_b^2\sigma_o^2/(H^2\sigma_b^2+\sigma_o^2)$.

In practice, the true state x_t (with $y_t=Hx_t$) is however not known, and the random variable z has to be approximated only from given realisations x_b and y_o and from known uncertainties σ_b and σ_o. The joint pdf itself has to be estimated. It reads:

$$f_{xy}^{GUESS}(x, y) = \frac{1}{2\pi\sigma_b\sigma_o}\exp\left(-\frac{1}{2}\frac{(x-x_b)^2}{\sigma_b^2}-\frac{1}{2}\frac{(y-y_o)^2}{\sigma_o^2}\right) \qquad \text{(A4.2)}$$

which supposes that the pdf of x and y are centred on x_b and y_o respectively (rather than on x_t and y_t which are unknown). The approximated joint pdf is shown in figure A4.1.b. The pdf of the random variable z is constructed from the approximated joint pdf, under the constraint that y=Hx, which reads $f_z^{GUESS}(z)=f_{xy}^{GUESS}(z, Hz)$. We define x_a such that for $z=x_a$, f_z^{GUESS} is maximal. x_a is the best estimate (i.e. most probable realisation) of our problem. This is also equivalent to finding the minimum of the cost function J that is found at the exponent of f_z^{GUESS}. The error variance of z (around x_a) is the one of f_z^{GUESS}, which reads

$\sigma_a^2=\sigma_b^2\sigma_o^2/(H^2\sigma_b^2+\sigma_o^2)$. The main message is that in the minimisation problem, because the true state is unknown, the entire probabilistic model (which best realization gives the best estimate) has to be approximated.

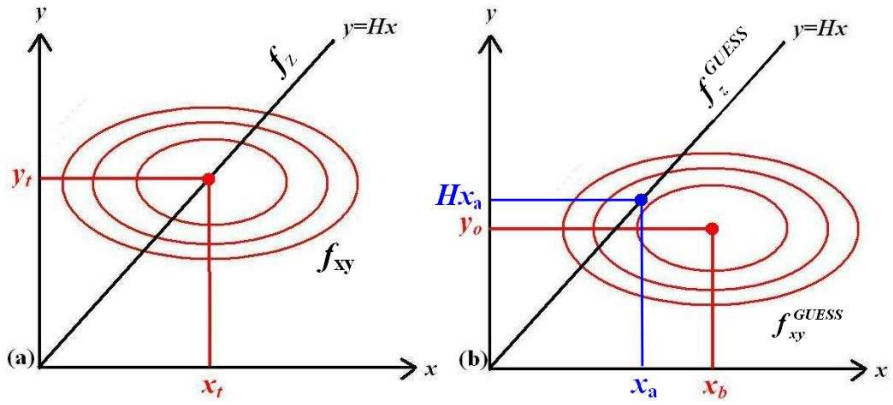

Figure A4.1: (a) Joint pdf $f_{xy}(x,y)$ for Gaussian distribution and straight line $y=Hx$. (b) Construction of the joint pdf $f_{xy}^{GUESS}(x,y)$ from estimates x_b and y_o, straight line $y=Hx$, and best estimate x_a.

5. Estimation of Baroclinic Structure Parameters

We have explored the possibility to correct parameters of the baroclinic structure in the model LODCA. The method remains identical to the EnKF method described in chapter 6. However we use the augmented vector approach (Evensen, 2009; Kondrashov and al., 2008) to additionally correct projection coefficients P_1, P_2 and P_3 of the model LODCA. Those parameters are simply added to the model background state in order to be corrected sequentially, and it is assumed a persistence model for their temporal evolution. Parameters are constantly perturbed considering uncorrelated errors that are proportional for each parameter to 10% of the standard values from Dewitte (2000). Also it is added a constraint on the sum of P_n parameters (supposedly constant), assuming a variance of errors proportional to 5% of the standard value (therefore the parameter $P_1+P_2+P_3$ is added in the model background state). The parameter estimation is shown in figure A5.1. The estimated parameters show an interannual variability, notably on P_2 and P_3. A limitation arising from this approach is that the small ensemble (N=100 members) does not permit the experience to be reproducible. In fact, when running the corrected run with a different random generation of uncertainties the variability of parameters is different (i.e. the sequential estimation does not converge). An alternative may be to consider a variational approach, or to consider the estimation of parameters alone. Despite this limitation, it may also be possible to filter timeseries of the parameters evolution (which is near interannual) to infer if the analysed decennal variability is in agreement with observed decennal changes in the ocean stratification (see chapter 5).

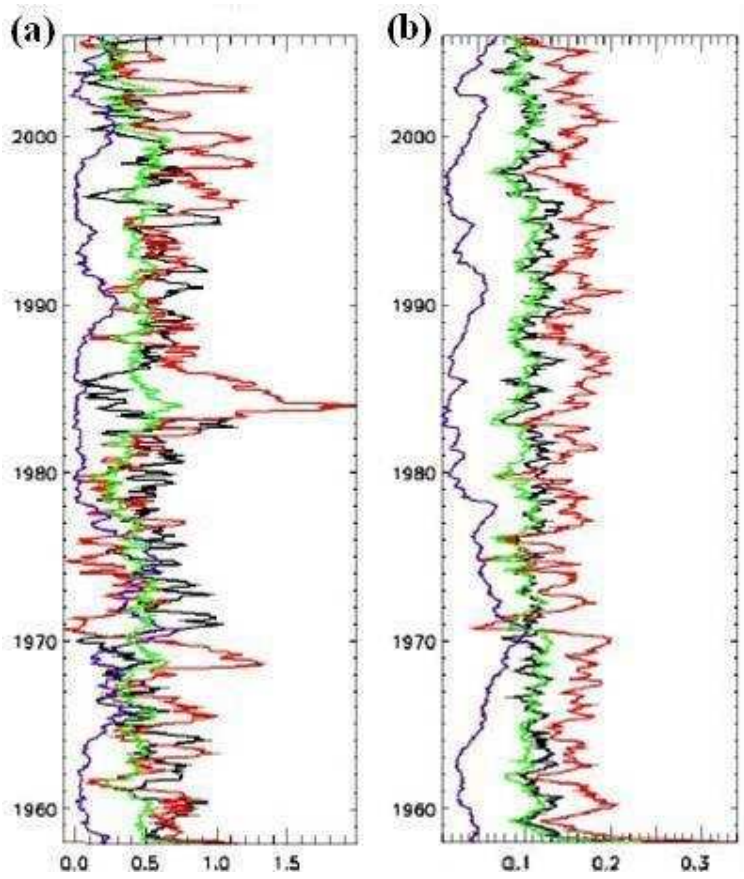

Figure A5.1: Evolution of corrected wind stress projection coefficients in the model LODCA, for (a) ensemble mean and (b) ensemble standard deviation of P_1 (black), P_2 (red), P_3 (blue), and $(P_1+ P_2+ P_3)/3$ (green), expressed in $(150\ mm)^{-1}$.

References

Author Publications

Thual, S., O. Thual, and B. Dewitte (2012a), Absolute or Convective instability in the equatorial Pacific and implications for ENSO, Q. J.Meteorol.Soc., 138:000-000. DOI:10.1002/qj.1988

Thual, S., B. Dewitte, S.-I. An, and N. Ayoub (2011), Sensitivity of ENSO to Stratification in a Recharge–Discharge Conceptual Model, J.Climate, **24**(16), 4332–4349.

Dewitte, B., J. Choi, S.-I. An, and S. Thual (2011), Vertical structure variability and equatorial waves during central Pacific and eastern Pacific El Niños in a coupled general circulation model, Clim.Dyn. pp. 1-15, doi:10.1007/s00382-011-1215-x

Dewitte, B., S. Thual, S.-W. Yeh, S.-I. An, B.-K. Moon, and B. S. Giese (2009), Low-Frequency Variability of Temperature in the Vicinity of the Equatorial Pacific Thermocline in SODA: Role of Equatorial Wave Dynamics and ENSO Asymmetry, J.Climate, 22(21), 5783–5795, doi:10.1175/2009JCLI2764.1.

Dewitte, B., S.-W. Yeh, and S. Thual (2012a), Reinterpreting the thermocline feedback in the western-central equatorial Pacific and its relationship with the ENSO modulation, Clim.Dyn, doi:10.1007/s00382-012-1504-z.

Next publications

Thual, S., B. Dewitte, S.-I. An, S. Illig, and N. Ayoub (2012c), Influence of Recent Stratification Changes on ENSO stability in a Conceptual Model of the Equatorial Pacific, submitted.

Thual, S., B. Dewitte, N. Ayoub, and O. Thual (2012d), A Recharge/Discharge Model of the Equatorial Pacific derived from Low-Frequency Approximation of First Equatorial Long-Waves Dynamics, submitted

Thual, S., N. Ayoub, and B. Dewitte (2012b), Constraint of the Recharge/Discharge Process of an Intermediate Complexity Model by Sea Level Assimilation, submitted.

References

An, S., and F. Jin (2000), An eigen analysis of the interdecadal changes in the structure and frequency of ENSO mode, Geophysical Research Letters, 27(16), 2573.

An, S.-I. (2009), A review of interdecadal changes in the nonlinearity of the El Niño-Southern Oscillation, Theoretical and Applied Climatology, 97(1-2), 29–40, doi:10.1007/s00704-008-0071-z.

An, S.-I. (2011), Atmospheric Responses of Gill-Type and Lindzen–Nigam Models to Global Warming, Journal of Climate, 24(23), 6165–6173, doi:10.1175/2011JCLI3971.

An, S.-I., and F.-F. Jin (2001), Collective Role of Thermocline and Zonal Advective Feedbacks in the ENSO Mode, Journal of Climate, 14(16), 3421–3432.

An, S.-I., and F.-F. Jin (2004), Nonlinearity and Asymmetry of ENSO, Journal of Climate, 17(12), 2399–2412, doi:10.1175/1520-0442(2004)017<2399:NAAOE>2.0.CO;2.

An, S.-I., and B. Wang (2000), Interdecadal Change of the Structure of the ENSO Mode and Its Impact on the ENSO Frequency, Journal of Climate, 13(12), 2044–2055.

An, S.-I., J.-S. Kug, Y.-G. Ham, and I.-S. Kang (2008), Successive Modulation of ENSO to the Future Greenhouse Warming, Journal of Climate, 21(1), 3–21, doi:10.1175/2007JCLI1500.1.

Ashok, K., S. K. Behera, S. A. Rao, H. Weng, and T. Yamagata (2007), El Niño Modoki and its possible teleconnection, J. Geophys. Res., 112.

Battisti, D. S., and A. C. Hirst (1989), Interannual Variability in a Tropical Atmosphere–Ocean Model: Influence of the Basic State, Ocean Geometry and Nonlinearity, Journal of the Atmospheric Sciences, 46(12), 1687–1712, doi:10.1175/1520-0469(1989)046<1687:IVIATA>2.0.CO;2.

Battisti, D. S., E. S. Sarachik, and A. C. Hirst (1999), A Consistent Model for the Large-Scale Steady Surface AtmosphericCirculation in the Tropics*, Journal of Climate, 12(10), 2956–2964, doi:10.1175/1520-0442(1999)012<2956:ACMFTL>2.0.CO;2.

Behringer, D. W., M. Ji, and A. Leetmaa (1998), An Improved Coupled Model for ENSO Prediction and Implications for Ocean Initialization. Part I: The Ocean Data Assimilation System, Monthly Weather Review, 126(4), 1013–1021, doi:10.1175/1520-0493(1998)126<1013:AICMFE>2.0.CO;2.

Bejarano, L., and F.-F. Jin (2008), Coexistence of Equatorial Coupled Modes of ENSO, Journal of Climate, 21(12), 3051–3067.

Belmadani, A., B. Dewitte, and S.-I. An (2010), ENSO Feedbacks and Associated Time Scales of Variability in a Multimodel Ensemble, Journal of Climate, 23(12), 3181–3204, doi:10.1175/2010JCLI2830.1.

Bennett, A. F., B. S. Chua, D. E. Harrison, and M. J. McPhaden (1998), Generalized Inversion of Tropical Atmosphere–Ocean Data and a Coupled Model of the Tropical Pacific, doi:10.1175/1520-0442(1998)011<1768:GIOTAO>2.0.CO;2.

Bennett, A. F., B. S. Chua, D. E. Harrison, and M. J. McPhaden (2000), Generalized Inversion of Tropical Atmosphere–Ocean (TAO) Data and a Coupled Model of the Tropical Pacific. Part II: The 1995–96 La Niña and 1997–98 El Niño, Journal of Climate, 13(15), 2770–2785, doi:10.1175/1520-0442(2000)013<2770:GIOTAO>2.0.CO;2.

Bjerknes, J. (1969), ATMOSPHERIC TELECONNECTIONS FROM THE EQUATORIAL PACIFIC, Monthly Weather Review, 97(3), 163–172, doi:10.1175/1520-0493(1969)097<0163:ATFTEP>2.3.CO;2.

Bjornsson, and S. A. Venegas (1997), A manual for EOF and SVD analysis of climatic data, 97-1.

Blumenthal, M. B., and M. A. Cane (1989), Accounting for Parameter Uncertainties in Model Verification: An Illustration with Tropical Sea Surface Temperature, Journal of Physical Oceanography, 19(6), 815–830, doi:10.1175/1520-0485(1989)019<0815:AFPUIM>2.0.CO;2.

Boulanger, J.-P., and C. Menkes (1995), Propagation and reflection of long equatorial waves in the Pacific Ocean during the 1992–1993 El Niño, J. Geophys. Res., 100(C12), PP. 25,041–25,059, doi:199510.1029/95JC02956.

Brown, J. N., and A. V. Fedorov (2008), Mean energy balance in the tropical Pacific Ocean, Journal of Marine Research, 66(1), 1–23, doi:10.1357/002224008784815757.

Brown, J. N., and A. V. Fedorov (2010), How Much Energy Is Transferred from the Winds to the Thermocline on ENSO Time Scales?, Journal of Climate, 23(6), 1563–1580, doi:10.1175/2009JCLI2914.1.

Brown, J. N., A. V. Fedorov, and E. Guilyardi (2010), How well do coupled models replicate ocean energetics relevant to ENSO?, Climate Dynamics, 36(11-12), 2147–2158, doi:10.1007/s00382-010-0926-8.

Buis, S., A. Piacentini, and D. Déclat (2006), PALM: a computational framework for assembling high performance computing applications, Concurrency and Computation: Practice and Experience, 18(2), 231–245, doi:10.1002/cpe.914.

Burgers, G. (2005), The simplest ENSO recharge oscillator, Geophysical Research Letters, 32(13), doi:10.1029/2005GL022951.

Burls, N. J., C. J. C. Reason, P. Penven, and S. G. Philander (2011), Similarities between the tropical Atlantic seasonal cycle and ENSO: An energetics perspective, J. Geophys. Res., 116, 25 PP., doi:201110.1029/2011JC007164.

Cane, M. A. (2005), The evolution of El Niño, past and future, Earth and Planetary Science Letters, 230(3-4), 227–240, doi:10.1016/j.epsl.2004.12.003.

Cane, M. A. (2010), Climate science: Decadal predictions in demand, Nature Geoscience, 3(4), 231–232, doi:10.1038/ngeo823.

Cane, M. A., and R. J. Patton (1984), A numerical model for low-frequency equatorial dynamics, Journal of physical oceanography, 14(12), 1853–1863.

Cañizares, R., A. Kaplan, M. A. Cane, D. Chen, and S. E. Zebiak (2001), Use of data assimilation via linear low-order models for the initialization of El Niño – Southern Oscillation predictions, J. Geophys. Res., 106(C12), PP. 30,947–30,959, doi:200110.1029/2000JC000622.

Carton, J. A., and B. S. Giese (2008), A Reanalysis of Ocean Climate Using Simple Ocean Data Assimilation (SODA), Monthly Weather Review, 136(8), 2999–3017, doi:10.1175/2007MWR1978.1.

Cassou, C. (2008), Intraseasonal interaction between the Madden Julian Oscillation and the North Atlantic Oscillation, Nature, 455(7212), 523–527, doi:10.1038/nature07286.

Chelton, D. B., R. A. deSzoeke, M. G. Schlax, K. El Naggar, and N. Siwertz (1998), Geographical Variability of the First Baroclinic Rossby Radius of Deformation, Journal of Physical Oceanography, 28(3), 433–460, doi:10.1175/1520-0485(1998)028<0433:GVOTFB>2.0.CO;2.

Chen, D. (2011), Indo-Pacific Tripole: AN Intrinsic Mode of Tropical Climate Variability, Advances in Geosciences, Volume 24: Ocean Science (OS), 24, 1.

Chen, D., and M. A. Cane (2008), El Niño prediction and predictability, Journal of Computational Physics, 227(7), 3625–3640, doi:10.1016/j.jcp.2007.05.014.

Chen, D., S. E. Zebiak, M. A. Cane, and A. J. Busalacchi (1997), Initialization and predictability of a coupled ENSO forecast model, Monthly weather review, 125(5), 773–788.

Chen, D., M. A. Cane, A. Kaplan, S. E. Zebiak, and D. Huang (2004), Predictability of El Nino over the past 148 years, Nature, 428(6984), 733–736, doi:10.1038/nature02439.

Choi, J., S.-I. An, B. Dewitte, and W. W. Hsieh (2009), Interactive Feedback between the Tropical Pacific Decadal Oscillation and ENSO in a Coupled General Circulation Model, Journal of climate, 22(24), 6597–6611.

Choi, J., S.-I. An, J.-S. Kug, and S.-W. Yeh (2011), The role of mean state on changes in El Niño's flavor, Climate Dynamics, 37(5-6), 1205–1215, doi:10.1007/s00382-010-0912-1.

Clarke, A. J. (2008), An introduction to the dynamics of El Niño and the southern oscillation, Academic Press.

Clarke, A. J. (2010), Analytical Theory for the Quasi-Steady and Low-Frequency Equatorial Ocean Response to Wind Forcing: The "Tilt" and "Warm Water Volume" Modes, Journal of Physical Oceanography, 40(1), 121–137.

Clarke, A. J., and S. Van Gorder (2003), Improving El Niño prediction using a space-time integration of Indo-Pacific winds and equatorial Pacific upper ocean heat content, Geophys. Res. Lett., 30, 4 PP., doi:200310.1029/2002GL016673.

Clarke, A. J., J. Wang, and S. Van Gorder (2000), A Simple Warm-Pool Displacement ENSO Model, Journal of Physical Oceanography, 30(7), 1679–1691, doi:10.1175/1520-0485(2000)030<1679:ASWPDE>2.0.CO;2.

Cobb, K. M., C. D. Charles, H. Cheng, and R. L. Edwards (2003), El Niño/Southern Oscillation and tropical Pacific climate during the last millennium, Nature, 424(6946), 271–276, doi:10.1038/nature01779.

Collins, M. et al. (2010), The impact of global warming on the tropical Pacific Ocean and El Nino, Nature Geoscience, 3(6), 391–397, doi:10.1038/ngeo868.

Courtier, P., J.-N. Thépaut, and A. Hollingsworth (1994), A strategy for operational implementation of 4D-Var, using an incremental approach, Quarterly Journal of the Royal Meteorological Society, 120(519), 1367–1387, doi:10.1002/qj.49712051912.

Delcroix, T., B. Dewitte, Y. duPenhoat, F. Masia, and J. Picaut (2000), Equatorial waves and warm pool displacements during the 1992–1998 El Niño Southern Oscillation events: Observation and modeling, J. Geophys. Res., 105(C11), PP. 26,045–26,062, doi:200010.1029/2000JC900113.

Dewitte, B. (2000), Sensitivity of an Intermediate Ocean–Atmosphere Coupled Model of the Tropical Pacific to Its Oceanic Vertical Structure, Journal of Climate, 13(13), 2363–2388, doi:10.1175/1520-0442(2000)013<2363:SOAIOA>2.0.CO;2.

Dewitte, B., and C. Perigaud (1996), El Niño-La Niña Events Simulated with Cane and Zebiak's Model and Observed with Satellite or In Situ Data. Part II: Model Forced with Observations, Journal of Climate, 9(6), 1188–1207, doi:10.1175/1520-0442(1996)009<1188:ENLNES>2.0.CO;2.

Dewitte, B., G. Reverdin, and C. Maes (1999), Vertical Structure of an OGCM Simulation of the Equatorial Pacific Ocean in 1985–94, Journal of Physical Oceanography, 29(7), 1542–1570, doi:10.1175/1520-0485(1999)029<1542:VSOAOS>2.0.CO;2.

Dewitte, B., D. Gushchina, Y. duPenhoat, and S. Lakeev (2002), On the importance of subsurface variability for ENSO simulation and prediction with intermediate coupled models of the Tropical Pacific: A case study for the 1997–1998 El Niño, Geophys. Res. Lett., 29, 5 PP., doi:200210.1029/2001GL014452.

Dewitte, B., S. Illig, L. Parent, Y. du Penhoat, L. Gourdeau, and J. Verron (2003), Tropical Pacific baroclinic mode contribution and associated long waves for the 1994–1999 period from an assimilation experiment with altimetric data, Journal of Geophysical Research, 108(C4), doi:10.1029/2002JC001362.

Dewitte, B., S.-W. Yeh, B.-K. Moon, C. Cibot, and L. Terray (2007), Rectification of ENSO Variability by Interdecadal Changes in the Equatorial Background Mean State in a CGCM Simulation, Journal of Climate, 20(10), 2002–2021, doi:10.1175/JCLI4110.1.

Dewitte, B., S. Thual, S.-W. Yeh, S.-I. An, B.-K. Moon, and B. S. Giese (2009), Low-Frequency Variability of Temperature in the Vicinity of the Equatorial Pacific Thermocline in SODA: Role of Equatorial Wave Dynamics and ENSO Asymmetry, Journal of Climate, 22(21), 5783–5795, doi:10.1175/2009JCLI2764.1.

Dewitte, B., S.-W. Yeh, and S. Thual (2012a), Reinterpreting the thermocline feedback in the western-central equatorial Pacific and its relationship with the ENSO modulation, Climate Dynamics, doi:10.1007/s00382-012-1504-z.

Dewitte, B., J. Choi, S.-I. An, and S. Thual (2012b), Vertical structure variability and equatorial waves during central Pacific and eastern Pacific El Niños in a coupled general circulation model, Climate Dynamics, 38(11-12), 2275–2289.

Dijkstra, H. A. (2006), The ENSO phenomenon: theory and mechanisms, Adv. Geosci., 6, 3–15, doi:10.5194/adgeo-6-3-2006.

Dimet, F.-X. L., and O. Talagrand (1986), Variational algorithms for analysis and assimilation of meteorological observations: theoretical aspects, Tellus A, 38A(2), 97–110, doi:10.1111/j.1600-0870.1986.tb00459.x.

DiNezio, P. N., A. C. Clement, G. A. Vecchi, B. J. Soden, B. P. Kirtman, and S.-K. Lee (2009), Climate Response of the Equatorial Pacific to Global Warming, Journal of Climate, 22(18), 4873–4892, doi:10.1175/2009JCLI2982.1.

Dommenget, D. (2010), The slab ocean El Niño, Geophysical Research Letters, 37(20).

Eisenman, I., L. Yu, and E. Tziperman (2005), Westerly Wind Bursts: ENSO's Tail Rather than the Dog?, Journal of Climate, 18(24), 5224–5238, doi:10.1175/JCLI3588.1.

Evensen, G. (2003), The Ensemble Kalman Filter: theoretical formulation and practical implementation, Ocean Dynamics, 53(4), 343–367, doi:10.1007/s10236-003-0036-9.

Evensen, G. (2007), Data Assimilation: The Ensemble Kalman Filter, Springer.

Evensen, G. (2009), The ensemble Kalman filter for combined state and parameter estimation: MONTE CARLO TECHNIQUES FOR DATA ASSIMILATION IN LARGE SYSTEMS, IEEE control systems, 29(3), 83–104.

Fedorov, A. V. (2007), Net energy dissipation rates in the tropical ocean and ENSO dynamics, Journal of climate, 20(6), 1108–1117.

Fedorov, A. V. (2010), Ocean Response to Wind Variations, Warm Water Volume, and Simple Models of ENSO in the Low-Frequency Approximation, Journal of Climate, 23(14), 3855–3873, doi:10.1175/2010JCLI3044.1.

Fedorov, A. V., and S. G. Philander (2000), Is El Niño Changing?, Science, 288(5473), 1997–2002, doi:10.1126/science.288.5473.1997.

Fedorov, A. V., and S. G. Philander (2001), A Stability Analysis of Tropical Ocean–Atmosphere Interactions: Bridging Measurements and Theory for El Niño, Journal of Climate, 14(14), 3086–3101.

Fischer, M., M. Latif, M. Flügel, and M. Ji (1997), The Impact of Data Assimilation on ENSO Simulations and Predictions, Monthly Weather Review, 125(5), 819–830, doi:10.1175/1520-0493(1997)125<0819:TIODAO>2.0.CO;2.

Gelb, A. (1974), Applied Optimal Estimation, MIT Press.

Gent, P. R., K. Óneill, and M. A. Cane (1983), A model of the semiannual oscillation in the equatorial Indian Ocean, Journal of physical oceanography, 13(12), 2148–2160.

Giese, B. S., and S. Ray (2011), El Niño variability in simple ocean data assimilation (SODA), 1871–2008, J. Geophys. Res., 116, 17 PP., doi:201110.1029/2010JC006695.

Gill, A. E. (1980), Some simple solutions for heat-induced tropical circulation, Quarterly Journal of the Royal Meteorological Society, 106(449), 447–462, doi:10.1002/qj.49710644905.

Goddard, L., and S. G. Philander (2000), The Energetics of El Niño and La Niña, Journal of Climate, 13(9), 1496–1516, doi:10.1175/1520-0442(2000)013<1496:TEOENO>2.0.CO;2.

Guilderson, T. P., and D. P. Schrag (1998), Abrupt Shift in Subsurface Temperatures in the Tropical Pacific Associated with Changes in El Niño, Science, 281(5374), 240–243, doi:10.1126/science.281.5374.240.

Guilyardi, E., A. Wittenberg, A. Fedorov, M. Collins, C. Wang, A. Capotondi, G. J. van Oldenborgh, and T. Stockdale (2009), Understanding El Niño in Ocean–Atmosphere General Circulation Models: Progress and Challenges, Bulletin of the American Meteorological Society, 90(3), 325–340, doi:10.1175/2008BAMS2387.1.

Ham, Y.-G., J.-S. Kug, and I.-S. Kang (2009), Optimal initial perturbations for El Nino ensemble prediction with ensemble Kalman filter, Climate Dynamics, 33(7-8), 959–973, doi:10.1007/s00382-009-0582-z.

Harrison, D. E., and G. A. Vecchi (1997), Westerly Wind Events in the Tropical Pacific, 1986–95*, Journal of Climate, 10(12), 3131–3156.

Hirst, A. C. (1986), Unstable and Damped Equatorial Modes in Simple Coupled Ocean-Atmosphere Models, Journal of the Atmospheric Sciences, 43(6), 606–632.

Hsiang, S. M., K. C. Meng, and M. A. Cane (2011), Civil conflicts are associated with the global climate, Nature, 476(7361), 438–441, doi:10.1038/nature10311.

Huerre, P., and P. A. Monkewitz (1990), Local And Global Instabilities In Spatially Developing Flows, Annual Review of Fluid Mechanics, 22(1), 473–537.

Illig, S., and B. Dewitte (2006), Local Coupled Equatorial Variability versus Remote ENSO Forcing in an Intermediate Coupled Model of the Tropical Atlantic, Journal of Climate, 19(20), 5227–5252, doi:10.1175/JCLI3922.1.

IPCC (2007), Climate Change 2007: Synthesis Report. Contribution of Working Groups I, II and III to the Fourth Assessment Report of the Intergovernmental Panel on Climate Change [Core Writing Team, Pachauri, R.K and Reisinger, A. (eds.)], IPCC, Geneva, Switzerland, 104 pp.

Izumo, T., J. Vialard, M. Lengaigne, C. de B. Montegut, S. K. Behera, J.-J. Luo, S. Cravatte, S. Masson, and T. Yamagata (2010), Influence of the state of the Indian Ocean Dipole on the following year's El Niño, Nature Geoscience, 3(3), 168–172, doi:10.1038/ngeo760.

Jansen, M. F., D. Dommenget, and N. Keenlyside (2009), Tropical Atmosphere–Ocean Interactions in a Conceptual Framework, Journal of Climate, 22(3), 550–567, doi:10.1175/2008JCLI2243.1.

Jin, F.-F. (1997a), An Equatorial Ocean Recharge Paradigm for ENSO. Part I: Conceptual Model, Journal of the Atmospheric Sciences, 54(7), 811–829.

Jin, F.-F. (1997b), An Equatorial Ocean Recharge Paradigm for ENSO. Part II: A Stripped-Down Coupled Model, Journal of the Atmospheric Sciences, 54(7), 830–847, doi:10.1175/1520-0469(1997)054<0830:AEORPF>2.0.CO;2.

Jin, F.-F., and S.-I. An (1999), Thermocline and Zonal Advective Feedbacks Within the Equatorial Ocean Recharge Oscillator Model for ENSO, Geophys. Res. Lett., 26(19), PP. 2989–2992, doi:199910.1029/1999GL002297.

Jin, F.-F., J. D. Neelin, and M. Ghil (1994), El Nino on the Devil's Staircase: Annual Subharmonic Steps to Chaos, Science, 264(5155), 70–72.

Jin, F.-F., S. T. Kim, and L. Bejarano (2006), A coupled-stability index for ENSO, Geophys. Res. Lett., 33, 5 PP., doi:200610.1029/2006GL027221.

Jin, F.-F., L. Lin, A. Timmermann, and J. Zhao (2007), Ensemble-mean dynamics of the ENSO recharge oscillator under state-dependent stochastic forcing, Geophys. Res. Lett., 34, 5 PP., doi:200710.1029/2006GL027372.

Kalman, R. (1960), A New Approach to Linear Filtering and Prediction Problems, Transactions of the ASME – Journal

of Basic Engineering, (82 (Series D)), 35–45.

Kang, I.-S., J.-S. Kug, S.-I. An, and F.-F. Jin (2004), A Near-Annual Pacific Ocean Basin Mode, Journal of Climate, 17(12), 2478–2488.

Keenlyside, N., and R. Kleeman (2002), Annual cycle of equatorial zonal currents in the Pacific, J. Geophys. Res., 107, 13 PP., doi:200210.1029/2000JC000711.

Kessler, W. S. (2002), Is ENSO a cycle or a series of events?, Geophysical Research Letters, 29(23).

Kim, S. T., and F.-F. Jin (2010a), An ENSO stability analysis. Part I: results from a hybrid coupled model, Climate Dynamics, 36(7-8), 1593–1607, doi:10.1007/s00382-010-0796-0.

Kim, S. T., and F.-F. Jin (2010b), An ENSO stability analysis. Part II: results from the twentieth and twenty-first century simulations of the CMIP3 models, Climate Dynamics, 36(7-8), 1609–1627, doi:10.1007/s00382-010-0872-5.

Kirtman, B. P., and P. S. Schopf (1998), Decadal Variability in ENSO Predictability and Prediction, Journal of Climate, 11(11), 2804–2822, doi:10.1175/1520-0442(1998)011<2804:DVIEPA>2.0.CO;2.

Kleeman, R. (2008), Stochastic theories for the irregularity of ENSO, Philosophical Transactions of the Royal Society A: Mathematical, Physical and Engineering Sciences, 366(1875), 2509 –2524.

Kleeman, R., A. M. Moore, and N. R. Smith (1995), Assimilation of subsurface thermal data into a simple ocean model for the initialization of an intermediate tropical coupled ocean-atmosphere forecast model, Monthly weather review, 123(10), 3103–3113.

Kondrashov, D., and et al. (2008), Data Assimilation for a Coupled Ocean–Atmosphere Model. Part II: Parameter Estimation, Monthly Weather Review, 136.

Kug, J.-S., F.-F. Jin, and S.-I. An (2009), Two Types of El Niño Events: Cold Tongue El Niño and Warm Pool El Niño, Journal of Climate, 22(6), 1499–1515.

Kug, J.-S., Y.-G. Ham, M. Kimoto, F.-F. Jin, and I.-S. Kang (2010a), New approach for optimal perturbation method in ensemble climate prediction with empirical singular vector, Climate dynamics, 35(2-3), 331–340.

Kug, J.-S., J. Choi, S.-I. An, F.-F. Jin, and A. T. Wittenberg (2010b), Warm Pool and Cold Tongue El Nino Events as Simulated by the GFDL 2.1 Coupled GCM, J. Clim., 23(5), 1226–1239, doi:10.1175/2009JCLI3293.1.

Latif, M., D. Anderson, T. Barnett, M. Cane, R. Kleeman, A. Leetmaa, J. O'Brien, A. Rosati, and E. Schneider (1998), A review of the predictability and prediction of ENSO, J. Geophys. Res., 103(C7), PP. 14,375–14,393, doi:199810.1029/97JC03413.

Lee, T., and M. J. McPhaden (2010), Increasing intensity of El Niño in the central-equatorial Pacific, Geophys. Res. Lett., 37, 5 PP., doi:201010.1029/2010GL044007.

Lee, Y.-K., S.-W. Yeh, B. Dewitte, B.-K. Moon, and J.-G. Jhun (2011), The influences of interannual stratification variability and wind stress forcing on ENSO before and after the 1976 climate shift, Theoretical and Applied Climatology, 107(3-4), 623–631, doi:10.1007/s00704-011-0514-9.

Lengaigne, M., U. Hausmann, G. Madec, C. Menkes, J. Vialard, and J. M. Molines (2011), Mechanisms controlling warm water volume interannual variations in the equatorial Pacific: diabatic versus adiabatic processes, Climate Dynamics, doi:10.1007/s00382-011-1051-z.

Lindzen, R. S., and S. Nigam (1987), On the Role of Sea Surface Temperature Gradients in Forcing Low-Level Winds and Convergence in the Tropics, Journal of the Atmospheric Sciences, 44(17), 2418–2436, doi:10.1175/1520-0469(1987)044<2418:OTROSS>2.0.CO;2.

Lloyd, J., E. Guilyardi, H. Weller, and J. Slingo (2009), The role of atmosphere feedbacks during ENSO in the CMIP3 models, Atmospheric Science Letters, 10(3), 170–176.

MacMynowski, D. G., and E. Tziperman (2008), Factors Affecting ENSO's Period, Journal of the Atmospheric Sciences, 65(5), 1570–1586, doi:10.1175/2007JAS2520.1.

Maes, C., J. Picaut, and S. Belamari (2002), Salinity barrier layer and onset of El Niño in a Pacific coupled model, Geophys. Res. Lett., 29, 4 PP., doi:200210.1029/2002GL016029.

Mantua, N., and S. Hare (2002), The Pacific Decadal Oscillation, Journal of Oceanography, 58(1), 35–44, doi:10.1023/A:1015820616384.

McCreary, J. P. (1981), A Linear Stratified Ocean Model of the Equatorial Undercurrent, Philosophical Transactions of the Royal Society of London. Series A, Mathematical and Physical Sciences, 298(1444), 603–635.

McPhaden, M. J. (2012), A 21st Century Shift in the Relationship between ENSO SST and Warm Water Volume Anomalies, Geophys. Res. Lett., doi:10.1029/2012GL051826.

McPhaden, M. J. et al. (1998), The Tropical Ocean-Global Atmosphere observing system: A decade of progress, Journal of geophysical research, 103(C7), 14169–14240.

McPhaden, M. J., S. E. Zebiak, and M. H. Glantz (2006), ENSO as an Integrating Concept in Earth Science, Science, 314(5806), 1740–1745, doi:10.1126/science.1132588.

Majda, A., and S. Stechmann (2009), The Skeleton of Tropical Intraseaonal Oscillations, PNAS, 106(21), 8417-8422.

Meinen, C. S., and M. J. McPhaden (2000), Observations of Warm Water Volume Changes in the Equatorial Pacific and Their Relationship to El Niño and La Niña, Journal of Climate, 13(20), 3551–3559.

Miller, R. N., and M. A. Cane (1989), A Kalman Filter Analysis of Sea Level Height in the Tropical Pacific, , doi:10.1175/1520-0485(1989)019<0773:AKFAOS>2.0.CO;2.

Monahan, A. H., J. C. Fyfe, M. H. P. Ambaum, D. B. Stephenson, and G. R. North (2009), Empirical Orthogonal Functions: The Medium is the Message, Journal of Climate, 22(24), 6501–6514, doi:10.1175/2009JCLI3062.1.

Moon, B.-K., S.-W. Yeh, B. Dewitte, J.-G. Jhun, I.-S. Kang, and B. P. Kirtman (2004), Vertical structure variability in the equatorial Pacific before and after the Pacific climate shift of the 1970s, Geophys. Res. Lett., 31, 4 PP., doi:200410.1029/2003GL018829.

Neelin, J., M. Latif, and F.-F. Jin (1994), Dynamics of Coupled Ocean-Atmosphere Models: The Tropical Problem, Annual Review of Fluid Mechanics, 26(1), 617–659.

Neelin, J. D. (1989), On the Intepretation of the Gill Model, Journal of the Atmospheric Sciences, 46(15), 2466–2468, doi:10.1175/1520-0469(1989)046<2466:OTIOTG>2.0.CO;2.

Neelin, J. D. (1991), The Slow Sea Surface Temperature Mode and the Fast-Wave Limit: Analytic Theory for Tropical Interannual Oscillations and Experiments in a Hybrid Coupled Model, Journal of the Atmospheric Sciences, 48(4), 584–606.

Neelin, J. D., D. S. Battisti, A. C. Hirst, F.-F. Jin, Y. Wakata, T. Yamagata, and S. E. Zebiak (1998), ENSO theory, Journal of Geophysical Research, 103(C7), 14261–14290.

Park, W., N. Keenlyside, M. Latif, A. Ströh, R. Redler, E. Roeckner, and G. Madec (2009), Tropical Pacific Climate and Its Response to Global Warming in the Kiel Climate Model, Journal of Climate, 22(1), 71–92, doi:10.1175/2008JCLI2261.1.

Philander, S. G., and A. Fedorov (2003), Is El Niño sporadic or cyclic?, Annual Review of Earth and Planetary Sciences, 31(1), 579–594.

Picaut, J., C. Menkès, J.-P. Boulanger, and Y. du Penhoat (1993), Dissipation in the Pacific Equatorial long wave model, TOGA Notes, 11–15.

Picaut, J., F. Masia, and Y. du Penhoat (1997), An Advective-Reflective Conceptual Model for the Oscillatory Nature of the ENSO, Science, 277(5326), 663 –666.

Press, W. H., S. A. Teukolsky, W. T. Vetterling, and B. P. Flannery (2007), Numerical Recipes 3rd Edition: The Art of Scientific Computing, 3rd ed., Cambridge University Press.

Schneider, E. K., B. Huang, Z. Zhu, D. G. Dewitt, J. L. Kinter, B. P. Kirtman, and J. Shukla (1999), Ocean data assimilation, initialization, and predictions of ENSO with a coupled GCM, Monthly weather review, 127(6), 1187–1207.

Schopf, P. S., and R. J. Burgman (2006), A Simple Mechanism for ENSO Residuals and Asymmetry, Journal of Climate, 19(13), 3167–3179.

Seager, R., A. R. Karspeck, M. A. Cane, Y. Kushnir, A. Giannini, A. Kaplan, B. Kerman, and J. Velez (2004), Predicting Pacific decadal variability, Geophysical monograph, 147, 105–120.

Shu, L., and A. J. Clarke (2002), Using an Ocean Model to Examine ENSO Dynamics, Journal of Physical Oceanography, 32(3), 903–923, doi:10.1175/1520-0485(2002)032<0903:UAOMTE>2.0.CO;2.

Singh, A., T. Delcroix, and S. Cravatte (2011), Contrasting the flavors of El Niño-Southern Oscillation using sea surface salinity observations, J. Geophys. Res., 116, 16 PP., doi:201110.1029/2010JC006862.

Stein, K., A. Timmermann, and N. Schneider (2011), Phase Synchronization of the El Niño-Southern Oscillation with the Annual Cycle, Physical Review Letters, 107(12), doi:10.1103/PhysRevLett.107.128501.

Stevenson, S., B. Fox-Kemper, M. Jochum, R. Neale, C. Deser, and G. Meehl (2012), Will There Be a Significant Change to El Niño in the Twenty-First Century?, Journal of Climate, 25(6), 2129–2145, doi:10.1175/JCLI-D-11-00252.1.

Suarez, M. J., and P. S. Schopf (1988), A Delayed Action Oscillator for ENSO, Journal of the Atmospheric Sciences, 45(21), 3283–3287.

Sun, C., Z. Hao, M. Ghil, and J. D. Neelin (2002), Data Assimilation for a Coupled Ocean–Atmosphere Model. Part I: Sequential State Estimation, Monthly Weather Review, 130(5), 1073–1099, doi:10.1175/1520-0493(2002)130<1073:DAFACO>2.0.CO;2.

Sun, D.-Z., and T. Zhang (2006), A regulatory effect of ENSO on the time-mean thermal stratification of the equatorial upper ocean, Geophys. Res. Lett., 33, 4 PP., doi:200610.1029/2005GL025296.

Suslov, S. A. (2006), Numerical aspects of searching convective/absolute instability transition, Journal of Computational Physics, 212(1), 188–217.

Takahashi, K., A. Montecinos, K. Goubanova, and B. Dewitte (2011), ENSO regimes: Reinterpreting the canonical and Modoki El Niño, Geophys. Res. Lett., 38, 5 PP., doi:201110.1029/2011GL047364.

Talagrand, O., and P. Courtier (1987), Variational Assimilation of Meteorological Observations With the Adjoint Vorticity Equation. I: Theory, Quarterly Journal of the Royal Meteorological Society, 113(478), 1311–1328, doi:10.1002/qj.49711347812.

Tang, Y., and W. W. Hsieh (2003), ENSO simulation and prediction in a hybrid coupled model with data assimilation, Journal of the Meteorological Society of Japan, 81(1), 1–19.

Terray, L., O. Thual, S. Belamari, M. Deque, P. Dandin, P. Delecluse, and C. Levy (1995), Climatology and Interannual Variability Simulated by the Arpege-Opa Coupled Model, Clim. Dyn., 11(8), 487–505, doi:10.1007/s003820050090.

Thual, S., B. Dewitte, S.-I. An, and N. Ayoub (2011), Sensitivity of ENSO to Stratification in a Recharge–Discharge Conceptual Model, Journal of Climate, 24(16), 4332–4349.

Thual, S., O. Thual, and B. Dewitte (2012a), Absolute or Convective instability in the equatorial Pacific and implications for ENSO, Quarterly Journal of the Royal Meteorological Society, 138, 000–000, doi:10.1002/qj.1988.

Thual, S., N. Ayoub, and B. Dewitte (2012b), Constraint of the Recharge/Discharge Process of an Intermediate Complexity Model by Sea Level Assimilation, submitted.

Thual, S., B. Dewitte, S.-I. An, S. Illig, and N. Ayoub (2012c), Influence of Recent Stratification Changes on ENSO stability in a Conceptual Model of the Equatorial Pacific, submitted

Thual, S., B. Dewitte, N. Ayoub, and O. Thual (2012d), A Recharge/Discharge Model of the Equatorial Pacific derived from Low-Frequency Approximation of First Equatorial Long-Waves Dynamics, submitted

Timmermann, A., and F.-F. Jin (2008), ENSO instability revisited, Geophsyical Research Abstracts, 10.

Timmermann, A., J. Oberhuber, A. Bacher, M. Esch, M. Latif, and E. Roeckner (1999), Increased El Nino frequency in a climate model forced by future greenhouse warming, Nature, 398(6729), 694–697, doi:10.1038/19505.

Timmermann, A., F.-F. Jin, and J. Abshagen (2003), A Nonlinear Theory for El Niño Bursting, Journal of the Atmospheric Sciences, 60(1), 152–165.

Torrence, C., and P. J. Webster (1999), Interdecadal changes in the ENSO-monsoon system, Journal of climate, 12(8), 2679–2690.

Tziperman, E., L. Stone, M. A. Cane, and H. Jarosh (1994), El Niño Chaos: Overlapping of Resonances Between the Seasonal Cycle and the Pacific Ocean-Atmosphere Oscillator, Science, 264(5155), 72 –74.

Ueno, G., T. Higuchi, T. Kagimoto, and N. Hirose (2004), Application of ensemble Kalman filter to coupled atmosphere-ocean model, AGU Fall Meeting Abstracts, -1, 0846.

Vecchi, G. A., and B. J. Soden (2007), Global Warming and the Weakening of the Tropical Circulation, Journal of Climate, 20(17), 4316–4340, doi:10.1175/JCLI4258.1.

Wang, B., and Y. Wang (1996), Temporal Structure of the Southern Oscillation as Revealed by Waveform and Wavelet Analysis, Journal of Climate, 9(7), 1586–1598, doi:10.1175/1520-0442(1996)009<1586:TSOTSO>2.0.CO;2.

Wang, B., and X. Xie (1998), Coupled Modes of the Warm Pool Climate System. Part I: The Role of Air–Sea Interaction in Maintaining Madden–Julian Oscillation, Journal of Climate, 11(8), 2116–2135.

Wang, C., and J. Picaut (2004), Understanding ENSO physics: A review, Geophysical monograph, 147, 21–48.

Weaver, A. T., J. Vialard, and D. L. T. Anderson (2003), Three- and Four-Dimensional Variational Assimilation with a General Circulation Model of the Tropical Pacific Ocean. Part I: Formulation, Internal Diagnostics, and Consistency Checks, Monthly Weather Review, 131(7), 1360–1378, doi:10.1175/1520-0493(2003)131<1360:TAFVAW>2.0.CO;2.

Weisberg, R. H., and C. Wang (1997), A Western Pacific Oscillator Paradigm for the El Niño-Southern Oscillation, Geophysical Research Letters, 24(7), 779.

Wunsch, C. (1996), The Ocean Circulation Inverse Problem, Cambridge University Press.

Yeh, S., B. Dewitte, J. Jhun, and I. Kang (2001), The characteristic oscillation induced by coupled processes between oceanic vertical modes and atmospheric modes in the tropical Pacific, Geophys. Res. Lett., 28(14), PP. 2847–2850, doi:200110.1029/2001GL012854.

Yeh, S.-W., J.-S. Kug, B. Dewitte, M.-H. Kwon, B. P. Kirtman, and F.-F. Jin (2009), El Nino in a changing climate, Nature, 461(7263), 511–514.

Yeh, S.-W., B. P. Kirtman, J.-S. Kug, W. Park, and M. Latif (2011), Natural variability of the central Pacific El Niño

event on multi-centennial timescales, Geophys. Res. Lett., 38, 5 PP., doi:201110.1029/2010GL045886.

Yu, J.-Y., H.-Y. Kao, T. Lee, and S. T. Kim (2011), Subsurface ocean temperature indices for Central-Pacific and Eastern-Pacific types of El Nino and La Nina events, Theoretical and applied climatology, 103(3-4), 337–344.

Zebiak, S. E., and M. A. Cane (1987), A model El Niño-Southern Oscillation, Monthly weather review, 115(10), 2262–2278.

Zelle, H., G. Appeldoorn, G. Burgers, and G. J. van Oldenborgh (2004), The Relationship between Sea Surface Temperature and Thermocline Depth in the Eastern Equatorial Pacific, Journal of Physical Oceanography, 34(3), 643–655, doi:10.1175/2523.1.

Zhang, C. (2005), Madden-Julian Oscillation, Rev. Geophys., 43, 36 PP., doi:200510.1029/2004RG000158.

Zheng, F., and J. Zhu (2010), Coupled assimilation for an intermediated coupled ENSO prediction model, Ocean Dyn., 60(5), 1061–1073, doi:10.1007/s10236-010-0307-1.

Zheng, F., J. Zhu, R.-H. Zhang, and G.-Q. Zhou (2006), Ensemble hindcasts of SST anomalies in the tropical Pacific using an intermediate coupled model, Geophys. Res. Lett., 33, 5 PP., doi:200610.1029/2006GL026994.

Table of Figures